UNIVERSITY OF CALIFORNIA SAN DIEGO

Springs and Wings: A robotic study of the insect flight system

A dissertation submitted in partial satisfaction of the
requirements for the degree Doctor of Philosophy

in

Engineering Sciences (Mechanical Engineering)

by

James Edmund Lynch

Committee in charge:

Professor Nick Gravish, Chair
Professor Shengqiang Cai
Professor Nigel Goldenfeld
Professor Miroslav Krstic
Professor Simon Sponberg

2023

The Dissertation of James Edmund Lynch is approved, and it is acceptable in quality and form for publication on microfilm and electronically.

University of California San Diego

2023

DEDICATION

To my parents, for their constant support and unwavering confidence that I can achieve whatever I set my mind to, and to Sarah, for helping me remember that there's a life outside the lab, too.

EPIGRAPH

One of the characteristics of modern biology is the breakdown of the boundaries which separate its subdivisions, and nowhere is this more fruitful than in behavioural studies where mechanics and physiology are integral to a more profound understanding.

J.W.S. Pringle (1957)

TABLE OF CONTENTS

LIST OF FIGURES

LIST OF TABLES

ACKNOWLEDGEMENTS

Chapter 1, in full, is a reprint of the material as it appears in the Journal of the Royal Society Interface as *Lynch J, Gau J, Sponberg S, Gravish N. Dimensional analysis of spring-wing systems reveals performance metrics for resonant flapping-wing flight, 2021*. The dissertation author was the primary investigator and first author of this paper.

Chapter 2, in full, is currently being prepared for submission for publication in Bioinspiration & Biomimetics as *Lynch J, Wold ES, Gau J, Sponberg S, Gravish N. Energetic and Control Tradeoffs in Spring-Wing Systems, 2023*. The dissertation author was the primary investigator and first author of this material.

Chapter 3, in part, is a reprint of the material as it appears in *Lynch J, Gau J, Sponberg S, Gravish N. Autonomous Actuation of Flapping Wing Robots Inspired by Asynchronous Insect Muscle. In: 2022 IEEE International Conference on Robotics and Automation (ICRA). Philadelphia, PA; 2022*. The dissertation author was the primary investigator and first author of this paper.

Chapter 4, in full, has been accepted for publication to appear in Nature as *Gau J, Lynch J, Aiello B, Wold ES, Gravish N, Sponberg S. Biophysical transitions in insect flight dynamics are bridged by common muscle physiology, 2023*. The dissertation author contributed equally with Gau and Aiello, and is co-first author of the paper.

VITA

2015	BS, Mechanical & Industrial Engineering, University of Massachusetts Amherst
2019	MS, Engineering Sciences (Mechanical Engineering), University of California San Diego
2018–2021	Teaching Assistant, Department of Mechanical & Aerospace Engineering University of California San Diego
2022	Instructor of Record, Matlab Programming for Engineering Analysis, Department of Mechanical & Aerospace Engineering, University of California San Diego
2023	PhD, Engineering Sciences (Mechanical Engineering), University of California San Diego

PUBLICATIONS

Lynch J, Wold ES, Gau J, Sponberg S, Gravish N. Energetic and Control Tradeoffs in Spring-Wing Systems. *Bioinspir. Biomim.* 2023 (in prep)

*Gau J, ***Lynch J**, *Aiello B, Wold ES, Gravish N, Sponberg S. Biophysical transitions in insect flight dynamics are bridged by common muscle physiology. *Nature*. 2023 (accepted, co-first author)

Delson N, **Lynch J**. Developing a Curiosity Mindset in Engineering Undergraduates Via Hands-On, Inquiry-Based Learning Activities with Hidden Discoveries. *In: 2023 ASEE Annual Conference & Exposition Proceedings*. 2023 (accepted)

Wold ES, **Lynch J**, Gravish N, Sponberg S. Structural damping renders the hawkmoth exoskeleton mechanically insensitive to non-sinusoidal deformations. *J R Soc Interface*. 2023 May;20(202):20230141.

Gao H, **Lynch J**, Gravish N. Soft Molds with Micro-Machined Internal Skeletons Improve Robustness of Flapping-Wing Robots. *Micromachines*. 2022 Sep 7;13(9).

Gao H, **Lynch J**, Gravish N. A compliant thorax design for robustness and elastic energy exchange in flapping-wing robots. *In: 2022 IEEE/RSJ International Conference on Intelligent Robots and Systems (IROS)*. 2022. p. 2693–700.

Lynch J, Gau J, Sponberg S, Gravish N. Autonomous Actuation of Flapping Wing Robots Inspired by Asynchronous Insect Muscle. *In: 2022 IEEE International Conference on Robotics and Automation (ICRA)*. Philadelphia, PA; 2022.

Gau J, Wold ES, **Lynch J**, Gravish N, Sponberg S. The hawkmoth wingbeat is not at resonance. *Biol Lett*. 2022 May;18(5):20220063.

Gau J, Gemilere R, (FM subteam) LV, **Lynch J**, Gravish N, Sponberg S. Rapid frequency modulation in a resonant system: aerial perturbation recovery in hawkmoths. *Proceedings of the Royal Society B: Biological Sciences*. 2021 May 26;288(1951):20210352.

Lynch J, Gau J, Sponberg S, Gravish N. Dimensional analysis of spring-wing systems reveals performance metrics for resonant flapping-wing flight. *J R Soc Interface*. 2021 Feb 17;18:20200888.

ABSTRACT OF THE DISSERTATION

Springs and Wings: A robotic study of the insect flight system

by

James Edmund Lynch

Doctor of Philosophy in Engineering Sciences (Mechanical Engineering)

University of California San Diego, 2023

Professor Nick Gravish, Chair

In the last decade, roboticists have had significant success building centimeter-scale flapping wing micro aerial vehicles (FWMAVs) inspired by the flight of insects. Evidence suggests that insects store and release energy in the thoracic exoskeleton to improve energy efficiency by flapping at resonance. Insect-inspired micro flying robots have also leveraged resonance to improve efficiency, but they have discovered that operating at the resonant frequency leads to issues with flight control. This research seeks to investigate the roles that elasticity, aerodynamics, and muscle dynamics play in the emergent dynamics of flapping flight by studying elastic flapping *spring-wing* systems using dynamically-scaled *robophysical* models of spring-wings. Studying the dynamics of a robot with comparable features enables the validation of

models from biology that are otherwise difficult to test in living insects, the generation of new hypotheses, and the development of novel FWMAV designs.

In Chapter 1, the spring-wing system is characterized via a nonlinear spring-mass-damper model. A robophysical model validates that such systems gain energetic benefits from operating at resonance, but reveals that the benefit scales with an underappreciated dimensionless ratio of inertial to aerodynamic forces, the Weis-Fogh number. We show through dimensional analysis that any real system, living or robotic, must balance the mechanical advantage gained from operating at resonance with diminishing returns in efficiency. Chapter 2 further explores the impact of the Weis-Fogh number on flapping dynamics, showing that responsiveness to control inputs is reduced and resistance to environmental perturbations is increased as the dimensionless ratio increases. Together with calculations of Weis-Fogh number in insects, these studies illustrate tradeoffs that drive evolution of resonant flight in nature and guide development of future FWMAVs with elastic energy exchange.

In the second half of the thesis, muscle dynamics are introduced in the form of a simplified model of self-excited asynchronous insect muscle. In Chapter 3, a form of velocity feedback, adapted from experiments on insect flight muscle, is developed and integrated with the spring-wing model, producing a system that generates steady flapping via limit-cycle oscillations despite the absence of periodic control inputs. The model is explored analytically, in simulation, and via implementation on the robotic spring-wing. Novel dynamic characteristics that enable adaptation to damage and passive response to wing collisions are described. Chapter 4 leverages the asynchronous feedback model as part of an interdisciplinary study of the evolution of asynchronous muscle. Phylogenetic analysis, direct measurement of insect muscle dynamics, and experiments on the robophysical system show that evolutionary transitions between periodically-forced and self-excited insect muscle were likely made possible by a ”bridge” in the dynamic parameter space that could be traversed under specific conditions. The asynchronous spring-wing model provides new insight into the flight and evolution of some of the most agile insects in nature, and presents a novel adaptive control scheme for future FWMAVs.

Introduction

0.1 Introduction & Background

Insects are the most speciose group of animals and are among the most successful and diverse groups of flying animals in history. Insect flight first evolved 350-400 million years ago during the Carboniferous period [1]. Since then, insect morphology has diversified such that today we can observe flying insects that vary in size from near-microscopic featherwing beetles (400 μm, 2.3 μg)[2] to giant silk moths with wingspans exceeding 25 centimeters and Goliath beetles whose mass exceeds 100 grams. Insects also feature a huge variety of wing sizes and shapes [3], muscle and thorax structures [4], [5], and flight control strategies [6]. They are ubquitous all over the world, in a large range of climates, and many are capable of impressive aerial maneuvers, long-distance travel, and/or navigating complex 3D environments to find food and avoid predation.

It is no surprise, then, that as roboticists sought to develop smaller and smaller flying robots, they looked to insects for inspiration. Despite the success of fixed-wing and rotor-based designs for larger unmanned aerial vehicles (UAVs), the scaling of electric motors and aerodynamic effects as robots get smaller means that traditional aircraft may be less efficient at the centimeter scale and smaller [7], [8]. On the other hand, as the mechanisms of flapping aerodynamics became more well understood [9], [10] and advances in micro-fabrication [11] and novel actuator designs [12] made miniaturization possible, the 2010's saw an explosion of interest in insect-scale, bioinspired flapping-wing micro-aerial vehicles (FWMAVs). Today, researchers have achieved controlled flight on tethered [13], [14] and untethered [15]–[18] FWMAVs at the

centimeter scale. They have integrated sensors [19]–[22] and implemented robots with a wide range of actuators including piezoelectric bending actuators, mini DC motors [23]–[25], soft DEA actuators [26], [27], and electromagnetic coils [28]. Others have developed autonomous control algorithms that can achieve not just stable hovering, but also impressive feats of agility [29].

However, the performance of insect-inspired FWMAVs still lags significantly behind that of insects in nature. This is due to limitations in fabrication, actuators, and battery power density, but also due to the complexity of nonlinear, history-dependent aerodynamics surrounding the flapping wing. Additionally, there remain gaps in the understanding of the insect flight system itself, where neural control, muscle dynamics, thorax and wing structure, and environmental interactions all influence flight behavior and performance. Measurement of individual elements can be very difficult, and despite advances in high framerate cameras and techniques like time-resolved microtomography [30] and in-vivo x-ray diffraction measurements on muscle [31], it is often impossible to measure characteristics of the neuromuscular system that drives wingbeats. Thus, other methods must be used.

The purpose of this thesis is to study the dynamics of flapping systems, both natural and robotic, with the goal of advancing *both* fields. To achieve this, we have utilized a mode of inquiry called *robophysics* that melds the fields of biology, physics, and robotics to test hypotheses that otherwise are difficult or impossible to measure in living systems.

0.1.1 Robophysics

Robophysics is defined by Aguilar and colleagues [32] as "the pursuit of fundamental principles governing movement and control of self-deforming entities... interacting with complex environments." A robophysical system differs from a bio-inspired robot in some important ways. Bio-inspired robots usually mimic the entirety of an organism, i.e. a flying insect, swimming fish, running cheetah, or slithering snake. Their success or failure is measured in terms of locomotion performance: speed, efficiency, robustness, etc. Thus the design goals typically center around

finding a working example, and then optimizing the design and/or controller based on whatever performance metrics the designers are using. However, optimizing a system for performance can often lead to a situation where the system fails once it encounters a new environment, and worse, it may fail for reasons that are not obvious to the designers, and therefore are difficult to fix. What is needed is a better understanding of the principles of locomotion through the world; armed with that deeper understanding, roboticists will be able to predict and avoid such issues.

A robophysical system is designed with the primary objective of learning the principles that underlie movement through natural environments. It is a fundamentally interdisciplinary approach, promoting a cycle wherein observations of animal (or robot) behavior lead to novel hypotheses, which are tested on minimal representations of the mechanical and environmental factors at play [33]. Results from those experiments can be used to develop and improve models of organisms, which informs future observations and promotes better design of future robots. The use of simplified systems promotes better understanding through abstraction, as opposed to more complex models that can be informative, but are sometimes difficult to interpret. Additionally, robophysical systems are able to survey the entirety of a parameter space, i.e. many different leg morphologies and stiffnesses [34] or wingstroke shapes [35], including those that don't occur in nature. Such studies have been crucial in developing and improving models of swimming [36], slithering locomotion [37], hopping, walking on granular media, and, critically for our study of insect flight, flapping aerodynamics [38], [39]

Robophysical studies of flapping wing aerodynamics

Until the latter part of the 20^{th} century, the production of lift and control of flight by insects was not well captured by aerodynamic theory. Not only were the aerodynamics involved nonlinear, unsteady, history dependent, and three-dimensional, but the small body size and high wingbeat frequencies (100-1000 Hz) of insects made it difficult even to measure. Thus, a number of studies turned to physical models that used scaled-up versions of wings moving through air [38], [40], [41] or viscous fluids [39], [42]–[46], which allowed them to match the

Reynolds number of wings moving at high speeds through air. Those studies produced a deeper understanding of various phenomena unique to flapping flight, including delayed stall, wing-wake interaction, and clap-and-fling [10]. For example, Dickinson & Sane [35], [39], [47], using their dynamically-scaled wing, were able to build a deep understanding of how wing rotation timing and rates could affect lift and drag production by studying the wingstroke kinematic parameter space. Those findings provided greater understanding of the forces involved when insects fly, and also helped to inform the development of computational fluid dynamics (CFD) methods [7] and eventually centimeter-scale FWMAVs [8]. Indeed, their empirical measurements of drag coefficients at intermediate Reynolds number were critical for our simplified aerodynamic modeling in Chapter 1 of this thesis.

However, in the effort to simplify analysis of those robophysical models, previous robophysical studies consisted of rigid, tightly controlled wings. This was important when attempting to study force production due to wing motion, but it overlooks some critical aspects of the real insect flight system. One important example is that the biological materials that make up the anatomy of insect thoraces and wings is significantly less stiff than the steel and rigid polymers that make up typical engineering systems. The flexibility of insect wings has become a focus of recent research, where computational, experimental, and comparative studies have shown their importance in lift production and robustness [48]. In the present study, we will seek to understand the internal dynamics of the muscles, thorax, and wing joints which interact with the complex aerodynamic environment and produce *emergent* wing kinematics that are not strictly controlled by the inputs to the system. We name these systems that involve significant elastic energy exchange in addition to nonlinear aerodynamic environmental interaction "spring-wing" systems.

0.1.2 Resonant flapping in a robophysical spring wing system

Ever since wing-clipping experiments in the 1950s [49], [50] showed that insect flapping frequency changes with the square root of wing inertia, it has been suggested that insects may

behave like a mechanical oscillator, storing and releasing elastic energy to improve efficiency during flapping. Around the same time, Torkel Weis-Fogh discovered the elastic material that could make it possible: resilin, a near-perfect elastic protein found in the thorax, joints, and tendons of flying insects and other arthropods [51]–[53]. Later, Weis-Fogh further argued that, indeed, elastic energy exchange is *necessary* for efficient flight in most insects, as well as hummingbirds [54], [55]. However, after those studies, little additional progress was made in understanding the dynamics and control implications of flight driven by such a resonant system.

Resonant systems are characterized by frequency-dependent dynamics where there exists a particular resonant frequency at which some output is maximized given some periodic input of constant magnitude. At the resonant frequency, a small input is magnified so that, for example, a motor with a low effective torque can drive high-amplitude oscillations thanks to the transformation of inertial (kinetic) energy into elastic (potential) energy and back. In engineering design, resonance is often avoided because it is possible for inputs at the resonant frequency to be magnified and potentially cause damage. For example, the resonant frequency of a wind turbine must be higher than the rate at which the rotors spin, or else the small periodic forces on the tower could be magnified and cause large, damaging oscillations. However, in a spring-wing system, operating at resonance allows an insect or robot at hover to minimize the amount of energy it uses to drive the wing and produce lift. This is easy to show in a linear spring-mass-damper type system, but no one had studied the unsteady, nonlinear aerodynamic interactions with a spring-wing in detail. We took a robophysical approach, creating a dynamically-scaled model of a spring-wing system based on a template model [56] of flapping systems with elasticity. The robotic spring-wing consists of a high-torque motor driven by commands from MATLAB, a fine-resolution optical encoder, a rigid wing flapping in water, and, critically, custom molded silicone torsion springs which provide high-strain, linear spring behavior during operation. The system was designed for automation, making it possible to run many trials at once with consistent results across batches of trials. The first half of this thesis deals with studies on the system when driven by a constant torque input, similar to the neurally-driven periodic muscle actuation of

so-called synchronous insects [4].

In **Chapter 1**, we used the robotic spring wing to evaluate the simplified spring-wing template model, testing to see to what degree it can be used to predict resonant behavior, despite the complex fluid dynamics involved. We found that the model predicted the resonant frequencies of the system, but underestimated the total aerodynamic and other non-conservative losses. Through dimensional analysis, we discovered that those additional losses, characterized by structural damping, scaled with the ratio of maximum inertial torque to maximum aerodynamic torque, a parameter that we named the *Weis-Fogh Number*. We found that most flying insects seemed to possess a Weis-Fogh number between 1 and 10 despite many orders of magnitude size difference, suggesting that this ratio may be an important measure of tradeoffs insects must make over evolutionary time between resonance, efficiency, and other performance metrics. In **Chapter 2**, we use the same robophysical model to study those efficiency, controllability, and robustness tradeoffs in systems flapping at resonance. We ran two sets of experiments to measure the influence of Weis-Fogh number on 1) the responsiveness of a resonant spring-wing to control inputs and 2) the robustness of a resonant spring-wing to external aerodynamic loads, as may be experienced by an insect flying in wind. The collected results of Chapters 1 and 2 have impacts both to the understanding of the factors driving evolutionary diversification in flying insects, and serve as a guide for engineers designing FWMAVs that take advantage of resonance.

0.1.3 Beyond Resonance: Active feedback and limit-cycle oscillations in asynchronous spring-wings

Having set a baseline of understanding of the periodically-driven spring-wing system, we introduced an additional factor: the active muscle dynamics of asynchronous insects. While many insects drive wingbeats using periodic signals from the nervous system that cause muscles to contract, others, like flies, bees, and beetles, utilize muscles that feature a property called *delayed-stretch activation*. These specialized muscles are flushed by the nervous system with Ca^{2+} ions to provide energy for contraction, and when they are stretched, they respond with a

relatively slow increase in tension that is "delayed" with respect to the stretch. The muscles are paired antagonistically, so when one contracts, the other is stretched, which causes it to contract, and thus the two muscles may oscillate 10-20 times per neural signal; the nerve pulses are not correlated with the flapping frequency, and hence the muscles are called *asynchronous* [4].

Asynchronous (or fibrillar) insect flight muscles were first described by Pringle [57] in flies, and in later detailed studies in beetles [58], [59]. In fact, Machin and Pringle used a biohybrid apparatus, connecting load cells, actuators, and other measurement devices to a live beetle muscle to study in detail the dynamic properties of asynchronous muscle. Since then, a great deal of work has gone into the understanding of the microscopic biochemical mechanisms that underlie the stretch activation and shortening deactivation of asynchronous muscle [60]–[70]. Today, it is not known with confidence exactly what mechanism drives stretch activation, other than that the ratios of certain proteins involved in the attachment of actin-myosin bonds are different in asynchronous muscles vs. synchronous [61], [71].

Despite that, there has been some work attempting to understand the stretch-activation phenomenon at a conceptual level, characterizing it based on a three-phase exponential process [59], [65], [72]–[74]. In those studies, the focus was to associate the phases of the phenomenon with the biomolecular processes inside the muscle to better understand the mechanism of stretch activation. Some had suggested that muscle dynamics should be associated with wingbeat frequency and other mechanical properties of the insect flight system [63], [73], but no one had attempted to integrate asynchronous muscle dynamics into a mechanical model of the insect thorax. Armed with our spring-wing model and robophysical system, we set out to define a feedback law that approximates asynchronous muscle dynamics and produces self-excited flapping. In **Chapter 3**, we detail the conversion of the three-phase dynamics into a linear transfer function. This conversion allowed us to use tools from dynamics, control theory, and nonlinear systems analysis to create a model of asynchronous spring-wings that produces a limit-cycle based, self-excited flapping oscillation that requires no periodic input. We analyzed the system, identifying boundaries in the parameter space where Hopf bifurcations occur and

oscillations spontaneously grow, and we performed numerical simulations to study the emergent dynamics. Then, we implemented the stretch-activation feedback law into our dynamically-scaled robotic spring wing, and discovered adaptive behaviors that enable robustness to wing damage or fabrication inconsistencies (in the case of a FWMAV) and protection against wing damage during collisions. We also detail the process of implementing self-excited flapping on small-scale FWMAVs that use both piezoelectric bending actuators and DC motors. Finally, in **Chapter 4**, we use the same framework to explore the implications of the discovery of stretch-activation in a supposedly synchronous - not asynchronous - insect. Previously, asynchronous muscle was thought to have been derived from a single ancestor [75], but analysis of more recent insect phylogenies found that insects transitioned to asynchronous from synchronous and back several times. We were able to show, via simulations and robotic models, that in cases where both synchronous and asynchronous forces are present, the two sets of dynamics can *synchronize* and transition smoothly between these two ways of operating that had long been thought to be functionally disconnected. Thus, this new model of asynchronous spring-wing flapping produces new understanding in both biology and robotics; producing a new tool for studying asynchronous dynamics which are so difficult to parse in living, flying insects, as well as introducing a new world of oscillator-based flying robots.

0.1.4 A robophysical study of spring-wings has benefits for both biology and robotics

Robophysics is all about the cycle of communication from biology to robotics and back. In the field of insect biomechanics, robophysics has been part of the story since the 1950's, when Machin & Pringle measured characteristics of beetle flight muscle using a complex electromechanical system that could provide virtual elastic and viscous loads to the actual insect muscle [59]. Later, motor-driven, dynamically-scaled flapping wings were critical to developing the theory and numerical modeling of flapping wing aerodynamics. This set of studies adds to this rich tradition by integrating elasticity, dimensional analysis, and linear and nonlinear

dynamics and control theory to build an understanding of the insect flight system as more than a set of muscles and wings. Biological systems are inherently interconnected, many-dimensional, and nonlinear; understanding the function of a system is rarely as simple as studying the separate part and "stitching" them back together, as is often possible in engineered systems. That means that in order to gain deep understanding of how animals move through the world, it's important to consider not just the observable kinematics, but also the internal forces, neural inputs, low-level distributed feedback, and material properties that make their behavior possible. When we look at the world of flying insects from this perspective, we gain the ability both to make sense of observations of insect behavior and to ask exciting new questions about the way that insects experience the world and move through it.

If we are able to develop a system-level understanding of how animals move, we will also find abundant opportunities for novel robot designs. We have already seen this play out in the field of walking robots, as well as in exoskeleton and prosthetics technology. Unlike the rigid, stiff-legged robots and simple lower-limb prosthetics of the past, more and more designs are incorporating lessons from nature, such as active stiffness modulation, variable proprioceptive feedback, and soft materials. These designs are often under-actuated, which saves weight and contributes to greater stability and robustness in natural environments, and their inherent softness often contributes to a safer and more experience for the humans they interact with. The work in this thesis is a step towards similar developments in the field of flapping wing micro-aerial vehicles, which could benefit from the adaptive properties of asynchronous flapping, as well as a deeper understanding of the tradeoffs that come with operating at resonance. Indeed, work has already begun on transitioning the ideas described in Chapters 3 and 4 into an insect-scale flying robot. The process of building and controlling that robot will produce a better robot, but it is crucial to recall the robophysical cycle and use what we learn to pose new questions in biology. If that happens, the rich interdisciplinary communities of engineers, biologists, and physicists around this research will continue to thrive and together produce knowledge which would otherwise be impossible to obtain alone.

Chapter 1

Dimensional Analysis of Spring-Wing Systems

1.1 Introduction

Flapping flight is one of the most energetically demanding modes of locomotion in nature and in engineered flying robotic systems. Actuators must provide power to overcome aerodynamic forces on the wings, generate inertial forces for oscillatory acceleration and deceleration, and counteract internal energy losses from imperfect power transmission [76]. If an oscillating wing is coupled to an elastic element such as a spring, the kinetic energy from the wing could be stored as elastic energy at the end of the wing-stroke and returned after stroke reversal. Many insects [51], [54], [76]–[78], birds [54], [79], and even bats [80] have spring-like elements in the form of elastic materials in their thoraxes, muscles, and tendons that may aid in reducing the energetic demands of flapping flight and improving flight efficiency (resonance) (Fig. 1.1a). However, the evidence that insects and birds operate near resonance largely relies on corelational observations of wingbeat frequency and wing inertia [50], [81], or energetics arguments comparing metabolic and aerodynamic power [54], [55], [82].

If animals do rely on elastic energy storage for improved efficiency, then there are implications for the dynamics and energetics of those systems. One major example is that, to benefit from a spring, flapping wings must be actuated at a specific resonance frequency governed by the spring stiffness, body morphology, and other factors such as aerodynamics and damping.

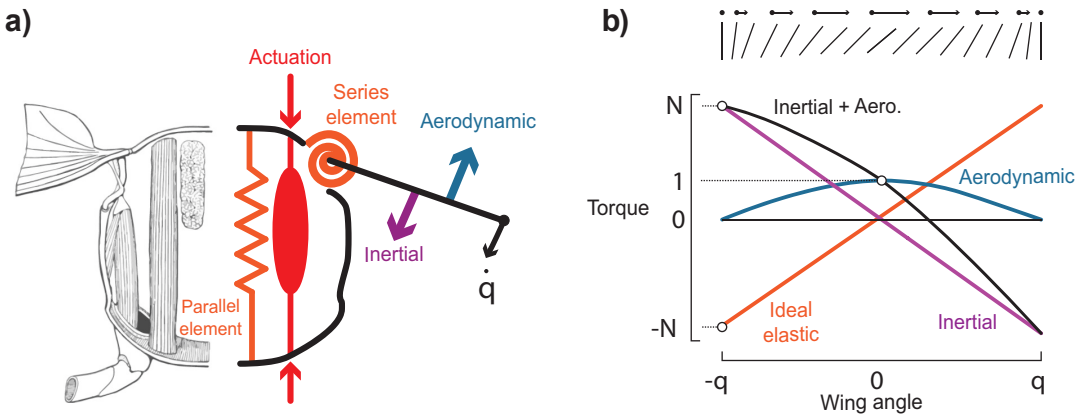

Figure 1.1. a) Flapping wing insects have elastic components in their thorax and wing hinge which can potentially act as spring elements to reduce the energetic demands of flapping wing flight. The left side of the image in a) shows an illustration of the muscle, thorax wall, and wing hinge of an insect. The right side of the image interprets it as a spring in parallel with the actuation source and a spring in series with the actuator, with aerodynamic and inertial forces that act on the rotating wing. b) Weis-fogh introduced a convenient way to visualize the relative magnitudes of torque acting on the wing hinge by normalizing all values to the peak aerodynamic torque. The units of both axes are dimensionless. The angle and velocity of the insect wing over the downstroke is shown by the lines above the plot. Image in (a) adapted from [84].

Flapping at a higher or lower frequency leads to inevitable reduction in flight performance. Early experiments on the relationship between wingbeat frequency and wing inertia provided compelling evidence that insects do oscillate their wings at resonance [50], [81]. However, these experiments relied only on the manipulation of wing inertia (without accompanying measurements of thorax stiffness) and thus do not provide direct comparison of the spring-wing system's resonant frequency and the wingbeat frequency. Recently, there has been some effort to measure insect thorax elasticity and frequency response [83], but experimental limitations leave room for questions about whether insects are, in fact, flapping at a resonant frequency.

The impact of operation on or off resonance is directly related to how much a particular flapping wing system benefits from the inclusion of a spring. A flyer with small wing inertia would have less excess kinetic energy to store and return in a spring than one with large wing inertia, but also would be less impacted by changes in wingbeat frequency. The question of where insects fall on this spectrum was first address by Weis-Fogh in his analysis of flapping

flight efficiency [55]. He introduced the dynamic efficiency (η) as the ratio of aerodynamic work to the combined inertial and aerodynamic work, which serves as a measure of how much energy is expended on useful aerodynamic work versus wasteful inertial work. Weis-Fogh provided an analysis of the scaling of η in the absence of elasticity by introducing the non-dimensional variable N, which is the ratio of peak inertial force to peak aerodynamic force over a wing-stroke. In flapping-wing flight without springs, η was shown to monotonically decrease with increasing N, thus requiring larger energy input at larger N to sustain flight. In subsequent text we refer to N as the Weis-Fogh number to reflect his contributions to flight energetics.

Examination of the sinusoidal motion of a wing in the absence of elasticity, reveals two sources of reaction force: inertial and aerodynamic forces. During a half-stroke of a wing, the inertial force associated with wing acceleration is at a maximum when the wing position is at its point of reversal, and inertial force decreases linearly with wing position and reaches zero at mid-stroke (Fig. 1.1b). At reversal, the wing speed is zero and thus the aerodynamic force at this point is zero, while at mid-stroke the aerodynamic force is maximum. Plotting these forces as a function of wing position (Fig. 1.1b) and normalized by peak aerodynamic force reveals that the inertial force has a maximum value of N, the Weis-Fogh number. Furthermore, the integration of these forces over the wing displacement provides the total inertial and aerodynamic work. As can be seen in Figure 1.1b an ideal spring exactly matched to the inertial force of the wing would exactly cancel out the inertial work over a cycle in a parallel spring-wing system. In such a case the dynamic efficiency of the system would be $\eta = 1$ and the system would be operating at resonance. However, it is less clear how internal damping, frequency modulation, and different spring arrangements modulate the dynamic efficiency.

The primary mechanism of elastic energy storage in insects is resilin, a highly-resilient elastic material first identified in patches of the locust exoskeleton was discovered and characterized in the 1960's by Weis-Fogh [51], [54], [77] (and subsequently identified in many other arthropods [53], [85]). It was shown to return greater than 97% of stored elastic energy, suggesting that insects have resilient components within their thorax that can facilitate efficient

energy exchange and return. Thus, the historical choice not to include internal losses in the computation of dynamic efficiency appears to be a simplification based on the assumption that the losses due to aerodynamic forces are significantly larger.

However, recent experiments to characterize the energy storage and return in the hawk-moth (*Manduca sexta*) thorax have also demonstrated that small but significant energy loss occurs from internal structural damping [76]. Similar structural damping was also observed in cyclic oscillation of cockroach legs [86], possibly suggesting a general character of energy loss in exoskeleton deformations. Structural damping is a form of energy loss different from the more familiar velocity-dependent viscous damping. Materials that are structurally damped exhibit energy loss that is frequency independent and is instead governed by oscillation amplitude and elastic coefficient [87]. This is consistent with the interpretation of structural damping as a result of internal, microscopic friction that is not dependent on velocity. While the presence of highly elastic resilin suggests significant potential benefits from elastic materials, internal damping may preclude the energetic benefits of elasticity in spring-wing systems.

Despite the more than sixty years of focus on resonance in insect flight, previous efforts at modeling or measuring spring-wing resonance in insects have fallen short by: 1) assuming that quasi-steady assumptions on aerodynamic forces in spring-wing resonance are valid, 2) not including the effect of energetic losses from imperfect elasticity, and 3) focusing predominantly on the contributions of parallel system elasticity while disregarding contributions or limitations of series-elastic elements. Most importantly, we lack a common modeling and analysis framework to compare and contrast the energetic benefits of resonance across insects and man-made systems such as robots. Inspired by the original calculations of Weis-Fogh, we seek in this paper to develop a set of equations that govern the dynamics of parallel and series spring-wing systems using non-dimensional parameters that allow for comparative examination.

In experiments we will measure how unsteady aerodynamic effects, specifically added mass and wing-wake interaction, influence the resonant behavior of a flapping wing at hover. In order to achieve this, we compare simulations of a spring-wing oscillator subject to quasi-

steady aerodynamic forces to a robophysical model of a flapping wing with known mechanical parameters subject to real fluid forces. Here we draw upon the work of van den Berg and Ellington [88], Sane and Dickinson [35], and others to use a flapping wing robot that is dynamically scaled to that of flying insects. Unlike those studies, we do not prescribe the wing kinematics, instead using an elastic element in series between the wing and motor to observe resonant dynamics and emergent wing kinematics produced by varying actuation parameters. From our experiments we will develop a model to understand how structural damping influences spring-wing dynamic efficiency using non-dimensional parameters. These efforts will provide a general understanding of how springs, wings, and body mechanics converge to enable energy efficient flapping motion as a function of morphology and wing kinematics.

1.2 Theoretical preliminaries: Assumptions and Motivation

To contextualize our study of spring-wing dynamics we first seek to outline the basic concepts of spring-wing systems. We will derive the equations of motion in the presence of aerodynamic and internal damping forces. We conclude this section with a non-dimensional representation of the equation of motion which produces two important parameters in spring-wing systems.

1.2.1 Undamped parallel and series wing-spring systems

The anatomies of flapping wing animals feature a wide range of elastic element configurations that contribute to their flapping wing dynamics. These arrangements can be expressed as combinations of springs in series and parallel with a moving inertial element, the wing (Fig. 1.1a). In both cases, the wing interacts with a time- and history-dependent nonlinear force from the surrounding fluid. To simplify the modeling of spring-wing systems, we consider the system as a one degree of freedom rotational joint (to emulate the wing hinge), where the joint angle θ is the wing angle along the stroke plane. If we neglect internal damping, the equation of motion for a

parallel spring-wing system about this joint is

$$I_t\ddot{\theta}(t) + k_p\theta(t) + Q_{aero}(t) = T_m(t) \tag{1.1}$$

where I_t is the total system inertia, k_p is the stiffness of the parallel elastic element, Q_{aero} is the aerodynamic drag torque, and $T_m(t)$ is the time dependent torque applied to the wing. In the parallel configuration, the spring undergoes the same displacement as the wing and the muscle (actuator) acts directly on both the mass and spring. Nearly all spring-wing modeling of the insect thorax [55] and micro-aerial vehicles [8], [23], [89]–[91] have considered the parallel spring arrangement where muscle (actuator) is in parallel arrangement with the spring.

In a series-elastic spring-wing system, a spring is placed between the actuator and the wing. Series elastic elements are well studied in vertebrate biomechanics as muscle-tendon units where a tendon is placed between the muscle and output [92]. Series elastic elements in flapping wing flight may similarly be found in the muscle tendon units of birds [79], [93]. In insects, series elasticity can arise from elastic tendons [94], elasticity in the wing hinge [51] or within the flight power muscle [4]. For simplicity of experiment design and to examine the differences between series and parallel systems, we analyze the series elastic spring-wing configuration. The equation of motion for a simple series elastic system may be written:

$$I_t\ddot{\theta}(t) + Q_{aero}(t) = k_s(\phi(t) - \theta(t)) \tag{1.2}$$

where the force acting on the wing arises from the displacement of input angle $\phi(t)$ relative to the wing angle θ (Fig 1.2a). The difference between the angles is the deflection of the series spring with stiffness k_s. When the system is at steady-state (hovering), the series and parallel cases can be treated equivalently by rearranging equation 1.2 to reflect the parallel configuration:

$$I_t\ddot{\theta}(t) + k_s\theta(t) + Q_{aero}(t) = k_s\phi(t) \tag{1.3}$$

1.2.2 Aerodynamic drag torque and added mass inertia

The wing experiences an aerodynamic resisting torque, Q_{aero}, that opposes wing movement through the fluid. To make analysis of this system tractable, we will use a quasi-steady blade element estimate of aerodynamic torque consistent with previous quasi-steady methods for spring-wing systems [55] and micro-aerial vehicles [8], [23], [89]–[91]. Following the standard conventions for the quasi-steady blade element method we express the aerodynamic drag torque:

$$\begin{aligned} Q_{aero} &= \underbrace{\frac{1}{2}\rho C_D(\alpha)\frac{R^5}{\text{Æ}R}\hat{r}_3^3}_{\Gamma}|\dot{\theta}|\dot{\theta} \\ &= \Gamma|\dot{\theta}|\dot{\theta} \end{aligned} \tag{1.4}$$

The variable Γ is the drag torque coefficient and is a function of wing geometry (span, R; aspect ratio, $\text{Æ}R$; non-dimensional radius of the third moment of wing area, $\hat{r}_3$); pitch angle, α; drag coefficient, $C_D(\alpha)$; and fluid density, ρ. Since we are considering aerodynamic torque about the wing hinge, Q_{aero} has units of [N m] and Γ has units of [N m s^2].

In addition to aerodynamic torque, the acceleration of a wing within a fluid leads to an additional inertia; an "added" or "virtual" mass, as it is sometimes called [95]. We use a method from [95] for modeling the mean added mass inertia, I_A (See Appendix A.1). The total inertia is computed as $I_t = I_{sys} + I_A$, where I_{sys} is the inertia of the wing and wing transmission. In the insect flight system, the wing hinge acts as a mechanical transmission, converting linear muscle actuation to angular wing motion. It is possible that additional inertial terms from the reflected inertia of the oscillating muscle and thorax may be important. However, there is little known

about the specific motion and inertia of the wing hinge transmission and the role of muscle and thoracic inertia, so we will disregard their effects in this manuscript.

1.2.3 Structural damping in the insect thorax

Recent experiments to measure the damping response of the hawkmoth (*Manduca sexta*) thorax [76] and cockroach (*Blaberus discoidalis*) leg joints [86] have both identified structural a.k.a. hysteretic damping as the dominant source of energy loss. Consistent with these observations, we seek to consider the effects of structural damping on spring-wing system dynamics. Structural damping is a common source of energy loss in biomaterials [96] that differs from viscous damping in that there is no velocity dependence in the structural damping force. For general oscillatory motion, the structural damping force can be included as a modification to the spring constant, $K = k(1 + i\gamma)$, where k represents either the parallel or series spring. The coefficient γ is the structural damping loss factor [87] which has been found to be $\gamma = 0.2$ for cockroach leg joints [86] and $\gamma = 0.1$ for the hawkmoth thorax [76]. For constant sinusoidal motion at a single frequency, ω, the structural damping force can be represented as a viscous-like force with a coefficient that scales with frequency:

$$Q_{struct} = \frac{\gamma k}{\omega}\dot{\beta} \tag{1.5}$$

where the angular velocity $\dot{\beta}$ is the relative speed of spring compression (for parallel system $\dot{\beta} = \dot{\theta}$ and series systems $\dot{\beta} = (\dot{\phi} - \dot{\theta})$. The presence of ω in the denominator makes the structural damping force frequency-independent, unlike typical viscous damping (See Appendix A.2 for derivation).

1.2.4 An organizational framework for spring-wing systems

In this final section of the motivation we introduce a set of non-dimensional variables that govern general spring-wing dynamics. As discussed in the introduction, the Weis-Fogh number N is the ratio of maximum inertial force compared to maximum aerodynamic force over a cycle. Assuming sinusoidal wing motion with amplitude θ_0 and frequency ω, the maximum inertial torque is $I_t\theta_0\omega^2$ and maximum aerodynamic torque is $\Gamma\theta_0^2\omega^2$ resulting in the Weis-Fogh number

$$N = \frac{I_t}{\Gamma\theta_0} \tag{1.6}$$

This quantity should dictate how important a role spring elements can play in energetic efficiency at hover. For $N < 1$, aerodynamic forces dominate and kinetic energy may be fully dissipated into the surrounding fluid over each wing stroke; no elastic storage is needed. However, for $N > 1$, excess kinetic energy from the wing can be recovered by a spring. Observations from biological and robotic flapping wing flyers indicate that N roughly varies between 1 and 10 for a broad range of insects [55].

In order to compare across insect species, we non-dimensionalize the dynamics, assuming the wing oscillates sinusoidally at a frequency ω, and with amplitude θ_0. We begin with the full dynamics equation for the parallel spring-wing system including structural damping:

$$I_t\ddot{\theta} + k_p\theta + \Gamma|\dot{\theta}|\dot{\theta} + \frac{\gamma k_p}{\omega}\dot{\theta} = T(t) \tag{1.7}$$

We introduce dimensionless wing angle q and dimensionless time τ and substitute into Eq. 1.7 (See Appendix A.3). We arrive at the following dimensionless equation of motion for the spring-wing system

$$\ddot{q}_w + \hat{K}_p q_w + \gamma\hat{K}_p\dot{q}_w + \frac{1}{N}|\dot{q}_w|\dot{q}_w = \hat{T}_p(t) \tag{1.8}$$

where we have defined the reduced parallel stiffness,

$$\hat{K}_p = \frac{k_p}{I_t \omega^2} \tag{1.9}$$

and the Weis-Fogh number, N is in the coefficient of the aerodynamic torque. The normalized torque in the parallel system is

$$\hat{T}_p(t) = \frac{T_p(t)}{I_t \theta_0 \omega^2} \tag{1.10}$$

Performing a similar substitution for the series system we arrive at the equation below

$$\ddot{q}_w + \hat{K}_s q_w + \gamma \hat{K}_s \dot{q}_w + \frac{1}{N} |\dot{q}_w| \dot{q}_w = \hat{T}_s(t) \tag{1.11}$$

where the normalized torque in the series system is

$$\hat{T}_s(t) = \frac{\hat{K}_s}{\theta_0} \left(\phi(t) + \frac{\gamma}{\omega} \dot{\phi} \right) \tag{1.12}$$

We provide a full derivation of these equation in the Appendix (A.3).

Through the change of variables in the parallel and series spring arrangements we have arrived at two nearly-identical non-dimensional dynamics equations in Equations 1.8 & 1.11. The differences between the series and parallel systems in this form are all contained in the actuation variables, $\hat{T}_s$ and $\hat{T}_p$. Thus, while the forced actuation of these system may result in different dynamics, the similar structure of the non-dimensional dynamics equations indicates that in both systems three variables likely govern the behavior: N, $\hat{K}$, and γ. As an exemplary demonstration of this, if either the series or parallel system is driven to steady-state oscillation and then the external actuation is turned off ($T = 0$ or $\phi = 0$), both equations 1.8 & 1.11 become equivalent. The objective of this paper is to seek to understand how N, $\hat{K}$, and γ influence dynamic efficiency and resonance of a simple series spring-wing system.

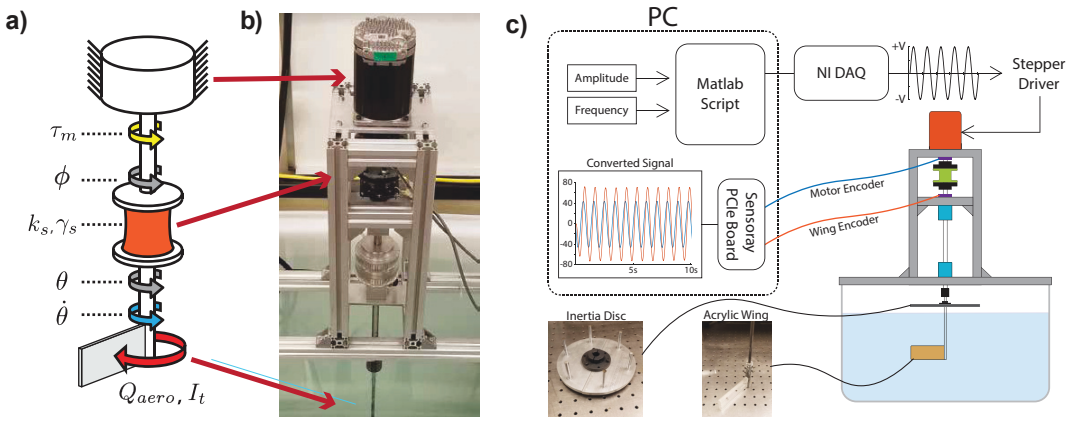

Figure 1.2. Schematic and details of the robophysical flapping wing experiments. a) A schematic of the system showing the stepper motor in series with a torsional spring connected to a rigid wing. b) A picture of the physical system. c) A diagram of the control and experimental operation of the robophysical system.

1.3 Experimental and numerical methods

1.3.1 Robophysical experiment design

We developed an experimental spring-wing system to study flapping wing behavior in the context of realistic fluid forces (Fig. 1.2). The quasi-steady modeling presented in the previous section greatly simplifies the unsteady, history-dependent aerodynamic phenomena involved in flapping flight. A dynamically-scaled physical wing serves as a reference against which we can evaluate the performance of the quasi-steady model. The system consists of a servo motor capable of accurate position control, a molded silicone torsional spring with linear elasticity and structural damping, and a simple fixed-pitch wing element attached to a rotary shaft and submerged in a 115-gallon plastic tank filled with water (30”x30”x30”, Chem-Tainer). The tank was selected to be large enough to minimize fluid interactions with the side walls, floor, and water surface. The wing is situated near the center of the tank, such that the wing is always at least 10 wing-chord-lengths from the walls and floor and 5 wing-chord-lengths from the surface of the water. This is consistent with other studies of flapping wings that use water as a working fluid [97]–[99] See Appendix A.4 for photos of components and further details.

Motor selection and system friction reduction

A high-torque servo motor (Teknic Clearpath SDSK) was chosen to drive the system under closed loop angular position control. The servo is able to provide substantially more torque than that experienced by the wing in the fluid, effectively decoupling the motor and wing dynamics. We monitor the motor and wing angle using two optical encoders (US Digital, 4096 CPR). To reduce the influence of friction on the wing motion we used two radial air bearings (New Way, #S301201) which resulted in negligible bearing friction. The shaft was supported vertically by an axial thrust bearing, which did contribute a small amount of friction.

Reynolds number scaling

To ensure that we match the aerodynamic behavior of small insect wings we chose experimental parameters to dynamically scale our system. Consistent with previous dynamically-scaled experiments [35], [39], we sought to maintain a Reynolds number in the range of that of small flapping wing insects, $Re = 100 - 10,000$. We define Reynolds number based on standard methods, using wingtip velocity as the flow speed and wing chord as the characteristic length [39]. We choose water as a working fluid ($\rho = 997 kg/m^3$) and chose wing geometry (rectangular, 10 x 3.6 x 0.5 cm) and a range of actuation parameters (10-64 deg amplitude, 0.5 to 4.1 Hz frequency) where the resulting wing kinematics had $Re \approx 10^3 - 10^4$. Note that since the wing amplitude is an emergent property of the system due to the series spring configuration, so too is the Reynolds number of an individual test.

Weis-Fogh number scaling

In order to achieve a wide range of Weis-Fogh number (Eqn. 1.6) in experiment, we must be able to adjust the ratio of peak inertial torque to peak aerodynamic torque. We chose to keep the drag torque coefficient Γ constant, so we vary N by changing wing inertia and wing amplitude θ_0. Wing inertia, I_t was varied by adding acrylic and aluminum discs to the wing shaft, leading to total inertias of I_t = [10.5, 15.9, 23.2]$\times 10^{-4}$ kg m^2. Our experiments resulted in

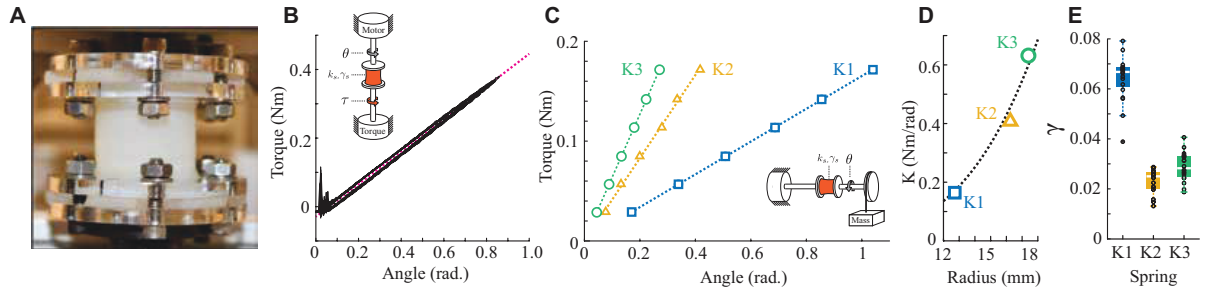

Figure 1.3. Characterization of silicone torsion springs. a) Photo of silicone torsion spring. Acrylic shaft couplers at the top and bottom clamp to the flanged ends of the spring. b Dynamic loading of the torsion spring (blue) results in a linear torque response with slight hysteresis effects. c) Static load test results for three silicone springs. d) Spring stiffness increases with the radius of the cylindrical region and follows an R^4 curve. e) Estimates of the hysteric loss factor for the 3 springs.

a range of N between 1 and 5 when operating at the resonant frequency, consistent with many insects [55].

Aerodynamic calculations

We used a rigid rectangular wing with a fixed vertical pitch ($\alpha = 0$), which simplifies modeling and motor control, and eliminates any energy storage and return from a flexible wing. The drag torque coefficient for a rectangular wing from Equation 1.4 is $\Gamma = 1.07 \times 10^{-3}$ kg m^2, where the coefficient of drag is constant at $C_D(0) = 3.4$ (taking this value from [35]). We also compute added mass inertia, I_A, for a calculated value of 3.465×10^{-4} kg m^2 (See Appendix A.1 for derivation).

Silicone spring fabrication and evaluation

We used custom fabricated silicone torsion springs for the series spring element (Fig. 1.3a). Silicone was chosen because it can be cast into custom shapes and has a linear elastic response over large strain. The springs were designed with a cylindrical profile with flanges on each end to facilitate coupling to the motor and wing shafts (Fig. 1.3a). Detailed information about the design and fabrication process may be found in §A.4.2.

We used three spring designs with torsional stiffness values of K_s = [0.163, 0.416,0.632]

N m rad^{-1}. Figure 1.3 shows the results of experiments to characterize the spring mechanical properties. We subjected springs to both cyclic and static loading conditions (Fig. 1.3a-b) to measure their elastic and damping properties. The spring torque response was linear over the range of angles tested (Fig. 1.3b-c) with stiffness values that are consistent with the predicted torsional stiffness (Fig. 1.3d). In dynamic testing we observed a small amount of hysteresis in cyclic loading experiments indicating the presence of damping within the spring (Fig. 1.3b). There is evidence that silicone rubber has a combination of viscous and structural damping [100], [101], so we set out to test whether a viscous or structural model fits best. Following a similar procedure as [76], we oscillated each spring sinusoidally across frequencies between 1 Hz and 10 Hz and amplitudes of 10, 20, and 30 degrees. We measured the angle-torque relationship during these tests and fit a viscous and a structural damping model to the data for each spring. We expected that the model that fit best would have the least variation in the fit coefficients across the range of frequencies. We computed the mean and standard deviation of the fit coefficients across the range of frequencies and found the standard deviation of the coefficients as a percentage of the mean coefficient. The standard deviations in the viscous model coefficients were 74.8%, 83.2%, and 62.1% of the mean for springs K1, K2, and K3, respectively, whereas those of the structural model were only 11.7%, 6%, 22.3%, respectively. Therefore, we chose to use the structural model to model the damping, with the knowledge that the true damping is more complex but outside the scope of this paper. We measured the structural loss moduli shown in (Fig. 1.3e). For comparison, the loss modulus is $\gamma = 0.1$ in Hawkmoths [76] and $\gamma = 0.2$ in the legs of Cockroaches [86].

Actuation and Data Acquisition

Each experiment consisted of driving the motor angle with a specified amplitude and frequency, $\phi = \phi_0 \sin 2\pi f t$. We varied input amplitude across ϕ_0 =[10 - 65] deg, in increments of 5° and frequency across f = [0.5 - 4] Hz in increments of 0.2 Hz. Digital step and direction signals were used to set the angular position trajectory of the Clearpath servo. Each test was run

for 30 seconds, during which encoder position readings were recorded from both the motor and wing by a NI PCIe board (#6323 Multifunction IO Device), sampled at 1kHz. Encoder readings were saved as text files in Matlab and processed.

1.3.2 Simulation

We developed numerical simulations that modeled the parallel and series configurations of the spring-wing system based off of Equations 1.1&1.2. The parameters of the simulations were based on measured and calculated parameters from the experiment. Simulations were performed in Matlab using the ODE45 numerical integration function. The integration algorithm performs an adaptive step integration with absolute and relative error tolerances set at 10^{-3} and 10^{-6}, respectively.

1.3.3 Data Analysis

We performed identical analysis of both simulation and experimental data. We collected wing and motor angle data, computed wing and motor angular velocity, and found the amplitude, frequency, and relative phase of each by fitting the data to functions $\theta(t)$ and $\phi(t)$, respectively:

$$\phi(t) = \phi_o \sin(\omega t) \tag{1.13}$$

$$\theta(t) = \theta_o \sin(\omega t + \psi) \tag{1.14}$$

See §A.4.3 for details.

In order to identify the resonant peak, we define a non-dimensional term, *kinematic gain*, which is the ratio of motor angle amplitude and wing angle amplitude:

$$G_K = \frac{\theta_o}{\phi_o} \tag{1.15}$$

For a resonant system, kinematic gain is maximum at the resonant frequency, ω_r (Fig. 1.4 a & b).

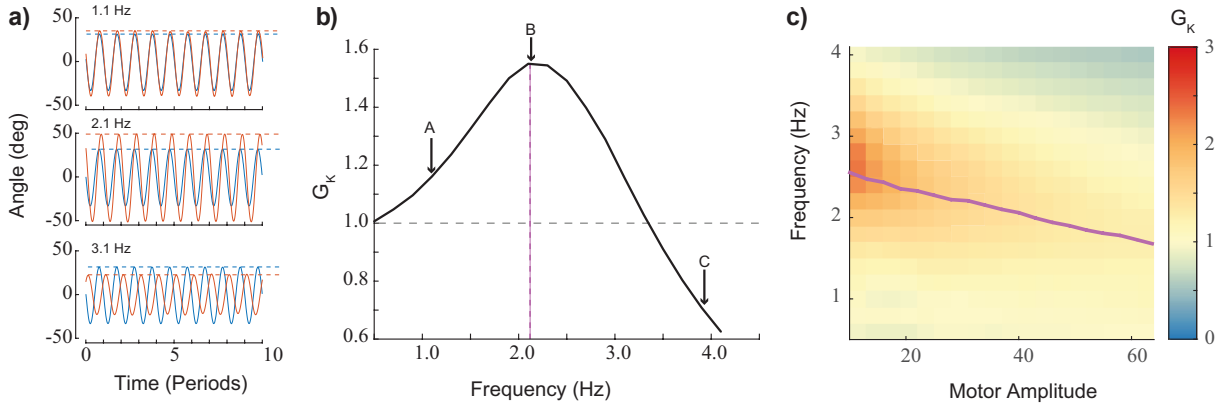

Figure 1.4. Overview of data processing method. a) Raw data in the form of encoder readings of the motor (blue) and wing (orange) positions are collected for each combination of actuation frequency and amplitude. The three graphs show that for the same motor actuation amplitude, the wing amplitude changes with frequency. b) We define kinematic gain (G_K) as the ratio between wing and motor amplitude, plot change in G_K over frequency, and identify peak G_K and resonance frequency. The plot in (b) is the resonance curve for motor amplitude = 31 deg, [K,I_t] = [0.416 Nm rad^{-1}, 10.5$\times$10^{-4} kg m^2]. c) Plot of G_K across all motor amplitudes and frequencies with the same mechanical parameters. Peak G_K and resonance frequencies fall along the purple line.

We also compute the quality factor of the oscillator dynamics, Q, using the following definition

$$Q = \frac{\omega_r}{\Delta\omega} \tag{1.16}$$

Where ω_r is the resonant frequency and $\Delta\omega$ is full width at half maximum. The quality factor is a metric of the sharpness of the resonant peak: high Q means kinematic gain, G_K drops off as ω moves away from the resonant frequency, while low Q means G_K changes slowly with varying ω.

In order to identify ω_r for a set input amplitude experiment, we locate the frequency that maximizes kinematic gain. We fit a 5th order polynomial to the 12 points closest to the peak measured G_K to get a smooth approximation of the resonance curve. The maximum value of the polynomial is the peak gain, and the frequency corresponding to it is the resonant frequency. When reporting N, dynamic efficiency, etc. "on resonance," we use the experimental configuration with a frequency closest to the resonant frequency. As a result, some nominally

resonant points are not exactly on the resonant peak, but may be off by as much as 0.1 Hz.

We use the position measurements, their derivatives, and the known mechanical parameters of the system to estimate the torques on the system: Aerodynamic, inertial, elastic, motor, and structural damping.

$$T_{aero}(t) = \Gamma|\dot{\theta}(t)|\dot{\theta}(t) \tag{1.17}$$

$$T_{inert}(t) = I\ddot{\theta}(t) \tag{1.18}$$

$$T_{elast}(t) = -T_{motor} = k_s(\phi(t) - \theta(t)) \tag{1.19}$$

$$T_d(t) = \frac{k_s\gamma}{\omega}\left(\dot{\phi(t)} - \dot{\theta}(t)\right) \tag{1.20}$$

Note that we compute the equivalent non-dimensional torques and kinematics using the terms defined in Equations 1.8 & 1.11.

Lastly, we compute the dynamic efficiency of the oscillatory motion. Weis-Fogh's definition of dynamic efficiency from the introduction neglects elasticity and internal damping, but for our purposes we need dynamic efficiency to take into account aerodynamic, inertial, elastic, and damping work. A simple way of doing so is to define the dynamic efficiency as the ratio of aerodynamic work to total work done by the actuator:

$$\begin{aligned}\eta &= \frac{W_{aero}}{W_{aero} + W_{inert} + W_{elast} + W_d} \\ &= \frac{W_{aero}}{W_{tot}}\end{aligned} \tag{1.21}$$

over a stroke (or equivalently a half-stroke). To calculate the aerodynamic and total work in experiment we use the following equations

$$W_{aero} = \int_{-\theta_o}^{\theta_o} T_{aero}\, d\theta \tag{1.22}$$

$$W_{tot} = \int_{-\theta_o}^{\theta_o} R(T_{motor})\, d\theta \tag{1.23}$$

Note that in the motor work integral, $R(x)$ is a rectification function defined as $R(x) = x$ for $x > 0$ and $R(x) = 0$ for $x < 0$. This rectification function accounts for the fact that negative mechanical work in insect flight muscle does not contribute significantly to metabolic energy expenditure [55], [82].

1.4 Results

1.4.1 Kinematic gain varies with actuation and system properties

We performed 3249 tests with varying input parameters (amplitude and frequency) and mechanical system parameters (spring stiffness and inertia) and measured the emergent wing kinematics (Fig 1.5). Results for the nine inertia and stiffness combinations are shown as heatmaps with color indicating kinematic gain. The arrows on the right and top of the figure denote the directions of increasing stiffness and inertia, respectively.

For all stiffness and inertia combinations, we observed that the peak G_K occurred at the lowest actuation amplitudes. At low amplitudes, aerodynamic damping is minimized and less energy is lost to the surrounding fluid, allowing for higher kinematic gain. The maximum kinematic gain increased with increasing system inertia in all cases, reaching a maximum when the system is a combination of a soft spring and high inertia (bottom right corner).

The resonant frequency decreased as the motor amplitude (and thus the emergent wing amplitude) increased. The dashed purple line in Figure 1.5 shows peak kinematic gain for each motor amplitude. This decrease in resonant frequency is consistent with simulation predictions shown as solid black lines in Figure 1.5. We discuss this model in the first discussion section below.

1.4.2 Flapping resonance with quasi-steady aerodynamics

Following the experiments, we sought to see how much of the observed dynamics is predicted by the simplified, quasi steady equations of motion described in Section 2. The real

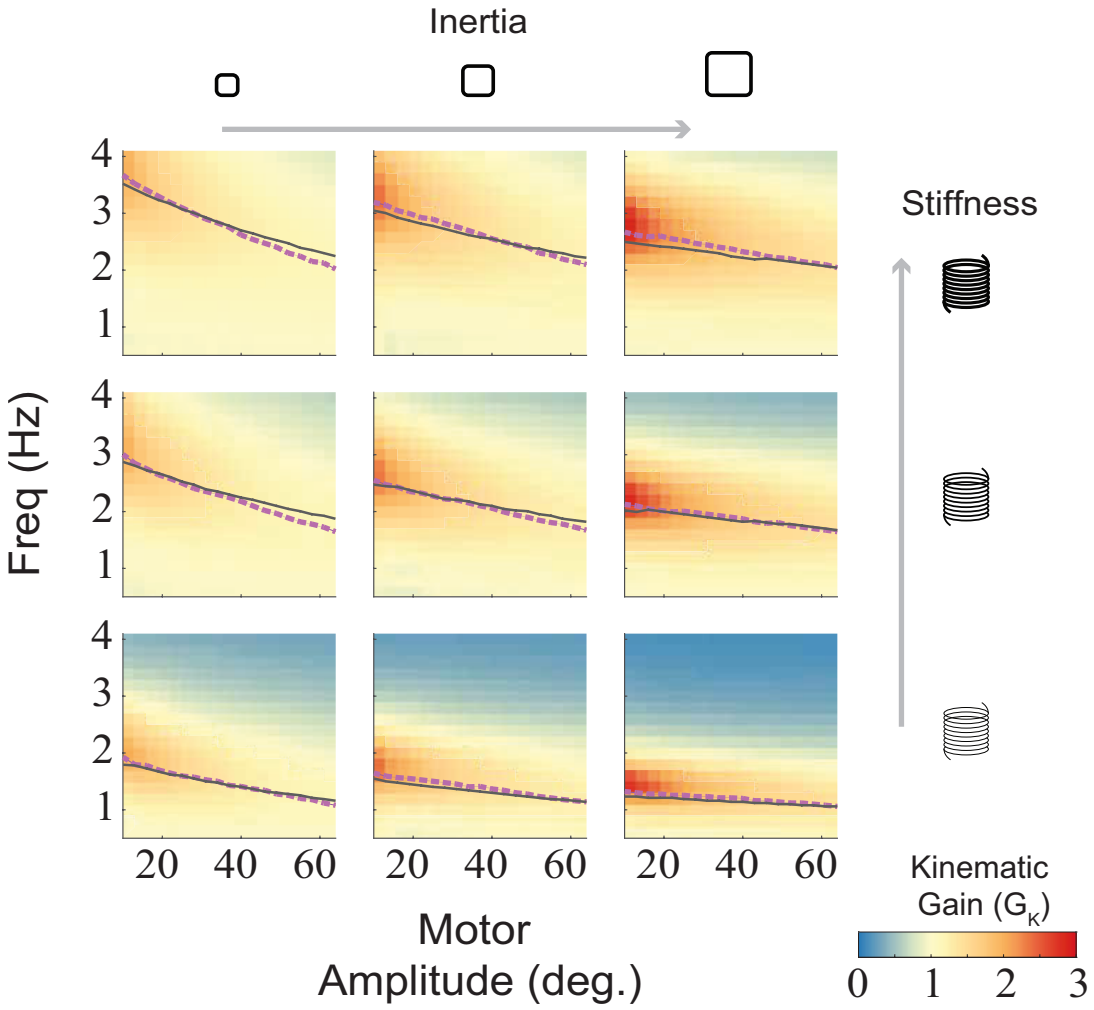

Figure 1.5. Results across all springs, inertias, actuation parameters. Peak G_K are plotted in purple dashed-lines. Peak G_K from simulation using measured system parameters and identical actuation are shown in solid black lines.

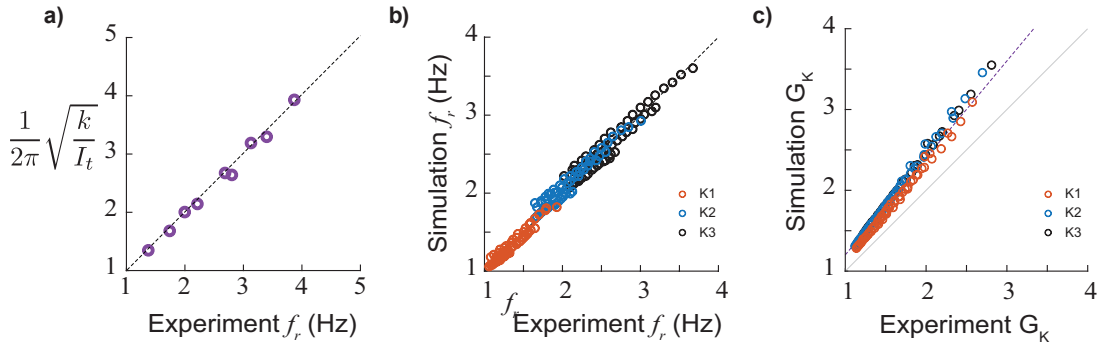

Figure 1.6. a) Comparison of system natural frequency from calculations to measured low-amplitude resonant frequency in oscillation experiments. b) Comparison of simulated resonance frequency to experimental. c) Comparison of simulated kinematic gain to experimental

aerodynamic loads on the wing are time- and history-dependent, so it is not clear to what degree those unsteady loads affect the resonance properties of the system at steady state.

Natural frequency of the system matches lightly-damped resonant frequency

At low motor amplitude, the system dynamics are only weakly affected by the aerodynamic force and thus the resonant frequency should be determined by the natural frequency of the spring-wing system. Comparison of the experimentally measured resonance frequency at the lowest amplitude with natural frequency computed from spring stiffness and inertia displays extremely good agreement (Fig. 1.6a). Thus our intuition is confirmed that low amplitude wing oscillation leads to small aerodynamic damping and the system better resembles a weakly-damped spring-mass oscillator.

Quasi-steady simulation predicts experimental resonant frequency

As motor and wing amplitude increase, we observe reductions in both kinematic gain and resonant frequency. This behavior is consistent with the quadratic velocity damping generated by the aerodynamic force on the wing and has been observed in other spring-wing experiments [89]. We sought to determine if a quasi-steady aerodynamics model was sufficient to model the spring-wing behavior observed in experiment. By performing numerical simulations with identical parameters as the experiments of Fig. 1.5 we measured the simulated resonant frequency across

all amplitudes. We find that the quasi-steady simulation resonant frequency agrees well with the experimental resonance frequency (Fig. 1.6b). This suggests that quasi-steady aerodynamic modeling is sufficient to capture the spring-wing relationship between amplitude and resonance frequency across all motor amplitudes.

Quasi-steady simulation over-predicts kinematic gain

Despite the agreement in resonant frequency, we observed a difference between the kinematic gain in the experiment and the simulation (Fig. 1.6c). The simulation over-predicted the kinematic gain for all resonance experiments by a maximum of 20% at the highest experimental gains. The over-prediction error grew with increasing gain, suggesting a systematic error in the modeling of the spring-wing system. The combination of disagreement between simulation and experiment in kinematic gain and the good agreement in resonant frequency suggests to us that unmodeled dissipation from system friction is likely the cause. Coulomb friction in the bearings would not influence the system resonant frequency, but would decrease the output amplitude, consistent with our observations. We opted not to include friction in our modeling for two reasons: 1) we kept only the biologically-relevant damping terms in the system equations, and 2) modeling friction can be complicated due in part to highly-nonlinear stick-slip phenomena [102].

1.4.3 Dynamic efficiency is amplitude and frequency dependent

To determine the efficacy of elastic springs for energy reduction in a flapping wing system, we calculated the dynamic efficiency, η, across all system and actuation parameters (Fig. 1.7). Generally we observe that dynamic efficiency is maximum along the resonance curves for all experiments. These results are consistent with the interpretation that maximum kinematic gain corresponds to maximum energetic benefits of having a spring, e.g. that the system is at resonance. Notably the dynamic efficiency is very sensitive to oscillation frequency for low motor amplitudes while higher motor amplitudes show a very broad dynamic efficiency. The results at high amplitude are consistent with the broad dynamic efficiency versus frequency

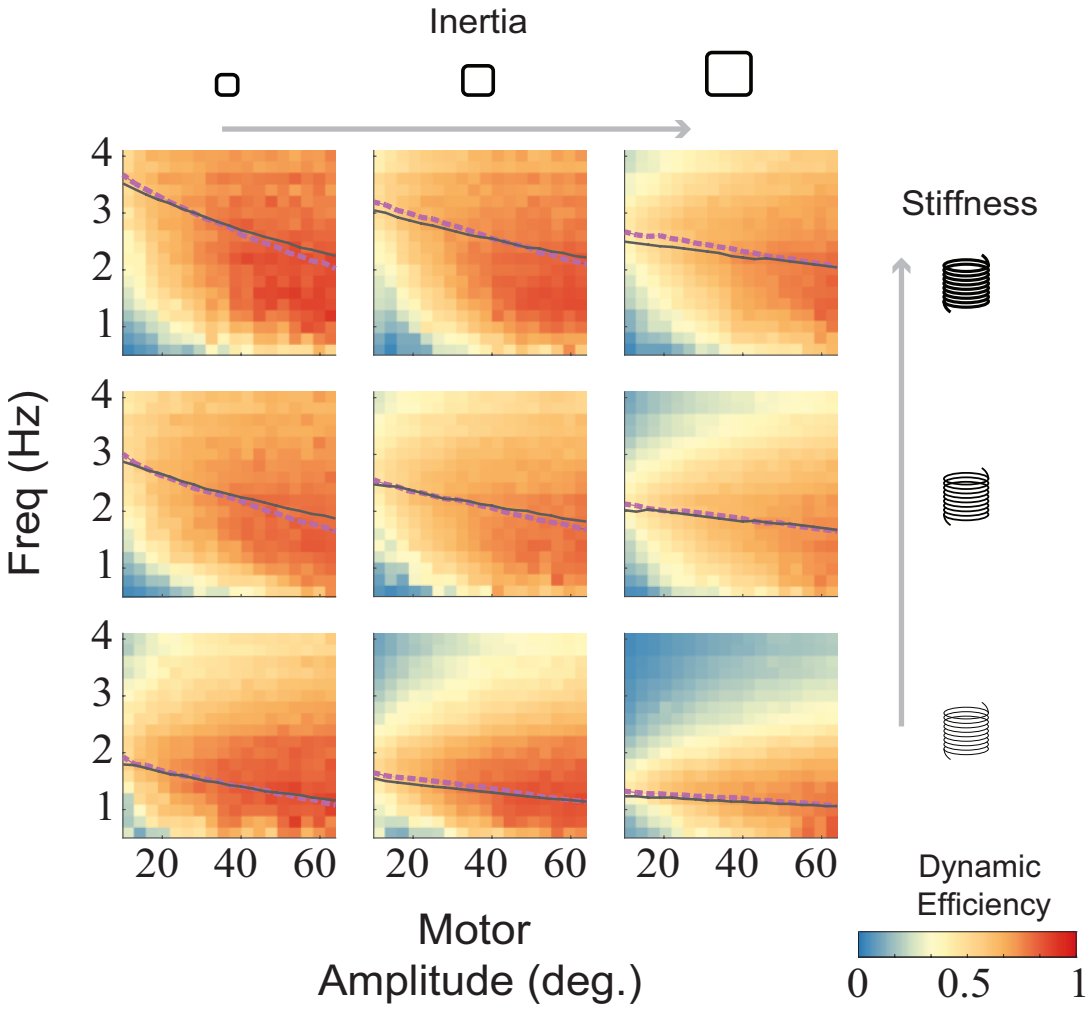

Figure 1.7. Dynamic efficiency as a function of motor amplitude and frequency. Experiments are ordered in increasing spring stiffness (rows) and inertia (columns) as indicated by the arrows and text. Dashed lines are experimentally determined resonance while solid lines are model predictions for resonance.

curves measured in experiments on a flapping wing robot in [23].

1.5 Discussion

In this discussion, we recall the preliminary framework established in Section 2. Through a change of variables we were able to express the equations of motion of the series and parallel spring-wing systems (Equations 1.1 & 1.2) with nearly identical expressions. In this discussion we now seek to interpret the series elastic experiment and simulation results above in the context of the non-dimensional variables: the reduced stiffness $\hat{K}$, the Weis-Fogh number N, and the structural damping coefficient γ.

1.5.1 The Weis-Fogh number, N governs resonant properties in spring-wing systems

The frequency response and kinematic gain of the spring-wing system indicates that the resonant behavior of the system is dependent on the flapping amplitude and frequency. In a standard spring-mass system with a viscous damper, frequency dependent kinematic gain is to be expected. However, the dependence of the system resonant frequency on oscillation amplitude in the series spring-wing system (Fig. 1.5) is different than that of the standard viscously-damped spring-mass system (unless the damping is close to a critical value). Similar to the way the spring-mass system is often reduced to non-dimensional ratios (damping ratio, ζ and reduced frequency, ω/ω_n) that govern the oscillation behavior, we here seek to show how the non-dimensional parameters of Equations 1.8 & 1.11 govern the resonance properties of the system.

N is a measure of aerodynamic damping in spring-wing resonance

An important metric of a resonant system is the quality factor, Q, a measure of how damped the oscillator is and which, in experiment, is the sensitivity of kinematic gain to frequency change. For a linear spring-mass system, Q is independent of oscillation amplitude, but it is inversely proportional to the damping ratio, ζ. In the non-dimensional spring-wing equations,

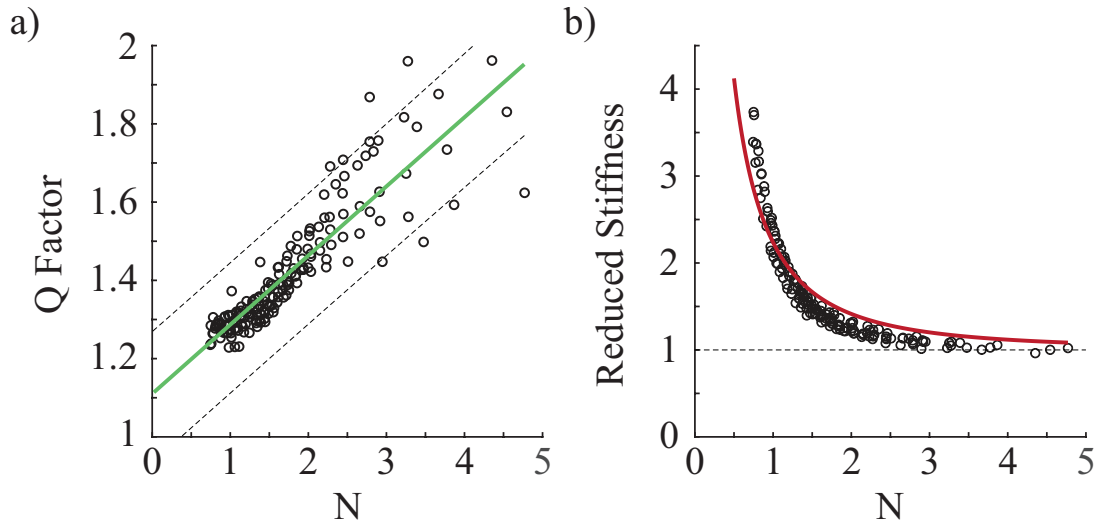

Figure 1.8. a) The quality factor of the oscillation as a function of Weis-Fogh number, N, in experiment with a linear fit and 95% confidence interval. b) Relationship between reduced stiffness $\hat{K}$ and Weis-Fogh number, N in experiment. The line represents the optimal stiffness-damping relationship (Eq. 1.25)

the two terms that govern system damping are the Weis-Fogh number, N (the prefactor of the aerodynamic term) and the structural damping loss modulus γ. We expect that for any useful spring-wing system, the energy loss due to aerodynamic damping should be much larger than the parasitic energy loss from internal structural damping. Thus, we are inspired to examine how quality factor varies with the Weis-Fogh number.

Examining the dependence of Q on the Weis-Fogh number, we observe that the quality factor grows approximately linearly with the Weis-Fogh number (Fig. 1.8a) across the ranges observed in experiment. Simulations further reveal a linear relationship between Weis-Fogh number and system quality factor given by

$$Q = c_1 N + c_2 \tag{1.24}$$

where $c_1 = 0.18 \pm 0.01$ and $c_2 = 1.11 \pm 0.03$ (95% CI). By analogy with the linear spring-mass system, the linear relationship between Q and N reveals that the quantity $\frac{1}{N}$ is comparable to the damping ratio for linear spring-mass systems.

The importance of this relationship is that Q has historically been used to evaluate the ability of insects to benefit from elastic energy storage. Ellington, using a version of Q defined as the ratio of peak kinetic energy versus energy dissipated per stroke, has reported Q values for a variety of insects such as the fruit-fly, *Drosophila melanogaster*, hawkmoth *Manduca sexta*, and the bumblebee *Bombus terrestris* [9]. Ellington uses those values to argue that insects would benefit from resonant dynamics. While it is not possible to directly compare the values he reports due to the use of different expressions for Q, we can use the functional relationship in equation 1.24, to also estimate quality factors for the fruit-fly ($N \leq 1$, $Q \approx 1.2$), the hawkmoth ($N = 3.6$, $Q \approx 1.7$), and the bumblebee ($N = 3.1$, $Q \approx 1.6$). Weis-Fogh numbers for the relevant animals were provided by Weis-Fogh in [55]. Quality factors above 1, in this case, confirm that insects may indeed benefit from resonance. By tying those values to N, however, we provide the added benefit of showing how Q factor may scale across species and enable comparison of a wider range of species of insect.

The resonant frequency of a series spring-wing system varies with N

Examination of the Weis-Fogh number shows that N grows inversely with wing amplitude (Equation 1.6). Thus, experiments that were performed at low motor amplitude correspond to spring-wing systems with large N. This observation, coupled with the insight from above, immediately provides understanding for why the resonant frequencies at low amplitudes match the system's natural frequency (Fig. 1.6a). At low amplitude (high N) the influence of damping is very small (scales as $\frac{1}{N}$) and thus increasing N in spring-wing systems results in minimizing the the effects of aerodynamic nonlinearity and energy loss.

However, this insight does not fully explain why the resonance frequency should change with amplitude. Examination of the relationship between the non-dimensional variables that relate frequency ($\hat{K}$) and damping (N) at resonance shows a tight locus of points that indicate a potential relationship (Fig. 1.8b). To understand this relationship we follow the method originally introduced by Bennett et al. for the analysis of series elasticity in whale flukes [103]. In that paper,

the authors determine the instantaneous aerodynamic, inertial, and elastic power contributions in the system and then minimize the total power consumption over a wing-stroke (see Appendix A.5) to identify an optimal combination of parameters. The combination of parameters that minimize total power is given by the following relationship:

$$\hat{K} = \sqrt{1 + 4/N^2} \tag{1.25}$$

We plot this relationship in Figure 1.8b and observe good agreement ($R^2 = 0.868$, $RMSE = 0.22$) between the predicted optimal series spring-wing relationship and observed relationship at resonance. The observed differences between experiment and theory could result from measurement error, or alternatively friction, structural damping, or aerodynamic effects that are unmodeled in the original derivation. However, solving Eqn. 1.25 in terms of the actual resonant frequency, ω_r and system parameters (see Appendix A.5) shows very good agreement over the frequency, motor amplitude parameter space (Fig. 1.5, black line). For completeness, we note that for a parallel spring-wing system, the resonance relationship is constant: $\hat{K} = 1$ for all N [103].

The overall intuition from this resonance analysis is that the Weis-Fogh number plays an important role in determining the spring-wing system's resonant behavior. Furthermore, the relationship between N and $\hat{K}$ at resonance implies that these two variables likely define a non-dimensional parameter space for general spring-wing systems of arbitrary morphology, mechanical properties, and actuation. In the following sections we will expand that space by exploring how N, $\hat{K}$, and structural loss factor γ influence dynamic efficiency.

1.5.2 Energy loss from structural damping scales with Weis-Fogh number in real spring-wing systems

Recent discoveries that structural damping in hawkmoth thoraxes [76] and cockroach legs [86] may cause significant energy loss prompts us to investigate how structural damping

contributes to spring-wing energetics. To gain insight into energy loss scaling, we consider the parallel arrangement of a spring and a wing (Fig. 1.1a). The parallel arrangement, as opposed to the series arrangement, is convenient because the spring (and structural damper) are subject to identical displacements as the wing hinge, and thus all forces (spring, damping, aerodynamic, and inertial) can be represented as functions of wing angle. In the series case, the actuation and wing trajectories are out of phase and therefore more complicated, if not impossible, to express analytically. In the parallel system, we can conveniently visualize all the relevant forces acting on the wing by plotting torque contributions versus wing angle (Fig. 1.1a and Fig. 1.9a).

We now consider the scaling of each of these forces with the non-dimensional system parameters. Following the method introduced by Weis-Fogh, we normalize all the non-dimensional torques (Equations 1.8) by the peak aerodynamic torque at mid-stroke. The result is the following set of non-dimensional torques, expressed as functions of normalized wing angle, q. The tilde symbol represents torques normalized by peak aerodynamic torque:

$$\begin{aligned}
\tilde{Q}_{aero} &= (1-q^2) \\
\tilde{Q}_{inertial} &= -Nq \\
\tilde{Q}_{elastic} &= \hat{K}Nq \\
\tilde{Q}_{structural} &= \gamma\hat{K}N\sqrt{1-q^2}
\end{aligned} \tag{1.26}$$

See Appendix A.6 for the full derivation of these terms and §A.7 for an additional derivation of the torque due to viscous damping.

In the parallel system, the ideal spring torque is exactly opposite the inertial torque and thus cancels the inertial work throughout the wing stroke, $\tilde{Q}_{elastic} = \tilde{Q}_{inertial}$. This relationship implies that $\hat{K} = 1$ in the ideal parallel system. Converting this expression back to dimensional form returns the expected relationship that defines a parallel resonant system, $k_p = I_t\omega^2$.

Critically for analysis of spring-wing energetics, all of these equations can be integrated

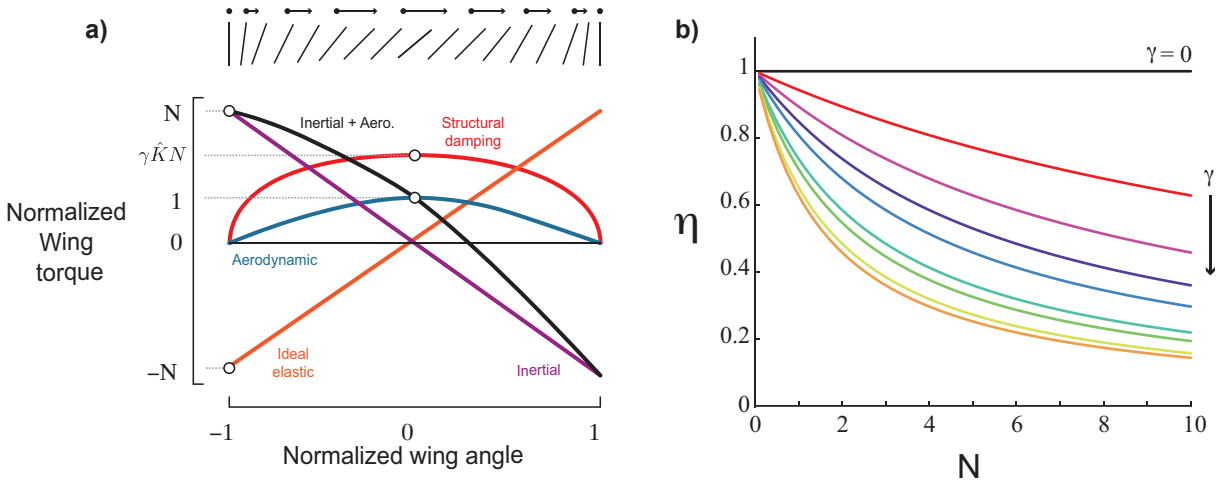

Figure 1.9. a) Non-dimensional torques acting on the wing hinge during the upstroke or downstroke. b) Theoretical dynamic efficiency (Eqn. 1.30) for a parallel spring-wing system. Top curve is $\gamma = 0$ and curves below are increases of γ in increments of 0.05.

over the wing stroke to provide expressions for the non-dimensional work the wing has performed. In the case of parallel resonance ($\hat{K} = 1$) we simply need to integrate the $\tilde{Q}_{aero}$ and $\tilde{Q}_{structural}$ terms since the inertial and elastic work exactly cancel. Performing these integrals over the range q =[-1, 1] results in the following expressions

$$\tilde{W}_{aero} = \frac{4}{3} \tag{1.27}$$

$$\tilde{W}_{structural} = \frac{\pi}{2}\gamma N \tag{1.28}$$

Since aerodynamic and structural damping work are the only sources of energy loss (and thus the only required energy input) in the system we can now express the dynamic efficiency in terms of these two energy losses.

$$\eta = \frac{\tilde{W}_{aero}}{\tilde{W}_{aero} + \tilde{W}_{structural}} \tag{1.29}$$

$$= \frac{1}{1 + \frac{3\pi}{8}\gamma N} \tag{1.30}$$

We now have an expression for the dynamic efficiency of a parallel spring-wing system operating at the resonance frequency. The dynamic efficiency is a function of only the Weis-Fogh number, N, and the structural damping γ. Examination of this expression indicates that if there is no structural damping in the system ($\gamma = 0$) the dynamic efficiency is constant, $\eta = 1$, across all N, indicating that all input work goes towards aerodynamic work at steady state. However, for any non-zero structural damping in the transmission, the dynamic efficiency is a monotonically decreasing function of N, since a portion of the input work must be diverted to overcome the internal structural damping.

This analysis of a parallel spring-wing system has provided insight into how structural damping influences the mechanical efficiency of the flight transmission, i.e. dynamic efficiency. We would like to consider the same theoretical analysis for a series spring-wing system, but in this case the theoretical approach becomes intractable. In a series spring-wing system, the relative phase difference between wing and actuator changes with actuation parameters and thus the relative spring extension (and rate of extension) is not as easily determined. Bennett et. al. [103] presented an elegant reformulation of the problem to generate a closed form expression for the actuator power required in a series spring-wing system. However, this method cannot be used to include structural damping because it would require knowledge of the actuator input kinematics. Thus, to determine the influence of structural damping in a series spring-wing system we will resort to numerical methods in the next section.

1.5.3 Structural damping reduces peak dynamic efficiency in series spring-wing systems

The dynamic efficiency η for series spring-wing systems was determined through numerical simulation of the non-dimensional equation of motion 1.11 across a range of N and $\hat{K}$. As expected in the case of no structural damping, $\gamma = 0$, the dynamic efficiency was $\eta = 1$ for all values of N and $\hat{K}$ along the series resonance curve, (Eqn. 1.25) (Fig. 1.10a). These simulations also allow us to observe how η varies across the full (N, $\hat{K}$) parameter space. In general, we

observe stronger sensitivity of η to changes in $\hat{K}$ as N increases. Recalling our analysis of the connection between quality factor and Weis-Fogh number N, it is clear that, for a spring-wing system with fixed morphology and no structural damping, as N increases, the variation of η with frequency becomes more significant.

For systems with non-zero structural damping, as expected in any real system (and as observed recently [76], [86]), the dynamic efficiency in general decreases with increasing N for all values of $\hat{K}$. For small structural damping ($\gamma = 0.1$; Fig. 1.10b) we observe a general similarity of the dynamic efficiency to the undamped case. The gradient of the dynamic efficiency can be observed by the spread of the contour lines, where a steep gradient is indicated by closely spaced contour lines. In the undamped case, the resonance relationship follows the line of minimum gradient in dynamic efficiency ($\min\nabla\eta$): the resonance curve exactly follows the contour line of $\eta = 1$ (and thus $\nabla\eta = 0$). Examination of η for increasing structural damping indicates the curve of minimum $\nabla\eta$ likely differs from the undamped resonance as illustrated in Fig. 1.10a, where the dashed lines represent estimates of the line of minimum gradient to guide the eye.

Evaluating the dynamic efficiency across the different values of γ shows that η monotonically decreases with N, consistent with our analysis of the parallel spring-wing system. In the inset of Figure 1.10b, we show the dynamic efficiency results at resonance for the experimental series spring-wing system. The experiment exhibits the same monotonically decreasing trend of η with N. However the magnitude of η in the experiment differs from that predicted by the simulation with structural damping alone. Thus, similar to the previous comparison of simulation and experiment (Fig. 1.6) we observe qualitatively similar trends between experiment and simulation, however the experiment exhibited lower η, likely due to additional sources of energy loss from friction and other unmodeled effects.

Overall, both the experimental and simulation results provide evidence that, for any spring-wing system with structural damping, the dynamic efficiency decreases monotonically with increasing N. Further, dimensional analysis of the viscous damping model (see Supplmental §A.7) suggests that internal damping of *many* types has the same effect on dynamic efficiency.

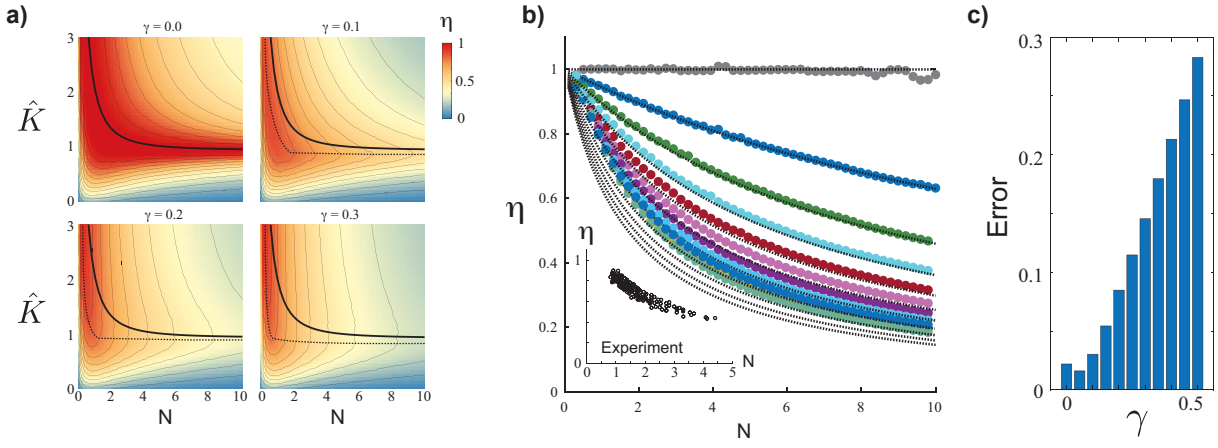

Figure 1.10. a) Simulation of dynamic efficiency in a series spring-wing system for four values of structural damping. The solid black line is the undamped resonance relationship between N and $\hat{K}$. The dashed lines are drawn to guide the eye along the estimated minimum of the dynamic efficiency gradient. b) Numerical calculations of dynamic efficiency along the undamped resonance relationship curves for $\gamma = [0, 0.5]$ in increments of 0.05. Dashed lines show results from a parallel spring-wing system at resonance for comparison. Inset shows the dynamic efficiency of the experimental spring-wing system at resonance. c) Sum of squares difference between the series simulation η and the parallel closed form η for varying amounts of structural damping (γ).

These results are a bit counter-intuitive from the discussion above, where quality factor is observed to scale linearly with N (Fig. 1.8a). For a perfect spring-wing system ($\gamma = 0$) it is true that increasing N diminishes the relative energy loss from aerodynamic work compared to the total energy of the oscillator (the definition of the quality factor). However, in the presence of internal energy losses, the actuators have to do extra work to overcome internal body damping, which scales with N. With internal damping, the quality factor might still be the same (since it is a ratio of energies) but the internal damping decreases the useful energy of the oscillator and thus dynamic efficiency.

1.5.4 Intermediate Weis-Fogh number may balance damping losses and elastic benefits

The scaling of dynamic efficiency with N may help explain why flapping wing insects and robots tend to have an N in the range of 1-10 across three orders of magnitude in body mass

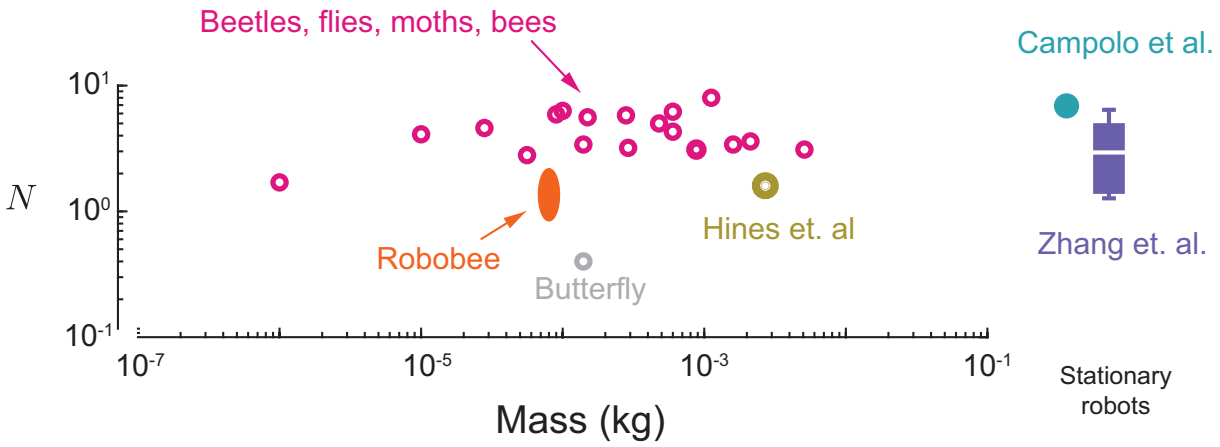

Figure 1.11. The Weis-Fogh number for flying insects and robots as a function of body mass (left plot) and in fixed flapping wing robots (right boxplot). Biological data is reported from [55], and robot data from [23], [24], [89], [104]. Most observed insects and robots lie within the mass-independent range of $N \in [1, 10]$.

(Fig. 1.11). A very low N means that aerodynamic forces dominate and wing kinetic energy will be dissipated by aerodynamic work rather than be stored in a spring [82]. High N, however, increases the internal energy losses from structural damping and reduces the benefits of elastic energy storage. Thus, flapping wing insects and birds with Weis-Fogh number in an intermediate range may balance the positive benefits of spring-wing energy exchange with the parasitic energy losses of internal structural damping. In order to achieve high dynamic efficiency at hover, wing geometries, flapping amplitudes, and wingbeat frequencies may be tuned to maintain operation in this restricted regime of Ns.

In addition to the constraints of damping, high N biological spring-wing systems may not be possible due to biomaterial or physiological constraints. For example, high N spring-wing systems that are capable of hover (implying modest wingbeat amplitude, θ_0) would require large wing inertia which may be impractical due to the possible imposition of extra system weight. Similarly, from the elastic materials perspective a high-N spring-wing system with large wing inertia would require extremely stiff and resilient elastic elements to operate at resonance. It may be that for extremely large N spring-wings the required elastic stiffness may exceed the practical regime of biological materials. Both of these considerations however do not necessarily limit

robotic systems from being developed with high N through appropriate inertial and stiffness design considerations.

Lastly, it is unlikely that dynamic efficiency at hover is the only factor that dictates this range of morphologies. Other factors, such as the effect of N on transient dynamics and control of wing kinematics, are likely to be significant. For example, in a spring-wing system with high-N the wing dynamics are dominated by inertial effects and thus wing kinematics are likely insensitive to transient changes in aerodynamic forces. Such a high-N system may have wingbeat kinematics that are relatively stable in the presence of gusts of wind. However, in the opposite case of a low-N spring-wing system, the flyer would be able to more easily modulate wing kinematics and possibly wingbeat frequency for control purposes. In these cases and others, the Weis-Fogh number may provide a baseline for insight in broad comparative study of flying insects, enabling identification of commonalities between species as well as exceptional cases that merit further study.

1.6 Conclusion

Many flapping wing insects and birds possess elastic elements in their body that may reduce the power demands of flapping wing flight. However, recent experiments have demonstrated that insects are also subjected to internal power loss from the deformation of their thorax. In this manuscript we have introduced three non-dimensional variables for general spring-wing systems that govern oscillatory behavior and dynamic efficiency. Inspired by the foundational work of Weis-Fogh, we re-introduce the ratio of maximum inertial force to aerodynamic force as the Weis-Fogh number, N. Experiments and simulation illustrate that N is a fundamental parameter of spring-wing systems, analogous to the quality factor of a linear spring-mass system. However, when spring-wing systems have internal structural damping, we observe that dynamic efficiency decreases with increasing N on resonance, reducing the potential for useful energy storage and return. Overall, these results provide a generic framework to understand spring-wing

systems which may enable us to learn more about the inter-relationships of morphology and actuation in flapping wing insects and birds.

Author Contributions

JL, JG, SS, and NG designed experiments, interpreted data, and wrote the paper. JL designed the robophysical model and ran all experiments. NG and JL performed simulations, data analysis, and dimensional analysis.

Acknowledgments

Thanks to Dennis Wu for his invaluable work on the early prototypes of the robophysical flapper device and to Eugene Lin for his help fabricating silicone springs.

Chapter 1, in full, is a reprint of the material as it appears in the Journal of the Royal Society Interface as *Lynch J, Gau J, Sponberg S, Gravish N. Dimensional analysis of spring-wing systems reveals performance metrics for resonant flapping-wing flight, 2021*. The dissertation author was the primary investigator and first author of this paper.

Chapter 2

Energetic and Control Tradeoffs in Spring-Wing Systems

2.1 Background & Motivation

Flapping flight is an extremely power-intensive mode of locomotion, requiring both high frequency and large forces to produce lift and perform agile maneuvers. Flying insects achieve efficient flight through a combination of specialized flight muscles [4] and elastic energy storage in the thorax, ten [51], [55], [82]. However, there has been limited work towards understanding the implications of this elastic energy storage and return for flight dynamics and control in flying insects.

2.1.1 Flapping flight as a resonant system

A consequence of these "spring-wing" dynamics is that there exist one (or more) resonant wingbeat frequencies at which flapping efficiency is maximized [105]. Operating at a resonant frequency that maximizes lift can enable mechanical advantage, allowing insects to produce smaller muscle forces for a particular set of flapping kinematics. Indeed, roboticists designing insect-scale flapping robots have found that incorporating elasticity and operating near resonance enables higher lift and greater payloads [18], [22], [26], [89], [91]. However, there are tradeoffs inherent in operating at resonance [89]. For example, the output wing amplitude is maximized at the resonant frequency, but any deviation from that frequency peak will result in a decrease

in wing amplitude, requiring more energy input per wingstroke, and thus potentially limiting the flapper's ability to quickly change wing kinematics. This means that a system with a sharp resonant peak has the benefit of improved efficiency, but would require larger torques or a longer time to change flapping amplitude or create wingbeat asymmetries to adjust the direction of flapping thrust. These tradeoffs are likely to be different for insects or robots with different physical characteristics, but it's not immediately clear how they scale because of the nonlinearity of flapping aerodynamics [106].

2.1.2 Hypothesis: Control and efficiency tradeoff scale with Weis-Fogh number, N

What effect does N have on a system's control authority? Consider two insects with the same wing geometry and flapping at the same amplitude, but with different overall wing inertias. The insect with a larger wing inertia would have to put more energy in to driving the wing to full amplitude, and the greater momentum of the wing would resist changes to that amplitude (Fig. 2.1b). Thus the insect with a larger N would tend to be more sluggish than an insect with lower N, and thus lower wing inertia. On the other hand, consider if the insects are flying in a crosswind and need to maintain their wingbeat amplitude to maintain hovering stably (Fig. 2.1c). This is a perturbation that acts through the aerodynamic damping term in Eq. 2.3, such that the aerodynamic torque becomes $\tau_{aero} = N^{-1}|\dot{x} - v|(\dot{x} - v)$. In this case, the insect with higher N is less affected by the perturbation, whereas the asymmetrical velocity effects on other insect may have a larger destabilizing affect. In summary, we hypothesize that the Weis-Fogh ratio is a governing parameter of both wingbeat response timescale (increases with N), and susceptibility to aerodynamic perturbations (decreases with N). These two performance metrics impact maneuverability and stability in competing ways, and thus present a potential dilemma for spring-wing resonant flight.

We set out to study the effects of Weis-Fogh number on 1) the responsiveness of a flapping system to control inputs, i.e. starting from stop or changing amplitude, and 2) the ability

of a flapper to maintain flapping kinematics when subjected to an asymmetrical aerodynamic perturbation. The following section sets out expectations based on an analytically tractable version of the spring-wing system with viscous damper. Then, we discuss two experiments on a dynamically-scaled spring-wing robot that measure, respectively, the time it takes for systems with different N to flap up to full amplitude and the ability of those systems to maintain sinusoidal flapping kinematics in the presence of a constant flow perturbation. Finally, we discuss the implications of these and prior results for the biomechanics of insect flight systems and the design of flapping-wing micro aerial vehicles (FWMAVs).

2.2 Theoretical preliminaries

2.2.1 The Weis-Fogh number governs spring-wing resonance dynamics

The Weis-Fogh number is named for Torkel Weis-Fogh, a pioneer in insect flight biomechanics and discoverer of the elastic protein resilin [51], and is defined as the ratio between maximum inertial and maximum aerodynamic torque during flapping:

$$N = \frac{\max(\tau_{inertia})}{\max(\tau_{aero})} \tag{2.1}$$

If a system has inertia I, aerodynamic drag coefficient Γ, and flaps sinusoidally with peak-to-peak amplitude θ_o, we can also write $N = I/(\Gamma\theta_o)$. Weis-Fogh introduced this term as a part of an argument about the necessity of elastic energy storage and return in the flight system of insects [55]. It expresses the relative influence of inertial and aerodynamic effects on the dynamics of a flapping wing; $N < 1$ means aerodynamic force dominates, whereas $N > 1$ means that inertial force is dominant (See Fig. 2.1a).

We found, through dimensional analysis and dynamically-scaled robotic experiments, that it also has a significant relationship to the resonant characteristics of spring-wing systems. We can write an equation of motion of a spring-wing system with structural (frequency-independent)

damping as defined in [106]:

$$I_t\ddot{\theta} + k\theta + \frac{k\gamma}{\omega}\dot{\theta} + \Gamma|\dot{\theta}|\dot{\theta} = \tau_{in} \tag{2.2}$$

where I_t is the total inertia of the wing plus added mass inertia, k is the spring stiffness, γ is the structural damping loss modulus [87], ω is the forcing frequency, and τ_{in} is the input torque. The system constitutes a forced harmonic oscillator with quadratic damping coefficient Γ and the aerodynamic term is typically much larger than the structural damping term [76]. The expression can also be written in non-dimensional form in terms of the dimensionless sinusoidal displacement q, the non-dimensinoal stiffness $\hat{K}$ (which is 1 when the system is driven at its natural frequency), the structural damping factor γ, and the Wies-Fogh number N [106]:

$$\ddot{q} + \hat{K}q + \hat{K}\gamma\dot{q} + N^{-1}|\dot{q}|\dot{q} = \tilde{\tau}_{in} \tag{2.3}$$

Previously we found that the dynamic efficiency when flapping at resonance, a measure of the amount of muscle work that goes directly to producing lift/overcoming drag, $\eta = \frac{W_{aero}}{W_{total}}$, scales with N in systems with *any* internal damping losses [106]

$$\eta = \frac{1}{1 + \frac{3\pi}{8}\gamma N} \tag{2.4}$$

Therefore, while it is beneficial to have an $N > 1$ for elastic energy exchange and resonance, higher values of N have diminishing returns in terms of peak efficiency.

2.2.2 Linear system analysis highlights stability and maneuverability tradeoffs in resonant spring-wing flight

To gain insight into how we should expect the spring-wing to behave in our start up and constant aerodynamic perturbation experiments, we start by studying the behavior of a linear spring-mass-damper. We choose to use the linear equations because the quadratic aerodynamic

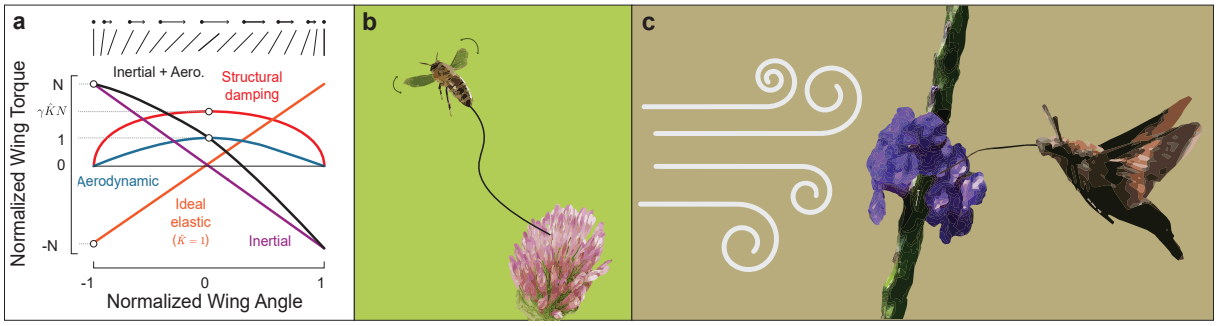

Figure 2.1. Weis-Fogh number and flight performance. a) A Weis-Fogh diagram, which illustrates the relationship between inertial, aerodynamic, elastic, and internal damping forces over a wing stroke [55], [106]. The Weis-Fogh number is labeled on the vertical axis. We hypothesize that increasing Weis-Fogh number correlates more sluggish take off from rest (b) and better resiliencec to aerodynamic perturbations (c).

damping in the spring-wing equations prohibit closed-form solutions. However, we will show that features of the linear system are analogous to the nonlinear version and draw conclusions based on that.

2.2.3 Normalized linear spring-mass-damper

Consider the forced linear spring-mass-damper equation:

$$m\ddot{x} + b\ddot{x} + kx = F_0 \sin(\omega t) \tag{2.5}$$

We can normalize the differential equation here by dividing by the mass, creating the classic 2nd-order ODE.

$$\ddot{x} + 2\xi\omega_n\ddot{x} + \omega_n^2 x = F_m \sin(\omega t) \tag{2.6}$$

where ω_n is the natural frequency of the system and ξ is the damping ratio, which dictates whether the system is over-, critically, or underdamped. The foring term F_m is defined as $F_m = \frac{F_0}{m}$ Another way to write 2.6 is by defining the quality factor $Q = \frac{1}{2\xi}$:

$$\ddot{x} + \frac{\omega_n}{Q}\dot{x} + \omega_n^2 x = F_m \sin(\omega t) \tag{2.7}$$

The quality factor here has a number of interpretations, but for our purposes, it represents the "steepness" of the resonance peak. $Q < 0.5$ results in an overdamped system with no peak, whereas high Q results in a tall and narrow resonance curve.

The time to full amplitude varies linearly with Q

The solution to Eq. 2.7 for $Q > 0,5$ is oscillatory motion that has an initial transient response that depends on initial conditions (which determine oscillation amplitude X_o and phase delay δ), followed by steady-state oscillatory behavior as $t \to \infty$

$$x(t) = X_0 e^{-\lambda t} \cos(\omega_d t - \delta) + R\cos(\omega t - \Delta) \tag{2.8}$$

where

$$\lambda = \frac{\omega_n}{2Q} \tag{2.9}$$

$$\omega_d = \omega_n^2 \sqrt{1 - \frac{1}{4Q^2}} \tag{2.10}$$

$$\omega_n = \sqrt{\frac{k}{m}} \tag{2.11}$$

$$R = \frac{F_m}{\sqrt{(\omega_n^2 - \omega^2)^2 + \frac{\omega_n^2}{Q^2}\omega^2}} \tag{2.12}$$

$$\tan\Delta = \frac{\omega_n \omega}{Q(\omega_n^2 - \omega^2)} \tag{2.13}$$

The rate of decay of the transient portion of the ODE solution is

$$\lambda = \frac{\omega_n}{2Q}, \tag{2.14}$$

which is inversely related to Q. To find the time it takes a forced system to achieve some percentage p of full amplitude, we define a small parameter $\varepsilon = 1 - p$ and solve for t_p

$$\varepsilon = e^{-\lambda_{tr} t_p} \tag{2.15}$$

$$\rightarrow t_p = \frac{-\ln \varepsilon}{\lambda_{tr}} \tag{2.16}$$

$$= \frac{-2\ln \varepsilon}{\omega_n} Q \tag{2.17}$$

or, expressed in terms of the natural period $T_n = 2\pi/\omega_n$

$$\frac{t_p}{T_n} = \hat{t}_p = \frac{-\ln \varepsilon}{\pi} Q \tag{2.18}$$

Thus we should expect to see that time it takes for transients to decay should be directly proportional to the quality factor Q, as shown in Fig. 2.2. Notably, $\frac{t_p}{T_n}$ represents a measure of

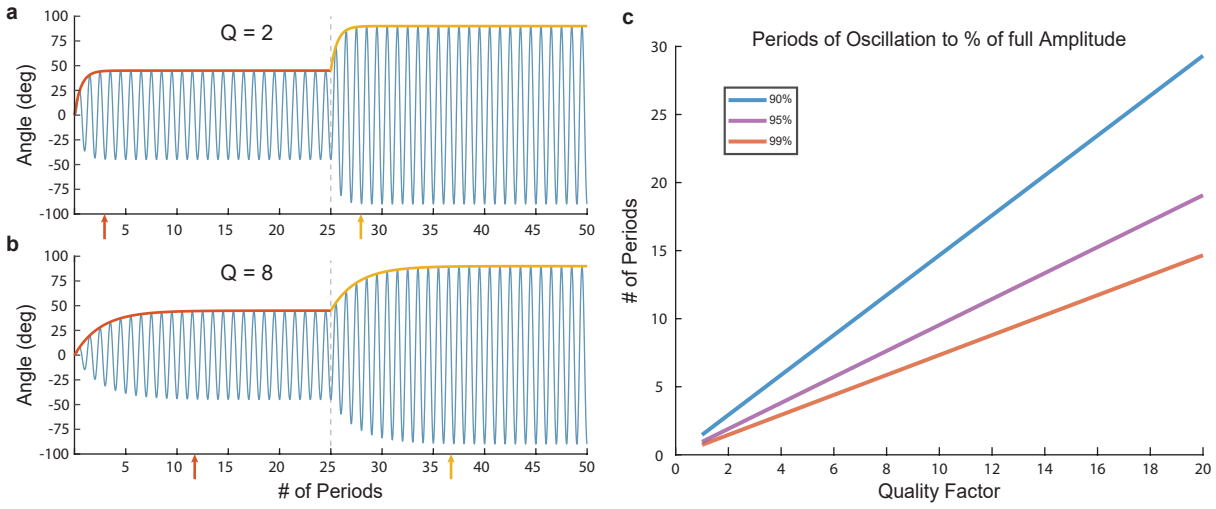

Figure 2.2. Time to full amplitude is proportional to Q. a and b show startup to 45 degree amplitude and an amplitude change from 45 to 90 deg for $Q = 2$ and $Q = 8$ respectively. The rise time is slower with higher Q, as shown in c for several values of p.

control bandwidth in the spring-wing flapping dynamics. An immediate change in oscillatory actuation force (F_0) will result in a time-lagged increase in the wingbeat amplitude that scales as $\frac{t_p}{T_n} \propto Q$. Thus, a spring-wing system with large quality factor will be more "sluggish" because

the control timescale will be large.

The relative influence of aerodynamic perturbations is inversely proportional to Q

Consider a wing flapping in a viscous flow such that the effective velocity at the wing is $\dot{x} - v$. Equation 2.7 can be rewritten

$$\ddot{x} + \frac{\omega_n}{Q}(\dot{x} - v) + \omega_n^2 x = F_m \sin(\omega t) \tag{2.19}$$

$$\rightarrow \ddot{x} + \frac{\omega_n}{Q}\dot{x} + \omega_n^2 x = F_m \sin(\omega t) + \frac{\omega_n}{Q} v \tag{2.20}$$

The effect of the perturbation after the transient has decayed is to introduce a torque that biases the spring in the direction of the external flow. The magnitude of the spring deflection is proportional to the flow velocity and is inversely proportional to Q. Thus the influence of an external flow ona linear flapping system is maller in a spring-wing system with higher Q.

2.2.4 Resonance presents competing influences on wing maneuverability and perturbation rejection

The previous two sections illustrated how the control timescale and susceptibility to aerodynamic perturbations are influenced by the resonant properties of a linear spring-mass-damper. The quality factor (Q) is an important metric in determining properties of a resonant system, and highlights potential tradeoffs in wing maneuverability and stability. Higher Q will result in a slower control response from actuation, yet external fluid forces acting on the wing will result in smaller disruption to wing motion. Lower Q will result in fast control response from actuation, however external fluid forces will cause disruption to the wingbeat kinematics. This linear systems analysis provides motivation for examining the role of spring-wing resonance in the timescales of control and susceptibility to aerodynamic perturbations in flapping wing systems.

2.2.5 The Weis-Fogh Number N is the quality factor of a spring-wing system

To compare the spring-wing and spring-mass equations one trick is to approximate the linear damping coefficient b with the aerodynamic damping coefficient Γ multiplied by the maximum velocity of the wing $\max(\dot{\theta}) = \theta_0\omega$. Thus, the damping term for both spring-mass and spring-wing equations are equivalent at mid-stroke where the wing velocity is highest. This is called the secant approximation and was used in [8]. We can define the following relationship for the linear damping coefficient that models the spring-wing

$$b_{sw} = \Gamma\theta_0\omega \tag{2.21}$$

Substituting this expression into the equation for the damping ratio yields the following

$$\begin{aligned}\xi &= \frac{b}{2m\omega_n} \\ &= \frac{\Gamma\theta_0\omega}{2m\omega_n} \\ &= \frac{1}{2N}\frac{\omega}{\omega_n}\end{aligned} \tag{2.22}$$

Thus, we see that the Weis-Fogh number has a natural connection to the damping ratio of a linear spring-mass system. If we make the assumption that the system is on resonance then the relationship is as follows

$$\xi = \frac{1}{2N} \tag{2.23}$$

We can push this analogy one step further if we consider how the quality-factor relates to the damping coefficient, and by extension the Weis-Fogh number.

$$\begin{aligned} Q &= \frac{1}{2\xi} \\ &= \frac{2N}{2} \\ &= N \end{aligned} \tag{2.24}$$

So here we have demonstrated that through the use of an approximation to model the spring-wing system as a linear spring-mass system we demonstrate that the Weis-Fogh number is exactly the quality factor. This corresponds to our measurements in [106].

We test the scaling relationship between Weis-Fogh number N and the dynamic behavior of spring wings via two experiments in a robophysical model. The first measures response to control inputs by measuring time to peak amplitude from rest, and the second measures the effect of environmental perturbations via measuring the effect of constant cross-flow on symmetry of flapping dynamics. The results suggest that in addition to its effect on peak dynamic efficiency, N illustrates the scaling of agility and perturbation rejection among insects and other small-scale flapping systems.

2.3 Experimental Methods

In a linear forced spring-mass-damper system, it is possible (as shown above) to derive exact solutions for the transient response of the system during start up or just after a finite perturbation. Those solutions show a clear relationship between the Q-factor, responsiveness, and robustness to environmental effects. We expect that the nonlinear analogue of Q, the Weis-Fogh number N, should have a similar relationship to the transient response of the spring-wings system. However, due to aerodynamic drag, the spring-wing equations of motion do not admit an exact solution. To demonstrate the relationship between N and the stability and agility of flapping

in spring-wing systems, we perform a series of experiments on a dynamically-scaled robotic spring-wing system. The robotic system is subject to real fluid forces at Reynolds numbers that are scaled to those experienced by insects and insect-scale robots.

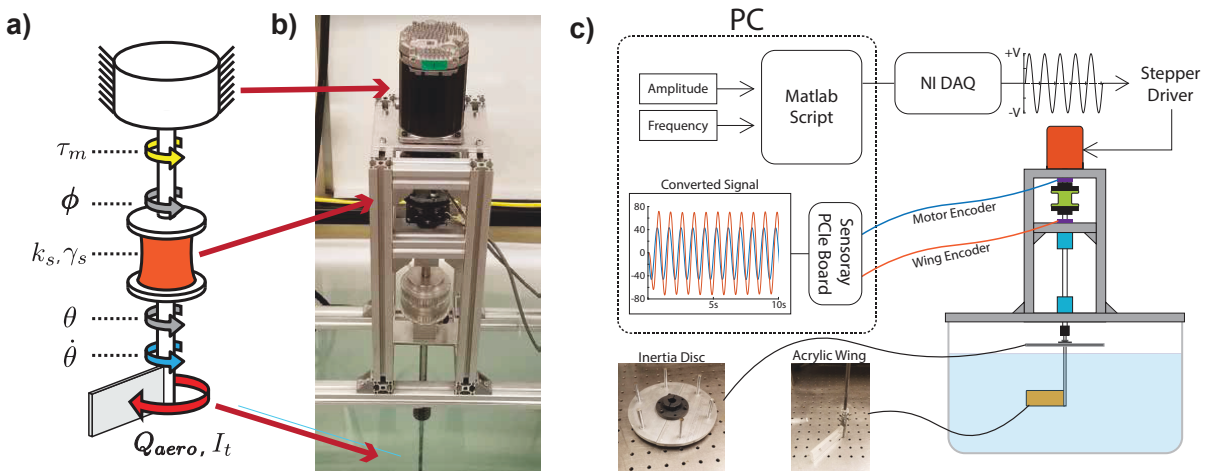

Figure 2.3. The series-elastic spring-wing system. a) Conceptual diagram indicating the angle input, linear spring with structural damping, and rigid fixed-pitch wing. b) Corresponding photo of the roboflapper indicating the ClearPath servo (Teknic), silicone torsion spring, and acrylic wing in a large tank of water. c) Diagram of the whole electromechanical system. See **Lynch2021-oc** for the full details

2.3.1 Dynamically-scaled, series elastic robophysical model

The robotic spring-wing system used in this paper was described in detail in **Lynch2021-oc** and is shown in Fig. 2.3. It consists of a high-torque servo motor (ClearPath) connected to a rigid, fixed pitch acrylic wing in a large tank of water. The elasticity comes from a molded silicone torsion spring in series with the wing 2.3. We created three springs from Dragon Skin 30 silicone (SmoothOn), varying the geometry so that they each had a different stiffness. We

Table 2.1. Inertia and spring stiffness values for the roboflapper

Inertia (kg m^2)	
IA	0.00105
IB	0.00149
IC	0.00233
ID	0.00476

Springs (Nm rad^{-1})	
K1	0.164
K2	0.416
K3	0.632

vary the overall inertia of the system by attaching mass to the main shaft of the flapper (above the water) in the form of acrylic and aluminum plates (Fig. 2.3c). See Table 2.1 for a list of the discrete inertia and stiffness values.

2.3.2 Controlling N, an emergent property of spring-wing flapping systems

We sought to compare the transient behavior of the flapper when it flaps with different values of N. However, due to the dependence on flapping amplitude θ_0, N is an *emergent* quality of a system, and therefore is difficult to prescribe directly. The following section describes the process of determining robotic system configurations for a range of $N = 1-10$ that are used for robustness and agility experiments.

Determine constraints

Based on the range of N seen in insects and flapping robots (Fig. 1.11), we sought to test 10 integer values of N, from $N = 1$ to $N = 10$. Since we're interested in resonant flapping performance, we require the forcing frequency be at the resonant frequency, defined by Eq. A.15. We previously validated that this expression accurately predicts the resonant frequency in a series elastic system in [106]. Additionally, we seek to minimize the range of Reynolds number (Re) across tests. The roboflapper is designed to operate within a range of Re that is similar to insects and small birds ($Re \in [10^2 - 10^4]$), and significant deviations out of that range introduce aerodynamic phenomena that may not be relevant to flapping flight at that scale.

Beyond those considerations, we are limited by constraints on the robotic system. Mechanically, we must use one of three silicone springs, one of four discrete inertial configurations, and the same wing with $\Gamma = 1.07 \times 10^{-3} Nm$. On the control side, we found that our system works best when the flapping amplitude is between $\approx$30 and 120^o peak-to-peak and the flapping frequency is between 0.5 and 3 Hz.

Table 2.2. Configurations for each value of Weis-Fogh number. Amplitude is given as half of the peak-to-peak wing stroke angle

N	Spring	Inertia	Amplitude (deg)	Frequency (Hz)
1	K1	IA	56.2	1.33
2	K1	IB	40.0	1.40
3	K2	IA	18.7	2.89
4	K2	IB	20.0	2.51
5	K2	IC	25.0	2.05
6	K3	ID	42.5	1.45
7	K3	ID	36.8	1.45
8	K3	ID	31.8	1.80
9	K3	ID	28.3	1.81
10	K3	ID	25.5	1.82

Choosing configurations for values of N

With three springs and four inertias, we have a total of 12 configurations of springs and inertia that are possible. We have continuous control of the amplitude and frequency within functional bounds. The process of choosing a configuration for each value of N is as follows:

1. Given a particular value of N, compute $\theta_o = \frac{I}{\Gamma N}$ for each of the four inertias. Exclude any configuration where $\theta_o > 60^o$

2. Compute the resonant frequency f_r based on the remaining inertias and the three available springs. Exclude any configurations where f_r is greater than 3 Hz or less than 1 Hz.

3. Compute the Reynolds number, $Re = \frac{\bar{U}_{tip}\bar{c}}{\nu}$, of flapping based on that amplitude and frequency as well as wing length and chord, 10 cm and 3.6 cm, respectively. Exclude configurations with $Re >\approx 15000$, which is near upper limit of Reynolds number for insects and hummingbirds [107].

4. Select a configuration for each value of N from the non-excluded configurations

The final selections are given in Table 2.2.

2.3.3 Experiment 1: Starting from Rest and Changing Amplitude

We sought to measure the effect of changing N on the time it takes for the system to respond to a change in input. A straightforward way of doing so is to measure the time it takes to flap up to full amplitude after startup. Furthermore, we measured the time it takes to reach a new amplitude after a change in the input.

For each test, the spring stiffness and inertia were set based on the configurations above. The system was driven by a sine wave position signal to the servo through Simulink Desktop Real-Time (Mathworks) and a PCIe 6343 interface (NI). The frequency is also set based on the configuration table, but the wing amplitude is not set explicitly because of the series-elasticity of the roboflapper. We found previously that modeling does not fully predict the kinematic gain between angular input and wing amplitude [106]. Therefore, for each configuration, we found the proper input amplitude to achieve the desired wingbeat amplitude iteratively using a separate Simulink Desktop Real-Time program, prior to the tests, and recorded the input amplitudes. When we performed each experiment, we used the input amplitudes to drive the system in open-loop, which was a fairly reliable way to dictate N (See 2.3).

Each test was run by starting the sinusoidal position signal and running for 15 flapping periods, long enough for the amplitude to stabilize (Fig. 2.4a). After 15 periods, the sinusoidal position signal was increased by 50%, and the experiment continued for a further 15 periods. This was repeated five times for each value of N and sampled at a rate of 1000 samples per period. Note that we refer to the number of periods and that each experiment was run at a different frequency (Table 2.2), so the total runtime varied. The final amplitude θ_0 was determined by fitting a sine curve to the last 5 periods of the each portion of the test using a bounded nonlinear least squares method in MATLAB. Then an exponential curve ($f(t) = \theta_0(1-e^{-\lambda t})$ was fit to the peaks of the absolute value of the wing angle in the start and step portions of the data, and the time to 95% of θ_0 was computed using $\hat{t}_{95} = -\ln(0.05)\lambda^{-1} f_r$ (Fig. 2.4b&c). To create the plots, N was recalculated based on actual experimental measurements, and mean and standard

deviation of both N and $\hat{t}_{95}$ were calculated.

2.3.4 Experiment 2: Effect of constant cross-flow

For the second experiment, we wanted to see how N relates to the flapping wing's ability to reject environmental disturbances. We did this by subjecting the flapping wing to a constant crossflow and measuring its deviation from a symmetrical sine wave. The flow was provided by a submerged aquarium pump (Simple Deluxe LGPUMP400G 400 GPH) fitted with a 1/2" diameter rubber tube. The outlet of the tube was positioned such that it was aligned with the acrylic wing in the tank and created the maximal passive deflection (see Figure 2.5a) against the spring, but did not interfere with flapping, i.e. there was no difference between flapping trajectory whether the tube was in place or not. We measured the torque on the wing when the pump was on and the flow was perpendicular with the wing. We found that the torque was approximately 0.01 Nm, only enough to deflect the softest spring about 3.5 degrees. The maximum peak aerodynamic torque across the experiments is for $N = 1$ and is $\tau_{amax} = \Gamma(\theta_0)^2(2\pi f)^2 = 0.072$ mNm. Thus the magnitude of the perturbation is significantly lower than the maximum drag induced by flapping motion, but is still enough to induce asymmetry in flapping.

We ran the flapper with a constant sinusoidal input that produced a wing amplitude consistent with the proper configuration at each value of N. We recorded the wing trajectory with the pump off to set a baseline at each value of N, then turned the pump on. We analyzed the impact of aerodynamic perturbation on the flapping kinematics by fitting a sine function to the wing trajectory at steady state using MATLAB functions (Mathworks) and recording the fit error (RMSE). The fit error was normalized to the flapping amplitude at that configuration so that it represents the fraction of flapping amplitude and is unitless. Additionally, we noted a change in steady flapping amplitude with the pump on, and plotted the relative change in amplitude from the no flow case to the constant flow case.

Table 2.3. Mean Experimental N values and standard deviations

Goal N	Actual N
1	1.0 ± 0.01
2	2.0 ± 0.01
3	3.0 ± 0.01
4	4.0 ± 0.01
5	5.0 ± 0.04
6	6.0 ± 0.01
7	6.9 ± 0.02
8	8.0 ± 0.02
9	9.0 ± 0.03
10	10.0 ± 0.03

2.4 Results

2.4.1 Start time and step time increase linearly with N

Having computed the time it takes the system to start up and get to 95% of the final flapping amplitude, we multiplied by the frequency of flapping, normalizing to the number of wing strokes. The results across N are shown in Fig. 2.4b. We see that there is a clear relationship between increasing N and increasing time to full amplitude. Configurations with $N = 1$ or 2 are at full amplitude within a single wingstroke, whereas $N = 8-10$ systems take four or more wingstrokes.

The relationship is linear ($t_{start} = 0.486N - 0.243$), but there is a small amount of spread both vertically and horizontally (Appendix, B.1) for each value of N. The vertical spread is to be expected due to fitting in the presence of noise, but we also found that the rise time was sensitive to whether or not the system was at exactly the resonant frequency, maximizing the kinematic gain ($G_k = \theta_o/\theta_{input}$). This was a more significant issue at higher N because of the steeper resonant curve, and the added mass of the system would have made it susceptible to small asymmetries and potentially larger friction, though that was mediated by thrust ball bearings. The horizontal spread indicates that we were not always *exactly* at the desired value of N. The means and standard deviations of N from 1-10 are shown in Table 2.3.

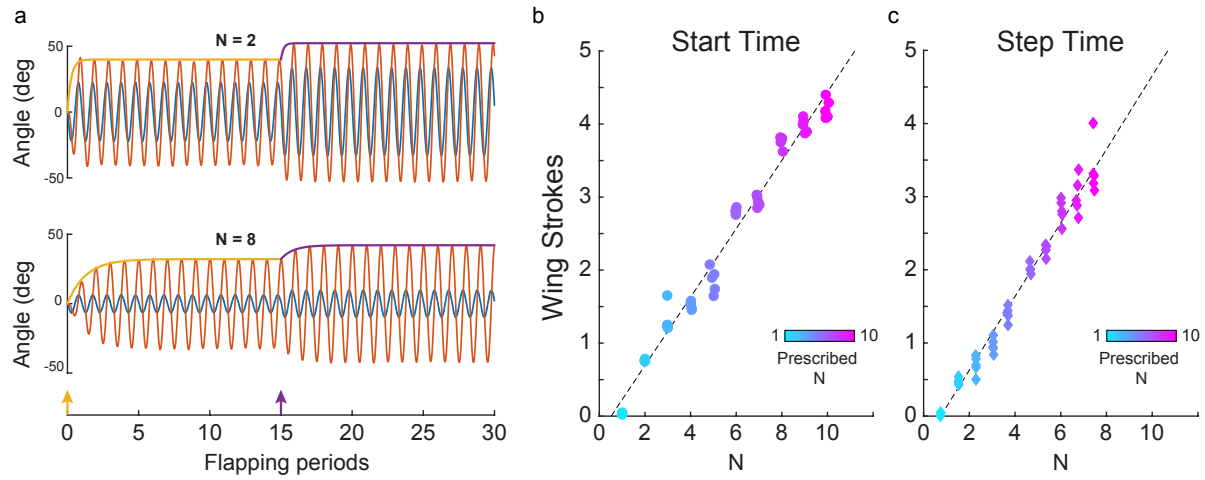

Figure 2.4. Responsiveness Experiments. a) We drive the series-elastic system via servo (blue) and measure the emergent flapping kinematics (orange). We fit exponential curves to the flapping peaks during start up (yellow) and after an input step (purple) 15 cycles after start. The exponential rates decrease with larger N. The measured time (in wing strokes) to full amplitude is linearly related to N (b & c). However, the effective value for N is less than prescribed after the step due to an increase in flapping amplitude (c).

The response time after a step increase in input also has a clear linear relationship with N (Fig. 2.4c). The linear fit is slightly different from the startup data ($t_{start} = 0.503N - 0.376$), but they largely fall upon the same line. The major difference between the two is that because of the change in amplitude after the step, the effective value of N is lower than it was before the step. The effect is a compression of the datapoints along the diagonal, since the response time decreases along with N.

2.4.2 Sinusoidality of wing kinematics decreases with increasing N

Figure 2.5 shows how increasing N results in more sinusoidal flapping kinematics in the presence of perturbations. Asymmetrically warping of the wing trajectory by an external flow leads to non-sinusoidal wing kinematics and a "lumpy" phase portrait (Fig. 2.5a). When there is no flow across the wing, wingstrokes are very close to sinusoidal (circular in phase space) regardless of N. When the flow is turned on, however the kinematics are affected significantly and deviate from sinusoidal (Fig. 2.5b). Note that the trajectories are "lumpier" when N is small,

but also that there's a decrease in flapping amplitude overall at higher N.

When we fit a sine wave to each trajectory in MATLAB, we are provided with "goodness of fit" metrics, including root mean squared error (RMSE), which quantify how well a sine wave fits to the data. This error will never reach zero, but for the no-flow case, it is small - just 0.76% of the flapping amplitude. We find that the error at low N is much higher than at high N, from a maximum error near 8% of the flapping amplitude, to a minimum just above the baseline fit error.

Based on Eq. 2.20 and our association of Q and N, we expect that the influence of asymmetric flow should be inversely proportional to N. We used built-in MATLAB functions to fit an inverse curve $AN^{-1}+C$ to the error data, setting $C = 0.0076$, the baseline no-flow error. The optimal curve ($P_{lin}(N) = 0.053N^{-1} + 0.0076$) based on the linear analysis does a fairly poor job of fitting the data ($R^2 = 0.80$). Thus we relaxed the constraint on the power of N and fit the curve $AN^{-B}+C$, which produced a curve ($P_{lin}(N) = 0.073N^{-1.745} + 0.0076$) that fit the data much more closely ($R^2 = 0.97$). Noting the reduction in flapping amplitude in the flow cases, we also measured the final amplitude for each N configuration and compared to the amplitude at that value of N. We found that the amplitude was consistently reduced by about 16.4%, regardless of N. This is unlike the expectation in the linear (viscous) case, where we would not expect to see a decrease in amplitude, just a shift in the center of oscillation.

2.5 Discussion

2.5.1 Control authority and Weis-Fogh number

We have shown that the time it takes for an insect or flapping-wing robot to respond to a control input is linearly related to N. Thus a flyer with a greater Weis-Fogh number - determined by their wing mass, wing shape, wing-stroke kinematics, and wing pitch kinematics - will have reduced control authority when it comes to starting, modulating, or stopping wing kinematics. In order to perform high-speed agile maneuvers, insects need to be able to quickly modulate lift

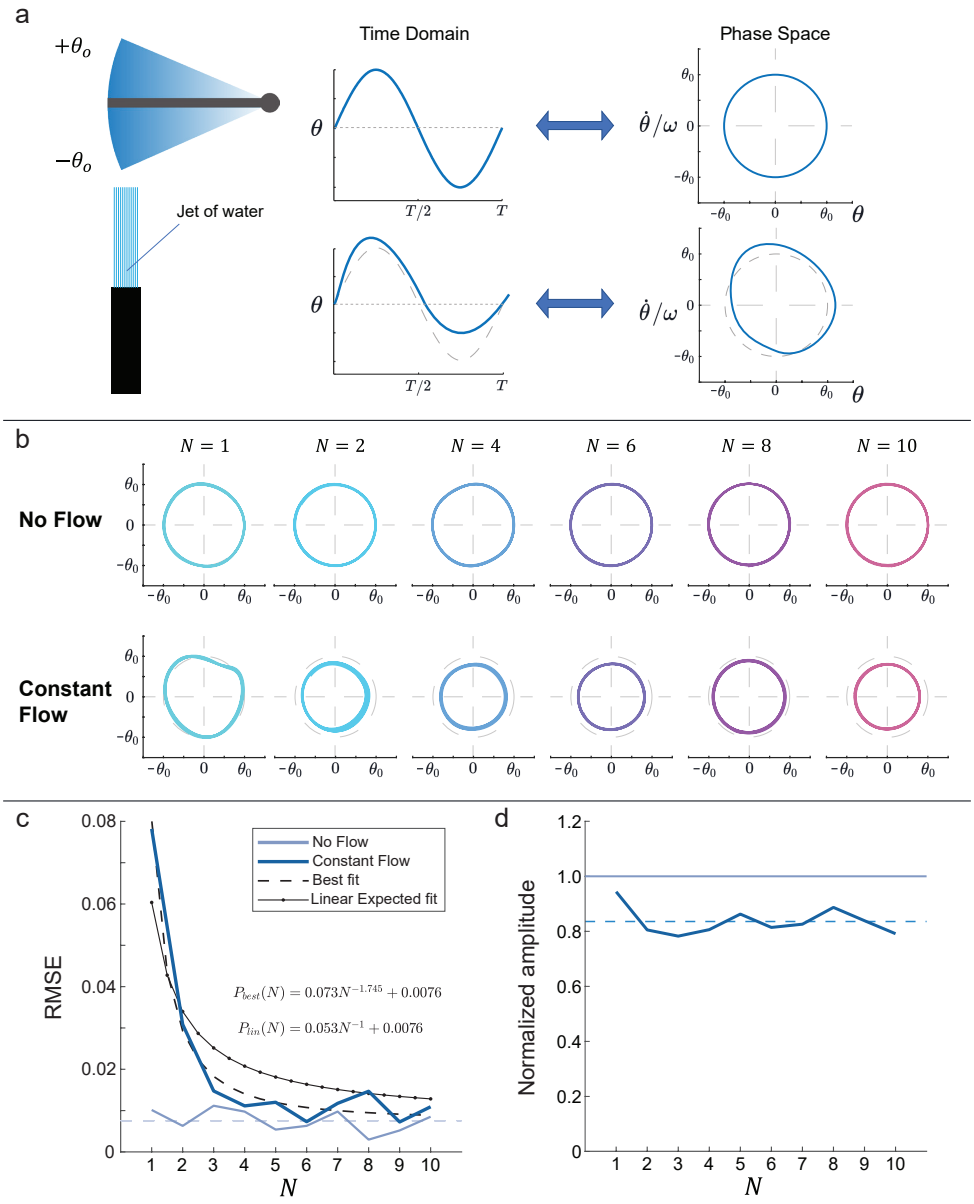

Figure 2.5. Description of the Constant flow experiments. a) Schematic of the orientation of the water jet relative to the wing, and conceptual representation of the effects of flow on time and phase domain plots. b) Variation in limit cycle plots across N. Plots show 2 periods of steady oscillation with and without flow, at different values of N. c) Plots of fit error for flow and no-flow cases across N, as well as fit lines for expected N^{-1} function and a best fit curve. d) Illustration of relative amplitude decrease across N, and mean at 84% of full amplitude.

and drag forces, which they can do by modulating amplitude, frequency [108], wing rotation [39], [109]. However, because of the increased inertial component of a high Weis-Fogh number, control inputs are likely to be damped out to some degree, especially if those inputs come from modulations of the flight muscle. Therefore, other methods, such as the modulation of wing angle of attack or joint characteristics via steering muscles [5] may be more effective at high N since they can modulate both amplitude *and* Weis-Fogh number by changing the aerodynamic characteristics of the wing.

Our input step experiments demonstrate that, since N is a function of flapping amplitude, changes to amplitude also change the control authority. Figure 2.6 shows the degree to which N and transient time shift due to the increase in amplitude. The arrows start at the points corresponding to the start up time and point to the location in the plane where the step time is located. The arrows more or less follow the trendline, and the length of the arrow is greater for larger starting values of N.

In engineering, control authority is critical for ensuring that a system can meet performance objectives like stabilization in the presence of disturbances and trajectory following. The loss of control authority - stalling in an airplane, for example - can lead to catastrophic failures if it is not regained in time. In insects, the ability to quickly maneuver through an array of obstacles or out of the grasp of a predator is similarly important. Since N is relatively easy to measure for a particular species of insect, requiring just estimates of wing mass, wing shape, and wing kinematic data, it may serve as a useful metric for an insect's relative ability to perform agile maneuvers.

2.5.2 Higher N provides greater stability in unpredictable natural environments

An insect that needs to be more agile may benefit from a lower N, but there is a tradeoff. At lower N, the inertia of the wing during flapping is on the same order as the aerodynamic forces, so environmental flow has a larger effect on flapping kinematics. This can pose issues for

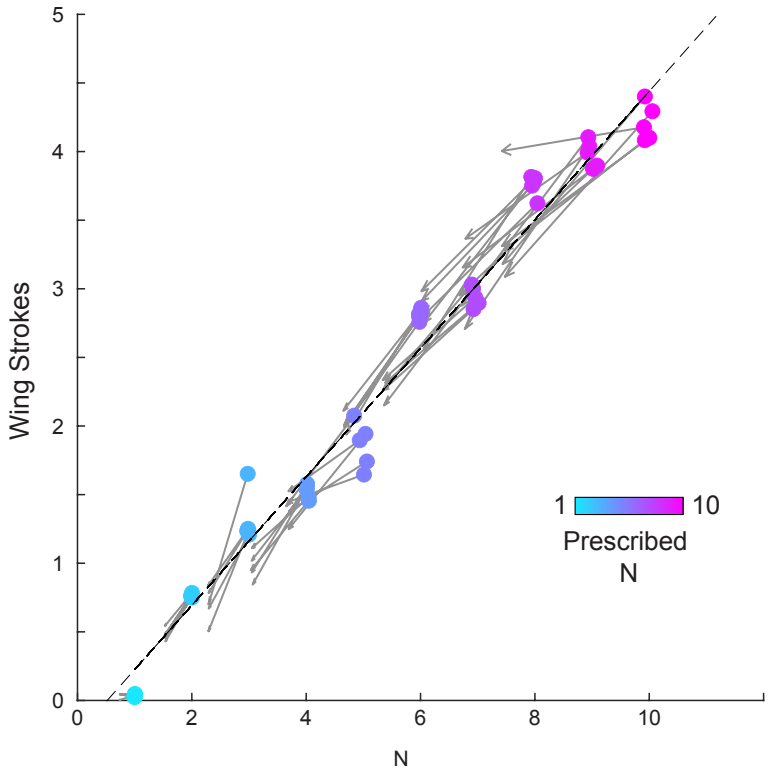

Figure 2.6. Amplitude increases due to a step increase in input amplitude lead to commensurate decreases in N and transient time. Data points are shown in color, and gray arrows indicate the movement due to increased control input. The arrows are all roughly aligned with the trendline.

an insect, since steady wingbeats are necessary to produce consistent lift. Our flow experiments show that an insect or FWMAV with body elasticity is less susceptible to disruptions from the environment when it has a high Weis-Fogh number. This means that a flapper that needs to fly in a windy environment may benefit from lower amplitude flapping, more massive wings, and/or wing shapes that minimize drag.

2.5.3 Weis-Fogh number as the quality factor of spring-wing systems

In the beginning of this chapter, we performed a series of analyses looking at the transient behavior of a linear spring-mass-damper as an analogue to the spring-wing system. We showed that the quality factor Q was linearly related to the start up time of the system and inversely related to the relative effect of external perturbations. Our experimental results with the nonlinear spring-wing system show similar trends, but with some crucial differences

Changing amplitude changes the transient time constant

As shown in Fig.2.6, the response time of the spring-wing to a control input depends not just on the magnitude of the input, but also on the amplitude of flapping. This is an inherently nonlinear phenomenon due to aerodynamic damping, and is not the case for the linear system. However, since the shift induced by the amplitude change (gray arrows, Fig. 2.6) follows the trendline fairly closely, it does seem that the relationship between N and response time is maintained despite the transient changes in N.

The actual relationship we expect between response time (defined at 95% of the full amplitude) and Q based on equation 2.18 is

$$\hat{t}_{95} = \frac{-\ln 0.05}{\pi} Q = 0.95Q \approx Q \tag{2.25}$$

If we inspect the trendline we fit to the start up time, we find the relationship

$$\hat{t}_{95} = 0.486N \approx \frac{N}{2} \tag{2.26}$$

Thus it appears that in this nonlinear case, N has the same effect on the transient response rate as $2Q$.

Nonlinear aerodynamics results in more stability at higher N

In the beginning of this chapter, we argued that an external flow should affect a linear spring-mass-damper less as Q increases, i.e.

$$F_{flow} = \frac{\omega_n}{Q} v \tag{2.27}$$

Thus we expected an inverse relationship between N and flapping non-sinusoidality. Additionally, we expected that a flow should cause a consistent off-center stretch in the spring, i.e. a steady-state offset in the positive x direction (Eq. 2.20), but maintain the same flapping amplitude.

In fact, we found that an inverse (N^{-1}) relationship did not fit the data well. Instead, a function with $N^{-1.745}$ fit better, suggesting that the quadratic relationship between the system and the flow asymmetry, $\Gamma|\dot{x}-v|(\dot{x}-v)$, introduces dynamics that result in greater kinematic stability. Additionally, we see that unlike in the linear system, the flapping amplitude *is* affected by the asymmetry, causing a decrease in overall amplitude. This would be detrimental to a high-N flapping flyer's ability to produce lift, but as long as it is not using maximum muscle strength during normal flapping, it should be able to increase the force it uses to drive the wings to achieve the necessary amplitude. This is in contrast with a low-N flyer, who would need to control amplitude variations within a single wingstroke to maintain smooth flapping, regardless of the strength of the muscle

2.5.4 Weis-Fogh number as a performance metric for flapping fliers - living or engineered

In this and previous work [106], we have shown that the Weis-Fogh number is a metric that encompasses important performance characteristics for flapping flight: dynamic efficiency, responsiveness/agility, and stability. When we observe the distribution of Weis-Fogh Number across a wide range of insects, we notice that, large or small, they seem to exist in the range of $N = 1-8$. There are some exceptions, of course, but they are characterized by the exceptionally small flying insects who fly at extremely low Reynolds numbers, and butterflies, whose exceptionally large wings an stuttering flight distinguish them from the controlled hovering of flies, bees, and hawkmoths. The fact that other insects who rely on fast wingbeats exist in this constrained range of parameters suggests that the variation in N reflects a balance of different performance tradeoffs

This principle is one that is a fundamental aspect of engineering design. In optimal control design, for example, the problem of finding an optimal controller for a particular linear

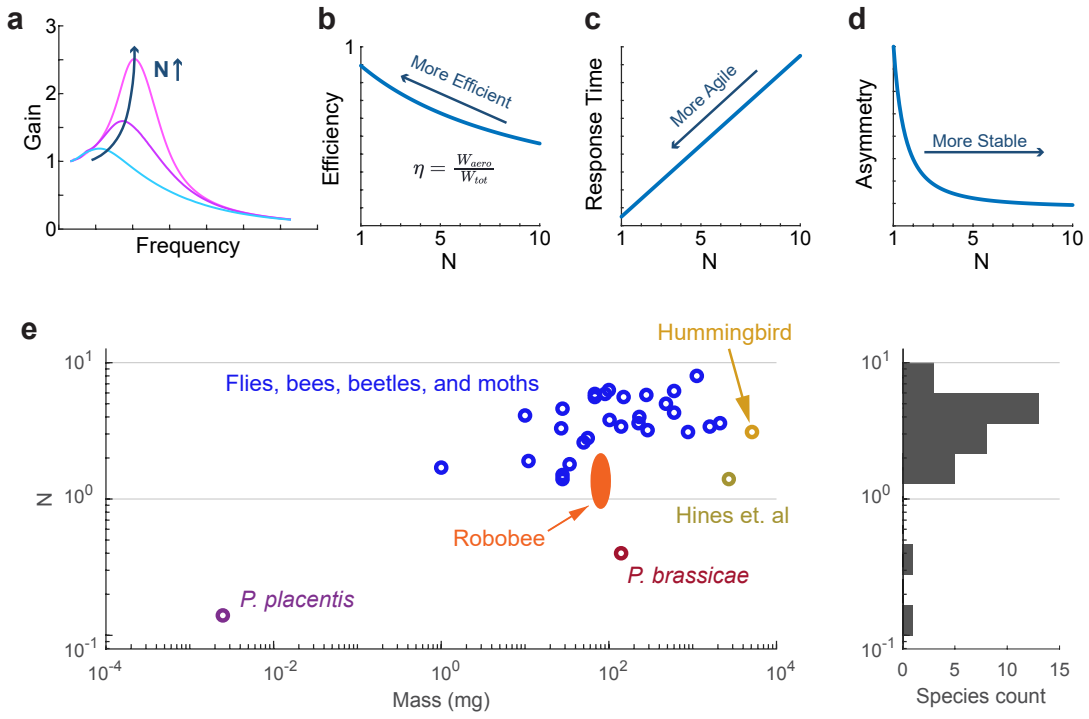

Figure 2.7. Flapping system performance tradeoffs. a) Higher N means greater flapping amplitude for a given actuator, b) but dynamic effiency decreases with higher N due to internal losses. c) Lower N also leads to faster response times, but d) more vulnerability to aerodynamic perturbations. e) This may point to an explanation for the number of insects (and FWMAVs) across orders of magnitude of size that remain within the range of $N = 1 - 8$. Values of N for insects are calculated based on data from Weis-Fogh [55], Ellington [95], and Farisenkov et al. [2]. Two robots are also plotted, the Harvard Robobee[22] and a larger FWMAV from Hines et al. [104]. See Appendix B for methods of computing N from the Ellington and Farisenkov data.

system with state x and input u is defined:

$$\dot{x} = Ax + Bu \tag{2.28}$$

$$J = \int_0^\infty \left[x^T Q x + u^T R u\right] dt \tag{2.29}$$

where J is a quadratic cost function that is weighted by matrices Q (unrelated to quality factor) and R. The choice of those matrices is an important one because the relative weighting emphasizes the importance of tracking a setpoint or trajectory (Q) vs the importance of minimizing control effort (R). Designing, say, a flying robot to track a fast-moving trajectory is possible by weighting the Q matrix heavily, but that may result in large control effort and energy use. Alternately, if a designer is working with a limited power supply or power-limited motor, it may be more important to emphasize control effort and sacrifice tracking speed or accuracy.

Similarly, mechanical system parameters can reflect tradeoffs between agility and stability. Fighter aircraft with adjustable wings are one example of a system that can shift from a more stable shape (wings extended) to a faster, more agile, but less stable configuration (wings folded). This has been taken to an extreme with fighter jets with forward-swept wings, like the Grumman X-29, which trades off high maneuverability for increased instability. Indeed, there is even some evidence that wing morphing in birds similarly leverages aerodynamic *instability* to improve flight performance [110].

Thus it makes sense that the evolutionary development of flapping flight should also balance energetics, agility, and stability. Perhaps the restriction of flapping animals to this region of $N = 1 - 8$ is the combined effect of 1) decreasing dynamic efficiency, 2) decreasing responsiveness, and 3) increasing stability with N. Those, combined with the necessity of elastic energy exchange to maintain efficient flight, may constitute a driver of evolutionary change.

Acknowledgements

Chapter 2, in full, is currently being prepared for submission for publication in Bioinspiration & Biomimetics as *Lynch J, Wold ES, Gau J, Sponberg S, Gravish N. Energetic and Control Tradeoffs in Spring-Wing Systems, 2023*. The dissertation author was the primary investigator and first author of this material.

Chapter 3

Self-Excited flapping in Asynchronous Spring-Wings

3.1 Introduction

Flying insects can be classified into one of two actuation strategies: synchronous and asynchronous (Fig. 3.1). Wingbeats generated by insects such as moths and locusts are "synchronous" with the periodic signals from the nervous system that cause muscles to contract; the rate of the wingbeats is set by the nervous system. On the other hand, insects such as bees and flies rely on the automatic response of the muscle to stretching. They are able to generate self-excited wingbeats whose frequency is not correlated with signals from the nervous system and are therefore "asynchronous" from the neural signals; the rate of wingbeats is set by muscle and body mechanics. A key specialization in asynchronous muscle is a phenomenon called *delayed stretch activation* (dSA). After the muscle is stretched, its tension increases, reaching a peak that is delayed in time w.r.t. the stretch (Fig. 3.2). When the muscle contracts, it also undergoes *shortening deactivation*, where the tension in the muscle similarly decreases in response to shortening [4], [67]. Due the lag in stretch-activated peak force, two such muscles arranged antagonistically in the insect thorax tend to naturally oscillate, flapping the wings with *no direct input* from the nervous system while sufficient energy is present. Efficiency is further improved by the shortening deactivation, since the agonist need not overcome the tension of the antagonist during contraction [111] The overall effect has been described as being similar a system with

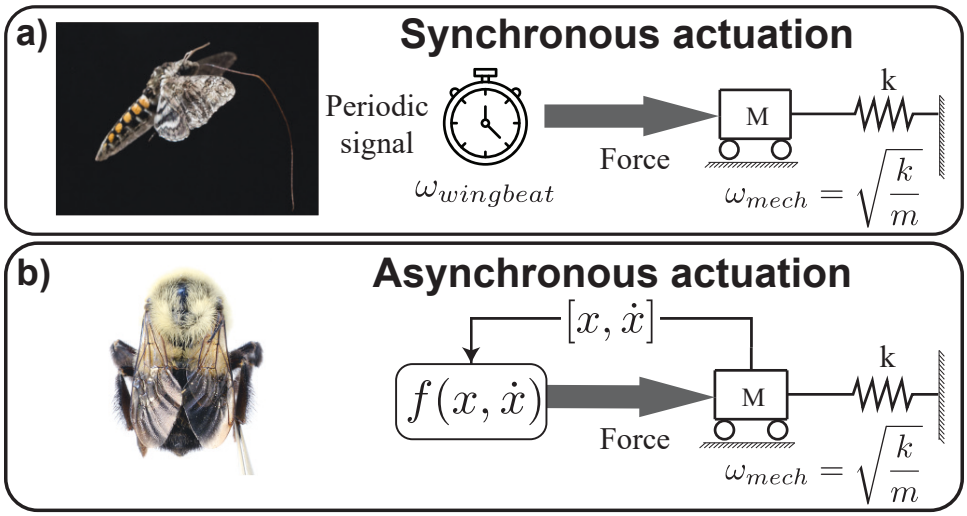

Figure 3.1. a) Insects such as moths use synchronous actuation. This is characterized by a periodic signal from an internal source with rate $\omega_{wingbeat}$. b) Bumblebees are an example of an insect using asynchronous actuation. This is characterized by feedback, where the rate of the mechanical system ω_{mech} interacts with the rate of the feedback $\omega_{feedback}$ to produce the wingbeat.

"negative viscosity", which sustains oscillations by injecting energy to overcome internal and external (aerodynamic) losses [59], [60] This adaptation is thought to enable the extremely high frequency (100-1000 Hz) wingstrokes of small insects, and may help enable efficient flight [4]

3.1.1 Asynchronous muscle background

Biologists have studied asynchronous muscle in isolation by carefully removing the muscles from the insect thorax and applying techniques adapted from materials science such as measuring dynamic stretch responses and measuring cyclic force-strain curves [58], [65], [70], [112], [113]. Their results have been used to characterize asynchronous muscle as an active material and compare muscle behavior across species [73], [111] and between lines of transgenic flies [71]. However, biologists have typically been interested in the elusive bio-molecular dynamics from which the dSA phenomenon arises in insect muscle [61]. To date, few have looked carefully at how asynchronous muscle dynamics affect the overall dynamics and control of an asynchronous insect. To improve our understanding of the mechanics of the insect flight system as a whole, it is necessary to characterize the system level behavior of asynchronous flight:

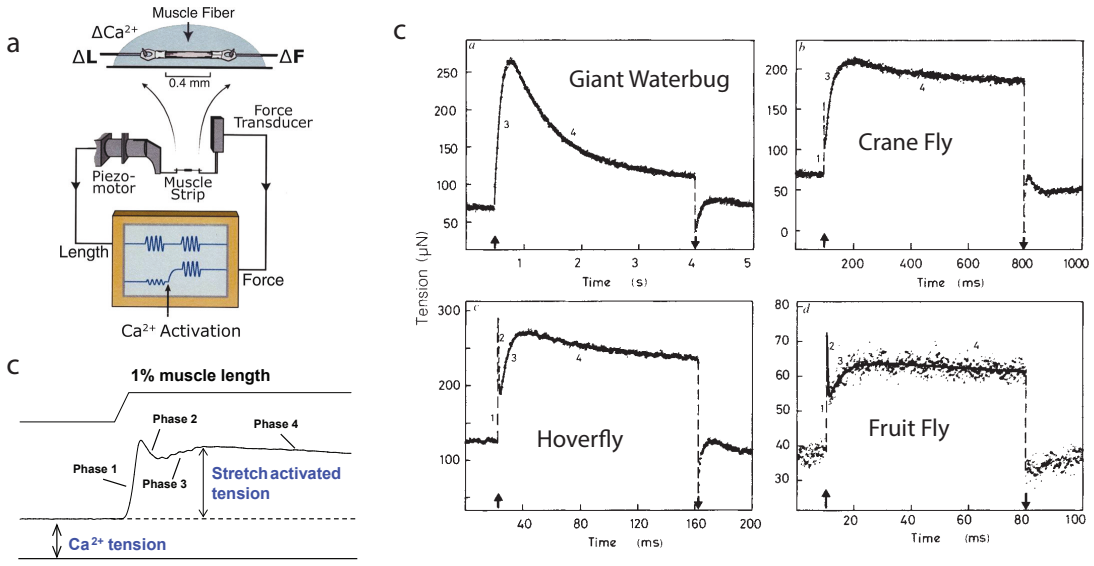

Figure 3.2. a) Diagram from Swank [74] illustrating the stretch-hold experiment. b) Example data showing 1% stretch and sample data from *Drosophila melanogaster*, with each phase of the transient dynamics labeled. b) Data from Molloy [73] illustrating the different rates of stretch activation in four insect species. Note that phase 2 is not shown in the waterbug trace (upper left) - this is due to limitations in the measurement setup, since the phase 2 dynamics are much faster than phase 3 and 4

the dynamical interactions between asynchronous muscle, the elastic thorax [5], [76], [114] and the complex aerodynamic forces on the wing [10], [107]. Asynchronous muscle actuation is thought to provide several distinct advantages to flying insects, including high wingbeat frequency (wbf), adaptive behavior after wing damage [50], [115], and separation of power and control [4], [5], [73], [112]. In order to understand how these advantages emerge from the coupling of muscle and mechanical dynamics, we have set out to generate a model that approximates the complex physics involved. By studying the simplified version of the complex asynchronous flight system and robotic models of the dynamics, we expect to glean insights into the dynamics and control of agile, efficient, and robust insect flight. A deeper understanding of asynchronous flight dynamics serves to help answer questions about the evolution and diversification of flying insects, and may also help to develop novel designs and control schemes for bioinspired flapping wing micro air vehicles (FWMAVs).

3.1.2 FWMAV Background

The field of bioinspired flapping-wing micro-air vehicles has seen major advancements in the last decade. Researchers have achieved controlled flight on tethered [13], [14] and untethered [15]–[18] FWMAVs at the centimeter scale. They have integrated sensors [19]–[22] and implemented robots with a wide range of actuators including piezo bending actuators, mini DC motors [23]–[25], soft DEA actuators [26], [27], and electromagnetic coils [28]. Others have developed autonomous control algorithms that (given sufficient knowledge of the state of the robot) can achieve not just stable hovering, but also impressive feats of agility [29]. The design, fabrication, and control tools now exist to design novel FWMAVs capable of flight.

However, the performance of such robots still lags behind that of their insect muses. The agility and versatility of insects like flies, bees, and dragonflies is unmatched by any FWMAV at similar scales. Untethered FWMAVs at the centimeter scale must be supplied with extremely high-power energy sources—lasers [116] or high-wattage light sources [15]—while insects are efficient enough to sustain flight over long distances during foraging and migration [117], [118]. Additionally, FWMAVs are often much more delicate than insects, constructed of 100-micron-thick carbon fiber, thin polymer sheets, and brittle piezoelectric materials. The dynamics of flight are sensitive to changes in mechanical properties (wing geometry, inertia, etc.), and yet insects are able to continue to fly despite damage caused by the environment or other animals [119], [120]. There is still much for us to learn about how insects achieve their impressive flight performance and translate these into advances in robotics. To the author's knowledge, all previous actuation of flapping wing robots have relied on synchronous actuation strategies. We hypothesize that asynchronous actuation methods may provide adaptive behaviors that could be beneficial for flapping wing robots.

In this chapter, we seek to establish principles of asynchronous actuation for flapping wing robots and to demonstrate some unique properties of dSA actuation for adaptive and resilient flapping wing dynamics. We will begin by deriving a differential equation for asynchronous

muscle dynamics based on a common function used to measure the strength and rate of stretch activation in muscle. We will then integrate it with the spring-wing equation of Chapter 1 to produce a nonlinear state-space model of asynchronous flapping that produces limit-cycle oscillations. The state-space model enables us to study the stability properties of the system, which determines the ranges of parameters that produce flapping. Through a combination of analytical and numerical tools, we then discuss the flapping dynamics, the influence of mechanical and muscle parameters, and potential methods for controlling oscillations. We present experiments in the robophysical model that show that an asynchronously-actuated robot has a compelling ability to rapidly adapt wingbeat properties and respond to collisions with no direct control. We implement asynchronous actuation in an insect-scale flapping wing as a proof of concept towards creating a full asynchronous FWMAV. Finally, we discuss the application requirements for asynchronous flapping systems of any type, and describe a sensorless implementation using a common DC motor.

3.2 A phenomenological input-output model of asynchronous muscle

The first step towards integrating dSA into a robotic flapping system is to express the observed behavior of asynchrononus muscle as a function of the state of the system. A typical experiment for quantifying stretch activation in asynchronous insect muscle is described in [74]. The indirect flight muscle (IFM) is dissected from an insect a muscle fiber is isolated from the muscle. The fiber is fixed between a load cell and a piezolectric actuator that can induce a step strain in the muscle on the order of 1% of the muscle resting length. The muscle is activated by the presence of Ca^{2+} ions in solution, and the load cell measures the tension in the muscle as the muscle is stretched quickly and held at a particular strain (Fig 3.2a). The characteristic transient behavior consists of four phases. First, the stretch causes a near-instantaneous rise in tension (phase 1). Next, there is a fast decay in tension characteristic of stress relaxation (phase 2). In

synchronous muscle, the tension continues to decay, but in asynchronous muscle, the tension starts rising again (phase 3) before reaching a peak and finally decaying to a final tension value (phase 4). Figure 3.2 shows the experiment setup and example data from Swank [74] and Molloy et al. [73].

The data from the experiment is fitted to a sum of three exponents plus an offset, capturing the relative strengths and rates of phase 2 through 4:

$$F_t = K_2 e^{-r_2 t} + K_3(1 - e^{-r_3 t}) + K_4 e^{-r_4 t} + c \tag{3.1}$$

3.2.1 Characteristics of the dSA fit function

It is helpful to pause here for a moment and consider the influence that the relative magnitudes of the parameters have on the shape described by this equation. First, we'll make some slight modifications to equation 3.1,

$$F_t = K_2 e^{-\psi r_3 t} - K_3 e^{-r_3 t} + K_4 e^{-\kappa r_3 t} + C \tag{3.2}$$

where we've defined $\psi = r_2/r_3$ and $\kappa = r_4/r_3$, and we've redefined $C = c + K_3$ so that it unambiguously represents the final tension in the muscle after the stretch. A representative curve is shown in Fig. 3.3.

Parameter ranges

While many studies fit Eq. 3.2 to insect data [62], [73], [74], [111], [121], few report all of the resulting fit parameters, typically only reporting the rates or tensions of interest, e.g. the phase 3 stretch activation rate or peak stretch-activated (SA) tension. However, some general trends are clear from studying the published data. See Appendix C.1 for a detailed look at curve fits to data from [73].

First, the rates for each phase are related as $r_2 > r_3 > r_4$. The exact ratios vary, but ψ is always greater than 1, and can be greater than 10 (see Appendix C.1). Additionally, κ is

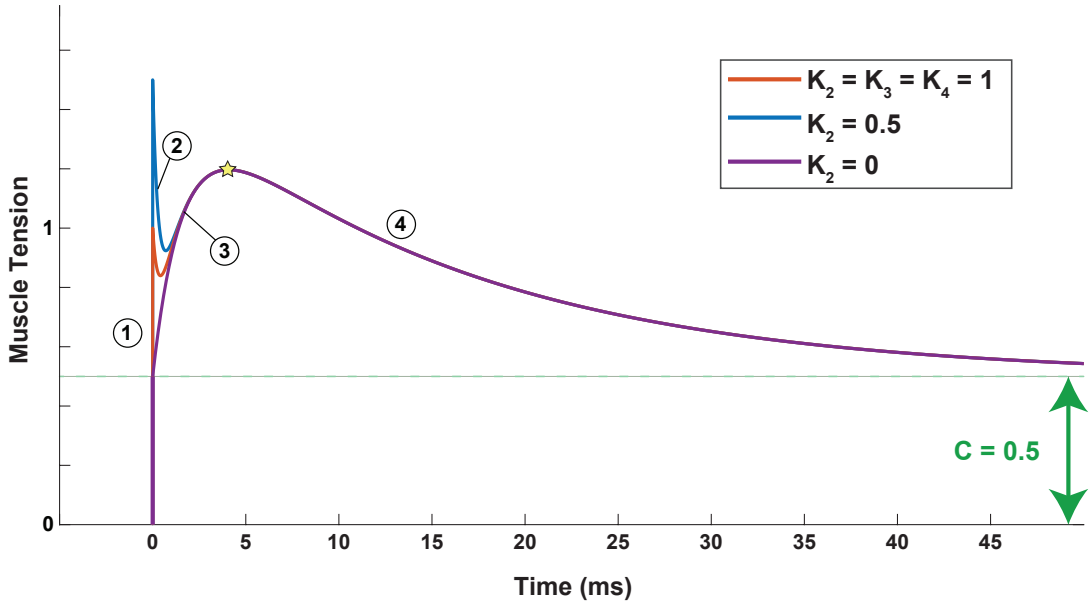

Figure 3.3. Example step responses with $r_3 = 628$ rad s^{-1} (100 Hz), $\psi = 5$, and $\kappa = 0.1$ based on Equation 3.2. C is an offset caused by passive stiffness, and phase 2 has little effect on the location of peak tension (yellow star)

defined on the range of (0,1), and is consistently less than 0.2. The phase 3 rate r_3 is on the order of the flapping frequency of the insect, as it has been shown to vary with wingbeat frequency across insect species [63], [73]. The gains K_2, K_3, K_4 and the offset C have units of tension, and are likely to vary based on the strength of muscle and/or size of insect [111]. Their relative magnitudes are harder to parse without a mechanistic model of the underlying mechanics, but we can assume they're similar in magnitude to each other. Some researchers have expressed these dynamics as a generalized Maxwell material model with an active element, where springs and dampers in series and parallel can express the elastic and viscous behavior of the muscle [59], [65], [72], [74]. See Appendix C.2 for a theoretical examination of this formulation that relates the fit parameters to material properties to help build intuition.

Peak Tension

The curve has two tension peaks - one immediately after the stretch ($t = 0$) and one a short time later after the stretch-activation has reached a maximum. The first maximum has the

value

$$F_t(0) = K_2 - K_3 + K_4 + C \tag{3.3}$$

The second peak (Fig. 3.3, yellow star) is a little trickier to compute. We'd like to first solve for the time t^* at which the peak occurs, but that isn't analytically tractable with three exponential terms. However, if we assume that $\psi >> 1$, which is typically true, the phase two dynamics should only have a small influence on peak tension time. Therefore, we drop the phase 2 term and solve for t^*:

$$\begin{aligned}
\frac{d}{dt}F_t(t^*) &= 0 \\
\rightarrow K_4\kappa r_3 e^{-\kappa r_3 t^*} &= K_3 r_3 e^{-r_3 t^*} \\
\rightarrow \ln K_4\kappa r_3 - \kappa r_3 t^* &= \ln K_3 r_3 - r_3 t^* \\
\rightarrow t^* &= \frac{\ln(\frac{K_4\kappa r_3}{K_3 r_3})}{\kappa r_3 - r_3} \\
t^* &= \frac{\ln(\frac{K_4}{K_3}\kappa)}{r_3(\kappa - 1)}
\end{aligned} \tag{3.4}$$

It can be shown that, given ψ is large (~ 10), the contribution of the phase 2 term is negligible at t^*, and in practice, Eq. 3.4 is very close to the actual value. This is an important characteristic time of the stretch-activation dynamics, and it is relatively easily measured from data, so it may be helpful to express the stretch-activation equation in terms of t^*. First we give the relationship between r_3 and t^*, using Eq. 3.4 and $\rho_4 = K_4/K_3$:

$$r_3 = \frac{\kappa - 1}{\ln(\rho_4\kappa)t^*} = \frac{c_3}{t^*} \tag{3.5}$$

Then,

$$F_t = K_2 e^{-\frac{c_3\psi}{t^*}t} - K_3 e^{-\frac{c_3}{t^*}t} + K_4 e^{-\frac{c_3\kappa}{c_3 t^*}t} + C \tag{3.6}$$

is the stretch-activation transient in terms of the peak tension time.

We can now proceed to derive an expression for the maximum tension, $F_{max} = F_t(t^*)$. Again, we'll drop the phase 2 component:

$$\begin{aligned} F_{max} &= -K_3 e^{-r_3 t^*} + K_4 e^{-r_4 t^*} + C \\ &= -K_3(\rho_4\kappa)^{\frac{1}{1-\kappa}} + K_4(\rho_4\kappa)^{\frac{\kappa}{1-\kappa}} + C \\ &= (K_4 - K_3\rho_4\kappa)(\rho_4\kappa)^{\frac{\kappa}{1-\kappa}} + C \\ F_{max} &= K_4(1-\kappa)(\rho_4\kappa)^{\frac{\kappa}{1-\kappa}} + C \end{aligned} \tag{3.7}$$

Note that F_{max} is not a function of the stretch-activation rate, just the *ratio* of the phase 3 and phase 4 rates, in addition to the passive stiffness C and the relative strengths of phase 3 and phase 4. When $K_3 = K_4$, this expression simplifies to

$$F_{max} = (1-\kappa)(\kappa)^{\frac{\kappa}{1-\kappa}} + C \tag{3.8}$$

3.2.2 A linear systems approach to modeling delayed stretch activation

The expression in Eq. 3.2 is the response of the system to a step in the muscle strain, which is equivalent to an impulse in the strain rate. This implies that Eq. 3.2 is the *impulse response of the muscle given strain rate as the input*. We can express the forcing function as a convolution of the impulse response with the strain rate,

$$f_{dSA}(t) = -g(t) * v(t) \triangleq \int_0^\infty g(\tau)v(t-\tau)d\tau \tag{3.9}$$

where $g(t) = K_2 e^{-\psi r_3 t} - K_3 e^{-r_3 t} + K_4 e^{-\kappa r_3 t} + C$ Note the negative sign, which is included to indicate that stretching in the positive direction induces a *negative* contraction force.

In the Laplace domain, convolution is a straightforward multiplication rather than an integration, i.e. $F_{dSA}(s) = G(s)V(s)$. Since an impulse in Laplace domain is unity (1), the Laplace transform of F_t is the transfer function $G(s)$ of the muscle. Obtaining the transfer function of the

muscle will provide the ability to integrate the muscle dynamics with the spring-wing dynamics using some straightforward linear systems analysis tools. Taking the Laplace transform of Eq. 3.2, we get

$$-\tilde{F}_{dSA}(s) = \frac{K_2}{s+r_2} - \frac{K_3}{s+r_3} + \frac{K_4}{s+r_4} + \frac{c}{s} \tag{3.10}$$

Note that this expression takes the same form as use by biologists in the muscle literature [65], [72]. Combining into a single rational function, we have quite a complex expression:

$$\frac{a_3 s^3 + a_2 s^2 + a_1 s + a_0}{s^4 + b_3 s^3 + b_2 s^2 + b_1 s} \tag{3.11}$$

with coefficients

$$\begin{aligned}
a_3 &= K_2 - K_3 + K_4 + c \\
a_2 &= K_2(r_3 + r_4) - K_3(r_2 + r_4) + K_4(r_2 + r_3) + c(r_2 + r_3 + r_4) \\
a_1 &= K_2 r_3 r_4 - K_3 r_2 r_4 + K_4 r_2 r_3 + c(r_2 r_3 + r_2 r_4 + r_3 r_4)) \\
a_0 &= c r_2 r_3 r_4 \\
b_3 &= r_2 + r_3 + r_4 \\
b_2 &= r_2 r_3 + r_2 r_4 + r_3 r_4 \\
b_1 &= r_2 r_3 r_4
\end{aligned}$$

We know that the c offset term is a result of the long term stiffness of the activated muscle. When the muscle is inside the body of the insect, we could argue that this stiffness is lumped together dynamically with the stiffness of the thorax itself. Therefore, if we assume that we can wrap it into the stiffness term in the spring-wing equation, we can set $c = 0$ and get a *slightly* simpler

expression:

$$\frac{(K_2 - K_3 + K_4)s^2 + (K_2(r_3 + r_4) - K_3(r_2 + r_4) + K_4(r_2 + r_3))s + (K_2 r_3 r_4 - K_3 r_2 r_4 + K_4 r_2 r_3)}{s^3 + (r_2 + r_3 + r_4)s^2 + (r_2 r_3 + r_2 r_4 + r_3 r_4)s + r_2 r_3 r_4} \tag{3.12}$$

Still, though, this has third-order dynamics and six parameters, which makes interpretability a challenge. Another simplification would be to wrap all of the gain terms into a single gain term, i.e. defining a gain term μ and setting $K_2 = K_3 = K_4 = 1$ gives us

$$\mu \left[\frac{s^2 + 2r_3 s + (r_3 r_4 - r_2 r_4 + r_2 r_3)}{s^3 + (r_2 + r_3 + r_4)s^2 + (r_2 r_3 + r_2 r_4 + r_3 r_4)s + r_2 r_3 r_4} \right] \tag{3.13}$$

Now we have everything in terms of rates, which can be defined in relative terms: $\psi = r_4/r_3,\ \kappa = r_4/r_3$.

$$\mu \left[\frac{s^2 + 2r_3 s + (\kappa - \kappa\psi + \psi) r_3^2}{s^3 + (1 + \psi + \kappa) r_3 s^2 + (\psi + \psi\kappa + \kappa) r_3^2 s + \psi\kappa r_3^3} \right] \tag{3.14}$$

However, this still isn't as simple as we'd like. We make one last simplification to drop the phase 2 dynamics entirely. We justify this by noting that r_3 is known to be related to the wingbeat frequency of insects, and that typically r_2 is much larger than wingbeat frequency. Thus, r_2 shouldn't have a significant effect on the dynamics of basic steady flapping, and our studies of the system dynamics should still be relevant. The form of the transfer function when we drop the phase 2 dynamics entirely is

$$G(s) = \frac{F_{dSA}(s)}{v(s)} = \frac{-\mu r_3 (1 - \kappa)}{s^2 + r_3(1 + \kappa)s + \kappa r_3^2} \tag{3.15}$$

Thus we have the transfer function that we'll use to integrate muscle dynamics into the spring-wing model. It still contains the rate of stretch activation, r_3, the rate of decay r_4 as the ratio κ, and a scaling term that captures the strength of the muscle, μ. Based on the form of the transfer function, the dSA phenomenon is qualitatively similar to a second-order low-pass filter on the velocity, fed back to the muscle as a force command. The cutoff frequency, ω_c is a function of r_3

and κ: $\omega_c = r_3\sqrt{\kappa}$. The damping ratio of the filter, $\xi = \frac{1+\kappa}{2\sqrt{\kappa}}$, is greater than 1 for all κ, so the filter is overdamped, and it has a DC gain of $\frac{-\mu(1-\kappa)}{\sqrt{\kappa}}$.

It's also useful to define the transfer function from strain to force, $F_{dSA}(s) = G'(s)X(s)$, which is just $G'(s) = sG(s)$ since $V(s) = sX(s)$ for strain X. Additionally, it may occasionally be useful to define a function g_0 that we can use to normalize the transfer function. For example, we might define g_0 as the integral under the simplified force curve associated with 3.15, $F_t = -e^{-r_3 t} + e^{-r_4 t}$, which is

$$g_0 = \frac{\kappa r_3}{1-\kappa} \tag{3.16}$$

When $G(s)$ is normalized using g_0, it takes exactly the form of an overdamped lowpass filter with cutoff frequency $r_3\sqrt{\kappa}$ and a gain of μ

$$\bar{G}(s) = \frac{G(s)}{g_0} = \frac{-\mu\kappa r_3^2}{s^2 + r_3(1+\kappa)s + \kappa r_3^2} \tag{3.17}$$

Armed with the Laplace transform of the muscle dynamics, we are able to reproduce some results from the asynchronous muscle literature and, importantly for our purposes, integrate asynchronous muscle into insect body mechanics to study the full asynchronous flight system.

3.2.3 Modeling other characteristics of muscle

Machin & Pringle [59] suggested that asynchronous muscle has linear dynamics given that the amplitude of strain is suitably small, so the linear transfer function may be appropriate in that context. However, we've simplified the dynamics quite a bit. Are the conclusions that we draw from these simplified dynamics still going to be relevant in the context of biological muscle? One way we can evaluate the question is by looking at the other methods (besides the step-hold experiment) that biologists use to measure characteristics of muscle.

Swank [74] describes in detail a suite of methods that have been used to measure muscle characteristics, including step-hold experiments, sinusoidal strain analysis, and work loop experiments. Additionally, researchers have studied the frequency dependence of work and

power production by asynchronous muscles [62], [71], [122] The following sections detail the effects of our simplifications through the lens of such experiments.

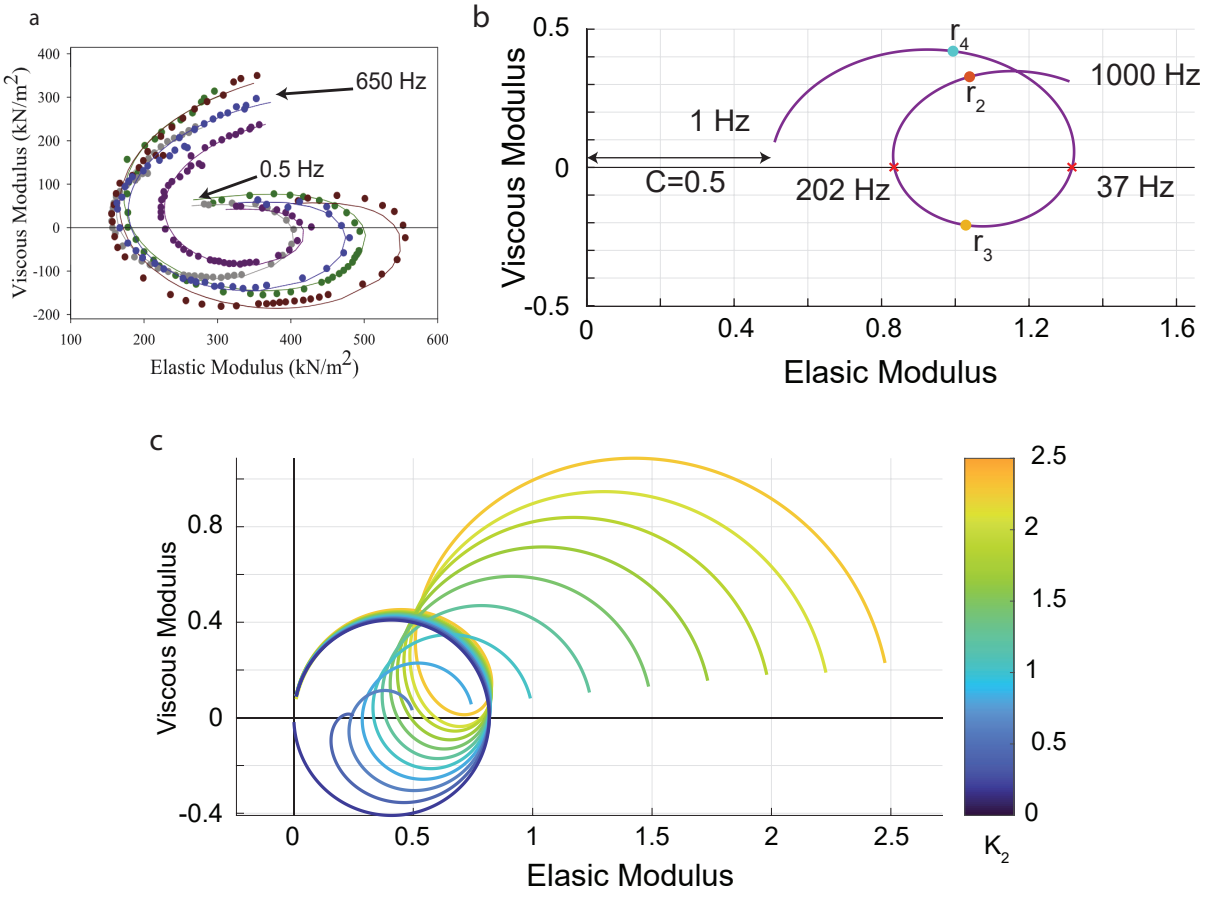

Figure 3.4. Dynamic Modulus Analysis. a) Real fly muscle data from Glasheen et al. [71] collected from 0.5 Hz to 650 Hz. b) Curve from 1 Hz to 1000 Hz With $K_2 = K_3 = K_4 = 1$, $r_3 = 100Hz$, $\psi = 5$, and $\kappa = 0.1$. Zero crossing frequencies are between r_4 and r_3 and r_3 and r_2, respectively. In between the crossings, the viscous modulus is negative, meaning that the muscle does positive work. c) Effect of varying the phase 2 gain, K_2. Note that there is no upper frequency bound when K_2 is small and that there are no zero crossings at all when K_2 is large.

Sinusoidal analysis

Biologists borrow techniques from viscoelastic materials analysis to understand the dynamic characteristics of insect flight muscle. An activated muscle is stretched via a low-amplitude sine wave, and the tension response is measured. Different characteristics, including viscoelastic behavior and work generated or dissipated by the muscle, can be measured over a

range of frequencies.

Dynamic Modulus of Muscle One way to gain insight into the dynamics of muscle is to compute the frequency-dependent complex modulus, which is also called the dynamic modulus. The dynamic modulus E^* is defined as the sum of the storage, E', and loss, E'' moduli, $E^* = E' + iE''$, where $i = \sqrt{-1}$ [72]. The storage modulus captures the in-phase (elastic) components of the dynamics, and the loss modulus captures the phase-shifted (viscous) components. In the muscle experiments, these moduli are computed based on the amplitude and phase of the tension response relative to the strain input and are plotted against each other (Fig. 3.4a). In linear systems theory, the plot of loss and storage modulus is also known as a Nyquist plot, which, for a transfer function $G(s)$, plots the real and complex components over a range of frequencies. Thus, since we have a transfer function representation of asynchronous muscle, $G'(s) = \frac{F_{dSA}(s)}{X(s)}$, we can simply generate the Nyquist plot to visualize the elastic (storage) and viscous (loss) components.

Figure 3.4b shows the Nyquist plot of $G'(s)$ with $K_2 = K_3 = K_4 = 1$, $r_3 = 2\pi(100)$, $\psi = 5$, and $\kappa = 0.1$. At low frequencies, the muscle response is dominated by the passive stiffness C and phase 4 dynamics, and the loss modulus is positive. However, when driven with a frequency closer to r_3, the loss modulus becomes negative, and the active force production of the muscle is able to do positive work. There is a band of frequencies where this negative viscosity persists, but eventually, the phase 4 dynamics take over, and the loss modulus becomes positive. The frequencies over which the loss modulus is negative are roughly centered on r_3 when all of the gains are equal; this is still true when we add in the scaling term μ, which uniformly scales the elastic and loss moduli, but does not affect the frequency terms. However, the relative magnitude of the gains is important, as is shown in Fig. 3.4c. If K_2 is greater than the gains on phase 3 and 4, the band of frequencies where the loss modulus is negative becomes narrower, until eventually it disappears altogether. Alternately, when K_2 is scaled down towards zero, the upper bound on frequencies that produce negative viscosity is increased until eventually at $K_2 = 0$ there is no upper bound. This observation is important to consider, because it means that our simplified muscle dynamics have no upper limit on frequencies at which the loss modulus is negative. Next,

we will look at the consequences this has on the muscle's ability to positive work.

Work Per Cycle and Cycle-Averaged Power

Using the same type of experiment, stretching muscle at small amplitudes over a range of frequencies and measuring tension, it is possible to calculate the work done by the muscle over a cycle, and the average power over that cycle. Work per cycle is defined as

$$W_{pc} = \int_0^T F_m(t)dx = \int_0^T F_m(t)v(t)dt \tag{3.18}$$

where T is the oscillation period, $1/f$, and $v(t)$ is the strain rate. The average power over a cycle is also simple to compute,

$$P_{ca} = \frac{1}{T}\int_0^T F_m(t)v(t)dt = \frac{W_{pc}}{T} = W_{pc}f \tag{3.19}$$

In asynchronous muscles, work and power tend to be negative at low frequencies, positive at intermediate frequencies, and negative again at high frequencies [62], [71], [122]. The center frequency of those intermediate range also seems to be related to the wingbeat frequency of the insect. In the example from Glasheen and colleagues [62] in Fig 3.5a, data from *Lethocerus* (giant waterbug, wbf ∼40 Hz [123] and *Drosophila* (fruitly, wbf ∼218 Hz [124]), respectively, show that peak power generation is at a much lower frequency for *Lethocerus* than *Drosophila*.

When we run a similar test on our asynchronous muscle transfer function with identical parameters ($K_2 = K_3 = K_4 = 1,\ \psi = 5$, and $\kappa = 0.1$), but two different values for r_3 (40 Hz and 218 Hz), we see something similar (Fig. 3.5b-i). Each power curve has two crossover frequencies, between which positive power (and work, Fig. 3.5b-ii) is done by the muscle, with a peak in between. The curve scales uniformly with the combined gain μ, and the while the frequencies at which peak work and peak power are different, they scale linearly with r_3 (Fig. 3.5c). The crossover frequency values are located between r_4 and r_3 and r_3 and r_4 rates, respectively, and actually match the crossover frequencies shown in the Nyquist plots in Fig. 3.4.

One can consider the range set by the upper and lower bounds as the range of frequencies at which the muscle can drive flapping. The extent of that range, relative to r_3, is set by the ratios ψ and κ (Fig. 3.5d-i,ii): Increasing ψ means increasing the upper bound while having a relatively small effect on the lower bound. If ψ is held constant and κ is increased, the lower bound moves closer to r_3 *and* the upper bound decreases, leading eventually to a condition where no positive power can be produced.

If the phase 2 gain, K_2, is varied, as was done in Figure. 3.4, we see a corollary to the result in the Nyquist plots (Fig. 3.6). While changing K_2 has little effect on the lower frequency bound, as K_2 approaches zero, the upper bound approaches infinity. Thus when K_2 is zero, there is no upper limit on freqencies at which the muscle can generate positive work and power, just as in the Nyquist plot there is no upper limit on the frequencies with negative viscous modulus. Meanwhile, the frequency of maximum work increases slightly, but is still near r_3.

3.2.4 Consequences of simplifications

Based on the analysis above, we can now evaluate the impact of our simplifications to the muscle transfer function in Equation 3.15. First, eliminating the offset term, C, is equivalent to lumping the muscle stiffness into the parallel stiffness. This has no effect on the power production of the muscle, and simplifies the definition of the natural frequency of the system, since it has just one lumped elastic element. Second, using a single gain μ to capture the strength of stretch activation does uniformly scale the magnitude of dynamic and work/power characteristics without affecting the frequency dependence (crossover frequencies). The relative ratios of the gains does have an effect on the frequency characteristics, but μ will allow us to modulate strength independently of muscle rate. Third, removing the phase 2 dynamics has the effect of removing an upper bound on frequencies at which the muscle generates positive work. There remains a frequency at which work is maximized, but average power has no maximum due to the relationship $P_{ca} = W_{pc} f$. However, the peak work per cycle frequency is not significantly effected when phase 2 is dropped. The frequencies at which work is done are largely dictated by

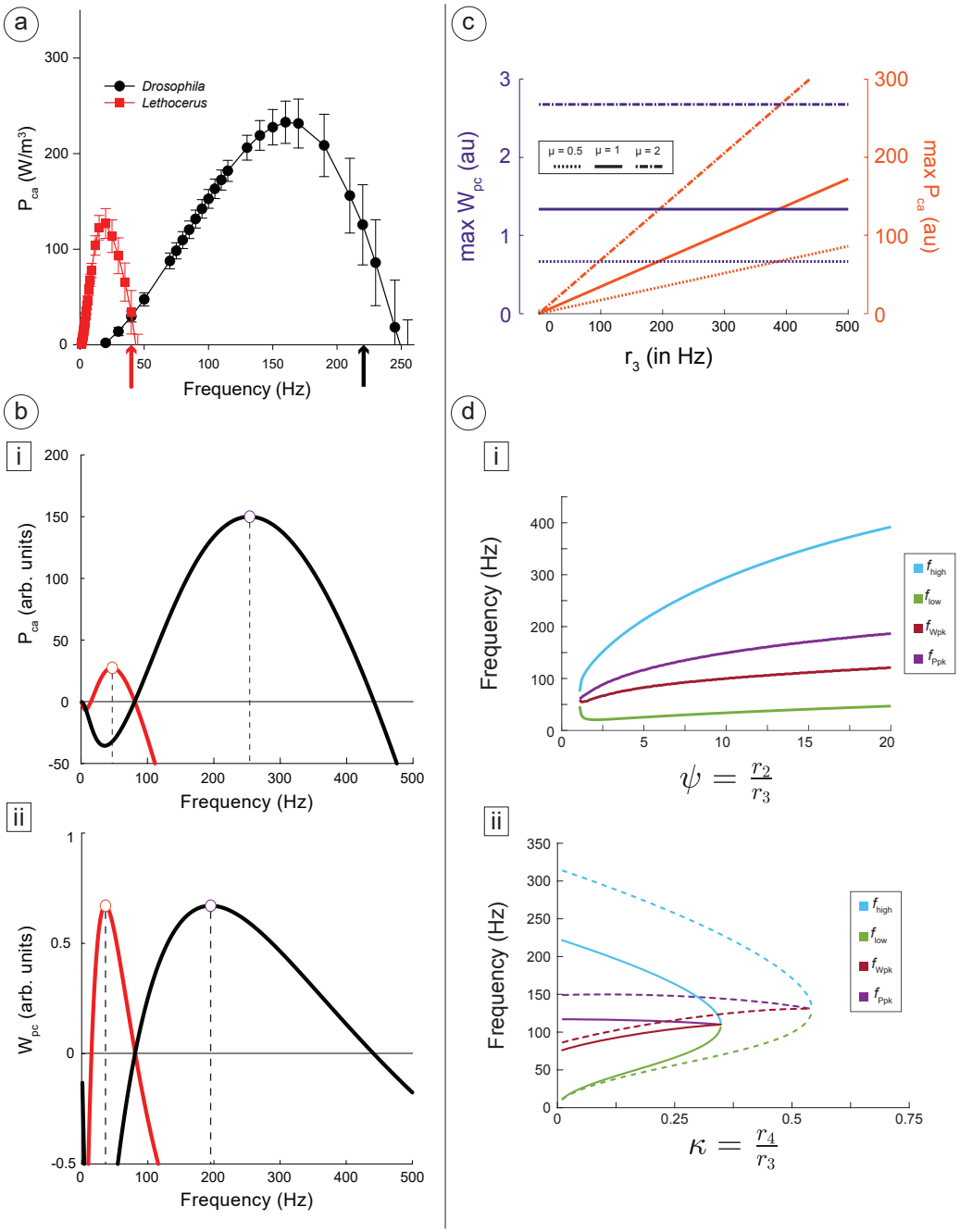

Figure 3.5. Work and Power Curves. a) Data from Glasheen and colleagues [62], showing the cycle-averaged power of *Lethocerus* and *Drosophila* when stretched (0.125% strain) at a range of frequencies. Wingbeat frequency for each insect shown with an arrow. b) Simulated power and work using the asynchronous transfer function with $r_3 = 2\pi\times218$ (black) and $r_3 = 2\pi\times40$ (red). c) μ scales the maximum work peak uniformly, and power scales linearly with r_3, implying that r_3 scales the peak frequencies linearly. d) (i) Increasing ψ increases the upper frequency bound and the peak and lower frequencies to a lesser extent. (ii) Increase κ causes the range of frequencies to decrease, until eventually positive work production is impossible. The critical value of κ is smaller when $\psi = 5$ (solid) than when $\psi = 10$ (dashed). Simulations with $r_3 = 100$, $\mu = 1$.

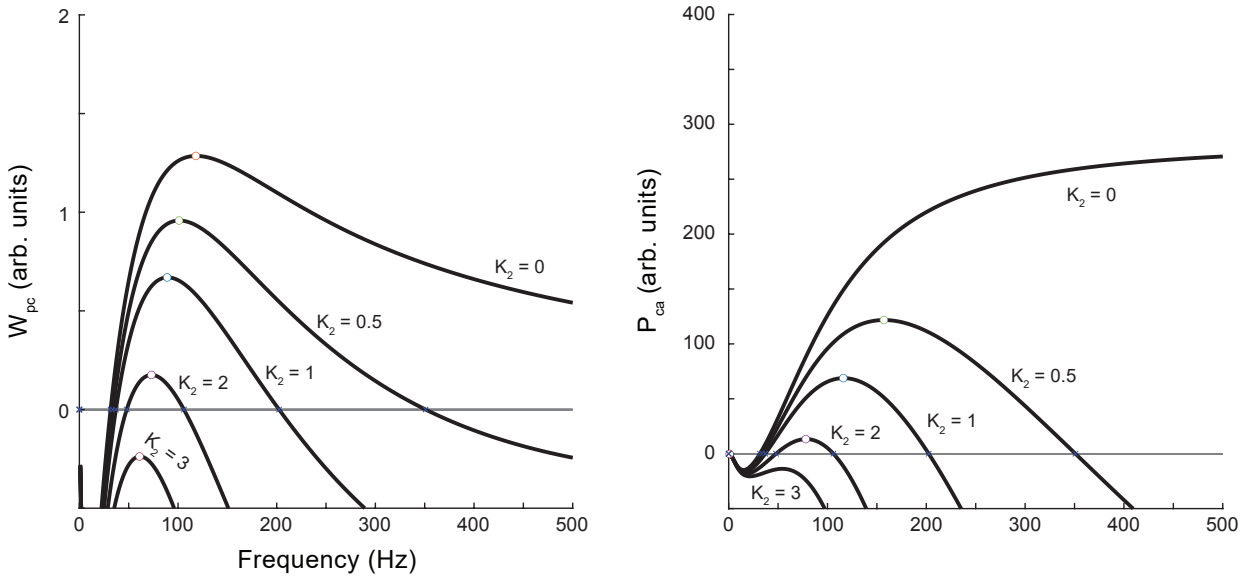

Figure 3.6. Effect of K_2 on work and power. Large phase 2 gain relative to phase 1 & 2 leads to no positive work, while $K_2 = 0$ eliminates the upper bound on positive work. Simulations with $r_3 = 100,\ \mu = 1,\ \psi = 5,\ \kappa = 0.1$

r_3, suggesting that our focus on r_3 as the rate variable, independent of the strength variable μ, is justified. Finally, the choice of κ appears to be important when phase 2 is included, in that choosing a large κ eventually leads to a condition where no positive work can be done because the upper and lower bounds "pinch off" the negative viscosity range of the muscle. However, when phase 2 is not present and there is no upper frequency, κ is less critical. For the rest of this work, we will choose $\kappa < 0.5$.

Beyond these simplifications, there are some significant factors in biological muscle that we do not attempt to capture. The dynamics of real muscle are extremely sensitive to a variety of conditions, including activation levels (Ca^{2+} concentration), muscle preparation, and strain amplitude [62], [74]. Comparison between measurements performed by different researchers is often challenging because it is not always clear what differences are caused by differences in experimental conditions and which are caused by differences in muscle characteristics. Additionally, experiments in the lab are often performed in very different conditions than in-vivo. Sinusoidal analysis is often performed at amplitudes well below the in-vivo muscle strain, which

is significant because the tension magnitude scales with muscle strain, and nonlinearities in the muscle are introduced when amplitudes are larger [59]. The difficulty of knowing exactly what forces are produced by muscle, combined with the difficulty of predicting aerodynamic forces, means that the following analysis will focus on the *relative* impact on varying muscle strength and rate, rather than attempting to quantify exact muscle forces.

3.2.5 The asynchronous spring-wing system equations

Next, we will integrate the simplified muscle dynamics into our spring-wing equation to produce an asynchronous spring wing system. As illustrated above, the force output is the product of the transfer function and the velocity input:

$$F_{dSA}(s) = G(s)v(s) = \left[\frac{-\mu\alpha_1}{s^2+\alpha_2 s+\alpha_3}\right] v(s) \tag{3.20}$$

Where we've defined $\alpha_1 = r_3(1-\kappa),\ \alpha_2 = r_3(1+\kappa),\ \alpha_3 = \kappa r_3^2$. We can distribute the denominator of $G(s)$ and take the inverse Laplace transform:

$$s^2F_{dSA}(s) + \alpha_2 sF_{dSA}(s) + \alpha_3 F_{dSA}(s) = -\mu\alpha_1 V(s) \tag{3.21}$$

$$\mathscr{L}^{-1} \Rightarrow \ddot{F}_{dSA} + \alpha_2\dot{F}_{dSA} + \alpha_3 F_{dSA} = -\mu\alpha_1 v \tag{3.22}$$

To connect the dSA actuation dynamics to the inertial, elastic, and aerodynamic elements of the flight system, we use the nonlinear spring-wing equation to describe flapping systems with internal elasticity.

The version we use here is slightly different than in Chapters 1 and 2, informed by the indirect actuation of insect muscle, as described in [76], [108]. We define a transmission ratio

$$T = \frac{\theta}{x} = \frac{\theta}{\varepsilon L} \tag{3.23}$$

where θ is the wing angle, ε is the muscle strain, and L is the resting muscle length. The

equations of motion in terms of inertia I, stiffness k, drag torque coefficient Γ, and the applied torque $\tau_{applied}$, as well as transmission ratio T is:

$$I\ddot{\theta} + \Gamma|\dot{\theta}|\dot{\theta} + \frac{k}{T^2}\theta = \frac{F_{dSA}}{T} \tag{3.24}$$

The asynchronous muscle dynamics dictate the torque applied to the system and are scaled by a gain coefficient, μ (units: Nm rad^{-1}), so we may write the combined equations of motion:

$$\begin{aligned} I\ddot{\theta} + \Gamma|\dot{\theta}|\dot{\theta} + \frac{k}{T^2}\theta &= \frac{F_d}{T} \\ \ddot{F}_d + \alpha_2\dot{F}_d + \alpha_3 F_d &= \frac{-\mu\alpha_1}{LT}\dot{\theta} \end{aligned} \tag{3.25}$$

Note that we've used the fact that $v = \dot{\varepsilon}$ and thus $v = \frac{\dot{\theta}}{LT}$. Solving these equations simultaneously gives the trajectory of the flapping wing, $\theta(t)$. The prevalence of asynchronous insects that employ dSA actuation suggests that this system can produce stable limit cycle oscillations from the balance between quadratic aerodynamic damping and strain-rate dependent muscle actuation. However, this is not guaranteed. For example, there may exist combinations of feedback and mechanical parameters that *do not* result in oscillations, or other regimes in which more exotic dynamical behaviors appear (exponential growth, chaos, etc.). It is necessary to identify the conditions under which a stable limit cycle can be expected to form.

3.2.6 Asynchronous wingbeats result from a linear instability

The stationary state, $\left[\theta, \dot{\theta}, F_d, \dot{F}_d\right] = 0$, is a fixed point of the asynchronous dynamical system (Eq. 3.25). We now seek to understand if this fixed point is stable or unstable. We ask the following question: if there is a small perturbation to the closed-loop system with dSA feedback, will oscillations tend to decay back to the origin or will they grow?

The system described in Eqs. 3.25 is nonlinear and so we can define a new state vector

$\mathbf{s} = [\theta, \dot{\theta}, F_d, \dot{F}_d]$

$$
\begin{aligned}
\dot{s}_1 &= s_2 \\
\dot{s}_2 &= \frac{s_3}{IT} - \hat{\Gamma}|s_2|s_2 - \omega_n^2 s_1 \\
\dot{s}_3 &= s_4 \\
\dot{s}_4 &= \frac{-\mu\alpha_1}{LT} s_2 - \alpha_2 s_4 - \alpha_3 s_3
\end{aligned}
$$

where we have defined $\hat{\Gamma} = \Gamma/I$ and $\omega_n = \sqrt{\frac{k}{IT^2}}$. We next linearize about the point $\boldsymbol{s} = 0$, constructing the Jacobian and the linear dynamics about the stationary state:

$$
\dot{\mathbf{s}} = \begin{bmatrix} 0 & 1 & 0 & 0 \\ -\omega_n^2 & 0 & \frac{1}{IT} & 0 \\ 0 & 0 & 0 & 1 \\ 0 & \frac{-\mu\alpha_1}{LT} & -\alpha_3 & -\alpha_2 \end{bmatrix} \mathbf{s} \tag{3.26}
$$

The growth or decay of perturbations from the stationary state are determined by the eigenvalues of the Jacobian. The characteristic equation for the linear system is

$$
\lambda^4 + \alpha_2\lambda^3 + (\omega_n^2 + \alpha_3)\lambda^2 + (\alpha_2\omega_n^2 + \frac{\alpha_1\mu}{ILT^2})\lambda + \alpha_3\omega_n^2 = 0 \tag{3.27}
$$

with eigenvalues $\lambda_j = a_j + i\omega_j$.

The sign of the real part of the largest eigenvalue dictates whether a perturbation away from the stationary point will tend to decay (stable) or grow (unstable). Understanding the conditions on the stability boundary will enable us to choose relevant feedback parameters to induce oscillations.

We can determine the boundary between decaying and growing solutions by setting the real part of the eigenvalue to zero, e.g. $\lambda = i\omega$, where ω is the frequency of oscillation. Plugging

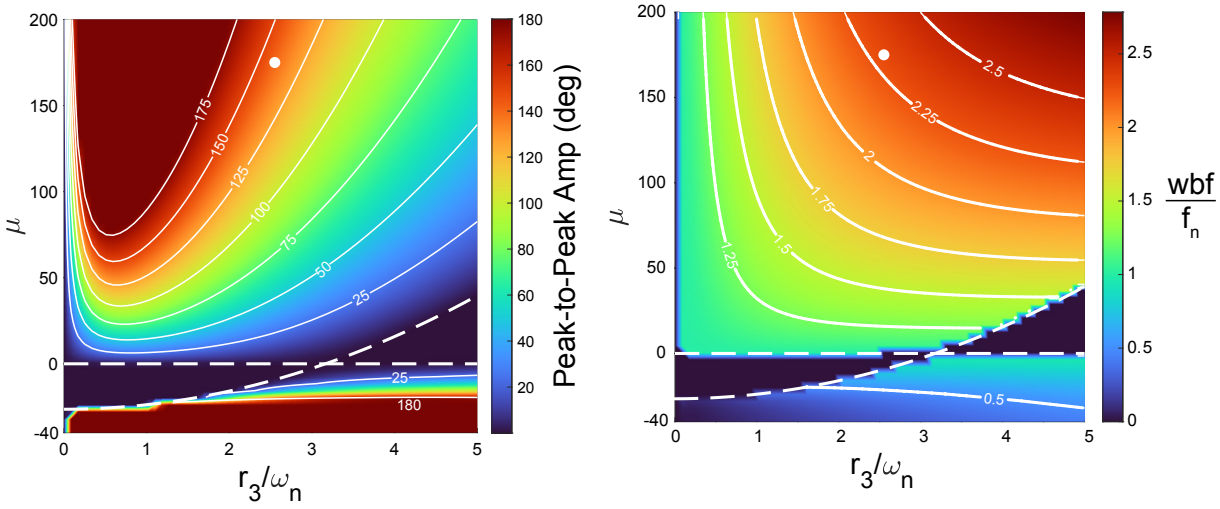

Figure 3.7. Plots of amplitude and frequency of dSA limit-cycle oscillations as a function of r_3/ω_n and μ. Dashed lines indicate calculated stability boundaries separating stable limit-cycle oscillations (large μ, r_3) from stationary behavior (small μ, r_3) from equation 3.31. Positive μ represents "pulling" when stretched, whereas negative μ "pushes" when stretched. a) Peak-to-peak amplitude of oscillation grows with increasing μ and non-monotonically varies with r_3. Output is saturated at 180 degrees. Amplitude is extremely sensitive to changes in μ in the negative regime. b) Wingbeat frequency (wbf) increases with r_3 and μ. It is always greater than f_n when μ is positive,and less than f_n when μ is negative. The white dots represent the intersection of typical amplitude and frequency of a bumblebee.

in for λ and separating the real and imaginary parts, we get two equations:

$$\text{Real}: \qquad \omega^4 - (\omega_n^2 + \alpha_3)\omega^2 + \alpha_3\omega_n^2 = 0 \tag{3.28}$$

$$\text{Imag}: \qquad \alpha_2(\omega_n^2 - \omega^2) + \alpha_1\hat{\mu} = 0 \tag{3.29}$$

where $\hat{\mu} = \frac{\mu}{ILT^2}$. We are specifically interested in how the parameters, μ and r_3, influence the onset of asynchronous oscillations due to the instability of the stationary point. Recall the definitions of the coefficients, $\alpha_1 = r_3(1-\kappa)$, $\alpha_2 = r_3(1+\kappa)$, $\alpha_3 = \kappa r_3^2$.

The first equation is quadratic in ω^2. Solving, we get two solutions: $\omega^2 = \kappa r_3^2$ and $\omega^2 = \omega_n^2$. Plugging each into the second equation, we get a pair of equations:

$$\omega^2 = \omega_n^2 \longrightarrow \quad \hat{\mu} = 0 \tag{3.30}$$

$$\omega^2 = \alpha_3 \longrightarrow \quad \hat{\mu} = \frac{\alpha_2}{\alpha_1}(\alpha_3 - \omega_n^2) = \left(\frac{1+\kappa}{1-\kappa}\right)(\kappa r_3^2 - \omega_n^2) \tag{3.31}$$

Eq. 3.30 gives the trivial conditions (zero feedback gain = no oscillations), but Eq. 3.31 defines a relationship between the strength of the dSA feedback and its rate parameter, plotted in Fig. 3.7 (red line). The two equations define 4 quadrants in the $r_3 - \mu$ plane where perturbations tend to either grow or decay. The two curves are plotted as dashed lines in Figure 3.7

3.2.7 Emergence and properties of dSA limit cycles

In the previous section we demonstrated that for certain dSA parameters the stationary state is unstable and oscillations will grow. In a system with quadratic damping, a stable limit cycle may form where the system oscillates such that the energy input from the muscle over one period exactly balances the energy dissipated by the environment. In order to control flapping oscillations, we need to understand how the amplitude and frequency of oscillations vary with the system parameters. The nonlinear aerodynamic damping presents challenges to deriving analytical solutions of the system. However, we can study the behavior of the system via numerical simulation.

We simulated the nonlinear equations of motion in Matlab (R2022a, Mathworks) using the ode45 solver. Parameters for elasticity, inertia, aerodynamic drag, and transmission ratio were calculated to approximate values found in a bumblebee, which has asynchronous muscle (Table 3.1. The transmission ratio T is based on a typical flapping amplitude of 140 degrees peak-to-peak and an in-vivo muscle strain of 2% with a resting muscle length of 4mm.

We selected 0.1 as a value for κ, informed by the results in Appendix C1. We computed intercepts of Eq. 3.31,

$$r_3^* = \frac{\omega_n}{\sqrt{\kappa}}, \qquad \hat{\mu}^* = \frac{1+\kappa}{1-\kappa}\omega_n^2 \tag{3.32}$$

Table 3.1. Nonlinear simulation mechanical parameters

Parameter	**Value**	**Units**
Stiffness	5400	N m^{-1}
Inertia	2.4×10^{-11}	kg m^2
Drag	1.4×10^{-11}	kg m^2
Transmission	30500	rad m^{-1}

and defined ranges of $\mu = \hat{\mu}(ILT^2)$ and r_3 that span the regions around those intercepts. r_3 is varied from 0 to $5\omega_n$, and μ from -40 to 200, each with 100 steps. We ran simulations at each configuration and computed the amplitude and frequency of oscillations, which were typically sinusoidal. The results are shown in Fig. 3.7.

Our simulations confirm that the stability boundary in Eq. 3.31 does divide the plane into oscillatory and non-oscillatory regions. Systems in the region where $\mu < 0$ oscillate at frequencies below the natural frequency, and show significant sensitivity to changes in μ. The dark red regions show where oscillations are at their physical limit, 180 degrees peak-to-peak; beyond this, pairs of wings would likely collide and/or joint limits would come into play. When $\mu > 0$, however, amplitude and frequency vary more slowly. Systems in this region oscillate at frequencies above the natural frequency, and while increasing μ always increases amplitude, amplitude changes non-monotonically with r_3. The lines of constant amplitude and frequency have varying curvature across the parameter space, but when $r_3 > \omega_n$ they overlap such that there is a unique combination of r_3 and μ that produces a particular amplitude and frequency. The white dot in Figure 3.7 indicates the in-vivo flapping amplitude (140 deg) and frequency (180 Hz) of a bumblebee, which is achieved when $r_3 = 2.55\omega_n$ and $\mu = 175$ ($\hat{\mu} = 1.96 \times 10^6$) This suggests a potential method of control for these systems where amplitude and frequency may be set based on the strength and rate parameters of the muscle.

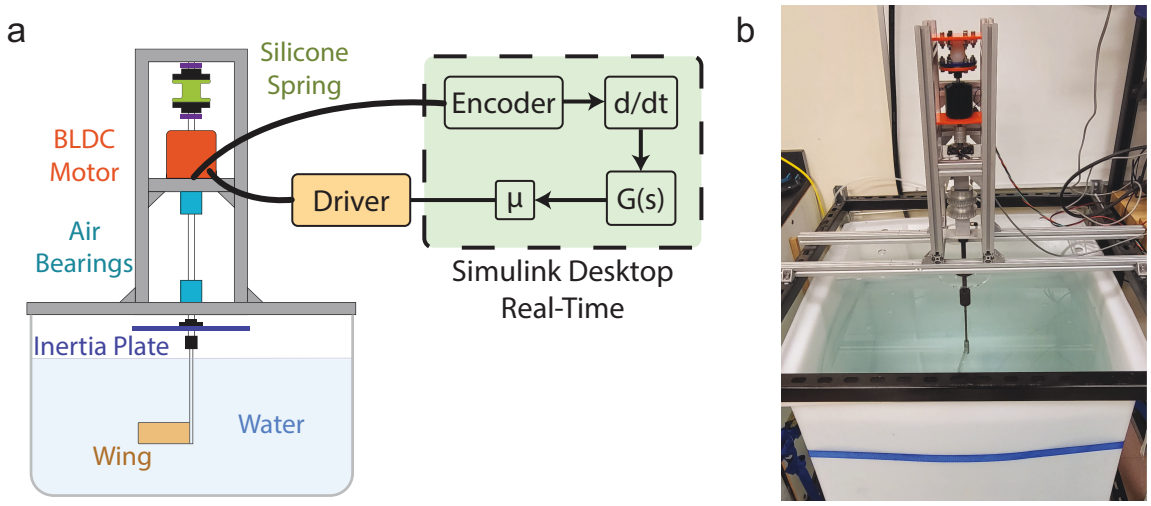

Figure 3.8. a) Diagram of the dynamically-scaled robotic model and control scheme. b) A photo of the system

3.3 Implementation in a scaled robotic model

In this section we describe experiments on a dynamically-scaled robotic flapping wing. The robophysical system has well-characterized mechanical parameters and is easily modified thanks to its modular design, enabling a range of tests that would be more difficult at a smaller scale.

3.3.1 Design of an asynchronous robotic spring-wing

The robophysical system we use in this study (Fig. 3.8) was adapted from a similar system described in [106]. It consists of an elastic element (a molded silicone torsion spring), a main shaft supported by a thrust bearing and radial air bearings, an optical rotary encoder (4096 CPR, US Digital), and a rigid, fixed-pitch acrylic wing in water. The inertia can be changed by fixing one of a set of inertia plates to the main shaft. Data collection and control of the system is done via a DAQ (PCIe 6323, NI) and Simulink Desktop Real-Time (SLDRT) (Mathworks), which enables hardware-in-the-loop control at a rate of 1000 samples/s.

The key feature of the asynchronous robotic model is the method of driving the system. We use a brushless DC motor (D6374 150KV, ODrive Robotics) and a motor driver to capable of closed-loop torque control at 10 kHz. The angular position of the wing is used as the input to a

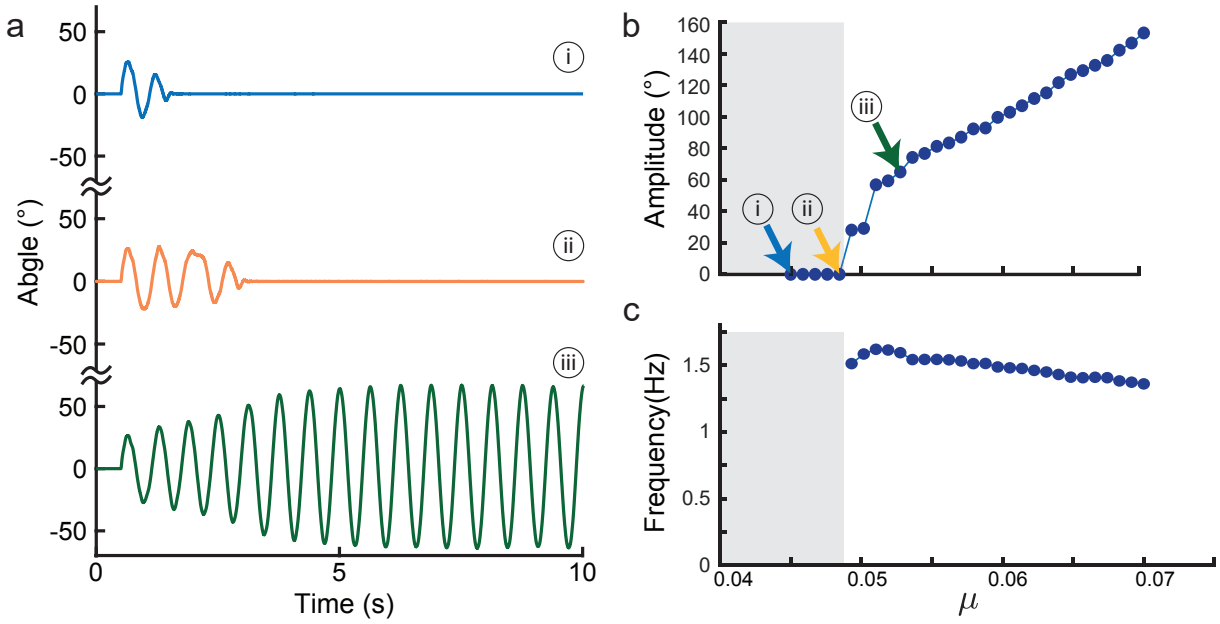

Figure 3.9. Results of increasing μ while keeping the mechanical parameters and r_3 constant ($k = 416\text{Nm rad}^{-1}$, $I = 1.96 \times 10^{-3}\text{kg m}^2$, $r_3 = 35\text{s}^{-1}$, and $\kappa = 0.5$). a) Three representative plots in the time domain: no oscillation (μ too low), a borderline case, and stable oscillations (μ large enough). b) The amplitude of oscillation increases as μ increases, and the frequency decreases slightly.

SLDRT model that implements the dSA transfer function (Eq. 3.15), multiplies the output by the strength, μ, and sends a torque command to the motor via USB, as shown in Fig. 3.8a. The direct torque control method eliminates the need to explicitly integrate the motor dynamics into the asynchronous ODE.

3.3.2 Controlling amplitude and frequency in a real system

We tested the effect of changing the value of μ in the robotic model while holding r_3 constant. The system parameters are as follows: Stiffness $k = 0.416$ Nm rad^{-1}, Inertia $I = 1.96 \times 10^{-3}$ kg m^2, $r_3 = 35s^{-1} = 2.4\omega_n$, and $\kappa = 0.5$. Since we are using a DC motor, $L = T = 1$ by definition. The value of r_3 places this configuration on the side of the stability boundary that should mean that it oscillates as long as $\mu > 0$. However, when we choose a small value for μ, we find that an initial perturbation actually tends to decay back to zero (Fig. 3.9a-i). In this case, the dSA feedback is not strong enough to overcome the effects of friction in the

bearings. We don't model friction in our simulations, but we can see that as $\hat{\mu} \to 0$ in Fig. 3.7a, the oscillation amplitude approaches zero. When friction is present in the system, arbitrarily small amplitudes are not possible, so the oscillation decays. Increasing μ leads to a "borderline" case where the system oscillates for a few periods before decaying again (Fig. 3.9a-ii). When μ finally crosses the threshold, stable oscillations result from an initial perturbation. We observe a roughly linear relationship between μ and amplitude, as well as a subtle decrease in oscillation frequency with increasing μ (Fig. 3.9, b and c)

3.3.3 Exemplary behaviors of dSA flapping wing systems

Beyond the control of flapping amplitude and frequency, we are able to examine novel behaviors of dSA flapping wing systems via the robophysical model. We observed that the asynchronous system was able to naturally adapt to changes in its mechanical properties. Additionally, the system features an extremely fast response to collisions with environmental obstacles, reducing the potential for serious damage to the wings or wing transmission.

Adaptation to changing mechanical parameters

Figure 3.10a shows the results of an experiment where additional mass is added to an inertia plate during an experiment. One might expect that the addition of extra inertia would cause the amplitude to decrease, as the motor now needs to move more mass. However, we see that as soon as the inertia of the system changes at $t = t^*$, the asynchronous flapper adjusts to the new loads on the system, actually increasing in amplitude and decreasing frequency. It *adapts* to the new system properties. Keeping the same values of r_3 and μ, we measured amplitude and frequency of oscillation for 4 different inertias. Figure 3.10b shows that this trend continues for higher inertias, suggesting that the product of amplitude and frequency remains roughly constant.

A robot with an adaptive control scheme like this is able to respond to changes to its mechanical properties automatically. This qualitatively has similarity to the adaptive oscillators explored for legged-locomotion, in which robots adjust gait and frequency when loads are added

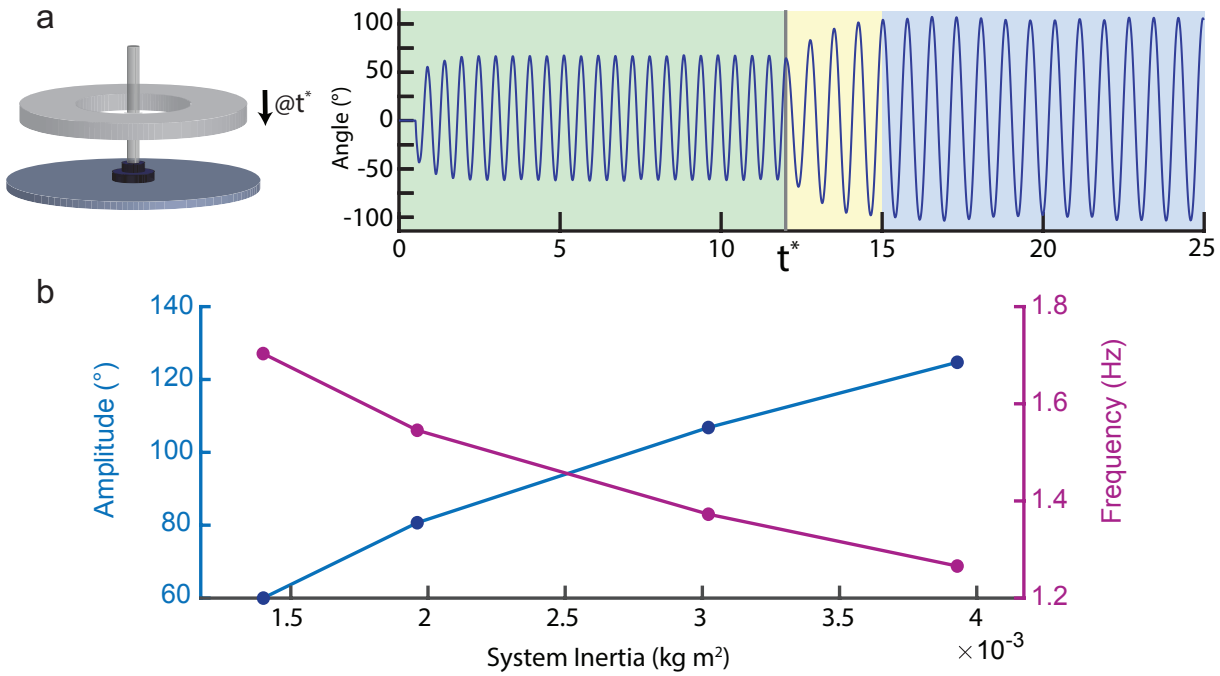

Figure 3.10. The asynchronous spring-wing adapts to changes in its mechanical system properties. a) When extra mass is added to the inertia plate on the large-scale robot model, the system transitions to a new amplitude and frequency. b) When we varied the inertia over a large range, we saw that increasing inertia decreases the frequency and increases the amplitude of the wingbeat

[125]. Damage to a wing or accumulation of debris may cause changes in wing inertia that would seriously impact the performance of a synchronously driven robot whose frequency is dictated by the resonance curve of the robot [89]. An asynchronously-driven robot, on the other hand, would simply adapt to a new frequency and amplitude that would still enable it to fly. As FWMAVs move from safe laboratory conditions to the more unpredictable world-at-large, adaptation to new situations will be ever more critical.

Fast response to collisions with the environment

Another inevitable consequence of operating in unstructured environments is collisions. The brittle actuator materials and delicate microstructures that make up typical FWMAVs make it all the more important to avoid or mediate damage from collisions. We wanted to investigate the response of the asynchronous system to a collision with a rigid object in the environment.

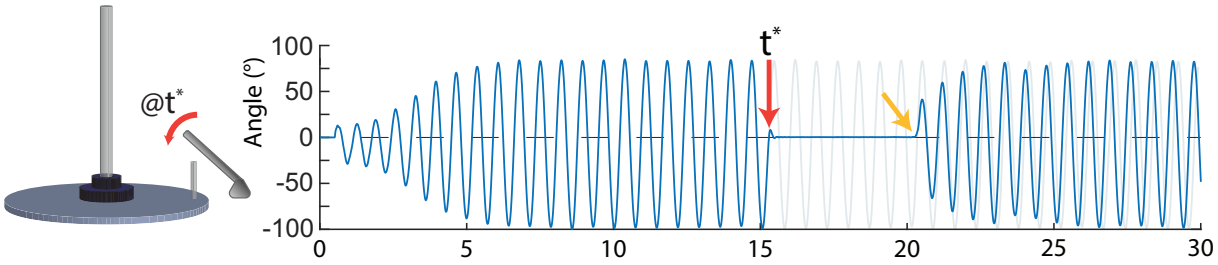

Figure 3.11. When the system collides with an obstacle at $t = t^*$, it naturally stops thanks to the dSA feedback law. It easily starts up again later as any small perturbation grows back to the original limit cycle

We fixed an inertia plate to the robotic model that included vertical posts and set the system to oscillate. At $t = t^*$, we interrupted the motion of the system by causing a post to collide with an obstacle. We observed that the system stopped almost immediately, well within a single period (Fig. 3.11). Very shortly after the angular velocity is reduced to zero, the dSA feedback also goes to zero, causing the actuator to stop driving the wing.

In the synchronous forcing case, represented by the light-colored trace in Fig. 3.11, the actuator is oblivious to the collision and continues to apply torque to the wing after it has already stopped, potentially causing damage to the wing structure. The low-level feedback inherent to asynchronous actuation enables the system to respond immediately, reducing the potential for damage. In addition, as soon as the system is perturbed again, after it is clear of the obstacle, it resumes flapping at the same amplitude and frequency. The asynchronous system naturally avoids damage and does it within a single oscillation period with no need for an explicit command to stop actuation. It may serve as a sort of distributed control, offloading some need for the flight controller to respond to environmental disturbances.

3.4 Insect-scale asynchronous flapping wing

As a proof-of-concept demonstration, we implemented dSA feedback on an insect-scale robotic wing. The wing apparatus, consisting of a thin polymer wing (15mm x 5mm x 0.1mm) supported by a carbon fiber frame, a PZT bimorph bending actuator, and a transmission, is based on the design from [13] (see Fig. 3.12a). Here, we used just a single wing, supported by acrylic brackets

instead of a carbon fiber airframe. We aligned a fiber optic displacement sensor (D21, Philtec) with the tip of the actuator to track the actuator displacement. Oscillations were induced by an aerodynamic perturbation provided by a toy vortex ring gun (Zero Blaster, zerotoys.com). We recorded high speed video of the system from the top down as the vortex crossed the wing. Frames from the video can be seen in Fig. 3.12b.

The output from the displacement sensor was fed into an NI DAQ (PCIe 6343) and used as input the same SLDRT model that implemented the dSA feedback law described in previous Section III. Typically, PZT bimorph actuators are driven by providing 3 voltage signals: a high-voltage bias (250V) on one side of the bimorph, a control signal (0V-250V) in the middle, and ground on the other side. Bending in the actuator is driven by the electrical potential between the signal and the two sides of the bimorph. To close the loop via dSA feedback, we took the derivative of the displacement to get velocity and fed the velocity into the dSA transfer function (Eq. 3.15) with $r_3 = 225$ Hz ($\sim 3\omega_n$). The output was converted to voltage and fed through an amplifier to the PZT control signal. As with the large-scale robotic model, we slowly increased μ until stable oscillations were observed. Fig. 3.12 shows the result of two tests: one with μ too small to overcome friction, and one with a large enough μ to induce oscillations. Larger values of μ may have provided larger amplitudes, but we used this minimum μ value in our testing to avoid overloading the actuator and the robot.

3.5 Conclusion & Future Work

In this paper we derive and study the first dynamical system representation of asynchronous wingbeat actuation in flapping wing robots and insects. The dSA feedback control law that we have described here is a novel method of achieving flapping in robots. Asynchronous actuation in current FWMAVs is simple to implement and requires only 1) a state estimate via strain gauge, encoder, gyroscope, or other sensor and 2) knowledge of the internal dynamics of the actuator. The method can be applied to a wide range of actuators using relatively simple

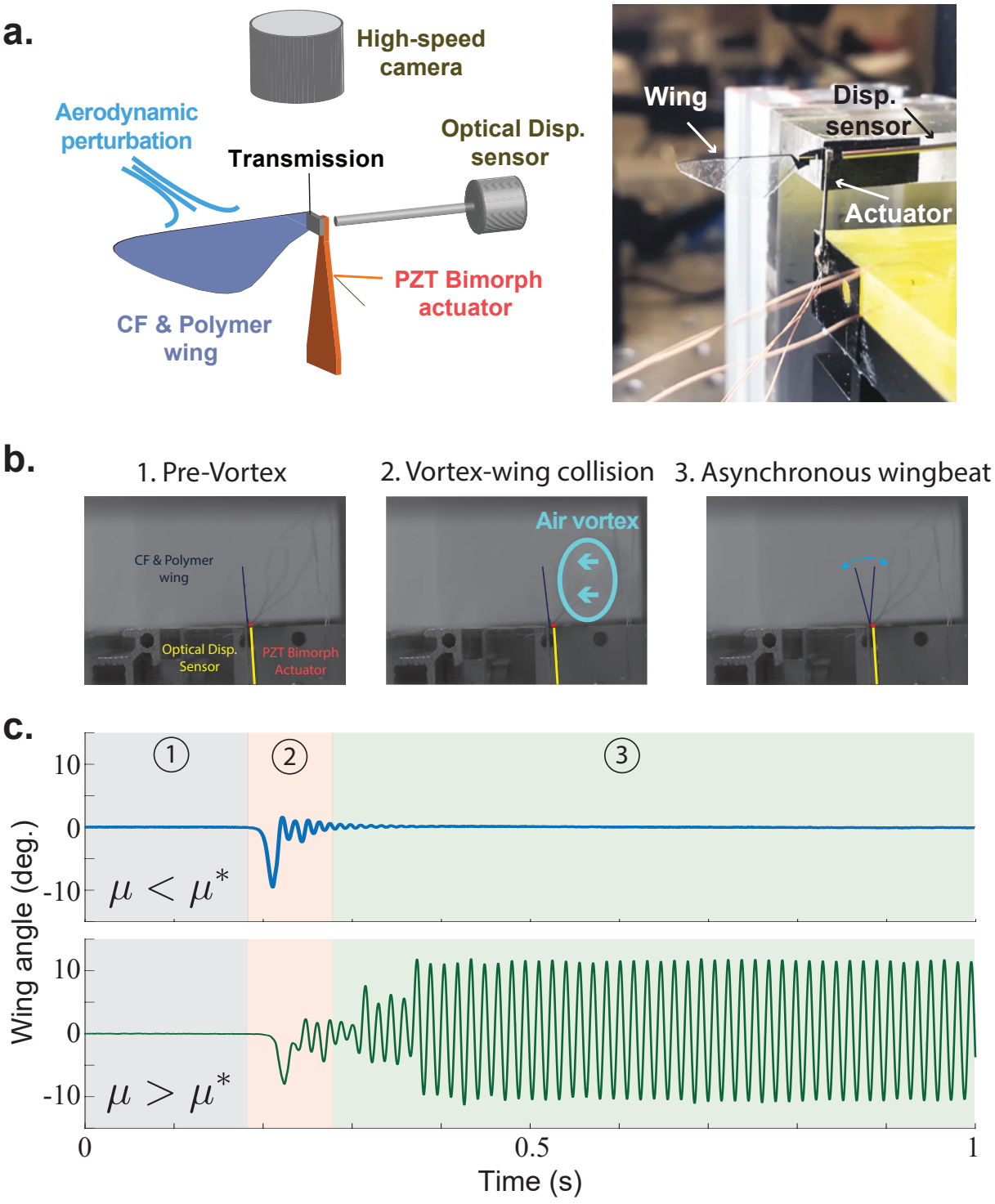

Figure 3.12. a) Robobee wing experiment diagram, side and top views and photo of the setup. b) High-speed video stills before, during, and after vortex perturbation. c) Wingbeat dynamics when μ value is too low (top) and when μ is increased above the oscillation threshold (bottom). Numbered regions correspond to the images in b.

analog hardware or simple digital logic. The resulting system naturally oscillates powered and can be controlled by adjusting the feedback parameters OR by changing the mechanical properties (e.g. wing inertia) of the robot.

While our implementation of asynchronous actuation relied on actuators, sensors, and a feedback loop, the dSA response of insect flight muscle is "material" property of the muscle. Thus asynchronous wingbeats emerge from the lowest level of mechanical feedback within asynchronous insects. Future work to engineer such low-level feedback properties into active materials and circuits will be of great interest for future FWMAVs.

Acknowledgements

Chapter 3, in part, is a reprint of the material as it appears in *Lynch J, Gau J, Sponberg S, Gravish N. Autonomous Actuation of Flapping Wing Robots Inspired by Asynchronous Insect Muscle. In: 2022 IEEE International Conference on Robotics and Automation (ICRA). Philadelphia, PA; 2022*. The dissertation author was the primary investigator and first author of this paper.

Chapter 4

Transitions between Synchronous and Asynchronous Flapping

4.1 Asynchronous Insect Flight Muscle Background & Motivation

Unlike the many insects that power each wingstroke with one-to-one, "synchronous" neural activation of flight muscles at up to ≈100 Hz (Fig. 4.1a), some insect species require high power output at even higher frequencies. In these asynchronous species, the flight power muscles possess a delayed stretch activation (dSA) response [4], which causes wing oscillations to self-excite without the need for regular timing from the nervous system (Fig. 4.1a). This delayed stretch activation is a physiological property of some muscles in which an imposed stretch causes a time-lagged rise in tension even under constant activation (Fig. 4.1b). Neural activation potentiates asynchronous muscle through the sustained release of calcium, but oscillations arise due to the antagonistic action of two muscles, both with delayed stretch activation properties. Although insects with asynchronous muscle evolved from synchronous ancestors, these two modes of flight have been widely thought of as distinct strategies, but with multiple transitions between them [67], [75]. However, with new phylogenies of flying insects and dynamic systems modeling of insect wing mechanics, we have the opportunity to reexamine this dichotomy and why repeated transitions can occur.

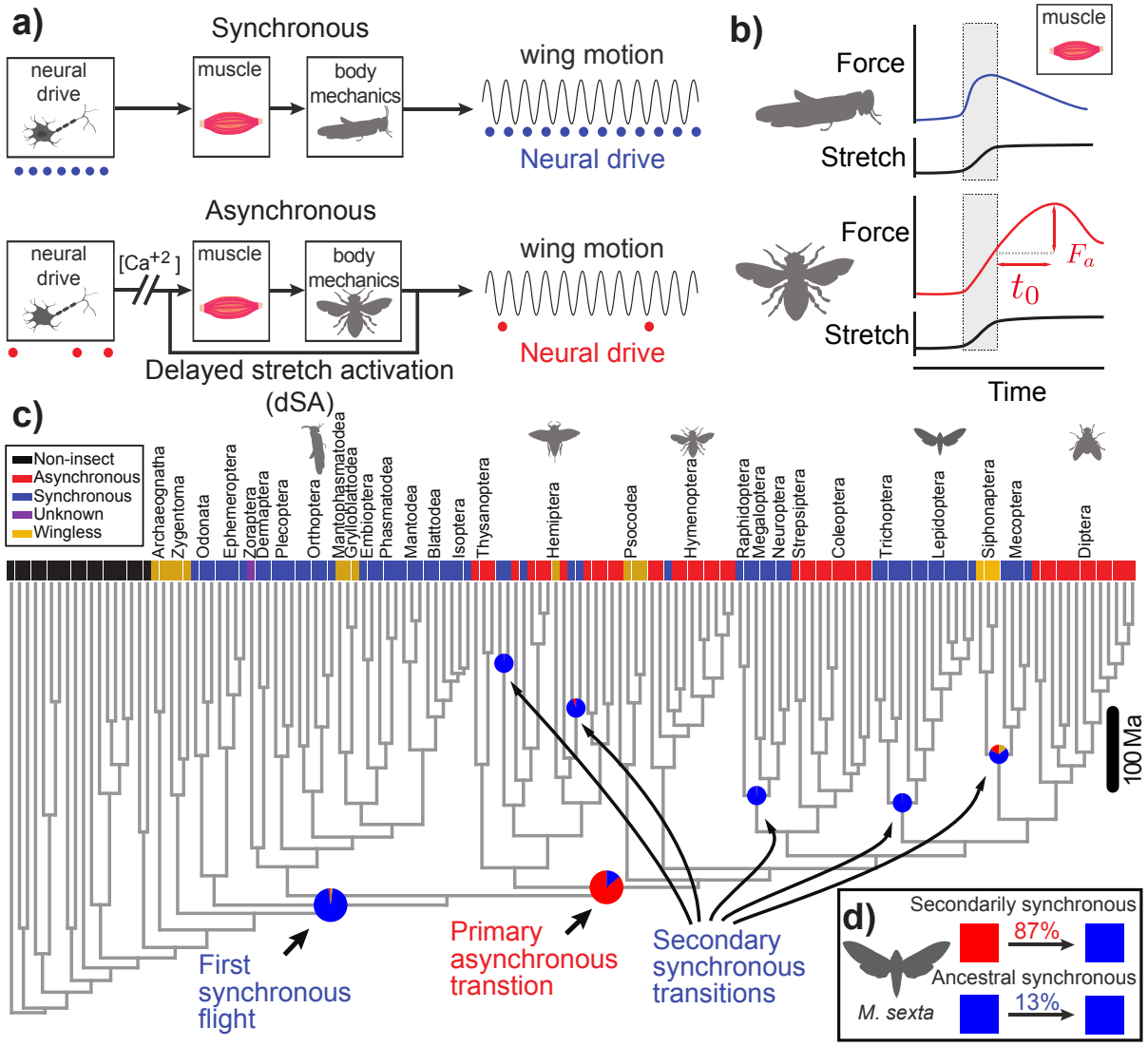

Figure 4.1. Phylogenetic comparative analysis of insect wingbeat actuation reveals a likely single origin of asynchronous flight muscle. a) Synchronous muscle has a 1:1 relationship between neural activation (blue dots) and muscle contraction. Asynchronous muscle contraction is independent of the precise timing of neural activation (red dots), arising from delayed stretch activation (dSA) [4]. b) The physiological signature of a aysnchronous muscle is that when impulsively stretched it produced a delayed force of magnitude F_a that peaks after a characteristic time, t_0, determined by the rising and falling rate constants r_3 and r_4 (see methods).c) Ancestral state reconstruction[126] reveals based on muscle ultrastructure (not physiology) that a single evolutionary origin of asynchronous fiber types is most likely using an insect-wide phylogeny resolved to the ordinal level [127]. Tip states were identified from literature for orders with a conserved muscle type, and, in orders with known interspecific muscle type variation (Hemiptera, Psocodea, Hymenoptera, see Methods). d) By iteratively constraining ancestral nodes (see Methods), we find that the synchronous flight muscles of Lepidopterans (including *M. sexta* are most likely evolved from a asynchronous ancestor ("secondarily synchronous") as opposed to having only synchronous ancestors (plesiomorphic).

4.2 Asynchrony has likely evolved only once in flight muscle, with many reversions to synchrony

4.2.1 Phylogenetic state reconstruction

We first examined the evolution of synchrony and asynchrony using maximum likelihood phylogenetic state reconstruction [126] (see Methods). We find that there has most likely been only one evolution of flight muscle asynchrony at the order level. There is an 86% likelihood of a single transition from synchronous to asynchronous in the ancestor of the clade of Thysanoptera + Hemiptera + Psocodea + holometabolous insects (Node 200) occurring 407 million years ago (Fig. 4.1c, Extended Data Figures D.1, D.2, D.3, Supp. Data Table 1, 2). Although asynchrony was thought to have evolved 7-10 times throughout insect flight [4], [75], [128], earlier analyses were not done using phylogenetic ancestral state reconstruction. Only recently has an insect-wide phylogeny enabled resolution of the major orders [127]. We established the state of extant species from existing literature on muscle ultrastructure and histology (see Supplementary Data Table S1). We first assumed an equal rates model of evolution and utilized a Markov chain Monte Carlo approach to estimate the state of ancient insects. In the most likely reconstruction, there have been many independent reversions back to synchronous flight muscle from the single origin of asynchrony at the order level. Species with this reversion are secondarily synchronous flyers (Fig. 4.1c, Extended Data Figure D.3). We found that Mecoptera, Lepidoptera, Neuroptera, Megaloptera, and Raphidoptera are all most likely secondarily synchronous orders.

4.2.2 Result is consistent across models of evolution

This pattern of transitions is consistent across alternative models of evolution. The best fit model (all transition rates different with ambiguous coding of wingless species) actually produced a 100% reconstruction of a single asynchronous origin at Node 200. However, even if muscle structural data is available across most orders, we still only have samples from a small number of all insect species. Therefore, we show the more conservative equal rates model

(Fig. 4.1c). Incorporating heterogenous rates across the phylogeny [129], [130] did not produce better model fits (see Supplementary Information IIA). Ancestral state reconstruction can change with more sampling and different phylogenetic reconstructions, but the current best evidence supports a single origin of asynchrony at the order level. Most importantly, our analysis raises the possibility that the physiological properties associated with asynchrony, such as delayed stretch activation, could be conserved in secondarily synchronous fliers. If so, this would provide evidence that both modes can co-occur across the phylogeny even if the muscle ultrastructure appears as a specific type.

4.3 Secondary synchronous fliers can maintain asynchronous capacity

Previous tests of the synchronous flight muscle of locusts (Fig. 4.1b), found no evidence for delayed stretch activation [4]. This contributed to the idea that delayed stretch activation was a specialization restricted to asynchronous muscle and that there is a dichotomy in muscle properties associated with the two flight modes. In the presence of tonic calcium levels maintained by a relatively slow neural drive, asynchronous muscles exhibit delayed stretch activation and also a delayed drop in force following shortening (delayed shortening deactivation) [4], [75]. These complementary effects enable power production by establishing a time delay between force and displacement. However, because orthopterans (including the ancestors to modern locusts) diverged from other insects before the first asynchronous fliers, the lack of delayed stretch activation in locusts may not generalize to secondarily synchronous insects (Fig. 4.1c). We next explored whether asynchronous muscle properties were conserved in the hawkmoth species *Manduca sexta* – a secondarily synchronous lepidopteran (Fig. 4.1d).

4.3.1 Measurements of stretch-activation in *Mandua sexta*

Unlike in the locust example, we identified a delayed increase in force following stretch in *M. sexta* flight muscle – the hallmark feature of delayed stretch activation (Fig. 4.2a,b). After

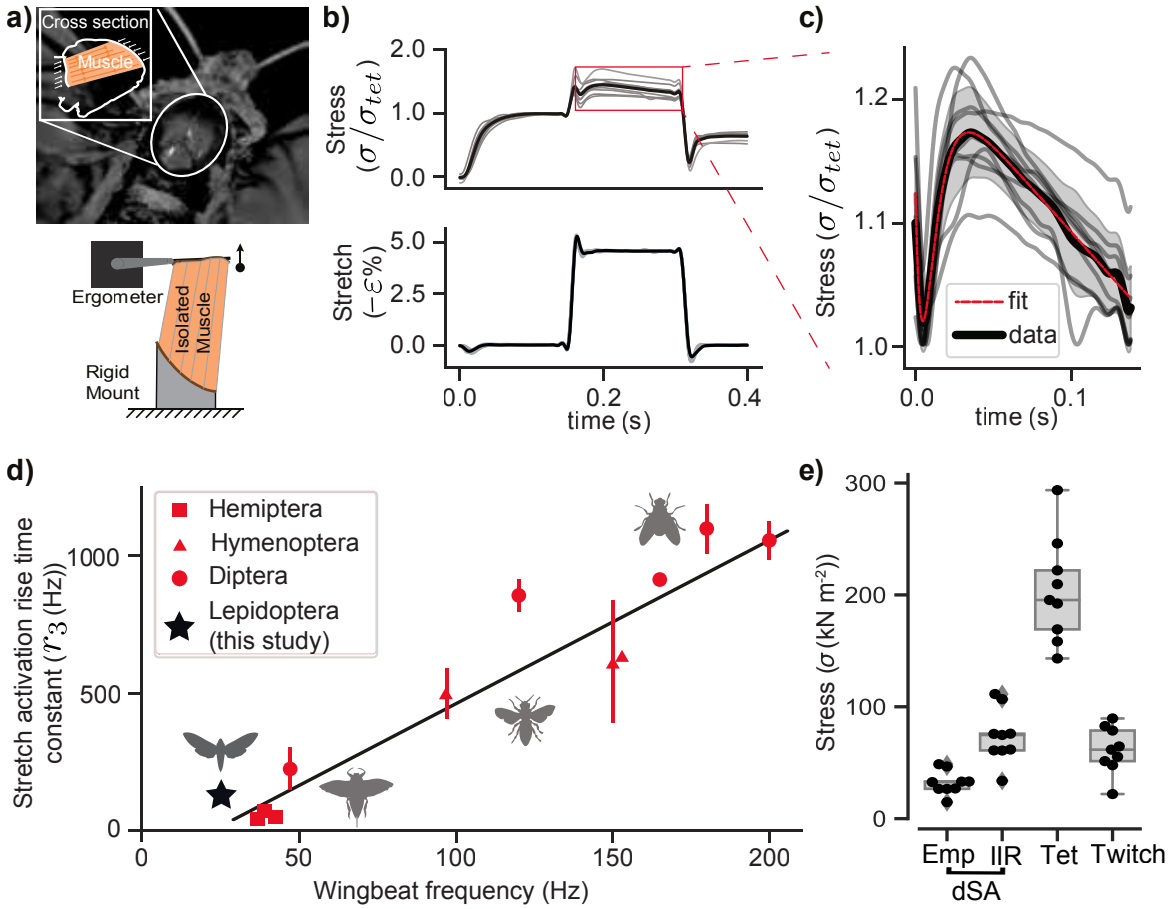

Figure 4.2. Secondarily synchronous hawkmoth flight muscle exhibits delayed stretch activation – a hallmark of asynchronous flight. a) *M. sexta* intact, downstroke flight muscle, (dorsolongitundinal muscles, DLMs, N=9, 1 trial per individual), was mounted on an ergometer and electrically stimulated at 150 Hz to establish tetanus. Muscle viability was maintained using a saline drip at a constant 35 °C. b) We applied stretch-hold-release-hold strains, matching *in vivo* strain amplitudes of 4.5% [131] while measuring stress normalized to tetanus. Positive strain (ε) and force are defined in the shortening direction (opposite stretch). Experiments reveal delayed force increase characteristic of asynchrnous muscle physiology. Black line denotes mean muscle stress normalized to tetanic stress, gray lines show individual trials. c) Magnification of the box in (b) shows the delayed stretch activation (dSA) response. A sum of exponentials mathematical formulation of delayed stretch activation (Eq. D.1 – red line) accurately fits the mean normalized stress (black line). The initial transient is the viscoeleastic response of the muscle and the subsequent rise and fall is the stretch activation d) Despite being synchronous, *M. sexta's* delayed stretch activation rising rate constant, r_3, lies near the prior empirical finding of a linear relationship between r_3 and wingbeat frequency by Molloy[73] (123.4 ± 52.6 s^{-1} at 25 hz – black star, error bars obscured). We scaled r_3 values to ambient temperature using published relationships (Eq. 2 & 3 from Molloy *et al.* [73]). Hemiptera, Diptera, and Hymenoptera data and black regression line plotted from Molloy *et al.* [73]. e) Peak stress for *M. sexta* delayed stretch activation (F_a), tetanus, and twitch. Delayed stretch activation (dSA) stress is shown with (IIR) and without (Emp) infinite impulse response correction (see Methods). Boxplots denote mean, quartiles, and range of the raw data; circles denote individual data points.

reaching 203 $\pm$ 44 kN m^{-2} during constant activation at 0% strain, we stretched the primary flight downstroke muscles (DLMs) to 4.5% strain and observed a subsequent increase in stress of 32.1 $\pm$ 9.9 kN m^{-2} that was delayed by 29.0 $\pm$ 6.6 ms after the conclusion of the stretch. However, following shortening we did not observe delayed shortening deactivation. Many stretch-hold-release-hold experiments on asynchronous muscle detect both delayed stretch activation and delayed shortening deactivation [4], [73], [132], while others observe delayed stretch activation without delayed shortening deactivation [64], [69]. Delayed shortening deactivation may be driven by distinct molecular mechanisms and may not be a necessary feature for asynchrony. Thus, while *M. sexta* is a synchronous flyer, their flight muscle exhibits the necessary physiological properties to enable asynchronous flight.

4.3.2 The rate of delayed stretch activation in *M. sexta* is comparable to asynchronous insects

The presence of delayed stretch activation in a synchronous insect creates a dilemma: Why does delayed stretch activation not cause wingstrokes that are asynchronous in *M. sexta*? This limitation could arise from ineffective timing or insufficient magnitude of the delayed stretch activation. The timing of the delayed stretch activation response is typically characterized by fitting a sum of three exponential terms with rate constants r_2, r_3, and r_4 [73] (Red curve Fig. 4.2c, and see Methods). The rate constants represent three phases of delayed stretch activation: a fast drop in tension (r_2) corresponding to the fall of the viscoelastic response (stress relaxation), a delayed tension rise associated with stretch activation (r_3), and a slow drop in tension as stretch activation decays (r_4). The rising rate of stretch activation tension (r_3) is linearly related to wingbeat frequency in asynchronous insects [73] and is linked to the rates of crossbridge attachment and detachment [133]. These relationships suggest that r_3 is the single critical parameter that establishes the time delay necessary for self-excitation.

Although the rate of delayed stretch activation in *M. sexta* is sufficient for asynchrony, the magnitude of delayed stretch activation is likely too low to generate self-excited oscillations.

We found that the relationship between delayed stretch activation rate constant, r_3, and wingbeat frequency of 25 Hz in *M. sexta* is consistent with the broad scaling relationship observed by Molloy across asynchronous insects [73], [134] (Fig. 4.2d, see Methods), which suggests that a hawkmoth could be asynchronous (Fig. 4.2c).

4.3.3 The magnitude of delayed stretch activation is much smaller than in asynchronous insects

However, the magnitude of delayed stretch activation was only 36.2 $\pm$ 13.6% of the tetanic force (Fig. 4.2e). Direct comparison to literature is difficult because of varying experimental conditions [62], but the ratio of delayed stretch activation magnitude to tetanus is typically between 100-300% in asynchronous beetles, waterbugs, and flies [73], [135]. Even correcting for the non-instantaneous stretch used in the physiological experiment, the idealized delayed stretch activation response (an infinite impulse response – IIR) is still far below tetanic force in *M. sexta* (Fig. 4.2e). So *M. sexta* seems to be a synchronous flyer not because it lacks the physiological capabilities for asynchronous activation, but rather because it occupies a region of delayed stretch activation parameter space where asynchrononus forces are not sufficient to dominate the neurally driven activation and relaxation of flight muscle (synchronous forcing). Additionally, *M. sexta* muscle likely reuptakes calcium more quickly than most asynchronous muscles further reducing the significance of the delayed stretch activation contribution to *in vivo* flight conditions.

4.3.4 Molecular components of asynchronous muscle are conserved in secondarily synchronous insects

However, if the delayed stretch activation magnitude were larger, then it is possible that *M. sexta* could generate asynchronous wingbeats. It is not precisely known what mechanism controls the magnitude and rate of delayed stretch activation [136], but it is dependent on calcium levels and likely involves recruitment of additional myosin heads (crossbridges) through stretch-sensitive myofilament proteins [69], [137]. In asynchronous insects, neural activation

typically only recruits 30% of crossbridges which explains why the stretch activation can far exceed tetanic activation [138]. One possible way this is regulated is by the ratio of isoforms of the regulatory molecule troponin which promotes release of myosin-binding sites [61]. This ratio is correlated with asynchronous force output [62], [139]. Surprisingly, the stretch-activated troponin isoforms found in asynchronous insects and implicated in delayed stretch activation are also found in *M. sexta* [139], [140]. This provides one possible mechanism for residual delayed stretch activation in moths. Our physiological results indicate that delayed stretch activation can be present in quite reduced magnitudes and it is already known that the rate constants can vary widely [73]. The flight muscles of different asynchronous (and synchronous) orders may have further specialized, especially in extreme cases of performance which may contribute to the molecular differences observed in some groups [141]–[143]. Our dresults show that conserved molecular components are potentially part of the same continuous dynamical parameter space that spans across synchronous and asynchronous flight modes.

4.4 A single dynamics framework for asynchronous and synchronous flight

The presence of delayed stretch activation in a synchronous insect, coupled with evidence of many evolutionary transitions from asynchrony to synchrony, suggests that synchronous and stretch-activated contractions can be two regimes of a single actuation strategy. Building on the extensive characterization of synchronous and asynchronous flight muscle [67], [73], quasi-steady flapping aerodynamics [134], [144], [145], and body mechanics [55], [76], [106], we next developed a biologically grounded model of insect flight in which we can control the relative contributions of synchronous and asynchronous forcing (Fig. 4.3a). We coupled models of both synchronous and asynchronous forcing to an established mechanics model that includes the elasticity of the deformable exoskeleton, wing inertia, and aerodynamic loads [76], [106] (Fig. 4.3a).

4.4.1 A feedback model of delayed stretch activation

We developed a model of delayed stretch activation that captures the strain-dependent force output of asynchronous muscles (see Methods). Delayed stretch activation acts as a filter (convolution) that transforms strain rate into force through a velocity impulse response function. Furthermore, the force response to a stretch-hold-release-hold (step) strain input approximates this response function to an impulsive stretch. This filter can then be applied to continuously varying patterns of strain (such as during a wingstroke) provided it remains in the linear regime (See Supplementary Information IIB). Prior experiments have demonstrated that for low amplitudes the delayed stretch activation response is linear [146], justifying this approach.

Figure 4.3. Transitions between synchronous and asynchronous modes requires alignment of synchronous and asynchronous rates a) The simulated hawkmoth with body mechanics (Eq. 4.2), a model of delayed stretch activation based on a filter (convolution) of the muscle strain rate (Eq. D.6, D.7), and an interpolation factor K_r, which changes the relative strength of stretch-activated (asynchronous) forcing relative to the neurogenic (synchronous) force development in flight muscle (Eq. 4.1). b) The cycle-averaged power of emergent wingbeats spanning K_r and rate of delayed stretch activation normalized to the natural frequency of the mechancis (t_0/T_n). We observed high-power flapping at both extremes, but intermediate modes only generated significant power along a bridge where the rate of stretch activation produces asynchronous wingstrokes at the same frequency as the synchronous drive (25 Hz). *M. sexta* is plotted on the same figure based on our measurements of t_0/T_n and K_r. c) Emergent wingbeat frequencies (f) normalized by the synchronous drive frequency (f_s). Blue indicates regions where the emergent wingbeat frequency is entrained to the synchronous driving frequency ($f = f_s$). The red regions indicate where the asynchronous dynamics dominate and the forcing is predominantly stretch activated ($f \neq f_s$). The gray line indicates boundary between synchronous- and asynchronous-dominant dynamics. d) A robophysical system ("roboflapper") implementing delayed stretch activation feedback, plus real-world fluid physics and friction. e) and f) are qualitatively similar to the simulations in b) and c), validating our findings in a real system. However, at low K_r and high t_0/T_n emergent asynchronous wingbeats were not able to be produced due to system friction (white region in upper left). Experiments were run on a 20x20 grid of parameters with outputs averaged over 15 seconds of steady-state data. g) A centimeter-scale robotic wing modeled after the Harvard robobee [13] consisting of (1) wing, (2) transmission, (3) carbon fiber frame, (4) piezoelectric bending actuator, and (5) displacement sensor for measuring wing angle. h) and i) show the effects on oscillation kinematics of transitioning from synchronous ($K_r = 1$) to asynchronous ($K_r = 0$) in real time on a single test platform. The blue and red colors indicate the synchronous (blue) and asynchronous (red) regimes. Transitions are smooth when synchronous and asynchronous frequencies are approximately equal (blue and red markers, respectively). However, when the synchronous frequency substantially differs from the asynchronous frequency, interference between synchronous and asynchronous dynamics causes the oscillation amplitude and emergent frequency to fluctuate during the transition regime.

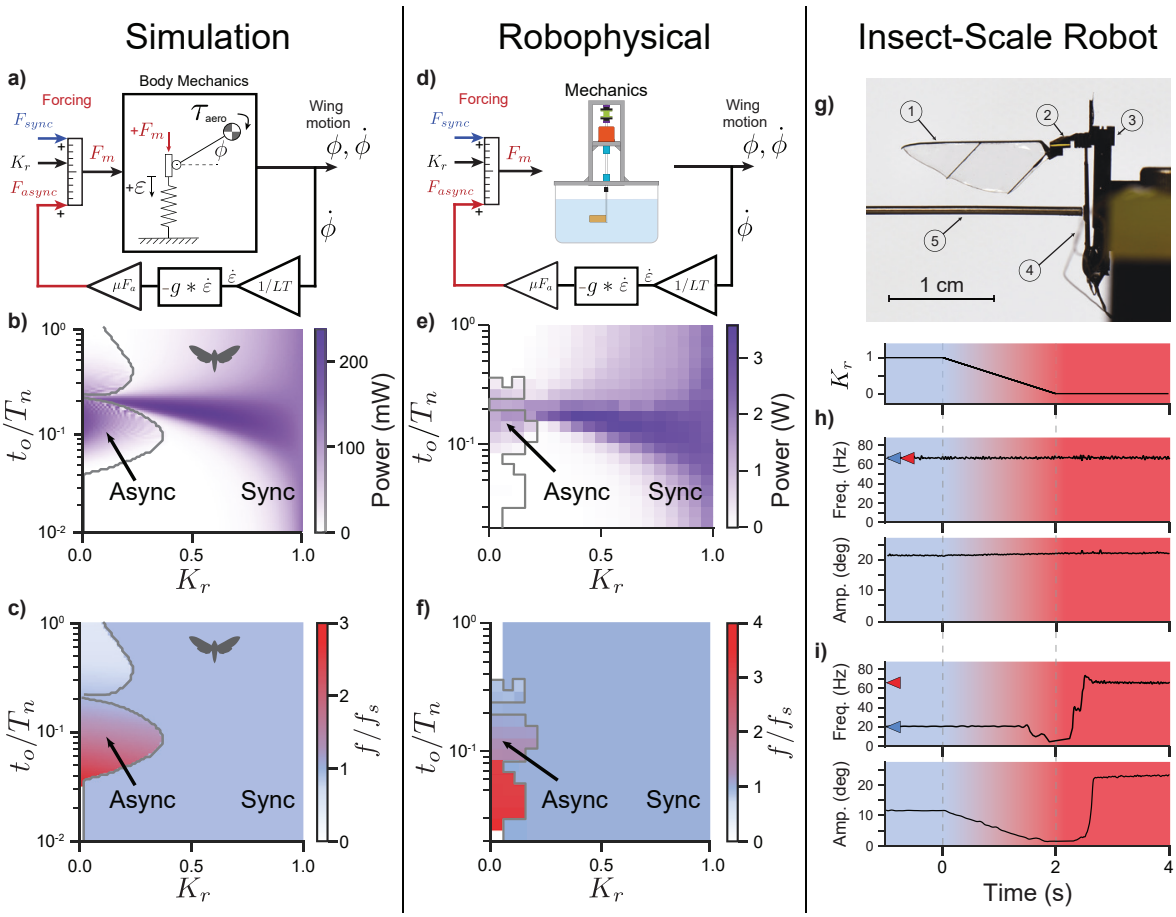
Simulation
Robophysical
Insect-Scale Robot
a)
Body Mechanics
Forcing
Wing motion
b)
c)
d)
Mechanics
e)
f)
g)
1 cm
h)
i)
Async
Sync
Power (mW)
Power (W)
Freq. (Hz)
Amp. (deg)
Time (s)

We fit the convolution filter to the stretch-hold-release-hold response as $F_{async}(\dot{\varepsilon},t) = \mu F_a(-g * \dot{\varepsilon})(t)$, where F_a is the magnitude of the asynchronous forcing (Fig. 4.1b), $\dot{\varepsilon}$ is the muscle strain rate, and g is the velocity impulse response (Fig. 4.3a, 4.4 and see Methods). We include μ as a scaling factor that tunes the kernel such that $max(F_{async}(t)) = F_a$ in stretch-hold-release-hold experiments (Fig. 4.1b, 4.2c). The negative sign in front of the convolution indicates that a negative strain (muscle stretch) induces a positive (shortening) force response (muscle physiology conventions define positive in the shortening direction). The muscle strain rate scales with wing angular velocity by a factor of LT, where L is the resting length of the muscle, and T is the transmission ratio of angular wing displacement to linear muscle displacement, $LT\dot{\varepsilon}(t) = \dot{\phi}(t)$. Values of L and T are taken from the literature [131], [147]. To validate our delayed stretch activation model, we showed that it could capture the asynchronous response of *M. sexta* from our experiments and also that it could reconstruct the muscle power of *Lethocerus indicus* and *Vespula vulgaris*, which are asynchronous species (see Supplementary Information IIB).

4.4.2 Interpolation of synchronous and asynchronous dynamics

In the synchronous case, $F_{sync}(t) = F_s \sin(2\pi f_s t)$ where F_s is the synchronous forcing amplitude defined as the force necessary to elicit wingstrokes with a realistic sweep angle of 117 degrees in our model under purely synchronous activation (2720 mN in *M. sexta*, see Methods) and f_s is the synchronous wingbeat frequency (25 Hz). We then combined both types of forcing via an interpolation factor, $K_r \in [0,1]$, to obtain the total muscle force, F_m, where

$$F_m(\dot{\varepsilon},t) = K_r F_{sync}(t) + (1-K_r)F_{async}(\dot{\varepsilon},t). \tag{4.1}$$

The value of K_r reflects the relative importance of synchronous versus asynchronous forcing in the system. Biologically, a high K_r means that the force change and crossbridge recruitment due to neural activation is large compared to the crossbridge recruitment due to stretch activation.

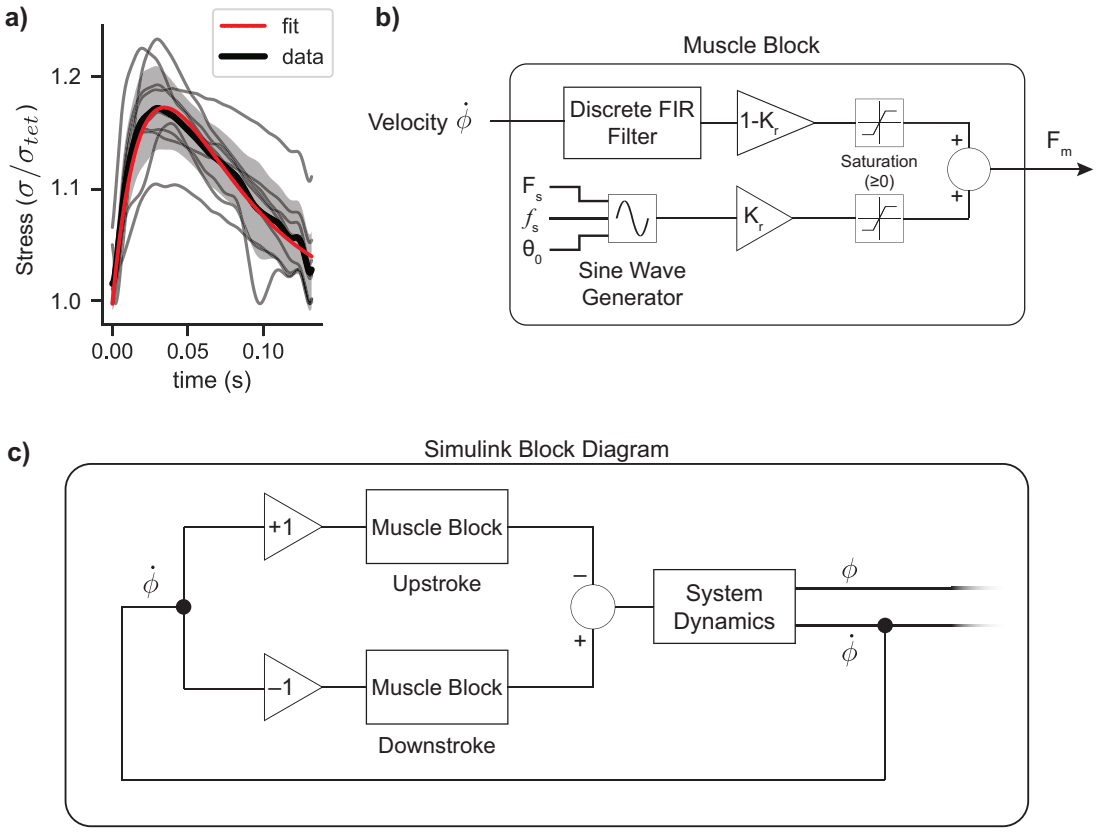

Figure 4.4. Details of simulation of delayed stretch activation. a) A two parameter model fit (r_3 and r_4) of phases 3 and 4 of the *M. sexta* delayed stretch activation response (Eq. D.2). b) Diagram of the muscle block alone. Output is a weighted sum of asynchronous feedback and synchronous forcing, saturated such that it exerts force only in one direction. The sine generator has a phase, θ_0, of 0 for the upstroke muscle and π for the downstroke muscle so that together the two muscles generate sinusoidal forcing. c) Block diagram of simulation of antagonistic muscles under both delayed stretch activation and synchronous forcing.

The sensitivity of flight muscle to calcium compared to the stretch sensitivity of the myofilaments gives a plausible mechanism for K_r to vary across species and over evolutionary timescales. Because in-flight measurements of F_a and F_s are unavailable, we approximate K_r using the ratio of asynchronous to synchronous forces measured from isolated muscle under static conditions (see Supplementary Information). In *M. sexta* for example, K_r is relatively high (0.6) reflecting that the magnitude of the delayed stretch activation response is low compared to the forces generated via neural activation alone. Asynchronous species produce a delayed stretch activation force several times higher than isometric tetanus [4] and would have a very low K_r. By adjusting

K_r from fully synchronous ($K_r = 1$) to fully asynchronous ($K_r = 0$), we can explore the emergent interactions of synchronous and stretch-activated forcing in the same system.

4.4.3 Incorporating passive spring-wing dynamics

The interactions between strain-dependent forcing and passive mechanics may play a key role in establishing self-excited oscillations. To incorporate these interactions, we first modeled aerodynamic damping using a quasi-steady approximation with aerodynamic torque equal to the wing angular velocity squared, multiplied by a coefficient (Γ) that accounts for wing shape, air density, and experimentally measured drag coefficients [134] (See Methods Eq. D.10). We then used prior estimates of *M. sexta* wing inertia (I) [134], thorax elasticity (k) [76], and transmission ratio (T) [147]. This yields our mechanics model which we refer to as a "spring-wing" system:

$$\frac{F_m}{T} = I\ddot{\phi} + \Gamma|\dot{\phi}|\dot{\phi} + \frac{k}{T^2}\phi. \tag{4.2}$$

This equation captures the indirect actuation of synchronous and asynchronous insect flight muscle, which act via the deformation of the thorax in parallel with the muscle to sweep the wings back and forth. Measurements of the *M. sexta* thorax are well approximated by a linear elastic spring in parallel with muscle [76].

To reduce the complexity of the delayed stretch activation model we combine (r_3, r_4) to one time scale t_0 (see Methods), which is the rise time to peak force (Fig. 4.1b). To compare across systems we then nondimensionalize this time by normalizing to T_n, the natural period of the wing-thorax system. T_n is determined by the body mechanics alone,

$$T_n = 2\pi\sqrt{\frac{I}{k}}. \tag{4.3}$$

The interactions between synchronous forcing amplitude and frequency, delayed stretch activation rates, and mechanical time constants define a parameter space that encompasses both

synchronous and asynchronous oscillations. As expected, while *M. sexta* does have delayed stretch activation, it is firmly in the synchronous regime ($K_r = 0.6$, $t_0/T_n = 0.54$). Its wingstrokes are largely unaffected by delayed stretch activation (Fig. 4.3b). Delayed stretch activation, while present in *M.sexta*, has been reduced to a point where it is less consequential at least at steady-state, although it may still play a role under perturbed conditions with faster strains and frequency modulation [108].

4.5 Simulation Results

4.5.1 Simulation parameter sweep with hawkmoth mechanics

Using these same hawkmoth mechanics, we simulated the rest of the parameter space (Fig. 4.3b,c). The asynchronous regime is capable of generating large amplitude limit-cycle oscillations even with hawkmoth mechanics, but would require much lower K_r. As the time to reach peak force of the asynchronous muscle (t_0) is increased we observe a bifurcation where asynchronous wingbeats appear as t_0/T_n crosses a critical value (see Extended Data Figure Fig. D.7). When t_0 is small the muscle tension increase is faster than the natural oscillation frequency of the body, and thus the delayed stretch activation acts as a brake. However, when t_0 is large enough (i.e. the muscle response is sufficiently slow), the delayed stretch activation force is produced during the oscillatory contraction phase and self-excited oscillations occur. We found that these regimes of qualitatively distinct oscillations, one periodically forced (synchronous) and one self-excited (asynchronous), are both able to generate wing kinematics with comparable amplitudes and frequencies. However, as we transition between these two regimes by varying K_r, we observed complex dynamics where synchronous and asynchronous modes interact.

4.5.2 A bridge in parameter space enables smooth transitions between synchrony and asynchrony

A major function of the flight musculature is to power flight. Therefore, a gradual transition between synchrony and asynchrony is only evolutionarily feasible if a set of high-power,

steady periodic oscillations connects the two regimes. Based on our simulations, smooth transitions between the synchronous and asynchronous modes are possible, but only with appropriate matching of the muscular and mechanical timescales. Both synchronous and asynchronous oscillations are capable of producing high power (Fig. 4.3b). However, at intermediate values of K_r, synchronous and asynchronous dynamics are both present, and high-power oscillations only occur along a "bridge" where the synchronous and asynchronous dynamics do not interfere (Fig. 4.3c). Thus, transitions in insect flight actuation modes are possible across this parameter space, but cannot occur when the muscle parameters have diverged off of this bridge.

For the hawkmoth parameters, the origin of the bridge occurs at $t_0/T_n \approx 0.2$ along the $K_r = 0$ axis, which is the location in parameter space where the asynchronous emergent frequency and the synchronous frequency exactly match (see Extended Data Figure D.7). As the synchronous forcing becomes stronger relative to the asynchronous dynamics, we see that the region near $t_0/T_n \approx 0.2$ becomes entrained to the synchronous frequency [148]. Entrainment is the process where a self-excited oscillating system is forced to oscillate exactly at the frequency of an external driving frequency (a phenomenon called an Arnold tongue [148]). As we move away from the bridge along the t_0/T_n axis, there is a bifurcation and the the asynchronous and synchronous frequencies diverge, ending the entrainment, and leading to emergent asynchronous oscillations (Figure 4.5). Crossing between these two regimes leads to significant interference between these oscillatory modes, thus leading to lower power, less smooth flapping trajectories that are unsuitable for flight (see Supplemental Figure D.8 & D.5). The gray lines in Fig. 4.3 illustrate the boundary between the synchronous and asynchronous dynamics. Thus, while complex aerodynamics phenomena[149] and sensory-motor feedback systems[150] can exhibit unpredictable flapping wing behavior, our results indicate that even simplified fluid and body mechanics under combined synchronous and asynchronous actuation are sufficient to lead to erratic wingbeat dynamics.

Matching muscular and mechanical timescales is evidently a critical requirement for both synchronous and asynchronous power production. However, variation in the strength

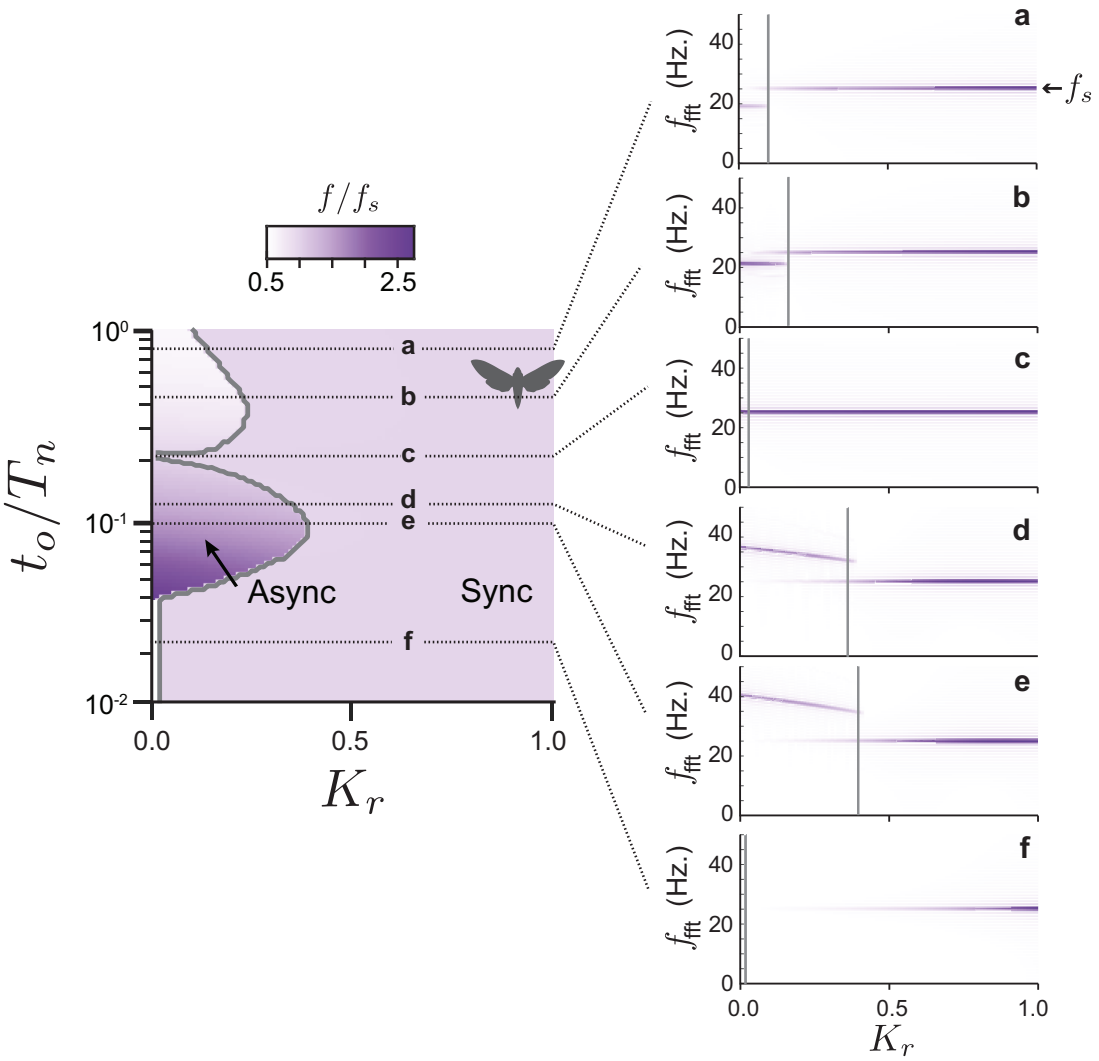

Figure 4.5. Emergent frequency and Fourier transform of wingbeats versus K_r in simulation. Left plot shows the normalized emergent frequency (f/f_s) from Fig. 4.3a using a continuous colormap. Six horizontal lines correspond to values of t_0/T_n where we examined the Fourier transform of the emergent wingbeats. The six plots in the right column show heatmaps of the Fourier transform of wingbeat at each value of K_r. As t_0 decreases (from top to bottom), the emergent asynchronous frequency varies, and we see mixing of asynchronous and synchronous dynamics near the boundary between async and sync regions (shown in gray). The bridge between synchronous and asynchronous regimes occurs when the emergent async frequency is exactly equal to the synchronous driving frequency (Plot **c** in right column).

of the delayed stretch activation response (changing K_r), its timescale (t_0), or the resonant mechanics of the thorax and wings (T_n) could enable smooth, gradual transitions across the bridge, especially over evolutionary timescales. Biologically these parameters will be closely tied

to the molecular components of the delayed stretch activation, such as the crossbridging binding, calcium responsiveness, and troponin isoforms mentioned earlier. Evolutionary transitions need not necessarily be smooth, however our model and analysis reveals the existence of a pathway for gradual transitions between a fully synchronous and asynchronous regime even while maintaining high-power wing strokes. This bridge may have facilitated the many subsequent shifts between asynchrony and synchrony (Fig. 4.1c). However clades like Lepidoptera, which appear uniformly synchronous, may have subsequently specialized away from the bridge, reflected by *M. sexta's* location in the model simulation.

4.6 Robotic results

4.6.1 A robophysical model achieves both flapping regimes

To test the hypothesis that insects can realize both synchronous and asynchronous oscillations simply by changing a ratio of timescales and an interpolation factor, we built a dynamically scaled robophysical spring-wing system, the roboflapper (Fig. 4.3d, Supplemental Figures 4.4 & D.4). Unlike previous robophysical investigations of flapping wing flight [38], [39], we did not directly prescribe wing angle versus time in our roboflapper. Instead, we provided torque commands to a motor that were either feedforward periodic (e.g. synchronous sinusoidal forcing), or velocity feedback generated (e.g. real-time delayed stretch activation dynamics model) and the wing angle versus time was an emergent property (see Methods). To mimic aerodynamic damping and the body elasticity of indirect actuation the motor was in parallel with a silicone molded torsional spring driving a dynamically scaled wing[106].

High-power synchronous and asynchronous regimes emerge in a single dynamically scaled robophysical system as in the hawkmoth simulations (Fig. 4.3e,f and Movie S1). As in simulation, these regions are connected by a narrow bridge that enables high-power transitions between the two regimes where the synchronous frequency matches the asynchronous frequency. Unlike the simulation, the fully asynchronous roboflapper $K_r = 0$ does not oscillate when t_0/T_n

exceeds ≈ 0.3, likely due to friction and viscous damping (see Supplementary Information IID) that are present in the experiment and not the simulation (Fig. 4.3f).

4.6.2 A robophysical model can transition from synchronous to asynchronous regimes in real time

Having shown that the robotic system produced similar flapping behavior as the simulation, we wanted to see if the system could transition smoothly between synchronous and asynchronous modes as K_r varies in real time. We hypothesize that insects may have similarly transitioned over evolutionary timescales, and that effective flapping can only occur when stretch-activation and synchronous rates are matched.

To illustrate this, we chose stretch activation feedback parameters that produced $f_a =$ 3.2Hz and $\sim$100 deg peak-to-peak flapping. We also defined a sinusoidal forcing $F_{sync} = F_s \sin(2\pi f_s t)$ that produces the same amplitude when $f_s = f_a$. The roboflapper was started in a fully asynchronous state ($K_r = 0$) for 3 seconds, transitioned to fully synchronous ($K_r = 1$) over 3 seconds, held again, and transitioned back and forth several times. The same process was repeated for four ratios of f_s to f_a: $f_s/f_a = [0.5, 1.0, 1.1, 1.5]$ The results of the experiments, shown in Fig. 4.6, show that transitions across the parameter space are robust and reversible, but only smooth when on the dynamical bridge.

4.6.3 A synchronous insect-scale robot can smoothly transition to asynchrony

The robophysical model tested our dynamics framework over a wide range of parameters in a real system. We next test whether these dynamics could produce both synchronous and asynchronous oscillations at the scale of an insect. Demonstrating synchronous to asynchronous transitions at the centimeter scale is important because unsteady aerodynamics do not necessarily scale as quasi-steady phenomena and mechanical systems at small scales can have unexpected emergent behavior [151]. Moreover, state-of-the-art insect-scale robots currently utilize a time-periodic voltage input to excite a piezoelectric actuator at the resonance frequency of the

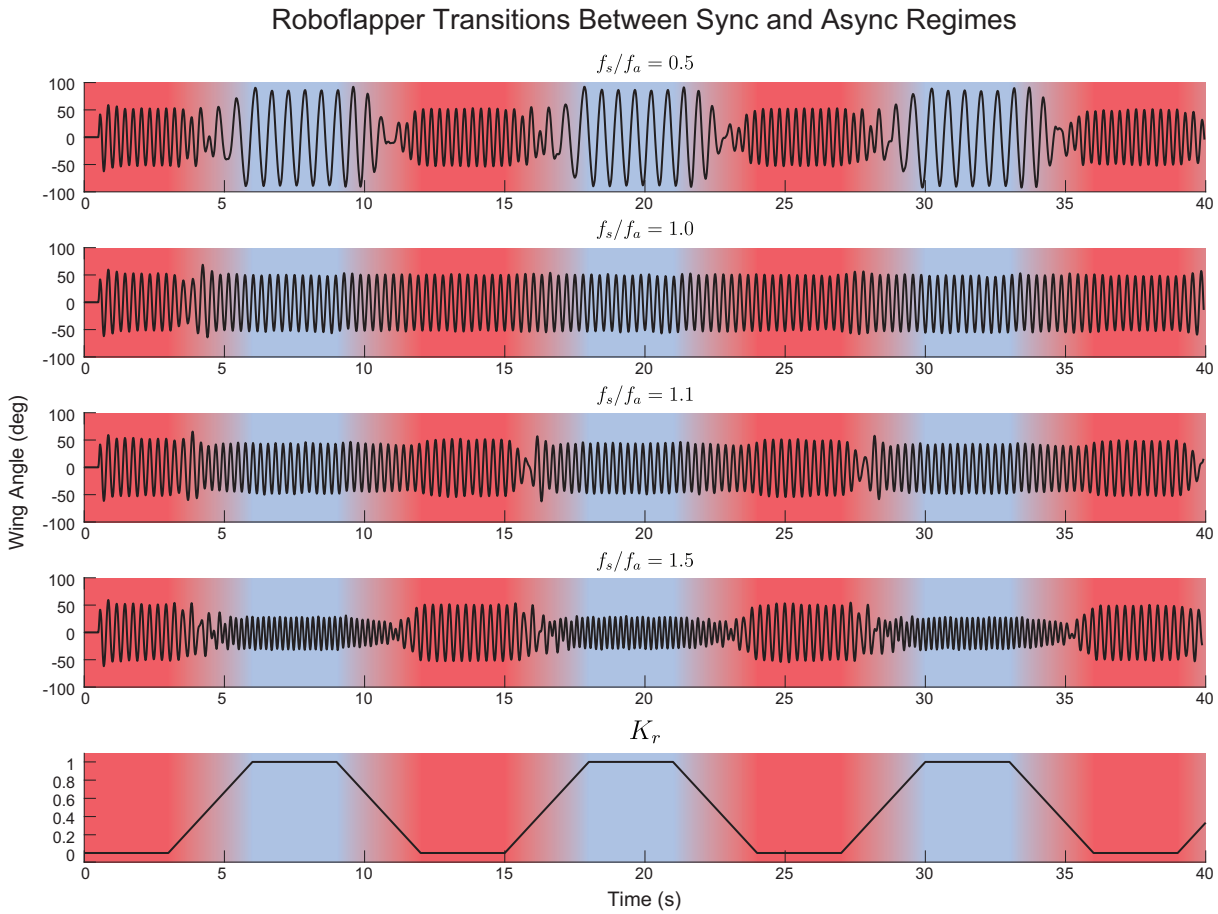

Figure 4.6. Reversible transitions across the synch-asynch bridge. Smooth transitions occur only when the synchronous and emergent asynchronous frequencies are matched. In all other cases, including when the frequencies are nearly matched but not quite, we see interference as the dynamics transition from one mode and frequency to another. There are also signs of phase entrainment when the system goes from asynch to synch along the bridge (second plot, 3-5 sec).

mechanical system (i.e. the Harvard "robobee" [13], [152]). The robobee can achieve untethered flight, but only if there is a sufficient power source [15]. It uses wingbeat frequencies ($\approx$ 50-170 Hz)[13], [22] comparable to many asynchronous insects [73], yet relies on time-periodic actuation. This prompted us to explore whether a similar platform can generate self-excited oscillations with the addition of delayed stretch activation (Fig. 4.3g).

To generate delayed stretch activation in the robobee, we used a fiber-optic displacement sensor to estimate wing velocity. The instantaneous wing velocity was supplied to a real-time delayed stretch activation dynamics model (the same as for the robophysical system with

parameters adapted for the robobee) and the output of this model was converted to a voltage that was amplified and supplied to the piezoelectric actuator. Thus, we were able to establish a real-time feedback loop between wing velocity and actuator voltage that could generate asynchronous wingbeats of the robobee. By combining the outputs of feedforward synchronous actuation, and delayed stretch activation (Eq. 4.1) in real-time experiments we were able to demonstrate transitions between synchronous and asynchronous oscillations in this robot. We found that we could generate stable oscillations in both the fully asynchronous and fully synchronous modes (Fig. 4.3g,h, Fig. D.6, and Movies S2 and S3).

Having shown that we can generate asynchronous flapping in an insect-scale robot, we wanted to see if the same system could transition smoothly between synchronous and asynchronous modes as K_r varies as shown in the dynamically-scaled roboflapper experiment above. The synchronous forcing frequency, f_s, was set to either: 1) match the emergent oscillation frequency of the fully asynchronous system with $r_3 = 225, r_4 = 135$, 67 Hz, (Movie S2), or 2) not match the asynchronous system, i.e. $f_s = 20$ Hz (Movie S3). Additional experiments at other frequencies were also performed, as can be seen in Supplemental Fig. D.6 We started by setting $K_r = 1$ (fully synchronous) and allowing the system to reach a stable amplitude. Then, we changed K_r linearly from 1 to 0 over two seconds in the Simulink real-time control system. When $f_s = f_a$, there is no appreciable change in amplitude, and high-power oscillations are maintained across the full range of K_r (Fig. 4.3h). However, when $f_s \neq f_a$, interference causes the amplitude to decrease as the asynchronous and synchronous dynamics interfere (Fig. 4.3i). Eventually, oscillations develop in the fully asynchronous system, but only after interference from synchronous dynamics is no longer present.

4.7 Discussion

By capturing one of the key evolutionary innovations that enabled high frequency insect flight, this framework may unlock the potential for robotic systems to benefit from both

asynchronous and synchronous actuation modes. For insects, asynchronous muscle enabled the decoupling between muscle contractions and neural input that enables wingbeat frequencies to exceed the limits of neural firing frequency [4], [5], [75], [153]. An asynchronous flapping-wing robot may benefit from this decoupling of power and control. Moreover, the ability to transition between synchronous and asynchronous modes suggests opportunities for even more versatile control.

4.7.1 Shared dynamics and transitions in insect flight modes

Through introduction of a dynamical model for delayed stretch activation we have revealed new insights into asynchronous wingbeat generation in insect flight. When combined with synchronous actuation, this unified spring-wing framework recapitulates the transition between synchronous and asynchronous regimes. Furthermore, both types of actuation can coexist even when a dominant wingbeat strategy emerges. Overall, broader physiological testing of delayed stretch activation, especially in other synchronous species and those close to the bridge, may further resolve the nuances in these two modes of insect flight. Mapping specific parameters of stretch-activation myosin recruitment, delayed stretch activation time constants, troponin isoform ratios, and calcium activation would connect the potential molecular basis of asynchronous and synchronous flight to the model parameter space across more species. This framework also provides a starting point for the examination of how more complex models of body dynamics, muscle force production, and aerodynamics contribute to the emergent wingstroke oscillations of flapping wing insects.

The coupling of indirectly actuated wings to an elastic thorax (spring-wing mechanics), with both periodic neural activation and delayed stretch activation enables multiple solutions to the challenges of high-power, periodic wingstrokes. Given that the capacity for asynchronous flight was gained and then preserved even in secondarily synchronous descendants (Fig. 4.1d, 4.2c), transitions between the two flight modes are not necessarily caused by a switch in morphology or physiology. However, asynchronous and synchronous flight muscle do have

different ultrastructure and can show molecular adaptations to each mode of flight [75], [128], [141], [153]–[155]. Still, their physiological properties (embodied in our model by K_r and t_0/T_n) can manifest on a continuum. This may explain the multiple evolutionary transitions between asynchrony and synchrony within insects. It is likely that highly-specialized fliers, like many dipterans and hymenopterans, have further specializations to enhance asynchronous flight [136], [141], [142], [156], [157], but these do not preclude a common underlying physiological mechanism for delayed stretch activation which can vary in magnitude and timing. Supporting this, we see multiple asynchronous-synchronous transitions in the earlier diverging orders like Hemiptera (Fig. 4.1c). This also suggests that hemipterans and other orders with multiple transitions may have muscle physiological parameters closer to the bridge in parameter space, thereby enabling more frequent transitions.

The evolutionary history of insects has shown a great deal of diversification in flight strategies. Central to these patterns are the transitions between synchronous and asynchronous modes. Taken together, our evolutionary reconstructions, muscle physiology results, dynamics simulations, and robotic models show that the capacity for both synchronous and asynchronous flight can exist in the same system. Moreover, we demonstrate that when synchronous and asynchronous actuation modes act harmoniously there can be an evolutionary pathway (a bridge) between asynchronous to synchronous regimes that enables smooth, high-power wingbeats across these two extremes.

Acknowledgements

Chapter 4, in full, has been accepted for publication to appear in Nature as *Gau J, Lynch J, Aiello B, Wold ES, Gravish N, Sponberg S. Biophysical transitions in insect flight dynamics are bridged by common muscle physiology, 2023*. The dissertation author contributed equally with Gau and Aiello, and is co-first author of the paper.

Appendix A

Supplementary to Chapter 1

A.1 Computing added mass inertia

The standard method for computing added mass is to treat the added mass as a cylindrical volume of fluid that surrounds the wing [95]. The dimensions of the cylinder are defined by the dimensions of the wing: the radius is half the mean chord length, $\bar{c}/2$, the length is single wing span R measured from wing hinge to wing tip, and the density is the fluid density ρ. The added rotational inertia is thus the rotational inertia of a cylinder of mass m_A that rotates about its base:

$$m_A = \rho \frac{\pi}{4} R \bar{c}^2$$
$$I_A = \frac{1}{16} m_A \bar{c}^2 + \frac{1}{3} m_A R^2$$

In our system, with $\bar{c} = 3.5$ cm, $R = 10$ cm, $\rho_{H_2O} = 977\ \frac{kg}{m^3}$, added mass inerita $I_A = 3.465 \times 10^{-4}\ kg\ m^2$.

A.2 Structural damping modeling

Structural damping for generic oscillatory motion can be represented as an additional complex term in the spring stiffness parameter:

$$K = k(1 + i\gamma) \tag{A.1}$$

However, this representation is not convenient for numerical modeling because of the complex term. If we assume that the oscillatory motion is sinusoidal, it is possible to express structural damping another way. Beginning with a generic spring-wing equation

$$I_t\ddot{x} + k(1+i\gamma)x + \Gamma\dot{x}^2 = 0$$

we make the substitutions $x = Xe^{i\omega t}$ and $\dot{x} = i\omega Xe^{i\omega t}$:

$$I_t\ddot{x} + kXe^{i\omega t} + \gamma kiXe^{i\omega t} + \Gamma\dot{x}^2 = 0$$

Using the definition $\frac{\dot{x}}{\omega} = iXe^{i\omega t}$, we can rearrange:

$$I_t\ddot{x} + kx + \frac{\gamma k}{\omega}\dot{x} + \Gamma\dot{x}^2 = 0 \tag{A.2}$$

Thus, the structural damping term can be represented as a viscous damper that is normalized by the oscillation frequency, implying frequency-independent viscous damping.

A.3 Derivation of the non-dimensional spring-wing equations

We introduce dimensionless time and angle parameters normalized to wing oscillation amplitude and frequency:

$$\tau = \omega t,\ q_w = \frac{\theta}{\theta_0},\ \dot{q}_w = \frac{\dot{\theta}}{\omega\theta_0},\ \ddot{q}_w = \frac{\ddot{\theta}}{\omega^2\theta_0}$$

Plugging these terms into Eq. 1.7 and rearranging coefficients, we obtain

$$I_t\theta_0\omega^2\ddot{q}_w + k_p\theta_0 q_w + \frac{\gamma k_p}{\omega}\omega\theta_0 q_w + \Gamma\theta_0^2\omega^2|\dot{q}_w|\dot{q}_w = T_p(t)$$

$$\ddot{q}_w + \frac{k_p}{I_t\omega^2}q_w + \frac{\gamma k_p}{I_t\omega^2}\dot{q}_w + \frac{\Gamma\theta_0}{I_t}|\dot{q}_w|\dot{q}_w = \frac{T_p(t)}{I_t\theta_0\omega^2}$$

$$\ddot{q}_w + \hat{K}_p q_w + \gamma\hat{K}_p\dot{q}_w + \frac{1}{N}|\dot{q}_w|\dot{q}_w = \hat{T}_p(t) \tag{A.3}$$

Eq. A.3 is a forced nonlinear oscillator defined by non-dimensional parameters $\hat{K}$, the reduced stiffness; γ, the structural damping loss modulus; and N, the Weis-Fogh number.

Performing a similar substitution for the series system we arrive at the equation

$$\ddot{q}_w + \hat{K}_s q_w + \gamma\hat{K}_s\dot{q}_w + \frac{1}{N}|\dot{q}_w|\dot{q}_w = \hat{T}_s(t) \tag{A.4}$$

which is identical to Eq. A.3 except for the normalized torque, which is now defined as

$$\hat{T}_s(t) = \frac{\hat{K}_s}{\theta_0}\left(\phi(t) + \frac{\gamma}{\omega}\dot{\phi}\right) \tag{A.5}$$

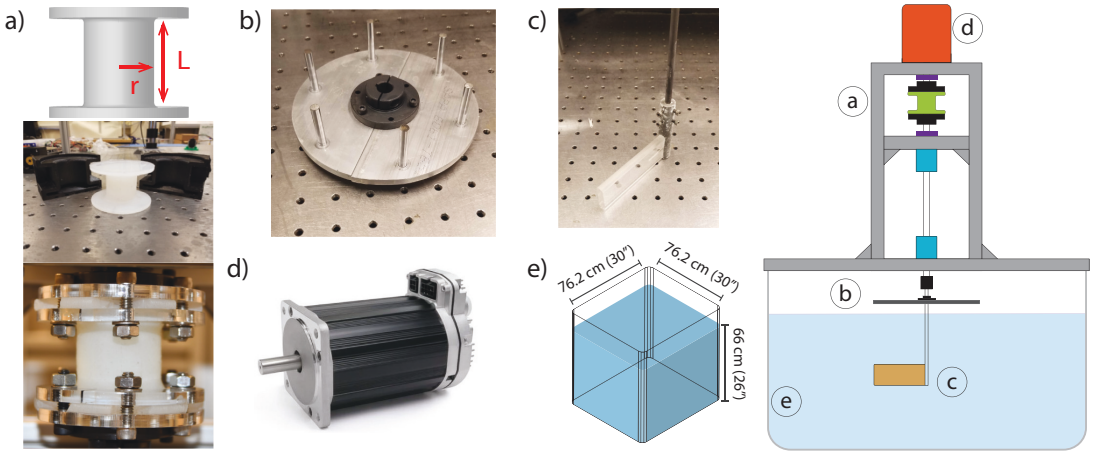

Figure A.1. Robophysical system component detail. A diagram of the system is shown at the right, with labels for each of the components. a) the design process of the silicone torsion spring, from 3D CAD model based on desired dimensions to 3D-printed mold for silicone to completed spring with acrylic adapter plates and steel flange couplers. b) An aluminum inertia plate used to change the overall system inertia. c) The fixed-pitch acrylic wing with aluminum hub and 1/4" steel shaft. d) Teknic Clearpath SDSK Motor used to drive the system (photo from Teknic). e) Dimensions of the 115-gallon rectangular tank (Chem-Tainer) as well as water depth.

A.4 Robophysical system details

In Figure A.1 we show the elements of the robophysical system. The left column of Fig. A.1 shows the design process of the silicone torsion spring, from 3D CAD model based on desired dimensions (top-left) to 3D-printed mold for silicone (mid-left) to completed spring with acrylic adapter plates and steel flange couplers (bottom-left). In Fig. A.1b we show the aluminum inertia plate that was used to change the overall system inertia. Fig. A.1c shows the fixed-pitch acrylic wing with aluminum hub and 1/4" steel shaft. We used a Teknic Clearpath SDSK Motor used to drive the system (A.1d). The dimensions of the 115-gallon rectangular tank as well as water depth are shown in Fig. A.1e.

A.4.1 Computing drag torque coefficient

We follow the standard methods for blade-element analysis of quasi-steady flapping wings. The wing is broken into differential chord elements, each of which experiences a

differential aerodynamic torque,

$$\mathrm{d}Q_{aero} = \frac{1}{2} r\rho \left(r\dot{\theta}\right)^2 C_D(\alpha) c(r) \mathrm{d}r \tag{A.6}$$

The differential torques along the wing can be integrated across the entire wing shape resulting in the following equations

For simplicity we express the velocity dependence of the aerodynamic torque as, $\dot{\theta}^2$, and the sign dependence on the direction of motion is implied. The aerodynamic torque is governed by both the wing speed and the aerodynamic torque constant, Γ, which itself is a function of wing geometry (wing radial length, R and shape factor r_3), wing pitch angle (α), and fluid density (ρ). The drag coefficient, $C_D(\alpha)$, is dependent on the pitch angle of the wing, α, which is 0 when the wing is vertical, and $\pi/2$ when the wing is horizontal. The drag coefficient we use was measured at Reynolds numbers relevant to flies ($Re = 200$) via a robophysical flapping wing by Dickinson and colleagues [39]:

$$C_D(\alpha) = 1.92 - 1.55\cos(2.04\alpha - 9.82) \tag{A.7}$$

Since our wing is always vertical ($\alpha = 0$), we use $C_D(0) = 3.35$.

A.4.2 Design and fabrication of silicone springs

We designed and 3D-printed two-piece molds for casting the springs. Each mold was treated with Ease Release 200^{TM} (Smooth On) before being filled with a common silicone material used in soft-robotics, Dragonskin^{TM} 30A silicone (Smooth-On) **Marechal2020-op**. Care was taken to de-gas the silicone in a vacuum chamber before filling the mold. The silicone molds were allowed to cure in a positive pressure chamber for at least 24 hours before removal and use.

The dimensions of the springs were determined by the desired spring stiffness. The

torsional stiffness of a silicone spring is given by the stiffness equation for a twisting cylinder:

$$k_s = \frac{\mu \pi R^4}{2L} \tag{A.8}$$

where μ is the shear modulus, R is the spring radius, and L is the spring length. We used three spring designs of constant length and radius 13, 16, 18 mm corresponding to torsional stiffness values of k_s = [0.163, 0.416,0.632] Nm/rad.

A.4.3 Data Processing

Analysis of both experiment and simulation data relied on the wing and motor angle data. To generate a consistent sampling time of all experiments we interpolated position measurements to a constant sample rate. The measured angle data was filtered with a 5th-order Butterworth filter at cutoff frequency of 10Hz (approximately 2.5 times greater than the peak driving frequency). Velocity was computed through numerical differentiation of the filtered position, and similarly acceleration from the filtered velocity.

We observed that the wing trajectories were consistent with a single frequency sine wave except when actuation frequency or amplitude approached the epxerimental limits (at low-amplitude and high-frequency and at high-amplitude). We used a nonlinear least-squares sine fit to find amplitude and phase of the motor, $\phi(t)$, and wing, $\theta(t)$, trajectories respectively.

A.5 Derivation of non-dimensional resonance frequency for series system

The following derivation is based on the process in **bennett˙elastic˙1987**. For a system with a spring with stiffness k in series with an actuator that drives a mass m subject to aerodynamic loading, $\Gamma \dot{x}^2$, the power driving the mass, P_w is the sum of the aerodynamic and inertial forces times the velocity:

$$P_m = (F_a + F_i)\dot{x} = (\Gamma \dot{x}^2 + m\ddot{x})\dot{x} \tag{A.9}$$

The strain energy in the spring, E, is

$$E = \frac{1}{2}k^{-1}(F_a + F_i) = \frac{1}{2}k^{-1}\left(\Gamma\dot{x}^2 + m\ddot{x}\right)^2 \tag{A.10}$$

Since the motor must both move the mass and compress the spring, the actuator power, P_{act}, is defined

$$\begin{aligned} P_{act} &= P_m + \dot{E} \\ P_{act} &= \left(\Gamma\dot{x}^2 + m\ddot{x}\right)\left[\dot{x} + k^{-1}\left(2\Gamma\dot{x}\ddot{x} + m\dddot{x}\right)\right] \end{aligned} \tag{A.11}$$

If we assume that the mass follows a sinusoidal trajectory, $x(t) = x_0 \sin\omega t$, we can compute the derivatives and plug into A.11:

$$P_{act} = x_0^2\omega^3 \cos\omega t\left[\Gamma x_0 \cos^2\omega t - m\sin\omega t\right]\left[1 - k^{-1}\omega^2(2\Gamma x_0 \sin\omega t + m)\right] \tag{A.12}$$

If we define a non-dimensional actuator power, $\hat{P}_{act} = \frac{P_{act}}{mx_0^2\omega^3}$, we can get the non-dimensional expression:

$$\hat{P}_{act} = \cos\omega t\left(N^{-1}\cos^2\omega t - \sin\omega t\right)\left[1 - \hat{K}^{-1}(2N^{-1}\sin\omega t + 1)\right] \tag{A.13}$$

Bennett et al. showed that this actuator power expression is minimized when it is always greater than zero over half an oscillation period. The relationship between $\hat{K}$ and N that guarantees that condition is

$$\hat{K} = \sqrt{1 + 4N^{-2}} \tag{A.14}$$

Eq. A.14 describes the of spring, mass, aerodynamic damping and oscillation amplitude to get

resonant oscillation at a particular frequency. Recalling that $\hat{K} = \frac{k}{m\omega^2}$, $N = \frac{m}{\Gamma x_0}$, and natural frequency $\omega_n^2 = \frac{k}{m}$ we can get an expression for that frequency:

$$\omega_r^2 = \frac{k}{\sqrt{m^2 + 4\Gamma^2 x_0^2}} = \frac{\omega_n^2}{\sqrt{1 + 4N^{-2}}} \tag{A.15}$$

A.6 Derivation of non-dimensional wing torques in the parallel system

Here we provide the full derivation for the non-dimensional work presented in Eq. 1.27 and 1.28. We start from the non-dimensional force terms in the parallel system dynamics (Eqn. 1.8). We make the assumption of sinusoidal wing motion, such that

$$\begin{aligned} q &= \sin(\tau) \\ \dot{q} &= \cos(\tau) \\ \ddot{q} &= -\sin(\tau) \\ &= -q \end{aligned}$$

Substituting these expressions in for the individual force terms in the parallel system and multiplying by the aerodynamic force in those equations results in

$$\begin{aligned} \tilde{Q}_{aero} &= \cos^2(\tau) \\ \tilde{Q}_{inertial} &= -Nq \\ \tilde{Q}_{idealelastic} &= \hat{K}Nq \\ \tilde{Q}_{structural} &= \gamma\hat{K}N\cos(\tau) \end{aligned}$$

In order to write $\tilde{Q}_{aero}$ and $\tilde{Q}_{structural}$ in terms of wing angle we can use the following trigonometric relationship

$$\begin{aligned}\cos^2(\tau) &= 1-\sin^2(\tau)\\ &= 1-q^2 \qquad \text{(A.16)}\\ \cos(\tau) &= \sqrt{1-q^2} \qquad \text{(A.17)}\end{aligned}$$

Substituting in the expressions of $\cos(\tau)$ and $\cos^2(\tau)$ yields the non-dimensional work equations in terms of just the normalized wing angle, q.

A.7 Derivation of non-dimensional wing torque due to viscous damping

We can use the same method as in the above section to show that the relationship between the Weis-Fogh number N and the dynamic efficiency holds true even if we change the damping model. If we choose a viscous damping model where torque is proportional to velocity, $\tau_{viscous} = c_v\dot{\theta}$, we can get the non-dimensional torque term as in Eq. 1.8:

$$\hat{\tau}_{viscous} = \frac{c_v\theta_o\omega}{I\theta_o\omega^2}\dot{q} = 2\zeta\sqrt{\hat{K}}\dot{q} \qquad \text{(A.18)}$$

where we have used the standard definition of the harmonic-oscillator damping ratio, $\zeta = \frac{c_v}{2I\omega_n}$. The damping ratio must be less than one for resonance to be possible. Multiplying by the maximum aerodynamic force, we arruve at the non-dimensional torque

$$\tilde{Q}_{viscous} = 2\zeta N\sqrt{\hat{K}}\cos(\tau) = 2\zeta N\sqrt{\hat{K}(1-q^2)} \qquad \text{(A.19)}$$

which scales linearly with N, the same as the structural damping torque. Therefore, viscous damping leads to a dynamic efficiency that monotonically decreases with the Weis-Fogh number resulting in the same qualitative result as with structural damping.

Appendix B

Supplementary to Chapter 2

B.1 Rise time with error bars

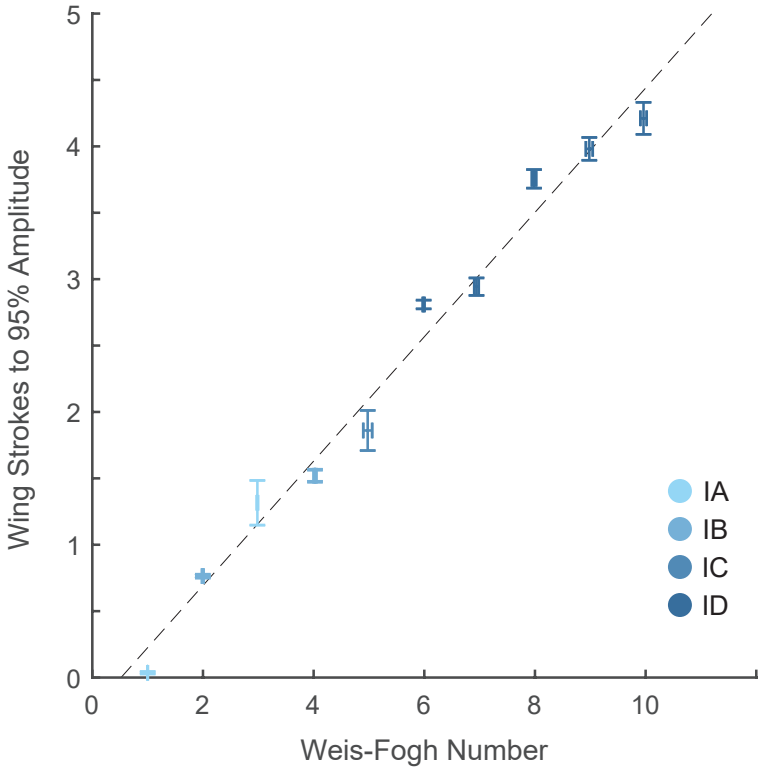

Figure B.1. Mean time to full amplitude versus N, with error bars showing standard deviations

B.2 Computing N for *Paratuposa placentis*

When the maximum aerodynamic and inertial torques are not available to compute the Weis-Fogh number, it is also possible to approximate using the aerodynamic and inertial power. Note, this approximation assumes sinusoidal wingstrokes, which is far from guaranteed; however, this gives a first-order approximation that can be improved through deeper analysis

Given a sinusoidal wing trajectory $\phi = \phi_o \sin(\omega t)$, the inertial and aerodynamic torques on the wing, according to 2.2, are

$$T_i = I\ddot{\phi} = -I\phi_o\omega^2 \sin(\omega t) \tag{B.1}$$

$$T_a = \Gamma|\dot{\phi}|\dot{\phi} = \Gamma|\phi_o^2\omega^2|\cos(\omega t)|\cos(\omega t) \tag{B.2}$$

The respective inertia and aerodynamic powers are therefore

$$P_i = T_i\dot{\phi} \quad = (-I\phi_o\omega^2\sin(\omega t))\phi_o\omega\cos(\omega t) = -0.5I\phi_o^2\omega^3\sin(2\omega t) \tag{B.3}$$

$$\begin{aligned} P_a = T_a\dot{\phi} \qquad &= [\Gamma\phi_o^2\omega^2|\cos(\omega t)|\cos(\omega t)]\phi_o\omega\cos(\omega t) \\ &= \Gamma\phi_o^3\omega^3|\cos(\omega t)|\cos^2(\omega t) \end{aligned} \tag{B.4}$$

The maximum magnitudes are $|P_i|_{max} = 0.5I\phi_o^2\omega^3$ and $|P_a|_{max} = \Gamma\phi_o^3\omega^3$. Therefore,

$$\frac{|P_i|_{max}}{|P_a|_{max}} = \frac{I}{2\Gamma\phi_o} = \frac{N}{2} \tag{B.5}$$

and

$$N = 2 \times \frac{|P_i|_{max}}{|P_a|_{max}} \tag{B.6}$$

Based on this relationship, we can inspect figure 3e from [2] and see that there is a maximum (mass specific) aerodynamic power of $\sim$110 W kg^{-1} and inertial power of $\sim$7.8 W kg^{-1}. Thus $N \approx 0.14$. We were able to place it on the chart in Fig. 2.7 using the fact that the body mass is 2.43 ± 0.19 μg[2].

The same method is used to compute N for the insect parameters reported in [158]

Appendix C

Supplementary to Chapter 3

C.1 Molloy 1987 Curve Fits

Molloy and colleagues studied the asynchronous flight muscle of four species of flying insect [73]. They fit Eq. 3.2 to stretch-hold experiments and showed that the rate of tension increase, r_3, was linearly related to wingbeat frequency across species. However, they did not report the rest of their fitting parameters or many other details of the fit routine, so we do not know what those parameters might have been. In order to be confident that we're using relevant parameters for our asynchronous spring-wing modeling, it would be helpful to know how *all* of the fit parameters vary across insects.

C.1.1 Digitizing data

WebPlotDigitizer (Rohatgi, https://automeris.io/WebPlotDigitizer/) was used to extract the data from the figure shown in Fig. 3.2c and import it to MATLAB (Mathworks, R2022a). The digitized data is shown in Fig. C.1. In order to improve fitting performance, especially for the high-speed of the fruitfly dynamics, data was interpolated and some non-unique datapoints were removed prior to fitting.

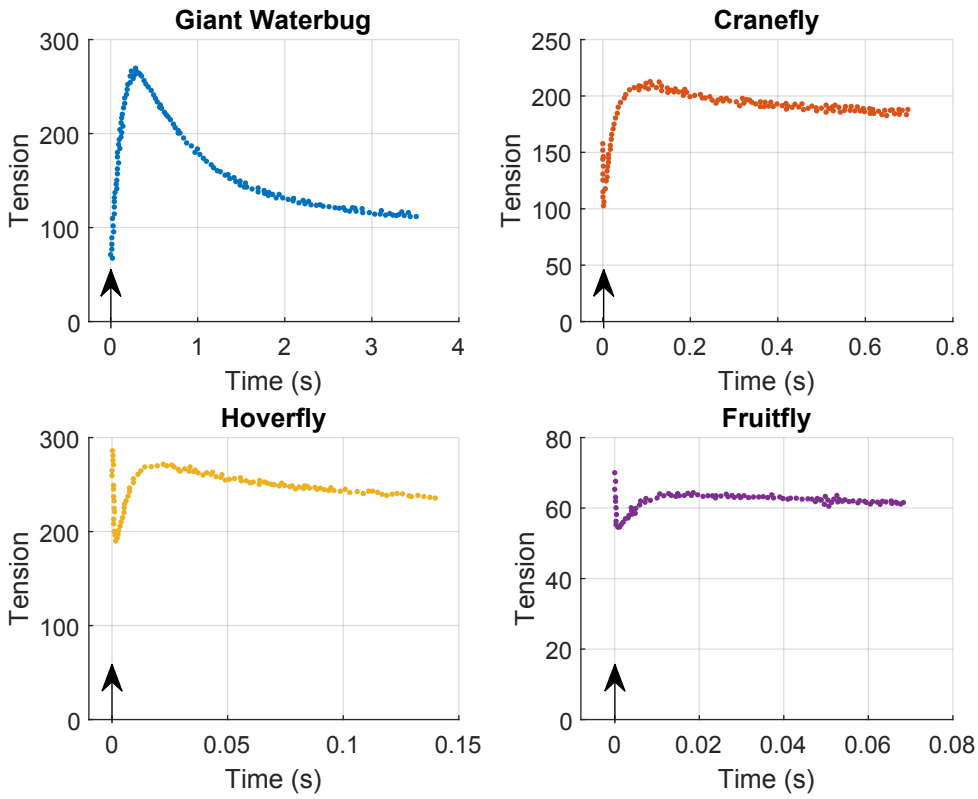

Figure C.1. Digitized data from [73] showing the stretch-hold response of Giant Waterbug, Cranefly, Hoverfly, and Fruitfly data, respectively.

C.1.2 Curve Fitting

All fitting was done using the Curve Fitter tool in MATLAB R2022a. MATLAB scripts and data are available upon request.

Procedure

Data for each insect was loaded into the tool, and a custom fit function was defined,

$$F_t = K_2 e^{-r_2 t} + K_3(1 - e^{-r_3 t}) + K_4 e^{-r_4 t} + c \tag{C.1}$$

In the case of the giant waterbug, the resolution of the sensor was insufficient to capture the phase 2 dynamics, and therefore the fit function is defined with $K_2 = 0$. Bounds were set such that all parameters are greater than zero, c is less than the value of the last datapoint (since the offset sets

the asymptote of the curve), and $\kappa < 0.5$. The fit is extremely sensitive to local minima due to nonlinearities, so care was taken to choose informed initial conditions which were iteratively improved over multiple fits. The tool performed a nonlinear least squares optimization with tolerances set to 10^{-6} and a maximum of 10,000 iterations. The resulting fits all had R^2 values greated than 0.94.

Results

The curves fit well to the data, plotted in Figure C.2 (GF: $R^2 = 0.998$, RMSE = 2.4;CF: $R^2 = 0.964$, RMSE = 4.8; HF: $R^2 = 0.948$, RMSE = 4.6; FF: $R^2 = 0.993$, RMSE = 0.26). The individual parameters and their 95% confidence intervals as reported by the curve fitting tool are plotted in C.3. The black dots are the fit values, and the vertical lines span the 95% CI; thus, longer lines indicate less certainty. In many cases, the confidence interval is hidden by the black dot. The insects are ordered in the same way that they were ordered by Molloy, which also corresponds to decreasing size and increasing wingbeat frequency. The terms λ and κ are defined as ratios of r_2 to r_3 and r_4 to r_3, respectively.

The data are fairly messy, especially in the variability of gain terms K_n and in the ratios λ - more data would be needed to identify any trends. However, we can observe that phase 2 dynamics are typically much faster (10 or more times faster) than phase 3 ($\lambda > 1$). Additionally, phase 4 is much slower than phase 3 ($\kappa < 0.2$), and it seems that in smaller, higher-wbf insects, the ratio decreases progressively. In the fruitfly case, it is so slow that the fit routine struggled to get a confident result for the passive stiffness c because the experiment ended before there could be substantial decay after the tension case. Meanwhile, there appears to be a trend where passive stiffness and r_3 both increase with smaller size and/or higher wingbeat frequency. The r_3 result is reported by the Molloy and colleagues in the paper, and the increased muscle stiffness in fruitflies and others has been noted by other researchers [4], [5], [159].

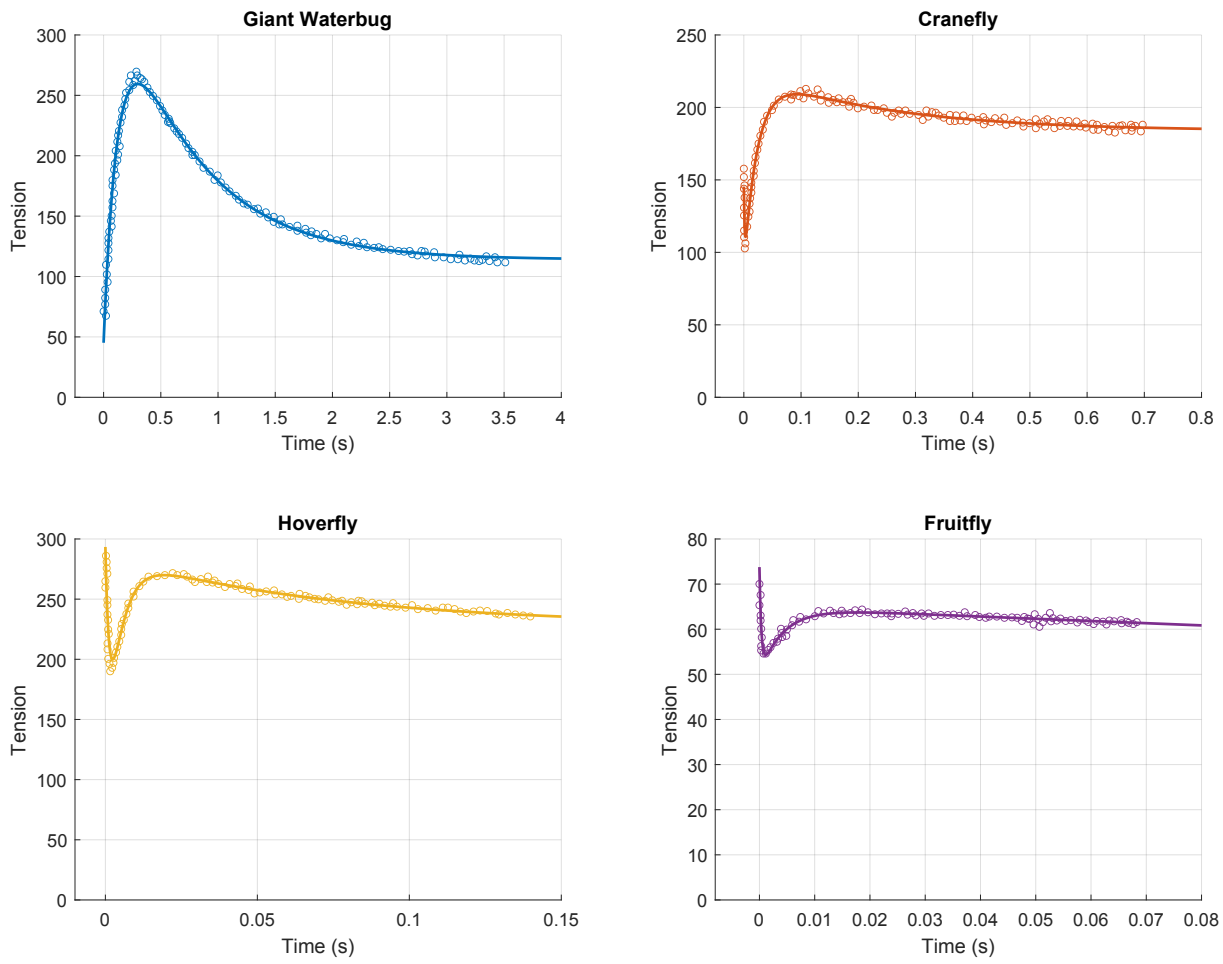

Figure C.2. Raw data and curve fits for the giant waterbug, cranefly, hoverfly, and fruitfly from Molloy. [73]

C.1.3 Conclusions

The results presented here are not sufficient to make general claims about asynchronous muscles across species, but for our purposes, it is a starting point. More, and cleaner, data is necessary, as well as considerations of many fine details of the experimental setup. However, three facts will be helpful in choosing logical parameters during simulations and other analysis:

1. Phase 2 is $\sim$10x faster than phase 3, which is 5-50x faster than phase 4

2. Phase 3 rate, r_3, increases with flapping frequency

3. Gains K_2, K_3, and K_4 are the same order of magnitude

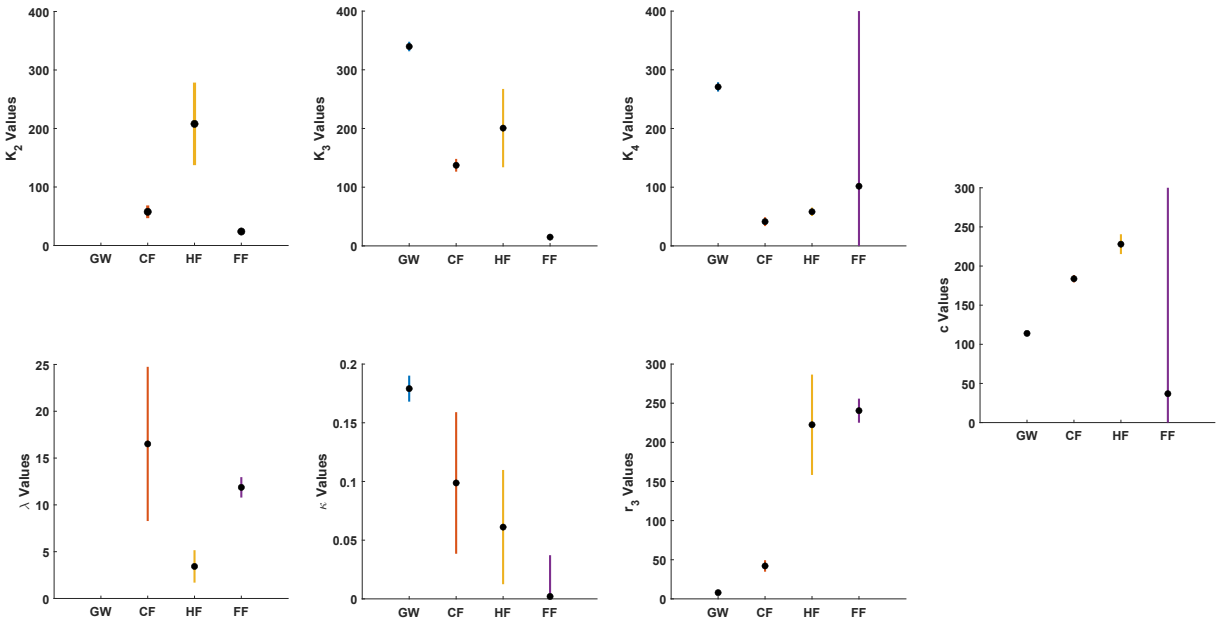

Figure C.3. dSA Fit Parameters for the four insects. Fit parameter with bars showing the 95% CI for each

C.2 Physical interpretation of the dSA equation

Historically, delayed-stretch activation has been measured using a step-strain test that measures the force response of the muscle to stretching. The data is then fit to a sum of exponential terms. Looking at the relative rates of the different exponential terms is one way to compare muscles from different insects [62], [73], [111], [121] and across genetically-modified organisms [71]. The equation used to fit the data is given in Eq C.1. The equation breaks the transient tension in the muscle into three distinct phases plus an offset: a fast decay right after stretching (phase 2), a rise in tension caused by stretch activation (phase 3), and a relatively slower decay in tension following the rise (phase 4). The offset term c represents passive stiffness of the muscle after a long time has passed.

While the actual mechanics of stretch activation are likely related to mechanical regulation of actin and myosin attachments in the sarcomere [61], an equation like that above is useful for gaining insight into the relationships between active, work producing aspects of muscle and passive energy loss. Indeed, muscle has a history of being represented as a system of springs,

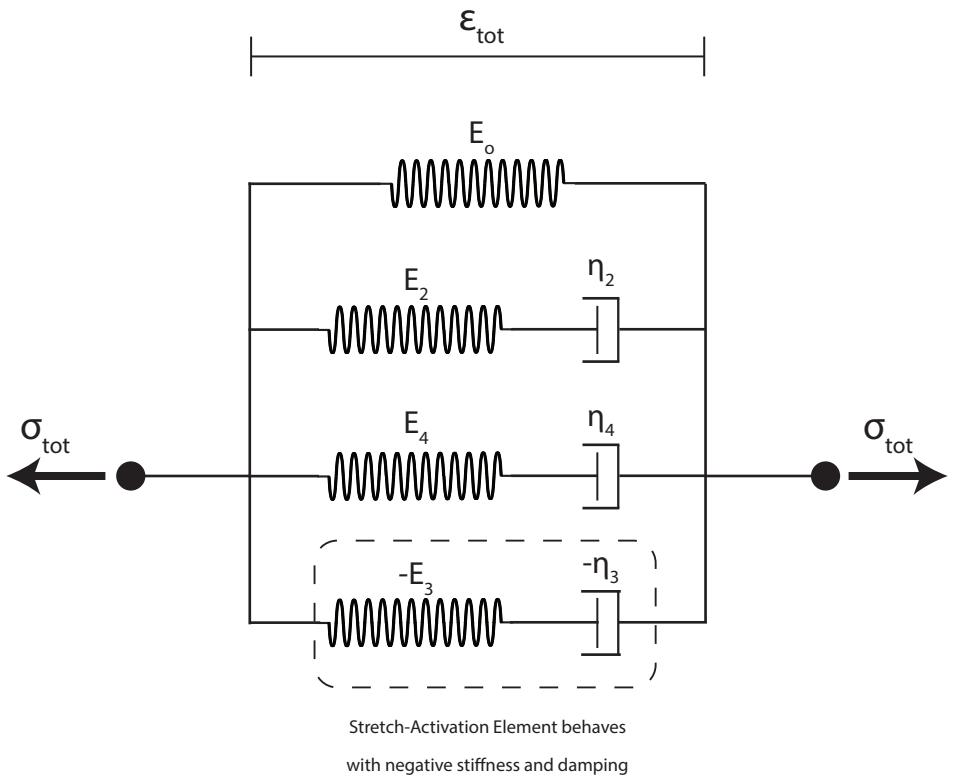

Figure C.4. Generalized Maxwell model of stretch-activated muscle. Stretch-activation dynamics behave like a negative Maxwell element

dampers, and active elements [72], [160], [161].

In that context, consider the linear system in Fig. C.4. It consists of three Maxwell elements (spring and damper in series) plus a fourth spring in parallel. The Maxwell element that represents stretch activation is different from the others in that it has a *negative* stiffness and viscosity. This is not necessarily physical, but it represents the "negative viscosity" effect that was first described by Machin & Pringle [59].

Each parallel element experiences the same strain, and the total stress is the sum of the stresses in each element. For each of the Maxwell elements, we can express a stress-strain relationship in the Laplace domain:

$$\sigma_i + \frac{\eta_i}{E_i}\dot{\sigma}_i = \eta_i \dot{\varepsilon} \quad \Rightarrow^{\mathscr{L}} \quad \bar{\sigma}_i = \left(\frac{sE_i}{s + \frac{E_i}{\eta_i}} \right) \bar{\varepsilon} \tag{C.2}$$

Summing up the stresses for all of the elements, we get:

$$\bar{\sigma}_{tot} = \left(E_o + \frac{sE_2}{s+\frac{E_2}{\eta_2}} + \frac{sE_4}{s+\frac{E_4}{\eta_4}} - \frac{sE_3}{s-\frac{-E_3}{-\eta_3}} \right) \bar{\varepsilon} \tag{C.3}$$

In the stretch-hold experiment, the strain is a step function with a set strain maximum, i.e. $\varepsilon = \varepsilon_0 H(t)$, where ε_o is the stretch fraction, $\Delta\varepsilon/L$. The Laplace transform of $H(t)$ gives $\bar{\varepsilon} = \frac{\varepsilon_o}{s}$, and plugging into equation 3:

$$\bar{\sigma}_{tot} = \left(\frac{E_o}{s} + \frac{E_2}{s+\frac{E_2}{\eta_2}} + \frac{E_4}{s+\frac{E_4}{\eta_4}} - \frac{E_3}{s-\frac{E_3}{\eta_3}} \right) \varepsilon_o \tag{C.4}$$

It's straightforward to take the inverse Laplace transform of Eq. C.4 to get the time course of stress:

$$\begin{aligned} \sigma(t) &= \left(E_o + E_3 + E_2 e^{-\frac{E_2}{\eta_2}t} + E_4 e^{-\frac{E_4}{\eta_4}t} - E_3 e^{-\frac{E_3}{\eta_3}t} \right) \varepsilon_o \\ \Rightarrow \frac{\sigma_{dSA}(t)}{\varepsilon_o} &= E_2 e^{-\frac{E_2}{\eta_2}t} - E_3 e^{-\frac{E_3}{\eta_3}t} + E_4 e^{-\frac{E_4}{\eta_4}t} + E_o \qquad \text{(C.5)} \\ &= E_2 e^{-\frac{E_2}{\eta_2}t} + E_3(1 - e^{-\frac{E_3}{\eta_3}t}) + E_4 e^{-\frac{E_4}{\eta_4}t} + (E_o - E_3) \qquad \text{(C.6)} \end{aligned}$$

If we use the relationship between muscle tension and muscle stress, $F_t = \sigma_{dSA} A$, where A is the muscle cross-sectional area, we can convert the expression into the force caused by a step strain, with the same units as Eq. C.1.

Some observations we can make by comparing the Generalized Maxwell model equation vs the fit function:

- $K_2 = E_2\varepsilon_o,\ K_3 = E_3 A\varepsilon_o,\ K_4 = E_4 A\varepsilon_o$ and $c = E_o - E_3$ are related to the *stiffness* of the different elements.
- The rates $r_2 = \frac{E_2}{\eta_2}$, $r_3 = \frac{E_3}{\eta_3}$, $r_4 = \frac{E_4}{\eta_4}$ are functions of the stiffness and damping moduli, i.e. the relaxation rates of the three elements

- The offset term c is a function of the parallel stiffness of the muscle *and* the strength of stretch-activation. The stiffness of an activated asynchronous muscle is larger than a similar synchronous muscle after a stretch [4]

When it comes to designing an asynchronous artificial muscle or actuator, this representation helps to clarify the necessary requirement for an active element. While the dSA dynamics which produce oscillations and were discussed in Chapter 4 are relatively simple, it is necessary to have this negative viscosity effect, created via feedback, in order to have a system that does work. A negative spring-damper is non-physical, but even a simple PD-controlled motor combined with viscoelastic damping elements would be sufficient to produce similar behavior.

Appendix D

Supplementary to Chapter 4

D.1 Methods

D.1.1 Ancestral state reconstruction

Muscle type labeling

We encoded the orders Odonata, Ephemeroptera, Dermaptera, Plecoptera, Orthoptera, Embioptera, Phasmatodea, Mantodea, Blattodea, Isoptera, Raphidioptera, Megaloptera, Neuroptera, Trichoptera, Lepidoptera, and Mecoptera as synchronous and the orders Thysanoptera, Strepsiptera, Coleoptera, and Diptera as asynchronous [75], [128], [153], [154], [162]. Muscle type in Zoraptera remains unknown, and the orders Mantophasmatodea, Grylloblattodea, Siphonaptera are all wingless. The three remaining orders, Hemiptera, Psocodea, and Hymenoptera are known to have both synchronous and asynchronous species [75], [128], [153], [162], [163]. The muscle type for each tip species of the insect phylogeny and its associated reference are included as a raw data file (Supplementary Data Table S1 - Species muscle type with sources). We also conducted a more detailed literature analysis on all orders.

Psocodea. Psocodea is a particularly notable clade that has the potential to strongly influence the ancestral state and single origin of asynchronous muscle. This order is historically considered to have mixed muscle types [75] based on the muscle structure data for various species [128]. Of the tip species present in the phylogeny used in this study, we were able to discern muscle types based on muscle structural data or absence of wings (see Fig. 1). Muscle

structure data for the longest-branched species (Ectopsocus) are inferred from a closely related species investigated by Cullen [128] and the wingless state of other tip species was determined through multiple sources [164], [165]. Additional confirmation of the states of this group was completed by cross referencing the phylogeny used in this study (Fig. 1) with a more densely sampled phylogeny of Psocodea [166] and searching for additional muscle type data for Psocodea species not represented in the phylogeny used in this study. We found that one species (*Trogium pulsatorium*) belonging to the most ancient suborder within the group (Trogiomorpha) is reported to have synchronous flight muscle (Cullen, 1974). The next most ancient subclade (suborder: Psocomorpha) within Psocodea is known to have multiple species with asynchronous flight muscle based on its structure [128]. Data from a more recently diverging clade, the Amphientometae infraorder (within the Troctomorpha suborder), are absent and the remaining species of the larger clade (Troctomorpha), where Amphientometae is nested, are wingless [164], [165].

All evidence together suggests that the ancestral state of Psocodea is asynchronous. However, there remains uncertainty in this group due to poor muscle data and their large degree of winglessness. Using scaling relationships based on body mass and measurements of Psocodea wing sizes, it seems likely that most winged Psocodean species fly with wing beat frequencies well over 100 Hz (150-500 Hz), even when we allow body mass to differ by an order of magnitude from 0.1 mg to 1 mg [167]–[169]. Wing beat frequencies above 100 Hz are strongly associated with the evolution of asynchronous flight muscle. Second, in support of our scaling argument, other authors report that all species of winged Psocodea are asynchronous based on their necessarily high wing beat frequencies [170], directly conflicting with the muscle type data from Cullen (1974). Finally, the winged clade of unknown muscle type, Amphientometae, has a most recent common ancestor with the Psocomorpha clade, which does possess asynchrounous muscle [128]. If Amphientometae does have asynchronous muscle as expected, this would most likely result in an asynchronous ancestral condition of the entire Psocodea order. Thus, multiple lines of evidence support asynchronous muscle type as the ancestral condition of this clade with

possibly a single, independent reversion to synchrony within the Trogiomorpha clade, which is not present in the phylogeny used in this study.

Hemiptera. Although Hemiptera is another clade with interspecific variation in muscle type we are again confident in our reconstruction of the ancestral state. First, many species of Hemiptera were investigated by [128] and the clade is relatively well sampled in the phylogeny used in this study. In addition, we mapped additional muscle type data from [128] onto a more densely sampled Hemiptera phylogeny [171] for at least one species from most (19 of 29) families. Here, we find that all investigated species from the Heteroptera suborder, which includes 20 (11 of which have been investigated) of the 29 families present in the Johnson *et al.* phylogeny [171], use asynchronous flight muscle [128]. Second, two of the four longest branch families with the most ancient diverging Hemiptera suborder (Sternorrhyncha) are also asynchronous. The Sternorrhyncha suborder is only represented by two synchronous species in the phylogeny used in this study and thus is likely overweighted when inferring the ancestral condition of this group. Despite that, we still recover an ancestral condition of asynchronous muscle. Other authors reviewing known muscle types and flight neuromechanics also concluded that most Hemiptera species rely on asynchronous flight muscle [170].

Two additional phylogeny tips within Hemiptera from the genera (*Xenophysella* and *Nilaparvata*) did not have published muscle structure data from any species within the same family, warranting further investigation. First, we code the *Xenophysella* tip as wingless because the majority of investigated species (24 of 25) from the Coleorrhyncha suborder that includes *Xenophysella* are reported to be flightless [172]. Second, we code the *Nilaparvata* tip as asynchronous for the following reasons: *Nilaparvata* myofibril diameter has been reported as 1.8 microns in insects three days post-emergence [173], which is above the 1.5 microns threshold for differentiating synchronous from asynchronous muscle [128], [163]. From transmission electron microscopy of *Nilaparvata*, the sarcoplasmic reticulum appears to be sparse [173] which is a proposed hallmark of asynchronous muscle [128]. Despite this evidence, there is still some uncertainty about the *Nilaparvata* muscle type for the following reasons: a different

species (*Sogatella furcifera*) from the same family (Delphacidae) is reported to have muscle with myofibril diameters ranging between 1.5 to 2.0 (1.7) microns 3 days post emergence [174], which also falls on the border of the diameter (1.5 microns) used to differentiate muscle type in this group [128]. Further, *Nilaparvata* belongs to the Fulgoroidea superfamily [171]. The Fulgoroidea superfamily shares a most recent common ancestor with the Membracoidea superfamily based on the Johnson *et al.* (2018) Hemiptera phylogeny [171], and Membracoidea contains species of both synchronous and asynchronous muscle type [128], making the identification of *Nilaparvata* equivocal based on its phylogenetic position alone. However, the most direct histological evidence supports our classification of *Nilaparvata* as asynchronous.

The high variation of muscle type within Hemiptera makes this clade particularly interesting for future studies on the evolution of synchronous and asynchronous muscle physiology and structure. Based on our assessment of muscle type across Hemiptera, there appears to have been multiple reversions back and forth between the two types, where both types have likely evolved at least once from an ancestor of the other type. These bidirectional transitions within Hemiptera support the thesis that muscle physiology lies on a continuum rather than as two discrete types and may transition across the bridge in parameter space (Fig. 3b,e). Despite the diversity within Hemiptera, the reconstruction of the ancestral node is confidently asynchronous.

Hymenoptera. All Hymenoptera muscle types were assigned based on published muscle structures and supported by other investigations of muscle physiology. As noted above, variation in muscle myofibril diameter is directly related to muscle type, where myofibril diameters less than 1.5 microns are considered synchronous muscle [128]. Myofibril diameter was measured in 46 species distributed across the Hymenoptera phylogeny [175]. All but one of the 46 species are reported to have myofibril diameters greater than 1.5 microns [163]. A second line of evidence that relies on the muscle being defined as ”close-packed” versus ”fibrillar” supports these results [163]. Thus, while Hymenoptera is considered to be a group of mixed muscle type [75], we find the presence of synchronous muscle to be relatively rare. In support of these conclusions, [170] also reports that most species of Hymenoptera rely on asynchronous flight muscle.

All other clades: All other insect orders are reported to be invariant in flight muscle type or are known to be completely wingless. Therefore, we relied on their invariant classification from published reviews [4], [75], [162] where authors used total evidence from both muscle structure and physiology data across species of each order to determine the muscle type classification of each order. However, we do code the single Zoraptera tip as unknown because we could not find any data on any species from this order. The coding of this tip as synchronous, which would be the most conservative classification, does not impact our results.

Rate reconstruction implementation

We used a previously published molecular phylogeny grounded in fossil records spanning all insect orders [127], which modifies the fossil calibration of the extensive insect phylogeny developed by Misof et al. [1]. For ancestral state reconstruction, we assumed an equal rates model of evolution and used maximum likelihood estimation to estimate the posterior probability of ancestral states using the *Phytools* R Package [126]. These analyses were performed in RStudio (v. 1.1.383) using R (v. 4.0.2). In Supplementary Information section IIA we test other models of evolution using different characters states, allowing all rates to be different rather than equal, and consider hidden rates models, using the *Phytools* R Package [129], [176]. The latter allows for heterogenous rates of evolution but quickly increases the number of parameters in the model [129], [130], [176]. All models with a single rate class are consistent with the order level reconstruction of synchronoy and asynchrony, including the single origin of asynchrony at Node 200 (Thysanoptera + Hemiptera + Psocodea + holometabolous insects). Some models with multiple rate classes can produce more ambiguous reconstructions with more possible patterns but are significantly overfit as assessed by Akaike Information Criterion (AIC) values (See Supplementary Information IIA for further discussion).

We also determine the probability that the Lepidoptera clade evolved from synchronous ancestry without reverting from a single asynchronous ancestor (e.g. there were multiple, independent, more recent evolutions of asynchronous muscle for different synchronous orders). To do

so, we first recorded the probability that the node representing the origin of asynchronous muscle (Node 200) is synrchronous (Supplementary Data Table S2 - Ancestral state posterior probabilities per node). Next, we constrained that same ancient node (200) to be 100% synchronous and recorded the probability of synchrony in the next most recent node (218) in the branching path towards the origin of Lepidoptera. We iteratively continued this process, constraining each node between the origin of asynchronous muscle and the origin of the Lepidoptera clade (Node 255). We then multiplied the probability that each node is synchronous to calculate the total probability that the Lepidoptera clade evolved from a synchronous ancestor.

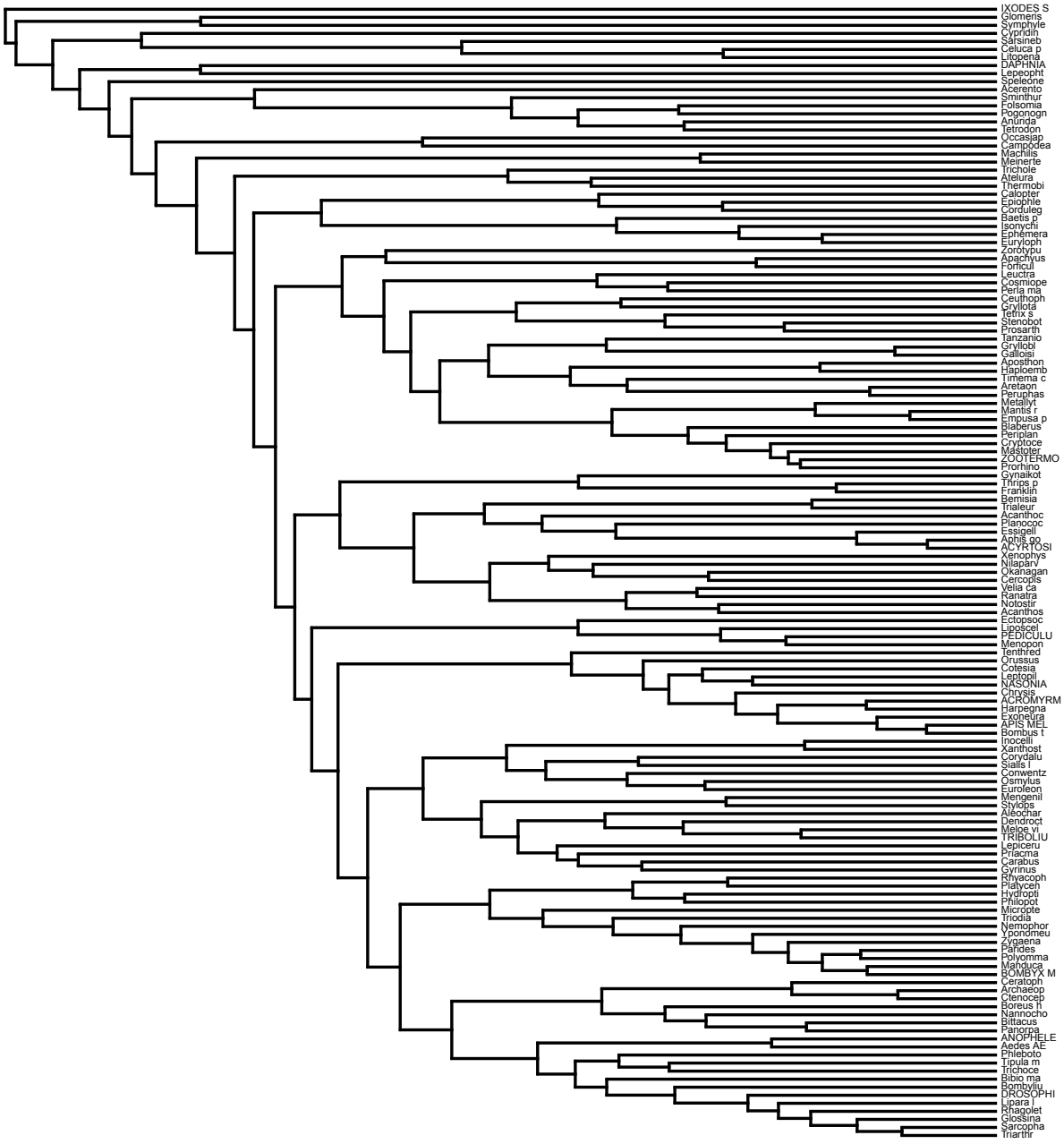

Figure D.1. The insect wide phylogeny. The insect wide phylogeny [127] used to conduct the ancestral state reconstruction of insect muscle type. The full name of every tip species can be found in raw data (Supplementary Data Table S1 – Species muscle type with sources). Node number labels are found in Extended Data Figure 2.

Figure D.2. The insect wide phylogeny with node number labels. The number of each node is overlayed on top of the insect wide phylogeny (Fig. 1c, Extended Data Figure 1). These node numbers are referenced in the table containing the posterior probability of the ancestral state for each ancestral node of the phylogeny (Supplementary Data Table S2 - Ancestral state posterior probabilities per node).

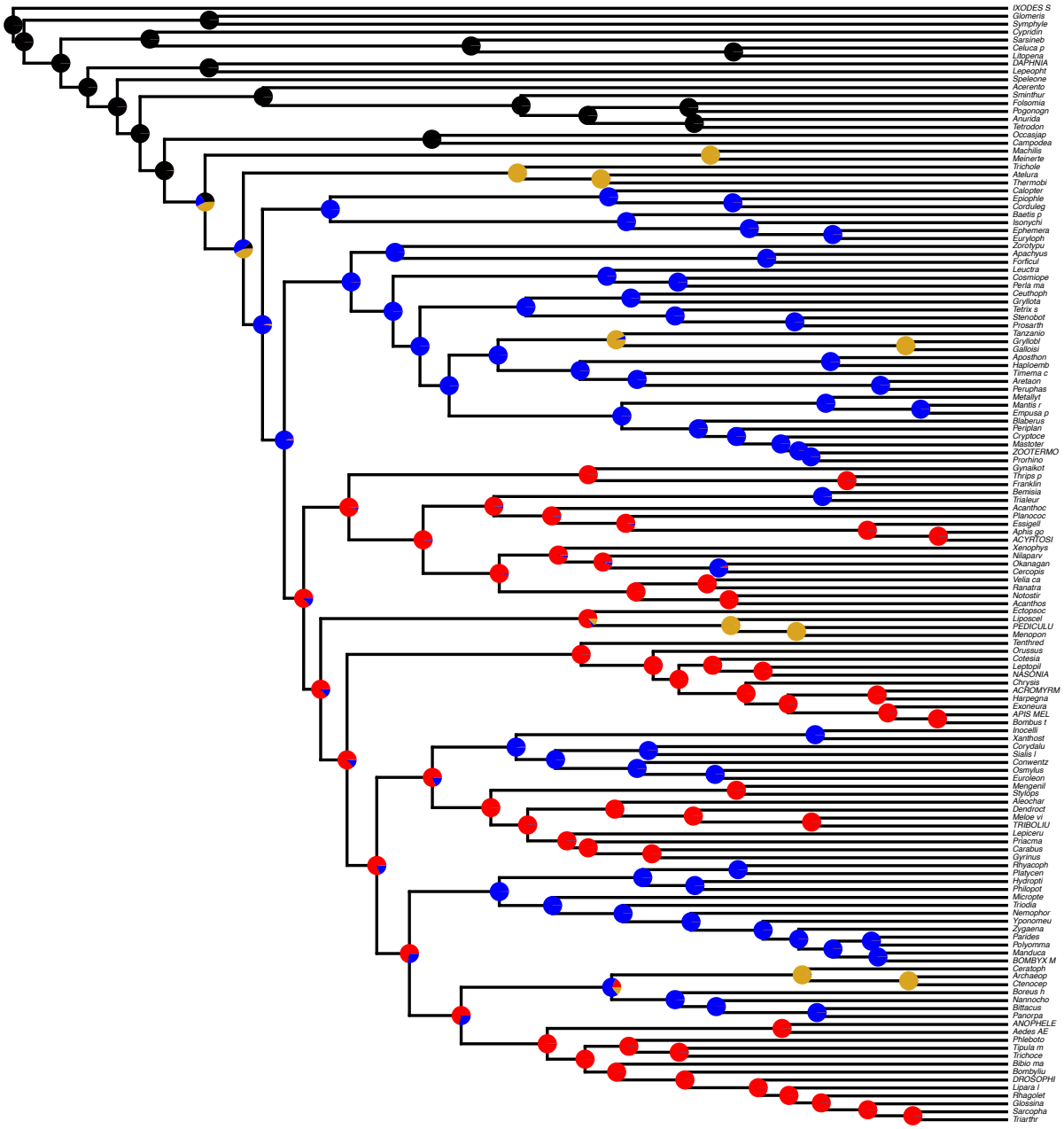

Figure D.3. The posterior probability of muscle type at each ancestral node. The pie chart at each ancestral node represents the posterior probability of muscle type. Data is found in Supplementary Data Table S2 - Ancestral state posterior probabilities per node. The node number for every node on the phylogeny is referenced in Extended Data Figure 2. All colors are consistent with Figure 1 of the main text.

D.1.2 Muscle physiology

Animals

Manduca sexta were obtained as pupae from a colony maintained at the University of Washington. Moths were kept on a 12h:12h light dark cycle. We used 6 females and 3 males with a mean body mass of 2.32 ± 0.46 g.

Experimental preparation

After a 30 min cold anesthesia, we removed the head, wings, abdomen, legs, and first thoracic segment from each moth to isolate the second and third thoracic segments. We then used digital calipers to measure the dorsal longitudinal muscle (DLM) length as the distance between the anterior and posterior phragma. These structures are the phsyiological attachment points of the DLMs. We measured a mean muscle length of 11.7 ± 0.5 mm.

We used a similar experimental paradigm as Tu & Daniel[131] for dynamic, whole muscle experiments on *M. sexta* DLMs. The key difference in our protocol is that we used a dual-mode ergometer (305C Muscle Lever, Aurora Scientific Inc. Aurora, ON, Canada) capable of prescribing a length trajectory while measuring the force necessary to follow that trajectory. For the anterior muscle attachment, we used cyanoacrylate glue to rigidly mount the anterior phragma to a custom three-dimensional printed ABS shaft, which was secured to our experimental table. For the posterior attachment, we attached a pair of tungsten prongs to the ergometer lever. We inserted these prongs at the invagination between the second and third thoracic segments. This ensures that the prongs adhere to the posterior face of the posterior phragma. Cyanoacrylate glue ensured a strong connection. In all preparations, we ensured that the anterior and posterior attachments were rigidly bonded following the experiment.

At this point, the intact second and third thoracic segments were rigidly mounted on our ergometer. We relieved any force buildup during this procedure by manually adjusting the ergometer length until the force reading was at zero. We then shortened the muscle by 2% because the *in vivo* muscle length during flight is 2% shorter than its length during rest [131].

We next decoupled the anterior and posterior sections of the muscle by removing a transverse ring of exoskeleton. To minimize inertial loads on the ergometer, we removed all other muscles and any remaining exoskeleton on the anterior side of the thorax. We made sure to excise the ganglia to prevent spontaneous muscle activation.

To activate the muscles, we inserted two tungsten electrodes into the anterior end of the muscle by piercing the exoskeleton of the anterior phragma. We repeated this procedure for the posterior side by piercing the posterior end of the scutum. To ensure muscle viability, we maintained a steady drip of saline and held a constant temperature of 35°C measured at the muscle.

Because Ca^{2+} is required for delayed stretch activation [4], we stimulated the muscles at 150 Hz to induce tetanus. We found that 150 Hz stimulation was the minimum stimulation frequency to establish a fused tetanus. Our experiments to measure delayed stretch activation consisted of a stretch-hold-release-hold cycle. We first maintained zero strain for 150 ms to enable a plateau in force, indicating constant activation (Fig. 2b), we stretched the muscle to *in vivo* strains (4.5%) at peak *in vivo* strain rates [131] while measuring muscle force output. We calculated peak *in vivo* strain rate as $\dot{\varepsilon}_0 = 2\pi f \varepsilon_0$, where f is the wingbeat frequency (25 Hz) and ε_0 is peak *in vivo* strain. We then held the strain constant for 150 ms. We returned the muscle to rest length at the same strain rate as before.

We measured the peak twitch, delayed stretch activation, and tetanic force produced by the muscle. In all cases, we normalized force production by the cross-sectional area of the muscle. To determine the rate constants of delayed stretch activation we fit the muscle force data with the equation

$$F_{step}(t) = K_2 e^{-r_2 t} + K_3(1 - e^{-r_3 t}) + K_4 e^{-r_4 t} + c \tag{D.1}$$

where K_i and r_i are the coefficients and rate constants associated with a particular phase of the delayed stretch activation response: a fast decay ($r_2 \gg$ wingbeat frequency), a slower rise ($r_3 \approx$ wingbeat frequency), and a very slow decay ($r_4 \ll$ wingbeat frequency). The constant c

represents the passive stiffness of the muscle. Phase 1 is the immediate material response of any muscle to a transient strain and is not relevant to characterizing delayed stretch activation. We quantified delayed stretch activation force magnitude as the difference between the lowest force immediately following stretch to the peak force during the plateau phase.

Following experiments, we removed and weighed the DLMs. We measured an average muscle mass of 0.123 ± 0.012 g. This corresponds to a body-mass normalized muscle mass of $5.28 \pm 1.41\%$, which is in rough agreement with prior measurements of $5.96 \pm 0.62\%$ [177]. From muscle length and muscle mass, we calculated a cross-sectional area of 10.7 ± 2 mm^2 under the assumption that muscle density is 1 g cm^{-3}.

Scaling the delayed stretch activation force due to non-ideal strain rate impulse

Our input stimulus to the ergometer for stretch-hold-release-hold experiments was a ramp with a speed matching the *in vivo* speed of muscle contraction in a hawkmoth. Our modeling assumes that r_3 is the rate of tension rise in response to an infinite impulse, which is not possible to implement in any real physical system. To examine the discrepancy between muscle's response to an infinite impulse and a non-ideal finite impulse, we follow the following procedure. First, we construct a rectangular pulse with a width and height that match the width and height of the actual strain rate pulse we imposed in experiment. We then compute the empirical transfer function between the sum-of-exponentials fit to our force data and the rectangular pulse. This transfer function represents the response of hawkmoth muscle to an infinite impulse in strain rate, and is equal to our fit multiplied by a scalar. We compute this scalar to be 2.29, by dividing the infinite impulse response (IIR) by our fit. We then scale our force data by this constant factor and plot it, labeled as "IIR" in Fig. 4.2e. Data presented in Fig. 4.2b-d is raw and unscaled by the method described here.

D.1.3 Delayed stretch activation model

To study how delayed stretch activation produces wing oscillations we needed to generate a feedback model for delayed stretch activation. No current detailed muscle model can predict both neural and stretch-activated force components under general dynamic conditions, in part because of limitations in our understanding of the multiscale interactions in muscle [178]. Thus, to model asynchronous force, we do not try to build a detailed molecular model that can predict force from arbitrary activation and strains. Instead, we seek to capture the basic functional input-output relations for delayed stretch activation between an imposed strain and the resulting force. We first constructed a reduced order model of the delayed stretch activation that was able to capture the stretch-hold-release-hold behavior we observed in experiment. This single parameter model is described by the "time to peak" (t_0) of the delayed stretch activation force response, which allows us to study how the relative timescales of delayed stretch activation (t_0), body mechanics (the natural resonance frequency, T_n), and the synchronous timescale ($\frac{1}{f_s}$) govern the emergent wingbeats. To implement delayed stretch activation in simulation, we then generated a computational representation of delayed stretch activation and coupled it to a computational representation of body mechanics.

One-parameter delayed stretch activation feedback model

Measurements of delayed stretch activation in the literature [74] consist of imposing a step change in muscle length and fitting the force response, $F_{step}(t)$, with a sum of three exponentials given by Equation D.1. The 7-parameter model was used to fit the delayed stretch activation response in the hawkmoth muscle (Fig. 4.2c). However, the initial viscoelastic drop following lengthening is unlikely to be important for generating self-excited oscillations, and the symmetry between r_2 and r_4 leaves those parameters sensitive to initial conditions of a curve fit procedure. Because the delay between stretch and force production is likely the critical feature of delayed stretch activation, we only considered the delayed tension rise (determined by r_3) and the delayed tension drop (determined by r_4). In doing so, we eliminated K_2 and r_2 from

the fit Equation D.1. We further eliminated the passive muscle stiffness from Eq. 4.2 because it does not contribute significantly to the elastic response of the thorax in *M. sexta* [76]. It is possible that active muscle stiffness contributes to body mechanics. Incorporating estimates of active muscle elasticity and body dissipation that may be present in the thorax does not affect the overall conclusions or features of the simulation (see Supplementary Information IID). We fit the Hawkmoth muscle data to the reduced convolution kernel,

$$g(t) = \frac{1}{g_0}\left(-e^{-r_3 t} + e^{-r_4 t}\right) \tag{D.2}$$

where g_0 is a scalar that normalizes by the area under the kernel (which depends on the kernel rate constants and has units of seconds). We sought to further reduce this convolution kernel to be parameterized by a single variable, the time to reach peak tension from a step input (t_0; Fig. 4.1b). We first assumed a constant ratio between r_3 and r_4 such that $r_4 = \kappa r_3$ (for *M. sexta* $\kappa = 0.62$). We can then solve for t_0, from the reduced kernel to obtain

$$t_0 = \frac{\ln(r_3/r_4)}{r_3 - r_4} \tag{D.3}$$

$$= \frac{\ln(\kappa)}{r_3(\kappa - 1)} \tag{D.4}$$

For hawkmoth muscle this yields a relationship between t_0 and r_3 of

$$t_0 = \frac{1.258}{r_3} \tag{D.5}$$

While our single parameter model is simplified from the classic 7-parameter delayed stretch activation model, the qualitative features of the Fig. 4.3 heatmaps and associated conclusions are insensitive to the precise value of κ.

Discrete FIR filter implementation

To implement delayed stretch activation in our simulation and robot experiments, we require a model of delayed stretch activation that can produce stretch dependent forces in "real-time" which can provide a delayed stretch activation force to the simulation or robotics experiments. We describe the delayed stretch activation response of asynchronous muscle as a convolution of the muscle strain velocity with a kernel, g, such that

$$F_{async}(t) = \mu F_a(-g * \dot{\varepsilon})(t) \tag{D.6}$$

where F_a is the asynchronous forcing magnitude and dictates the strength of the delayed stretch activation feedback.

We implement this convolution in simulation and in the robotic models in MATLAB simulink (R2020, Mathworks) using a finite impulse response (FIR) filter, which is an instantaneous (real-time at 10kHz) evaluation of a convolution operation. We construct the filter such that the input is the muscle strain rate, and the output is the delayed stretch activation force. We convert from the angular rotational units of our wing to actuator strain through the equation, $\dot{\phi} = LT\dot{\varepsilon}$, where we divide wing velocity ($\dot{\phi}$) by a factor of LT where L is the resting muscle or actuator length (in the robot models, $L = T = 1$). This yields the following delayed stretch activated force

$$F_{async}(t) = \mu \frac{F_a}{LT}(-g * \dot{\phi})(t) \tag{D.7}$$

The value of F_a is tuned to each system (simulation, roboflapper, and robobee wing, see below for details), but is not changed between experiments where the relative magnitudes of synchronous and asynchronous forcing are varied (i.e. when K_r is varied as in Fig. 4.3).

For simulations and experiment the delayed stretch activation force is generated from an FIR filter which requires a numerical evaluation of the convolution, $(-g * \dot{\phi})(t)$. First, we

generate the response curve $g(t)$ based on the delayed stretch activation parameters (r_3, r_4) in MATLAB (R2020, Mathworks), sampled at the system rate Δt over the simulation/experiment duration (simulation, roboflapper, and robobee wing, see below for details). The normalization parameter g_0 in Equation D.2 is the numerical area under the curve. We then find the value of t for which $g(t) < 0.01 * \max(g(t))$ and truncate the response since the finite impulse response filter requires a finite kernel. Lastly, we multiply the output of the numerical convolution by the coefficient $\frac{\mu F_a}{LT}$. The delayed stretch activation step response, $F_{async}(t)$, is thus represented as a vector of numbers that are supplied to "filter coefficients" input of the FIR block in Simulink. When synchronous and asynchronous forces are applied together we scale F_{async} by $(1 - K_r)$ according to the combined forcing equation (Eq. 4.1).

D.1.4 Hawkmoth simulation

Hawkmoth body mechanics model

We used a dynamics model of the wing rotation in the stroke plane (ϕ) for the hawkmoth which has previously been derived by Gau *et al.* [76]. In brief, we assumed a body mechanics model with aerodynamic drag whose magnitude depends on angular velocity squared ($|\dot{\phi}|\dot{\phi}$) with a constant drag coefficient (Γ), a parallel-elastic spring due to thorax elasticity (k), and rotational inertia from wing and added mass (I). These assumptions yield the equations of motion presented in Equation 4.2.

To generate equivalent torques from the linear muscle force and the linear thorax elasticity we require the transmission ratio between linear muscle displacement and the rotational wing movement. We assumed a linear transmission ratio such that $T = \phi / X$ where ϕ is the wing rotation and X is the linear displacement of the muscle and thorax. We calculated the transmission ratio for Manduca as $T = \phi_0 / X_0$, where ϕ_0 is the peak-to-peak wingstroke amplitude and X_0 is the peak-to-peak muscle displacement amplitude (values can be found in Table D.1 and Gau *et al.*[147]). The equivalent torque about the wing hinge produced by the muscle force F_m is given by F_m / T. The equivalent elastic torque from the thorax linear stiffness is calculated as

k/T^2. These two transformations can be derived using conservation of energy: work done at the rotational joint must equal work done on the linear elements (spring and muscle).

The wing inertia, I, includes the added mass effects from aerodynamics. Following the derivations of Ellington [179], wing inertia (I) is the sum of inertia due to wing mass (I_w) and added mass (I_a),

$$I_w = R_2^2(m) m_w L_w^2, \quad \text{and} \quad I_a = R_2^2(v) v L_w^2, \tag{D.8}$$

where $R_2(m)$ is the radius of the second moment of wing mass, $R_2(v)$ is the radius of the second moment of wing added mass, and L_w is the wing length. Note that in the aerodynamics literature, the second moments are often denoted r_2 and the wing length denoted R, but we change the convention here to avoid confusion with the rate constants, r, used in the delayed stretch activation experiments. Dimensional added mass (v) is defined as $v = \frac{2\rho\pi\hat{v}L_w^3}{\mathcal{AR}^2}$, where $\hat{v}$ is the non-dimensional added mass of the wing pair and $\mathcal{AR}$ is the aspect ratio of the wings. Parameter values are in Table D.1.

Table D.1. Hawkmoth simulation variable definitions and values

variable	value	description
k	2582 ± 510 N m^{-1}	thoracic stiffness[76]
I	5.69 ± 0.34 E-8 kg m^2 rad^{-1}	wing inertia
T	2230 ± 110 rad m^{-1}	transmission ratio
Γ	3.69 ± 0.33 E-8 kg m^2 rad^{-2}	damping coefficient
$R_2(m)$	0.383 ± 0.003	2nd moment of wing area[134]
$R_2(v)$	0.482 ± 0.001	2nd moment of added mass[134]
$R_2(s)$	0.518 ± 0.001	2nd moment of wing shape [134]
m_w	0.092 g	wing mass (both wings) [134]
$\hat{v}$	1.08	added mass [134]
ρ	1.225 kg m^{-3}	air density
A_w	1881 mm^2	wing area (both) [134]
$\mathcal{AR}$	5.53 ± 0.04	wing aspect ratio (both wings)[134]
L_w	51 mm	wing length [134]
$\tilde{C}_D$	1.5	drag coefficient [180]
l_{cp}	30.6 mm	aerodynamic center of pressure [180]
ϕ_0	$117 \pm 6°$	peak-to-peak wingstroke amp [134]
X_0	0.46 ± 0.02 mm	peak-to-peak muscle displacement amp [131]
F_s	2.72 N	zero-to-peak muscle force amp

The lumped aerodynamic parameter Γ was calculated by following the work of Whitney & Wood [8]. The quasi-steady aerodynamic drag force (F_{aero}) on insect wings over a single wingstroke can be modeled as

$$F_{aero} = \frac{1}{2}\rho \tilde{C}_D A_w \hat{R}_2^2(s) L_w^2 |\dot{\phi}|\dot{\phi}. \tag{D.9}$$

Setting the drag torque $\tau_{aero} = F_{aero} l_{cp}$ and $\tau_{aero} = \Gamma|\dot{\phi}|\dot{\phi}$, where l_{cp} is the center of pressure [180], yields the velocity-squared aerodynamic damping coefficient (Γ) as

$$\Gamma = \frac{1}{2}\rho \tilde{C}_D A_w \hat{R}_2^2(s) L_w^2 l_{cp} \tag{D.10}$$

Simulation details

We used MATLAB and Simulink (R2020, Mathworks) to run simulations of combined synchronous and asynchronous forcing on a mechanical model of the hawkmoth. Figure 4.4 b,c presents a representation of the Simulink model. The system dynamics block implements the equation of motion (Eq. 4.2) using hawkmoth parameters. It takes the combined muscle forcing as an input and generates the wing angle and angular velocity as outputs (Extended Data Figure 4.4b). The wing rotational velocity is then an input into the delayed stretch activation simulation described in the previous section and calculated by Equation D.7.

As insect flight is driven by pairs of antagonistic muscles, we represent the upstroke and downstroke muscles separately in our Simulink simulation. The antagonistic configuration means that the sign on both strain velocity and output force is different for each muscle, as shown in Extended Data Figure 4.4c. Additionally, a sine wave generator is used to produce synchronous forcing based on the amplitude F_s and frequency f_s. The output force is a weighted sum of synchronous and asynchronous forces defined by K_r.

Both the synchronous and asynchronous forces in the muscle block are saturated so that they only output tension forces. Additionally, the sine wave generators are operated with

different initial phase $\theta_0 = 0$ for the upstroke muscle and $\theta_0 = \pi$ for the downstroke muscle. The overall effect is that all of the *negative* torque is produced by the upstroke muscle, and all of the *positive* torque is produced by the downstroke muscle. The phase shift in the sine wave generator blocks also enforces that the fully synchronous output is identical to a single sinusoidal torque source.

Iterative force tuning procedure

The parameter K_r describes the relative amounts of synchronous and delayed stretch-activated forcing. To study how an insect that is actuated purely through delayed stretch activation ($K_r = 0$) can transition to being purely actuated through synchronous forcing ($K_r = 1$) we need to establish values of F_a and F_s that produce feasible wingbeat motions in both of these regimes. In the hawkmoth simulation we determined that a sinusoidal forcing amplitude of $F_s = 2720$ mN generates wingbeat kinematics that match in-vivo observation of 117 degrees peak-to-peak. This value was previously used to synchronously drive an identical simulation to physiological wingbeat amplitudes [147].

However, the wingbeat kinematics in the purely asynchronous regime ($K_r = 0$) are emergent and thus we need to determine an appropriate F_{async} that can drive our insect model to appropriate wingbeat kinematics. We used a simple iterative force tuning procedure to determine the value of F_{async} such that asynchronous actuation ($K_r = 0$) can produce wingbeats with peak-to-peak amplitude of $\phi_0 = 117^\circ$. We slowly increment the value of μ until the output steady-state wingbeat amplitude is within 1% of the desired amplitude of ϕ_0. In this way we ensure that the both synchronous ($K_r = 1$)and asynchronous ($K_r = 0$) actuation can produce the same wingbeat amplitudes.

Calculation of K_r for *M. sexta*

Direct computation of K_r for *Manduca* is challenging since realistic measures of muscle force from work loops will contain a mixture of synchronous and asynchronous effects, which are

unlikely to be distinguishable in practice. To address this issue, we take the following approach to estimate K_r using static measurements of muscle, which allow synchronous and asynchronous behavior to be measured separately.

We compute the ratio of asynchronous to total muscle force from muscle physiology and from simulation. We then equate these ratios and solve for the unique K_r that results in equality between experiment and simulation. We use the maximum dSA force from our stretch-hold-release-hold experiments, F_a, as a static representation of the asynchronous muscle force, and the tetanic muscle force F_{tet} as a static representation of the synchronous muscle force. Both F_a and F_{tet} are generated under maximum activation, and F_{tet} is measured isometrically, thus will not include any stretch-activated force. Total muscle force is then $F_a + F_{tet}$. Thus, the ratio of asynchronous to total muscle force in *Manduca* from experiment (denoted with subscript exp.) is:

$$\frac{F_{async,exp.}}{F_{total,exp.}} = \frac{F_a}{F_a + F_{tet}} \approx 0.12 \tag{D.11}$$

In simulation, the maximum purely asynchronous force amplitude can be found by setting $K_r = 0$ and taking the emergent amplitude of $F_{async}(t)$. Maximum purely synchronous force amplitude is simply $\max(F_s \sin(\omega t)) = F_s = 2.72$ N, the force required to drive the $K_r = 1$ system to in-vivo amplitude wingbeats. Since Manduca is neither purely synchronous nor asynchronous (i.e. $0 < K_r < 1$), the maximum asynchronous and synchronous forces must be multiplied by $(1 - K_r)$ and K_r respectively to yield an estimate of *in-vivo* contributions to total muscle force. Therefore, the ratio of asynchronous to total muscle force for a hybrid insect in simulation (denoted by subscript sim.) is:

$$\frac{F_{async,sim.}}{F_{total,sim.}} = \frac{(1 - K_r)\max(F_{async}(t)|K_r = 0)}{(1 - K_r)\max(F_{async}(t)|K_r = 0) + K_r F_s} \tag{D.12}$$

Finally, we set Eqs. 13 and 14 equal to one another and solve for the unique K_r that results. When we do this, we find that *Manduca* has $K_r \approx 0.6$. This construction relies on the

approximation that static muscle physiological measurements are representative (in relative magnitude terms) of oscillatory forces that would be measured in-vivo and in our simulation.

Simulation parameter sweep and analysis

To evaluate how the presence of both synchronous and delayed stretch activation in an insect muscle influences the wing kinematics we performed simulations varying both K_r and the time to reach peak tension of the delayed stretch activation, t_0. We incorporated mechanical timescales of the system by dividing t_0 by the natural period to yield the parameter t_0/T_n. For a given insect, T_n is assumed to be constant. To sweep across delayed stretch activation timescales, we adjusted r_3 via Eq. D.5 to sweep over a range of t_0/T_n values from 0.01 to 1. We varied K_r from 0 to 1. For each set of K_r and t_0/T_n values, we first calculated r_3 from t_0 (Eq. D.5). We then generated the delayed stretch activation kernel as described in the delayed stretch activation model section. With F_a from the section above, we could now combine synchronous and asynchronous forcing (Eq. 4.1). We initialized the wing position at 0.1 rad to initiate oscillations when there was no synchronous forcing. All simulations were performed with a fixed sample time of $\Delta t = 1 \times 10^{-4}$ s over a duration of 5 s.

For each set of parameter values, we recorded the emergent force F_m, wing position, and wing velocity. We determined the emergent oscillation frequency by taking the Fourier transform of the last 2.5 s of position and identifying the frequency with the largest magnitude. To calculate power, we extracted 5 periods of oscillation after the system reached steady state. We then numerically integrated force over position and divided by the time elapsed. Lastly, we computed the variation in the peak-to-peak wing amplitude by using the `findpeaks` command in Matlab to locate all the of wingbeat peaks. The amplitude variation is calculated as the standard deviation of the peak-to-peak wingbeat angles.

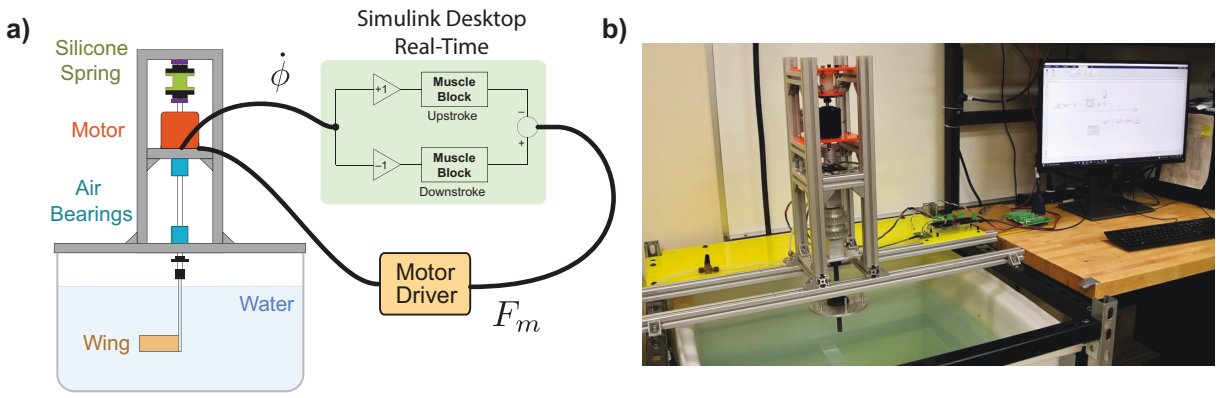

Figure D.4. Robophysical experiment setup and details. a) Schematic of the robophysical experiment. A dynamically scaled wing is immersed in a large water tank and is actuated by a brushless motor under torque control. An angular encoder measures the wing rotation and the calculated wing velocity is supplied to a Simulink simulation of delayed stretch activation. The combined output of delayed stretch activation (F_{async}) and the synchronous force (F_{sync}) is provided to the motor driver to actuate the wing. b) A photo of the experimental setup.

D.1.5 Dynamically scaled robophysical experiment

Robot details

Experiments were performed on a dynamically-scaled robophysical model described previously in Lynch *et. al.* [106]. The device consists of a silicone torsion spring with known, linear characteristics [106]; a brushless DC motor (ODrive Robotics, D6374) under closed-loop torque control; and a rigid, fixed-pitch acrylic wing submerged in a tank of water (Figure D.4). The wing span and chord (10 x 3.6 x 0.5 cm) were selected such that the wing, flapping in water with an amplitude between 10 and 60 degrees and frequency between 1 and 4 Hz, has a Reynolds number between 10^3 and 10^4, which is approximately the same range as *M. sexta*[134]. Friction is minimized via a set of radial air bearings and a thrust ball-bearing. We measured the spring stiffness and system inertia and calculated the wing drag torque coefficient (Extended Data Table D.2) [106]. We also calculated the natural period T_n of the robophysical system using Equation 4.3 as $T_n = 0.416$ s.

The robophysical experiment was designed to mimic the hawkmoth simulation, replacing

the virtual hawkmoth dynamics with those of a real system. We tracked wing angle using an optical encoder (US Digital, 4096 CPR) fixed to the wing shaft and a DAQ (National Instruments, PCIe 6323) sampled at 1 kHz. The encoder angle was used as input to a Simulink Desktop Real-Time (Mathworks) model running an identical combined forcing model as described previously in the sections on the delayed stretch activation model, and the hawkmoth simulations. The velocity was calculated by taking a derivative of the encoder position and fed into the model. The model prescribed a motor torque which was sent via USB serial connection to an open source motor controller (ODrive v3.6) that converted it to a current command to the brushless DC motor. The control loop for sensing wing position and sending torque commands to the motor ran at a sample time $\Delta t = 1 \times 10^{-3}$ s.

Experiment details

To study how the robophysical system transitions between delayed asynchronous and synchronous forcing modes (Fig. 4.3d-f) we varied K_r and t_0/T_n in experiments. The robophysical experiments used approximately the same range of actuation parameters as the simulation: K_r spanning 0 to 1 and t_0/T_n from 0.02 to 1. The synchronous gain was set manually so that oscillations did not trigger the overload-current safety features of the motor driver, and the asynchronous gain was set using the same iterative force tuning procedure described above. We ran experiments for 30 seconds and we measured output power and frequency over the last 15 seconds of the experiment.

In a separate set of experiments we studied the frequency entrainment properties of the robophysical system under combinations of both synchronous and asynchronous forcing. We first determined a value of F_a in experiment that yielded high-amplitude asynchronous oscillations (106 $\pm$3 degrees peak-to-peak) at 3.2 Hz. Next, we performed experiments with a constant F_a, but with varied synchronous frequency $f_s = [0.815, 6.515]$ Hz at three levels of forcing magnitude, $F_s^* = [0.1, 0.2, 0.3]F_s$, with respect to the purely synchronous forcing magnitude of F_s. We then measured the output wingbeat angle and computed: 1) the emergent frequency

using the peak frequency of the Fourier transform, and 2) the peak-to-peak variation in wingbeat amplitude. The results of this experiment are shown in Fig. D.5.

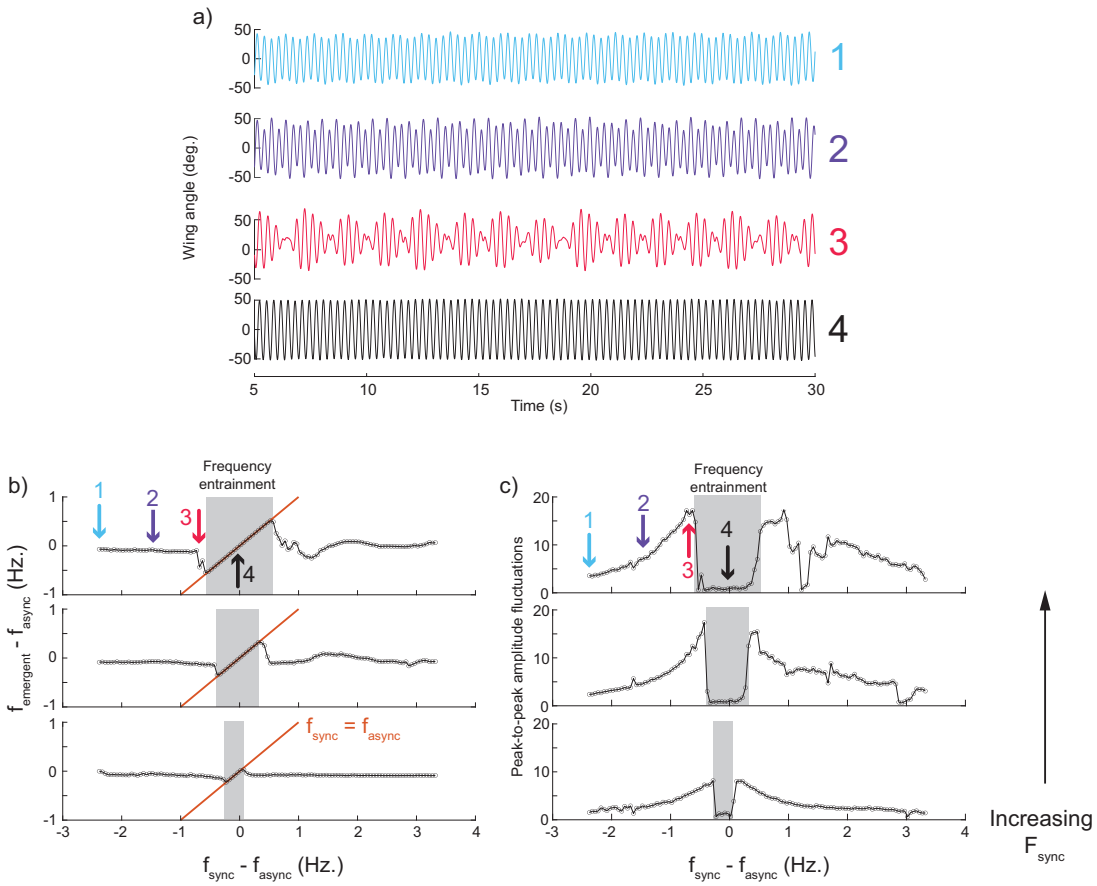

Figure D.5. Synchronous entrainment of asynchronous oscillations experiment. a) Emergent wingbeat angle versus time in experiments with a combination of asynchronous and synchronous actuation. The four plots correspond to varying the synchronous drive frequency compared to the emergent asynchronous frequency. The synchronous drive is increased from curves 1 through 4 as shown by the arrows in (b). As the synchronous drive frequency gets closer to the asynchronous frequency the wing motion exhibits large amplitude modulations due to a beat frequency between synchronous and asynchronous oscillations. However, when the synchronous drive is close enough the emergent wingbeat frequency entrains to the synchronous drive and the amplitude fluctuations disappear. b) The emergent wingbeat frequency compared to the driving wingbeat frequency. The gray region indicates frequency entrainment where the emergent frequency is exactly equal to the driving synchronous frequency. The three plots are of increasing synchronous forcing magnitude from bottom to top. c) The amplitude fluctuations increase as the synchronous frequency approaches the asynchronous frequency. However, when the driving frequency cross the Arnold tongue and the emergent frequency becomes entrained to the synchronous frequency, then the amplitude fluctuations disappear.

Table D.2. Dynamically-scaled robophysical system parameters

variable	value	description
k	0.525 N m	stiffness
I	0.0023 kg m^2	wing+system inertia
Γ	0.0017 kg m^2	damping torque coefficient
T	1	transmission ratio

D.1.6 Robobee experiment

We fabricated a single-winged version of a "dual-actuator" Harvard Robobee, following the Smart Composite Microstructure (SCM) process pioneered by the Harvard Microrobotics Lab [11], [13]. Wing parameter values are provided in Extended Data Table 3. The carbon fiber airframe, which holds the piezoelectric bending actuator and SCM transmission, was fixed to an acrylic mount on a manual translation stage to enable displacement sensor calibration.

In order to implement the delayed stretch activation model, it is necessary to estimate wing velocity in real time. We achieved this via a fiber-optic displacement sensor (D21, Philtec) pointed at a small piece of reflective tape glued to the bending actuator. The sensor is able to measure actuator displacement at which are fed into an a Simulink model that converts sensor voltage to displacement through a calibration curve, and then takes a numerical derivative to calculate wing rotational velocity. Wing rotational velocity is then supplied to an identical Simulink model as in the hawkmoth simulations and roboflapper experiments described above. The simulation of delayed stretch activation force was converted into an amplified voltage signal ($0V < V_{sig} < 200V$) and sent to the piezoelectric actuator resulting in wing oscillations. The control loop for sensing wing position and sending torque commands to the motor ran at a sample time $\Delta t = 1 \times 10^{-4}$ s. The asynchronous gain was chosen such that flapping angles were large but the actuator did not saturate, and the synchronous gain was set using the iterative force tuning procedure above. The Robobee flapping amplitudes did not exceed 50^o peak-to-peak. Observations of the Robobee wing angle were taken via a high framerate video camera (Phantom VEO-410) at 2500 FPS. Video frames were processed in MATLAB to get the wing angle.

Table D.3. Robobee parameters

variable	value	description
k	197.7 N m	stiffness
I	5.55E-11 kg m^2	wing inertia
Γ	5.68E-11 kg m^2	damping coefficient
T	3333 rad m^{-1}	transmission ratio

Flapping amplitude was estimated by finding oscillation peaks, and flapping period/frequency was estimated by computing the time between peaks and smoothing the resulting curve (Fig. D.6).

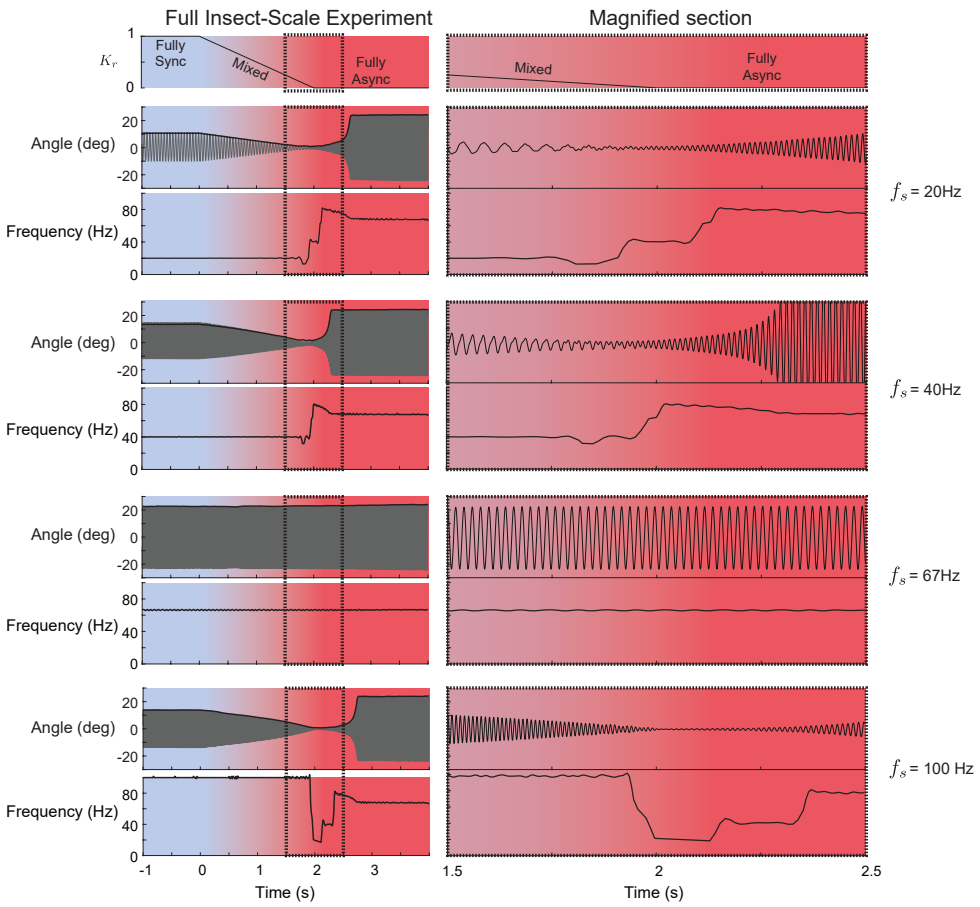

Figure D.6. Synchronous to asynchronous transitions in the robobee wing. Four tests at $f_s = [20, 40, 67, 100]$ Hz are shown in which the robobee is transitioned from synchronous to asynchronous forcing. Each experiment consisted of one second of synchronous flapping (blue region) at a particular frequency, followed by a 2 second transition in which K_r was linearly increased from $K_r = 1$ to $K_r = 0$ (top plot) followed by 2 seconds of 100% asynchronous operation (red region). The wingbeat angle and frequency are plotted for each of the four experiments (f_s is indicated on the right hand side). The left column shows the full time course of the experiments while the right column is a zoomed in region of the onset of fully asynchronous dynamics.

D.2 Additional Figures

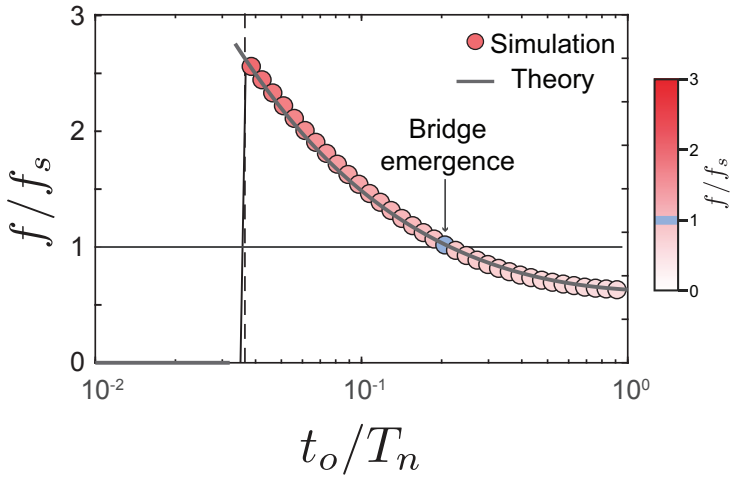

Figure D.7. Emergent frequency (f) normalized by the synchronous frequency (f_s) in the asynchronous regime ($K_r = 0$). As the time to peak force from delayed stretch activation (t_0) is increased the system undergoes a bifurcation in which steady wingbeats emerge. Dashed line is the prediction of this critical t_0/T_n from analysis of a linearized system. The emergent wingbeat frequency in simulation (circles) decreases as t_0 is increased. A linearized analysis of Equations 4.1 & 4.2 (See SI for details) is able to capture the emergent wingbeat frequency. The colormap of simulation points matches the heatmap of Fig. 4.3c,f. The bridge emerges when the emergent frequency from delayed stretch activation matches the synchronous frequency.

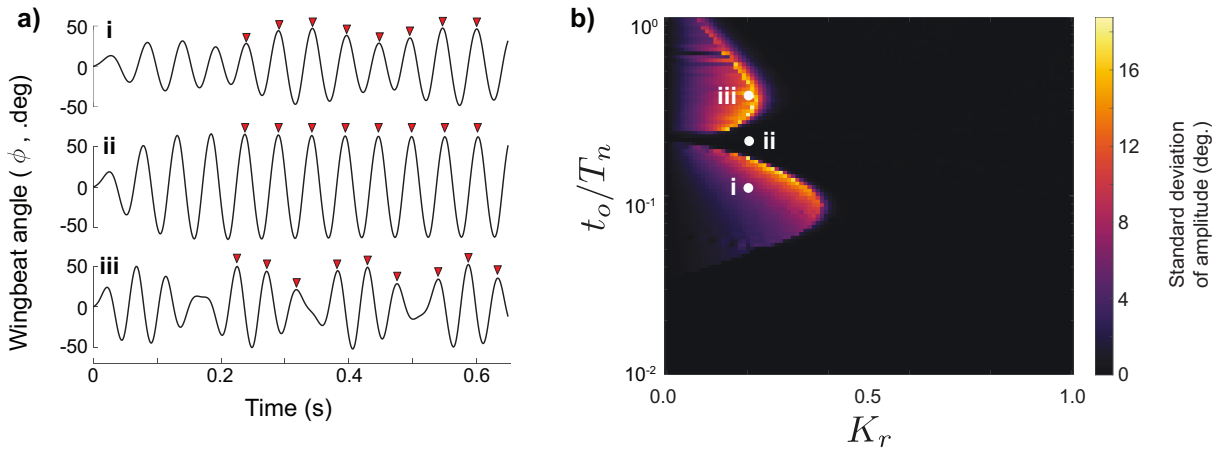

Figure D.8. Wingbeat amplitude variation in *M. sexta* simulations. a) The three plots show the wingbeat angle versus time at three different values of t_0/T_n, for a constant $K_r = 0.2$ (parameters for tests i, ii, and iii are shown in panel b). After transient oscillations die out we measure the amplitude of wingbeat peaks as a function of time (positive peaks are shown as red triangles). The top plot is an example in the asynchronous regime, displaying moderate amplitude fluctuations. The middle plot is the wing angle within the frequency locking synchronous regime (on the "bridge") where the wing amplitude is steady. Lastly, the bottom plot shows the wing motion in the asynchronous regime below the frequency locking "bridge". b) For all combinations of K_r and t_0/T_n we calculated the standard deviation of the wingbeat amplitudes which we show as a heatmap. Brighter regions of the plot correspond to where large stroke to stroke amplitude variation occurs (i.e. top and bottom plots in panel a). When the wingbeat is steady the amplitude variation is small these appear as the black regions. The boundaries between the synchronous and asynchronous regimes exhibit large amplitude fluctuations, while the bridge connects the synchronous and asynchronous regimes with smooth sinusoidal emergent wingbeats.

Data Availability

Trait data and posterior probabilities of the phylogenetic reconstructions are located in supplementary data table files. Raw physiological data for the muscle physiology experiments and data from the robophysical experiments are available at the Georgia Tech SmartTech data repository.

Code Availability

All code associated with simulations, robophysical models, and the robotics platform are available at the following public GitHub repository:

https://github.com/agilesystemslab/synch_asynch_sim.

Acknowledgments

This work was supported by US National Science Foundation RAISE grant no. IOS-2100858 to S.S. and N.G. and 1554790 (MPS-PoLS) and a Dunn Family Professorship to S.S. as well as the US National Science Foundation Physics of Living Systems SAVI student research network (GT node grant no. 1205878).

Bibliography

[1] B. Misof, R. G. Beutel, O. Niehuis, *et al.*, "Phylogenomics resolves the timing and pattern of insect evolution," *Science*, vol. 346, no. 6210, pp. 763–767, 2014.

[2] S. E. Farisenkov, D. Kolomenskiy, P. N. Petrov, *et al.*, "Novel flight style and light wings boost flight performance of tiny beetles," en, *Nature*, pp. 1–5, Jan. 2022.

[3] M. K. Salcedo, J. Hoffmann, S. Donoughe, and L. Mahadevan, "Computational analysis of size, shape and structure of insect wings," en, *Biol. Open*, vol. 8, no. 10, Oct. 2019.

[4] R. K. Josephson, J. G. Malamud, and D. R. Stokes, "Asynchronous Muscle: a Primer," en, *J. Exp. Biol.*, vol. 203, no. Pt 18, pp. 2713–2722, Sep. 2000.

[5] T. Deora, N. Gundiah, and S. P. Sane, "Mechanics of the thorax in flies," en, *J. Exp. Biol.*, vol. 220, no. Pt 8, pp. 1382–1395, Apr. 2017.

[6] T. Deora, S. S. Sane, and S. P. Sane, "Wings and halteres act as coupled dual oscillators in flies," en, *Elife*, vol. 10, Nov. 2021.

[7] L. Zheng, T. Hedrick, and R. Mittal, "A comparative study of the hovering efficiency of flapping and revolving wings," en, *Bioinspiration and Biomimetics*, vol. 8, no. 3, p. 036 001, May 2013.

[8] J. P. Whitney and R. J. Wood, "Conceptual design of flapping-wing micro air vehicles," en, *Bioinspiration and Biomimetics*, vol. 7, no. 3, p. 036 001, Apr. 2012.

[9] C. P. Ellington, "The novel aerodynamics of insect flight: applications to micro-air vehicles.," en, *J. Exp. Biol.*, vol. 202, no. Pt 23, pp. 3439–3448, 1999.

[10] S. P. Sane, "The aerodynamics of insect flight," en, *J. Exp. Biol.*, vol. 206, no. 23, pp. 4191–4208, Dec. 2003.

[11] R. J. Wood, S. Avadhanula, R. Sahai, E. Steltz, and R. S. Fearing, "Microrobot design using fiber reinforced composites," en, *J. Mech. Des.*, vol. 130, no. 5, p. 052 304, Mar. 2008.

[12] R. J. Wood, E. Steltz, and R. S. Fearing, "Optimal energy density piezoelectric bending actuators," en, *Sens. Actuators A Phys.*, vol. 119, no. 2, pp. 476–488, Apr. 2005.

[13] K. Y. Ma, P. Chirarattananon, S. B. Fuller, and R. J. Wood, "Controlled flight of a biologically inspired, insect-scale robot," EN, *Science*, vol. 340, no. 6132, pp. 603–607, May 2013.

[14] Z. Tu, F. Fei, J. Zhang, and X. Deng, "Acting Is Seeing: Navigating Tight Space Using Flapping Wings," in *2019 International Conference on Robotics and Automation (ICRA)*, May 2019, pp. 95–101.

[15] N. T. Jafferis, E. F. Helbling, M. Karpelson, and R. J. Wood, "Untethered flight of an insect-sized flapping-wing microscale aerial vehicle," en, *Nature*, vol. 570, no. 7762, pp. 491–495, 2019.

[16] G. C. H. E. de Croon, K. M. E. de Clercq, R. Ruijsink, B. Remes, and C. de Wagter, "Design, aerodynamics, and Vision-Based control of the DelFly," en, *International Journal of Micro Air Vehicles*, vol. 1, no. 2, pp. 71–97, 2009.

[17] M. Keennon, K. Klingebiel, and H. Won, "Development of the nano hummingbird: A tailless flapping wing micro air vehicle," en, Nashville, Tennessee: AIAA, 2012.

[18] Z. Tu, F. Fei, and X. Deng, "Untethered Flight of an At-Scale Dual-Motor Hummingbird Robot With Bio-Inspired Decoupled Wings," *IEEE Robotics and Automation Letters*, vol. 5, no. 3, pp. 4194–4201, Jul. 2020.

[19] S. B. Fuller, M. Karpelson, A. Censi, K. Y. Ma, and R. J. Wood, "Controlling free flight of a robotic fly using an onboard vision sensor inspired by insect ocelli," *J. R. Soc. Interface*, vol. 11, no. 97, p. 20 140 281, Aug. 2014.

[20] K. Jayaram, N. T. Jafferis, N. Doshi, B. Goldberg, and R. J. Wood, "Concomitant sensing and actuation for piezoelectric microrobots," en, *Smart Mater. Struct.*, vol. 27, no. 6, p. 065 028, May 2018.

[21] C. De Wagter, S. Tijmons, B. D. W. Remes, and G. C. H. E. de Croon, "Autonomous flight of a 20-gram flapping wing MAV with a 4-gram onboard stereo vision system," en, in *2014 IEEE International Conference on Robotics and Automation (ICRA)*, Hong Kong, China: IEEE, 2014, pp. 4982–4987.

[22] K. Y. Ma, P. Chirarattananon, and R. J. Wood, "Design and fabrication of an insect-scale flying robot for control autonomy," in *2015 IEEE/RSJ International Conference on Intelligent Robots and Systems (IROS)*, Sep. 2015, pp. 1558–1564.

[23] D. Campolo, M. Azhar, G. K. Lau, and M. Sitti, "Can DC motors directly drive flapping wings at high frequency and large wing strokes?" *IEEE/ASME Trans. Mechatron.*, vol. 19, no. 1, pp. 109–120, Feb. 2014.

[24] M. Azhar, D. Campolo, G.-K. Lau, and M. Sitti, "Flapping Wings with DC-Motors via Direct, Elastic Transmissions," en, *Proceedings of International Conference on Intelligent Unmanned Systems*, vol. 8, no. 0, 2012.

[25] M. Azhar, D. Campolo, G.-K. Lau, L. Hines, and M. Sitti, "Flapping wings via direct-driving by DC motors," in *2013 IEEE International Conference on Robotics and Automation*, May 2013, pp. 1397–1402.

[26] Y. Chen, H. Zhao, J. Mao, *et al.*, "Controlled flight of a microrobot powered by soft artificial muscles," en, *Nature*, vol. 575, no. April, pp. 324–329, Nov. 2019.

[27] S. Kim, Y.-H. Hsiao, Y. Lee, *et al.*, "Laser-assisted failure recovery for dielectric elastomer actuators in aerial robots," en, *Sci Robot*, vol. 8, no. 76, eadf4278, Mar. 2023.

[28] J. A. Roll, B. Cheng, and X. Deng, "An Electromagnetic Actuator for High-Frequency Flapping-Wing Microair Vehicles," *IEEE Trans. Rob.*, vol. 31, no. 2, pp. 400–414, Apr. 2015.

[29] M. Karasek, F. T. Muijres, C. D. Wagter, B. D. W. Remes, and G. C. H. E. De Croon, "A tailless aerial robotic flapper reveals that flies use torque coupling in rapid banked turns," *Science*, vol. 361, no. 6407, pp. 1089–1094, Sep. 2018.

[30] S. M. Walker, D. A. Schwyn, R. Mokso, *et al.*, "In Vivo Time-Resolved Microtomography Reveals the Mechanics of the Blowfly Flight Motor," en, *PLoS Biol.*, vol. 12, no. 3, p. 12, 2014.

[31] C. D. Williams, M. K. Salcedo, T. C. Irving, M. Regnier, and T. L. Daniel, "The length-tension curve in muscle depends on lattice spacing," en, *Proc. Biol. Sci.*, vol. 280, no. 1766, p. 20 130 697, Sep. 2013.

[32] J. Aguilar, T. Zhang, F. Qian, *et al.*, "A review on locomotion robophysics: The study of movement at the intersection of robotics, soft matter and dynamical systems," en, *Rep. Prog. Phys.*, vol. 79, no. 11, p. 110 001, Nov. 2016.

[33] N. Gravish and G. V. Lauder, "Robotics-inspired biology," en, *J. Exp. Biol.*, vol. 221, no. Pt 7, Mar. 2018.

[34] J. Seo, J. Kim, S. Park, and J. Cho, "A SLIP-based robot leg for decoupled spring-like behavior: Design and evaluation," *Int. J. Control Autom. Syst.*, vol. 17, no. 9, pp. 2388–2399, Sep. 2019.

[35] S. P. Sane and M. H. Dickinson, "The aerodynamic effects of wing rotation and a revised quasi-steady model of flapping flight," en, *Journal of Experimental Biology*, vol. 205, no. 8, pp. 1087–1096, 2002.

[36] A. Matta, J. Bayandor, F. Battaglia, and H. Pendar, "Effects of fish caudal fin sweep angle and kinematics on thrust production during low-speed thunniform swimming," en, *Biol. Open*, vol. 8, no. 7, Jul. 2019.

[37] Y. Ozkan-Aydin, B. Liu, A. C. Ferrero, M. Seidel, F. L. Hammond 3rd, and D. I. Goldman, "Lateral bending and buckling aids biological and robotic earthworm anchoring and locomotion," en, *Bioinspir. Biomim.*, vol. 17, no. 1, Nov. 2021.

[38] C. P. Ellington, C. van den Berg, A. P. Willmott, and A. L. R. Thomas, "Leading-edge vortices in insect flight," en, *Nature*, vol. 384, no. 6610, pp. 626–630, Dec. 1996.

[39] M. H. Dickinson, F. O. Lehmann, and S. P. Sane, "Wing rotation and the aerodynamics basis of insect flight," *Science*, vol. 284, no. June, pp. 1954–1960, 1999.

[40] L. Bennett, "Insect flight: Lift and rate of change of incidence," en, *Science*, vol. 167, no. 3915, pp. 177–179, Jan. 1970.

[41] T. Maxworthy, "Experiments on the Weis-Fogh mechanism of lift generation by insects in hovering flight. part 1. dynamics of the 'fling'," *J. Fluid Mech.*, vol. 93, no. 1, pp. 47–63, Jul. 1979.

[42] G. R. Spedding and T. Maxworthy, "The generation of circulation and lift in a rigid two-dimensional fling," *J. Fluid Mech.*, vol. 165, pp. 247–272, Apr. 1986.

[43] S. Sunada, K. Kawachi, I. Watanabe, and A. Azuma, "Fundamental analysis of three-dimensional 'near fling'," en, *J. Exp. Biol.*, vol. 183, no. 1, pp. 217–248, Oct. 1993.

[44] M. H. Dickinson and K. G. Götz, "Unsteady aerodynamic performance of model wings at low reynolds numbers," en, *J. Exp. Biol.*, vol. 174, no. 1, pp. 45–64, Jan. 1993.

[45] W. Lai, J. Yan, M. Motamed, and S. Green, "Force measurements on a scaled mechanical model of dragonfly in forward flight," in *ICAR '05. Proceedings., 12th International Conference on Advanced Robotics, 2005.*, Jul. 2005, pp. 595–600.

[46] V. T. Kasoju, C. L. Terrill, M. P. Ford, and A. Santhanakrishnan, "Leaky flow through simplified physical models of bristled wings of tiny insects during clap and fling," en, *Fluids Barriers CNS*, vol. 3, no. 2, p. 44, 2018.

[47] S. P. Sane and M. H. Dickinson, "The control of flight force by a flapping wing: Lift and drag production," en, *J. Exp. Biol.*, vol. 204, p. 20, 2001.

[48] H. E. Reid, R. K. Schwab, M. Maxcer, R. K. D. Peterson, E. L. Johnson, and M. Jankauski, "Wing flexibility reduces the energetic requirements of insect flight," en, *Bioinspir. Biomim.*, vol. 14, no. 5, p. 056 007, 2019.

[49] O. Sotavalta, "The essential factor regulating the wing-stroke frequency of insects in wing mutilation and loading experiments and in experiments at subatmospheric pressure," *Ann. Zool. Soc. Vanamo*, vol. 15, no. 2, pp. 1–66, 1952.

[50] C. H. Greenewalt, "The Wings of Insects and Birds as Mechanical Oscillators," *Proc. Am. Philos. Soc.*, vol. 104, no. 6, pp. 605–611, 1960.

[51] T. Weis-Fogh, "A rubber-like protein in insect cuticle," en, *J. Exp. Biol.*, vol. 37, no. 4, pp. 889–907, 1960.

[52] T. Weis-Fogh, *Molecular Interpreatation of the Elasticity of Resilin, a Rubber-like Protein*, 1961.

[53] S. O. Andersen and T. Weis-Fogh, "Resilin. A Rubberlike Protein in Arthropod Cuticle," in *Advances in Insect Physiology*, J. W. L. Beament, J. E. Treherne, and V. B. Wigglesworth, Eds., vol. 2, Academic Press, Jan. 1964, pp. 1–65.

[54] T. Weis-Fogh, "ENERGETICS OF HOVERING FLIGHT IN HUMMINGBIRDS AND IN DROSOPHILA," en, *J. Exp. Biol.*, vol. 56, p. 26, 1972.

[55] B. Y. T. Weis-fogh, "Quick Estimates of Flight Fitness in Hovering Animals, Including Novel mechanisms for Lift Production," en, *J. Exp. Biol.*, vol. 59, no. 1, pp. 169–230, Aug. 1973.

[56] R. J. Full, D. E. Koditschek, and R. J. Full, "Templates and anchors: neuromechanical hypotheses of legged locomotion on land," *J. Exp. Biol.*, vol. 2, no. 12, pp. 3–125, 1999.

[57] J. W. S. Pringle, "The excitation and contraction of the flight muscles of insects.," *J. Physiol.*, vol. 108, no. 2, pp. 226–232, 1949.

[58] K. E. Machin and J. W. S. Pringle, "The Physiology of Insect Fibrillar Muscle. II. Mechanical Properties of a Beetle Flight Muscle," en, *Proceedings of the Royal Society B: Biological Sciences*, vol. 151, no. 943, pp. 204–225, Dec. 1959.

[59] K. E. Machin and J. W. S. Pringle, "The Physiology of Insect Fibrillar Muscle. III. The Effect of Sinusoidal Changes of Length on a Beetle Flight Muscle," en, *Proceedings of the Royal Society of London. Series B. Biological Sciences*, vol. 152, no. 948, pp. 311–330, Jun. 1960.

[60] J. W. S. Pringle, "The contractile mechanism of insect fibrillar muscle," *Prog. Biophys. Mol. Biol.*, vol. 17, pp. 1–12, 1967.

[61] B. Bullard and A. Pastore, "Regulating the contraction of insect flight muscle," en, *J. Muscle Res. Cell Motil.*, vol. 32, no. 4-5, pp. 303–313, Dec. 2011.

[62] B. M. Glasheen, C. C. Eldred, L. C. Sullivan, *et al.*, "Stretch activation properties of *Drosophila* and *Lethocerus* indirect flight muscle suggest similar calcium-dependent mechanisms," *American Journal of Physiology-Cell Physiology*, vol. 313, no. 6, pp. C621–C631, Aug. 2017.

[63] J. W. S. Pringle, "The croonian lecture, 1977 - stretch activation of muscle: Function and mechanism," en, *Proc. R. Soc. Lond. B Biol. Sci.*, vol. 201, no. 1143, pp. 107–130, May 1978.

[64] M. Peckham, J. E. Molloy, J. C. Sparrow, and D. C. S. White, "Physiological properties of the dorsal longitudinal flight muscle and the tergal depressor of the trochanter muscle

of Drosophila melanogaster," en, *J. Muscle Res. Cell Motil.*, vol. 11, no. 3, pp. 203–215, Jun. 1990.

[65] S. Sicilia and D. A. Smith, "Theory of asynchronous oscillations in loaded insect flight muscle," *Math. Biosci.*, vol. 106, no. 2, pp. 159–201, 1991.

[66] A. Ayme-Southgate, R. Southgate, J. Saide, G. M. Benian, and M. L. Pardue, "Both synchronous and asynchronous muscle isoforms of projectin (the Drosophila bent locus product) contain functional kinase domains," *J. Cell Biol.*, vol. 128, no. 3, pp. 393–403, 1995.

[67] D. A. Syme and R. K. Josephson, "How to Build Fast Muscles: Synchronous and Asynchronous Designs," en, *Integr. Comp. Biol.*, vol. 42, no. 4, pp. 762–770, Aug. 2002.

[68] J. A. Henkin, D. W. Maughan, and J. O. Vigoreaux, "Mutations that affect flightin expression in Drosophila alter the viscoelastic properties of flight muscle fibers," en, *American Journal of Physiology - Cell Physiology*, vol. 286, no. 1 55-1, pp. C65–72, Jan. 2004.

[69] M. Linari, M. K. Reedy, M. C. Reedy, V. Lombardi, and G. Piazzesi, "Ca-activation and stretch-activation in insect flight muscle.," en, *Biophys. J.*, vol. 87, no. 2, pp. 1101–1111, Aug. 2004.

[70] D. M. Swank, V. K. Vishnudas, and D. W. Maughan, "An exceptionally fast actomyosin reaction powers insect flight muscle," en, *Proc. Natl. Acad. Sci. U. S. A.*, vol. 103, no. 46, pp. 17 543–17 547, Nov. 2006.

[71] B. M. Glasheen, S. Ramanath, M. Patel, *et al.*, "Five Alternative Myosin Converter Domains Influence Muscle Power, Stretch Activation, and Kinetics," en, *Biophys. J.*, vol. 114, no. 5, pp. 1142–1152, Mar. 2018.

[72] M. Kawai and P. W. Brandt, "Sinusoidal analysis: a high resolution method for correlating biochemical reactions with physiological processes in activated skeletal muscles of rabbit, frog and crayfish," en, *J. Muscle Res. Cell Motil.*, vol. 1, no. 3, pp. 279–303, 1980.

[73] J. E. Molloy, V. Kyrtatas, J. C. Sparrow, and D. C. S. White, "Kinetics of flight muscles from insects with different wingbeat frequencies," en, *Nature*, vol. 328, no. 6129, pp. 449–451, 1987.

[74] D. M. Swank, "Mechanical analysis of Drosophila indirect flight and jump muscles," en, *Methods*, Methods in invertebrate muscle biology, vol. 56, no. 1, pp. 69–77, Jan. 2012.

[75] R. Dudley, *The Biomechanics of Insect Flight: Form, Function, Evolution* (Princeton paperbacks), en, 2. print., 1. paperback print. Princeton, NJ: Princeton University Press, Sep. 2002, p. 476.

[76] J. Gau, N. Gravish, and S. Sponberg, "Indirect actuation reduces flight power requirements in Manduca sexta via elastic energy exchange," *J. R. Soc. Interface*, vol. 16, no. 161, p. 20 190 543, Dec. 2019.

[77] M. Jensen, T. Weis-Fogh, and J. W. S. Pringle, "Biology and Physics of Locust Flight. V. Strength and Elasticity of Locust Cuticle," *Philos. Trans. R. Soc. Lond. B Biol. Sci.*, vol. 245, no. 721, pp. 137–169, Oct. 1962.

[78] N. T. George, T. C. Irving, C. D. Williams, T. L. Daniel, H. Iwamoto, and N. Yagi, "The Cross-Bridge Spring: Can Cool Muscles Store Elastic Energy?" en, *Science*, vol. 340, no. 6137, pp. 1217–1220, Jun. 2013.

[79] R. Ingersoll and D. Lentink, "How the hummingbird wingbeat is tuned for efficient hovering," en, *J. Exp. Biol.*, vol. 221, no. 20, jeb178228, Oct. 2018.

[80] N. Konow, J. A. Cheney, T. J. Roberts, J. R. S. Waldman, and S. M. Swartz, "Spring or string: Does tendon elastic action influence wing muscle mechanics in bat flight?" en, *Proc. R. Soc. B*, vol. 282, no. 1816, p. 20 151 832, Oct. 2015.

[81] O. Sotavalta, "Flight-tone and wing-stroke frequency of insects and the dynamics of insect flight," en, *Nature*, vol. 170, no. 4338, pp. 1057–1058, Dec. 1952.

[82] M. H. Dickinson and J. R. B. Lighton, "Muscle efficiency and elastic storage in the flight motor of Drosophila," *Science*, vol. 268, no. 5207, pp. 87–90, May 1995.

[83] M. A. Jankauski, "Measuring the frequency response of the honeybee thorax," en, *Bioinspir. Biomim.*, vol. 15, no. 4, p. 046 002, May 2020.

[84] R. E. Snodgrass *et al.*, "Principles of insect morphology," *Principles of Insect Morphology.*, 1935.

[85] H. Bennet-Clark, "THE FIRST DESCRIPTION OF RESILIN," en, *J. Exp. Biol.*, vol. 210, no. 22, pp. 3879–3881, Nov. 2007.

[86] D. M. Dudek and R. J. Full, "Passive mechanical properties of legs from running insects," en, *J. Exp. Biol.*, vol. 209, no. Pt 8, pp. 1502–1515, Apr. 2006.

[87] C. F. Beards, *Engineering Vibration Analysis with Application to Control Systems*. Elsevier, 1995.

[88] C. van den Berg and C. P. Ellington, "The vortex wake of a 'hovering' model hawkmoth," en, *Philos. Trans. R. Soc. Lond. B Biol. Sci.*, vol. 352, no. 1351, pp. 317–328, Mar. 1997.

[89] N. T. Jafferis, M. A. Graule, and R. J. Wood, "Non-linear resonance modeling and system design improvements for underactuated flapping-wing vehicles," in *2016 IEEE International Conference on Robotics and Automation (ICRA)*, vol. 2016-June, May 2016, pp. 3234–3241.

[90] J. Zhang and X. Deng, "Resonance Principle for the Design of Flapping Wing Micro Air Vehicles," *IEEE Trans. Rob.*, vol. 33, no. 1, pp. 183–197, Feb. 2017.

[91] S. S. Baek, K. Y. Ma, and R. S. Fearing, "Efficient resonant drive of flapping-wing robots," en, in *2009 IEEE/RSJ International Conference on Intelligent Robots and Systems*, St. Louis, MO, USA: IEEE, 2009, pp. 2854–2860.

[92] T. J. Roberts and E. Azizi, "Flexible mechanisms: the diverse roles of biological springs in vertebrate movement," *J. Exp. Biol.*, vol. 214, no. 3, pp. 353–361, 2011.

[93] B. W. Tobalske and A. A. Biewener, "Contractile properties of the pigeon supracoracoideus during different modes of flight," en, *J. Exp. Biol.*, vol. 211, no. Pt 2, pp. 170–179, Jan. 2008.

[94] F. Baeumler and S. Buesse, "Resilin in the flight apparatus of odonata (insecta)-cap tendons and their biomechanical importance for flight," English, *Biol. Lett.*, vol. 15, no. 5, May 2019.

[95] C. P. Ellington, "THE AERODYNAMICS OF HOVERING INSECT FLIGHT: 4. AERODYNAMIC MECHANISMS," *Philos. Trans. R. Soc. Lond. B Biol. Sci.*, 1984.

[96] M. Gralka and K. Kroy, "Inelastic mechanics: A unifying principle in biomechanics," en, *Biochim. Biophys. Acta*, vol. 1853, no. 11 Pt B, pp. 3025–3037, Nov. 2015.

[97] M. Percin, Y. Hu, B. W. van Oudheusden, B. Remes, and F. Scarano, "Wing flexibility effects in Clap-and-Fling," en, *International Journal of Micro Air Vehicles*, vol. 3, no. 4, pp. 217–227, 2011.

[98] Y. Lu, G. X. Shen, and G. J. Lai, "Dual leading-edge vortices on flapping wings," *J. Exp. Biol.*, vol. 209, no. 24, p. 5005, Dec. 2006.

[99] Y. Lu and G. X. Shen, "Three-dimensional flow structures and evolution of the leading-edge vortices on a flapping wing," *J. Exp. Biol.*, vol. 211, no. 8, p. 1221, Apr. 2008.

[100] P. Balasubramanian, G. Ferrari, and M. Amabili, "Identification of the viscoelastic response and nonlinear damping of a rubber plate in nonlinear vibration regime," en, *Mech. Syst. Signal Process.*, vol. 111, pp. 376–398, Oct. 2018.

[101] C. T. Coots, "Measurement of the damping properties of silicone-based elastomers over wide temperature ranges," en, *J. Sound Vib.*, vol. 21, no. 2, pp. 133–147, 1972.

[102] J. R. Rice, N. Lapusta, and K. Ranjith, "Rate and state dependent friction and the stability of sliding between elastically deformable solids," *J. Mech. Phys. Solids*, vol. 49, no. 9, pp. 1865–1898, Sep. 2001.

[103] M. B. Bennett, R. F. Ker, and R. M. Alexander, "Elastic properties of structures in the tails of cetaceans (*Phocaena* and *Lagenorhynchus*) and their effect on the energy cost of swimming," *J. Zool.*, vol. 211, no. 1, pp. 177–192, 1987.

[104] L. Hines, D. Campolo, and M. Sitti, "Liftoff of a Motor-Driven, Flapping-Wing microaerial vehicle capable of resonance," *IEEE Trans. Rob.*, vol. 30, no. 1, pp. 220–232, Feb. 2014.

[105] A. Pons and T. Beatus, "Distinct forms of resonant optimality within insect indirect flight motors," en, *J. R. Soc. Interface*, vol. 19, no. 190, p. 20 220 080, May 2022.

[106] J. Lynch, J. Gau, S. Sponberg, and N. Gravish, "Dimensional analysis of spring-wing systems reveals performance metrics for resonant flapping-wing flight," EN, *J. R. Soc. Interface*, vol. 18, p. 20 200 888, Feb. 2021.

[107] D. D. Chin and D. Lentink, "Flapping wing aerodynamics: from insects to vertebrates," *J. Exp. Biol.*, vol. 219, no. 7, pp. 920–932, 2016.

[108] J. Gau, R. Gemilere, L.-V. (FM subteam), J. Lynch, N. Gravish, and S. Sponberg, "Rapid frequency modulation in a resonant system: Aerial perturbation recovery in hawkmoths," *Proceedings of the Royal Society B: Biological Sciences*, vol. 288, no. 1951, p. 20 210 352, May 2021.

[109] Y. E. Bayiz and B. Cheng, "State-space aerodynamic model reveals high force control authority and predictability in flapping flight," en, *J. R. Soc. Interface*, vol. 18, no. 181, p. 20 210 222, Aug. 2021.

[110] C. Harvey, V. B. Baliga, J. C. M. Wong, D. L. Altshuler, and D. J. Inman, "Birds can transition between stable and unstable states via wing morphing," en, *Nature*, vol. 603, no. 7902, pp. 648–653, Mar. 2022.

[111] A. K. Loya, S. K. Van Houten, B. M. Glasheen, and D. M. Swank, "Shortening deactivation: Quantifying a critical component of cyclical muscle contraction," en, *Am. J. Physiol. Cell Physiol.*, vol. 322, no. 4, pp. C653–C665, Apr. 2022.

[112] J. W. S. Pringle, "The mechanism of the myogenic rhythm of certain insect striated muscles," en, *J. Physiol.*, vol. 124, no. 2, pp. 269–291, 1954.

[113] R. K. Josephson and D. Young, "A synchronous insect muscle with an operating frequency greater than 500 hz," *J. Exp. Biol.*, vol. 118, no. 1, pp. 185–208, Sep. 1985.

[114] T. Deora, A. K. Singh, and S. P. Sane, "Electrophysiological Properties Under Heart Failure Conditions in a Human Ventricular Cell: A Modeling Study Mohamed," en, *Proceedings of the National Academy of Sciences*, vol. 112, no. 5, pp. 1481–1486, Feb. 2015.

[115] X. Meng, X. Liu, Z. Chen, J. Wu, and G. Chen, "Wing kinematics measurement and aerodynamics of hovering droneflies with wing damage," en, *Bioinspir. Biomim.*, vol. 18, no. 2, Feb. 2023.

[116] J. James, V. Iyer, Y. Chukewad, S. Gollakota, and S. B. Fuller, "Liftoff of a 190 mg Laser-Powered aerial vehicle: The lightest wireless robot to fly," in *2018 IEEE International Conference on Robotics and Automation (ICRA)*, May 2018, pp. 1–8.

[117] B. Kuhn-Neto, F. A. L. Contrera, M. S. Castro, and J. C. Nieh, "Long distance foraging and recruitment by a stingless bee, Melipona mandacaia," en, *Apidologie*, vol. 40, no. 4, pp. 472–480, Jul. 2009.

[118] J. R. Riley, D. Reynolds, S. Mukhopadhyay, M. R. Ghosh, and T. K. Sarkar, "Long-distance migration of aphids and other small insects in northeast India," *Eur. J. Entomol.*, vol. 92, pp. 639–653, Jan. 1995.

[119] Z. Tu, F. Fei, L. Liu, Y. Zhou, and X. Deng, "Flying With Damaged Wings: The Effect on Flight Capacity and Bio-Inspired Coping Strategies of a Flapping Wing Robot," *IEEE Robotics and Automation Letters*, vol. 6, no. 2, pp. 2114–2121, Apr. 2021.

[120] A. M. Mountcastle, T. M. Alexander, C. M. Switzer, and S. A. Combes, "Wing wear reduces bumblebee flight performance in a dynamic obstacle course," *Biol. Lett.*, vol. 12, no. 6, p. 20 160 294, Jun. 2016.

[121] L. E. Ford, A. F. Huxley, and R. M. Simmons, "Tension responses to sudden length change in stimulated frog muscle fibres near slack length," en, *J. Physiol.*, vol. 269, no. 2, pp. 441–515, Jul. 1977.

[122] N. Josephson, "Power output from a flight muscle of the bumblebee bombus terrestris. II. characterization of the parameters affecting power output," eng, *J. Exp. Biol.*, vol. 200, no. Pt 8, pp. 1227–1239, 1997.

[123] J. E. Molloy, "Active insect fibrillar flight muscle, its mechanical performance and Cross-Bridge kinetics," en, Ph.D. dissertation, 1988.

[124] S. N. Fry, R. Sayaman, and M. H. Dickinson, "The aerodynamics of hovering flight in drosophila," en, *J. Exp. Biol.*, vol. 208, no. Pt 12, pp. 2303–2318, Jun. 2005.

[125] J. Buchli, F. Iida, and A. Ijspeert, "Finding resonance: Adaptive frequency oscillators for dynamic legged locomotion," en, in *2006 IEEE/RSJ International Conference on Intelligent Robots and Systems*, Beijing, China: IEEE, 2006, pp. 3903–3909.

[126] L. J. Revell, "Phytools: An R package for phylogenetic comparative biology (and other things)," *Methods Ecol. Evol.*, vol. 3, no. 2, pp. 217–223, 2012.

[127] K. J. Tong, S. Duchêne, S. Y. W. Ho, and N. Lo, "Comment on "phylogenomics resolves the timing and pattern of insect evolution"," *Science*, vol. 349, no. 6247, p. 487, 2015.

[128] M. J. Cullen, "The distribution of asynchronous muscle in insects with particular reference to the Hemiptera: an electron microscope study," *Journal of Entomology Series A, General Entomology*, vol. 49, no. 1, pp. 17–41, 1974.

[129] J. D. Boyko and J. M. Beaulieu, "Generalized hidden Markov models for phylogenetic comparative datasets," *Methods Ecol. Evol.*, vol. 12, no. 3, pp. 468–478, 2021.

[130] B. King and M. S. Y. Lee, "Ancestral state reconstruction, rate heterogeneity, and the evolution of reptile viviparity," *Syst. Biol.*, vol. 64, no. 3, pp. 532–544, 2015.

[131] M. S. Tu and T. L. Daniel, "Submaximal power output from the dorsolongitudinal flight muscles of the hawkmoth Manduca sexta," *J. Exp. Biol.*, vol. 207, no. 26, pp. 4651–4662, 2004.

[132] R. K. Josephson and C. P. Ellington, "Power output from a flight muscle of the bumblebee Bombus terrestris .1. Some features of the dorso-ventral flight muscle," *J. Exp. Biol.*, vol. 200, no. 8, pp. 1215–1226, 1997.

[133] D. M. Swank, A. F. Knowles, J. A. Suggs, *et al.*, "The myosin converter domain modulates muscle performance," en, *Nat. Cell Biol.*, vol. 4, no. 4, pp. 312–316, Apr. 2002.

[134] A. P. Willmott and C. P. Ellington, "The mechanics of flight in the hawkmoth Manduca sexta II. Aerodynamic consequences of kinematic and morphological variation," *J. Exp. Biol.*, vol. 200, pp. 2723–2745, 1997.

[135] R. K. Josephson, J. G. Malamud, and D. R. Stokes, "Power output by an asynchronous flight muscle from a beetle.," *J. Exp. Biol.*, vol. 203, no. Pt 17, pp. 2667–2689, Sep. 2000.

[136] H. Iwamoto, "Synchrotron radiation x-ray diffraction techniques applied to insect flight muscle," *Int. J. Mol. Sci.*, vol. 19, no. 6, 2018.

[137] F.-O. Lehmann, D. A. Skandalis, and R. Berthé, "Calcium signalling indicates bilateral power balancing in the Drosophila flight muscle during manoeuvring flight.," *J. R. Soc. Interface*, vol. 10, no. 82, p. 20 121 050, May 2013.

[138] Q. Wang, C. Zhao, and D. M. Swank, "Calcium and stretch activation modulate power generation in Drosophila flight muscle," en, *Biophys. J.*, vol. 101, no. 9, pp. 2207–2213, Nov. 2011.

[139] B. Agianian, U. Krzic, F. Qiu, W. A. Linke, K. Leonard, and B. Bullard, "A troponin switch that regulates muscle contraction by stretch instead of calcium.," *EMBO J.*, vol. 23, no. 4, pp. 772–779, 2004.

[140] A. Ayme-Southgate, S. Feldman, and D. Fulmer, "Myofilament proteins in the synchronous flight muscles of Manduca sexta show both similarities and differences to Drosophila melanogaster," *Insect Biochem. Mol. Biol.*, vol. 62, pp. 174–182, 2015.

[141] S. L. Hooper and J. B. Thuma, "Invertebrate Muscles: Muscle Specific Genes and Proteins," *Physiol. Rev.*, vol. 85, no. 3, pp. 1001–1060, 2005.

[142] S. L. Hooper, K. H. Hobbs, and J. B. Thuma, "Invertebrate muscles: Thin and thick filament structure; molecular basis of contraction and its regulation, catch and asynchronous muscle," en, *Prog. Neurobiol.*, vol. 86, no. 2, pp. 72–127, Oct. 2008.

[143] H. Iwamoto, "Structure, function and evolution of insect flight muscle.," *Biophysics*, vol. 7, pp. 21–28, 2011.

[144] C. P. Ellington, "THE AERODYNAMICS OF HOVERING INSECT FLIGHT: 1. THE QUASI-STEADY ANALYSIS," *Philos. Trans. R. Soc. Lond. B Biol. Sci.*, 1984.

[145] G. J. Berman and Z. J. Wang, "Energy-minimizing kinematics in hovering insect flight," en, *J. Fluid Mech.*, vol. 582, pp. 153–168, 2007.

[146] B. R. Jewell and J. C. Ruegg, "Oscillatory contraction of insect fibrillar muscle after glycerol extraction," *Proceedings of the Royal Society of London. Series B, Biological Sciences*, vol. 164, no. 996, pp. 428–459, 1966.

[147] J. Gau, E. S. Wold, J. Lynch, N. Gravish, and S. Sponberg, "The hawkmoth wingbeat is not at resonance," en, *Biol. Lett.*, vol. 18, no. 5, p. 20 220 063, May 2022.

[148] A. Pikovsky, J. Kurths, M. Rosenblum, and J. Kurths, *Synchronization: A Universal Concept in Nonlinear Sciences*, en. Cambridge University Press, Apr. 2003.

[149] D. Lentink, G. F. Van Heijst, F. T. Muijres, and J. L. Van Leeuwen, "Vortex interactions with flapping wings and fins can be unpredictable," en, *Biol. Lett.*, vol. 6, no. 3, pp. 394–397, Jun. 2010.

[150] J. Bartussek, A. K. Mutlu, M. Zapotocky, and S. N. Fry, "Limit-cycle-based control of the myogenic wingbeat rhythm in the fruit fly *Drosophila*," en, *J. R. Soc. Interface*, vol. 10, no. 80, p. 20 121 013, Mar. 2013.

[151] M. Ilton, M. S. Bhamla, X. Ma, *et al.*, "The principles of cascading power limits in small, fast biological and engineered systems," en, *Science*, vol. 360, no. 6387, eaao1082, Apr. 2018.

[152] R. J. Wood, "The first takeoff of a biologically inspired at-scale robotic insect," *IEEE Trans. Rob.*, vol. 24, no. 2, pp. 341–347, Apr. 2008.

[153] J. W. S. Pringle, "The bidder lecture, 1980 the evolution of fibrillar muscle in insects," *Journal of Experiment Biology*, vol. 94, pp. 1–14, 1981.

[154] K. D. Roeder, "Movements of the thorax and potential changes in the thoracic muscles of insects during flight," *Biol. Bull.*, vol. 100, no. 2, pp. 95–106, 1951.

[155] D. S. Smith, "The Structure of Insect muscles," in *Insect Ultrastructure*, 1984, pp. 111–150.

[156] M. Dickinson, G. Farman, M. Frye, *et al.*, "Molecular dynamics of cyclically contracting insect flight muscle in vivo," *Nature*, vol. 433, no. 7023, pp. 330–333, 2005.

[157] H. Iwamoto and N. Yagi, "The molecular trigger for high-speed wing beats in a bee," *Science*, vol. 341, no. 6151, pp. 1243–1246, 2013.

[158] C. P. Ellington, "THE AERODYNAMICS OF HOVERING INSECT FLIGHT: 6. LIFT AND POWER REQUIREMENTS," *Philos. Trans. R. Soc. Lond. B Biol. Sci.*, 1984.

[159] A. Pons, I. Perl, O. Ben-Dov, R. Maya, and T. Beatus, "Solving the thoracic inverse problem in the fruit fly," en, *Bioinspir. Biomim.*, vol. 18, no. 4, May 2023.

[160] R. H. Miller, "Hill-Based muscle modeling," in *Handbook of Human Motion*, B. Müller, S. I. Wolf, G.-P. Brueggemann, *et al.*, Eds., Cham: Springer International Publishing, 2018, pp. 1–22.

[161] N. Thomas and R. A. Thornhill, "Negative viscosity and nonlinear elasticity of muscle cross-bridges," en, *Chaos Solitons Fractals*, vol. 5, no. 3-4, pp. 393–406, Mar. 1995.

[162] D. S. Smith and J. Kathirithamby, "Atypical 'fibrillar' flight muscle in strepsiptera," *Tissue and Cell*, vol. 16, no. 6, pp. 929–940, 1984.

[163] H. V. Daly, "Close-Packed and Fibrillar Muscles of the Hymenoptera," *Ann. Entomol. Soc. Am.*, vol. 56, no. 3, pp. 295–306, 1963.

[164] A. A. Polilov, "Anatomy of the adult and the first-instar nymph of the book louse, liposcelis bostrychophila (psocoptera, liposcelididae)," *Entomol. Rev.*, vol. 96, no. 9, pp. 1165–1181, 2016.

[165] S. J. Kraus and L. H. Glassman, "The crab louse—review of physiology and study of anatomy as seen by the scanning electron microscope," *J. Am. Vener. Dis. Assoc.*, vol. 2, pp. 12–18, 1976.

[166] R. S. De Moya, K. Yoshizawa, K. K. O. Walden, A. D. Sweet, C. H. Dietrich, and J. Kevin P, "Phylogenomics of parasitic and nonparasitic lice (insecta: Psocodea): Combining sequence data and exploring compositional bias solutions in next generation data sets," *Syst. Biol.*, vol. 70, no. 4, pp. 719–738, 2021.

[167] M. A. B. Deakin, "Formulae for insect wingbeat frequency," *J. Insect Sci.*, vol. 10, p. 96,

[168] C. K. Taylor, "The genus lithoseopsis (psocodea: Amphientomidae) in the western australian fauna, with description of the male of lithoseopsis humphreysi from barrow island," *Records of the Western Australian Museum, Supplement*, vol. 83, no. 1, p. 245, 2013.

[169] G. Enderlein, *The Scaly Winged Copeognatha: Monograph of the Amphientomidae, Lepidopsocidae, and Lepidillidae in Relation to Their Morphology and Taxonomy*. 1906.

[170] S. P. Sane, "Neurobiology and biomechanics of flight in miniature insects," *Curr. Opin. Neurobiol.*, vol. 41, pp. 158–166, 2016.

[171] K. P. Johnson, C. H. Dietrich, F. Friedrich, *et al.*, "Phylogenomics and the evolution of hemipteroid insects," *Proc. Natl. Acad. Sci. U. S. A.*, vol. 115, no. 50, pp. 12 775–12 780, 2018.

[172] M. Burrows, V. Hartung, and H. Hoch, "Jumping behaviour in a gondwanan relict insect (hemiptera: Coleorrhyncha: Peloridiidae)," *J. Exp. Biol.*, vol. 210, no. 18, pp. 3311–3318, 2007.

[173] D.-J. Wan, J. Chen, L.-B. Jiang, L.-Q. Ge, and J.-C. Wu, "Effects of the insecticide triazophos on the ultrastructure of the flight muscle of the brown planthopper nilaparvata lugens stål (hemiptera: Delphacidae)," *Crop Prot.*, vol. 43, pp. 54–59, 2013.

[174] M. G. Liu, C. X. Jiang, M. Mao, *et al.*, "Effect of the insecticide dinotefuran on the ultrastructure of the flight muscle of female sogatella furcifera (hemiptera: Delphacidae)," *J. Econ. Entomol.*, vol. 110, no. 2, pp. 632–640, 2017.

[175] J. M. Peters, N. Gravish, and S. A. Combes, "Wings as impellers: Honey bees co-opt flight system to induce nest ventilation and disperse pheromones," *J. Exp. Biol.*, vol. 220, no. April, pp. 2203–2209, 2017.

[176] J. M. Beaulieu, B. C. O'Meara, and M. J. Donoghue, "Identifying hidden rate changes in the evolution of a binary morphological character: The evolution of plant habit in campanulid angiosperms," *Syst. Biol.*, vol. 62, no. 5, pp. 725–737, 2013.

[177] M. S. Tu and T. L. Daniel, "Cardiac-like behavior of an insect flight muscle.," *J. Exp. Biol.*, vol. 207, no. 14, pp. 2455–2464, 2004.

[178] J. D. Powers, S. A. Malingen, M. Regnier, and T. L. Daniel, "The Sliding Filament Theory since Andrew Huxley: Multiscale and Multidisciplinary Muscle Research," *Annu. Rev. Biophys.*, vol. 50, pp. 373–400, 2021.

[179] C. P. Ellington, "THE AERODYNAMICS OF HOVERING INSECT FLIGHT: 2. MORPHOLOGICAL PARAMETERS," *Philos. Trans. R. Soc. Lond. B Biol. Sci.*, 1984.

[180] J. S. Han, J. K. Kim, J. W. Chang, and J. H. Han, "An improved quasi-steady aerodynamic model for insect wings that considers movement of the center of pressure," en, *Bioinspiration and Biomimetics*, vol. 10, no. 4, p. 046 014, Jul. 2015.